# Tuning the Electron-Phonon Interaction in Bismuth Selenide ($Bi_2Se_3$) Topological Insulator Nanostructures

Dissertation

zur Erlangung des Doktorgrades
an der Fakultät für Mathematik, Informatik und Naturwissenschaften
im Fachbereich Physik
der Universität Hamburg

vorgelegt von
**Christian Ikechukwu Nweze**

Hamburg
2022

| | |
|---|---|
| Gutachter der Dissertation: | Prof. Dr. Michael Rübhausen<br>Prof. Dr. Nils Huse |
| Zusammensetzung der Prüfungskommission: | Prof. Dr. Wolfgang J. Parak<br>Prof. Dr. Nils Huse<br>Prof. Dr. Michael Rübhausen<br>Dr. Robert Zierold<br>Prof. Dr. Daniela Pfannkuche |
| Vorsitzende der Prüfungskommission: | Prof. Dr. Daniela Pfannkuche |
| Vorsitzender des Fach-Promotionsausschusses Physik: | Prof. Dr. Wolfgang J. Parak |
| Leiter des Fachbereichs Physik: | Prof. Dr. Günter H.W. Sigl |
| Dekan der Fakultät MIN: | Prof. Dr.-Ing. Norbert Ritter |
| Datum der Disputation: | 25.10.2022 |

# Abstract

Three dimensional (3D) topological insulators (TIs) like bismuth selenide ($Bi_2Se_3$) are unique set of quantum materials that hold potentials for realizing Majorana Fermions and spintronics applications. Electrons at the metallic surface states of $Bi_2Se_3$ are spin textured and are immune to non-magnetic impurity backscattering. The extraordinary properties of $Bi_2Se_3$ can be modified by reducing the size of nanostructure, changing the shape and injecting carriers into the metallic surface states of $Bi_2Se_3$. The interplay between the interaction of the injected carriers and phonons in $Bi_2Se_3$ is studied with a nanoscopic Raman. We developed a nanoscopic Raman with beam spot size of $\approx$ 211 nm to reveal locally resolved information about charge transfer onto the metallic surface states of $Bi_2Se_3$. Geometrical two-dimensional (2D) nanoflakes (NFs) of $Bi_2Se_3$ on gold (Au) substrate reveal interface-enhanced Raman scattering, broadening of phonon linewidth and strong phonon renormalization induced by carriers injected from the Au substrate to the $Bi_2Se_3$ surface states. Geometrical confinement of $Bi_2Se_3$ cylindrical nanowires (NWs) from 2D limit to 1D result in splitting of the metallic surface states into sub-bands, opening of a gap at the Dirac point and lifting of the non-degenerate surface states because of a $\pi$-Berry Phase effect. Magnetic field of flux ratio $r = 0.5$ applied along the axis of $Bi_2Se_3$ NW nullifies the effect of the $\pi$-Berry Phase and thus closes the gap at the Dirac point (*i.e.* restores the non-degenerate surface states). The 2D to 1D crossover in $Bi_2Se_3$ cylindrical nanowire below 50 nm radius is marked by sudden appearance of plasmonic surface-enhanced Raman scattering (SERS) which dominates the electronic excitation spectrum. In plasmonic Au nanoparticles (AuNPs) injecting hot carriers into the $Bi_2Se_3$ nanoribbons (NRs) we report enhancement of phonon modes which is dependent on the excitation wavelength and the distance within the vicinity of AuNP. In resonance at 633 nm excitation wavelength and on 108 nm AuNP, we reveal that hot electrons are efficiently injected into $Bi_2Se_3$ NR which enhanced the phonon modes by a factor of 350. We attribute the behavior to double resonance effect induced by plasmonic AuNP and interband transition in $Bi_2Se_3$ TI.

# Zusammenfassung

Dreidimensionale (3D) topologische Isolatoren (Tls) wie Bismutselenid ($Bi_2Se_3$) sind einzigartige Quantenmaterialien, die das Potenzial haben, Majorana-Fermionen und Spintronik-Anwendungen zu realisieren. Elektronen auf den Oberflächenzuständen von $Bi_2Se_3$ sind spin-strukturiert und gegen Rückstreuung an nicht-magnetischen Verunreinigungen immun. Die außergewöhnlichen Eigenschaften von $Bi_2Se_3$ können modifiziert werden, wenn die Größe der Nanostruktur reduziert wird, die Form verändert wird, oder Ladungsträger in die Oberflächenzustände von $Bi_2Se_3$ injiziert werden. Das Zusammenspiel zwischen der Interaktion der injizierten Ladungsträger mit Phononen in $Bi_2Se_3$ wird in dieser Arbeit mit Raman-Spektroskopie mit einer örtlichen Auflösung im Nanometer-Bereich untersucht. Es wird ein Raman-Aufbau mit einer Spotgröße von $\approx$ 211 nm genutzt. Dieser Aufbau ermöglicht die lokale Untersuchung des Ladungstransfers auf die metallischen TI Oberflächenzustände. $Bi_2Se_3$ Nanoflocken (Nfs) auf einem Goldsubstrat zeigen einen durch Ladungsträger induzierten oberflächenverstärkten Raman-Streuquerschnitt, Verbreiterung und starke Renormalisierung der Phonon-Moden. Weiterhin wurde die geometrische Einschränkung von $Bi_2Se_3$ zylindrischen Nanodrähten (NWs) vom 2D Limit auf 1D untersucht. Im 1D Limit spalten die metallischen Oberflächenzustände in Unterbänder auf, was eine Lücke am Dirac-Punkt öffnet und die nicht-entarteten Oberflächenzustände auf Grund eines $\pi$-Berry Phaseneffektes anhebt. Ein magnetischer Fluss von r = 0.5, der entlang der Achse des $Bi_2Se_3$ NW angelegt wird, hebt den Effekt der $\pi$-Berry-Phase auf, schließt dadurch die Lücke am Dirac-Punkt und stellt die nicht entarteten Oberflächenzustände wieder her. Der Übergang aus dem 2D Limit hin zu 1D $Bi_2Se_3$ zylindrischen Nanostrukturen wird bei einem Radius unter 50 nm durch die oberflächenverstärkte Raman Streuung (SERS) gekennzeichnet. Per Manipulation der topologischen Oberflächenzustände von $Bi_2Se_3$ Nanoribbons (NRs) mit Au-Partikeln (AuNPs) wurde in Resonanz Hot Carrier Injection beobachtet, was sich im Raman-Experiment auf der Nanometer-Skala anhand einer Verstärkung der Phononen-Moden zeigt, die von der Anregungswellenlänge und der Entfernung zum Au-NP abhängt. In Resonanz bei einer Anregungswellenlänge von 633 nm und bei einer Nanopartikelgröße von 108 nm demonstrieren wir einen Raman-Verstärkungsfaktor von 350. Wir führen dieses Verhalten auf den Doppel-Resonanzeffekt zurück, der zum einen durch plasmonische AuNPs und zum anderen Interband-Übergänge in $Bi_2Se_3$ TI hervorgerufen werden.

# Dedication

*In loving memory of my wonderful mum, Christiana Nkemakonam Nweze, who passed-on in the course of writing this thesis on* ***20.08.2022*** *and my dad, Samuel Ejikeme Nweze (passed-on* ***24.06.2016****), whose visit to Flensburg, Germany, between* ***1965 - 1967*** *motivated my research in Hamburg, Germany.*

# Contents

# List of Figures

# Chapter 1

# General Introduction

## 1.1 Introduction

Over the past decade, research on topological insulating (TIs) materials is inexhaustibly advancing due to the intriguing exotic properties of their edge/surface states. It is not surprising that the properties of these unique materials are explained by the quantum mechanical theory [1] but rather the exotic behaviours associated with the edge/surface states. The unique nature of these materials is due to their insulating bulk with metallic edge/surface states that are time reversal symmetry protected Dirac fermions [2]. These materials hold potential for exciting effects such as Majorana fermions, charge fractionalization in a Bose Einstein condensate, anomalous quantization of magneto-electric coupling, magnetic monopole and also applications in spintronics, optoelectronics and quantum computing [3] [4] [5]. As TI are robust against disorder, energy per second dissipation could be greatly reduced and that is the advantage of TI materials over conventional conductors. Furthermore, the spin-momentum locking in TI surface states enables the conduction of spin-polarized currents over long distances without backscattering [6]. All these properties make TI an active research field.

A lot of materials are predicted and experimentally observed to have signatures that are peculiar to TIs, some of them have exotic edge states (Two-dimensional (2D) TIs) and some others have metallic surface states (Three-dimensional (3D) TIs) [1] [7]. Bismuth selenide ($Bi_2Se_3$) as an example of 3D TI, is predicted to has a simple band structure with the largest band gap of about 0.3 eV, a single Dirac point, and promising candidate for realizing Majorana fermions [1]. By manipulating and controlling the surface states of $Bi_2Se_3$, one can engineer TI devices with enhanced properties to match engineering requirements for optoelectronics devices [6] [8]. Therefore, it is extremely important to study the interaction between surface phonons in $Bi_2Se_3$ TI and injected carriers (either from gold substrate or from the resonantly excited surface plasmons in gold nanoparticles (AuNPs)), and how this interaction modifies and enhances the surface phonon dynamics. It is also interesting to examine the role played by surface plasmons as the size of cylindrical $Bi_2Se_3$ nanowires (NWs) is reduced geometrically from 2D limit to One-dimensional (1D).

In this work, we will report on (a) synthesis and characterization of $Bi_2Se_3$ nanoflakes (NFs), nanowires (NWs) and nanoribbons (NRs), (b) design and production of $Bi_2Se_3$ devices for transport measurement, (c) nanoscopic study of phonons in $Bi_2Se_3$ with a custom-made micro-Raman of beam spot diameter ≈ 211 ± 3 nm , (d) the geometric cross-over of $Bi_2Se_3$ NWs from 2D limit to 1D, and (e) manipulating the surface state of single crystalline $Bi_2Se_3$ NR with a single AuNP and gold substrate for optoelectronics applications.

This thesis is organized in chapters and each chapter has a specific aim. Chapter 1 focuses on introduction and a short review of low-dimensional TIs. Chapter 2 deals with the literature review of the physics of TIs and 3D TIs with emphasis on the $Bi_2Se_3$ TI. It also deals with the theoretical background of light matter interaction, bulk and surface states of $Bi_2Se_3$ TI. Surface plasmons in AuNPs, plasmons in $Bi_2Se_3$ TI and phonon-electron interaction will be highlighted. The theory of inelastic scattering and phonon propagation at the surface of $Bi_2Se_3$ will be discussed. We will mention the scientific questions that motivated this work and describe more specifically (a) the role of surface plasmons as the size of the $Bi_2Se_3$ is reduced from 2D limit to 1D, (b) the effect of injected carriers on the lattice dynamics of the surface states of $Bi_2Se_3$ TI. In chapter 3, we will present our experimental set-up, measurement and characterization techniques used in this work. The results and discussion will be the focus of Chapter 4. Finally, chapter 5 will concentrate on summary, conclusion, outlook and acknowledgments.

In the following section, we will first introduce the low-dimensional topological insulators (LDTIs).

## 1.2 Low-dimensional topological insulators

In topological insulators, the surface states are always obscured and suppressed by the bulk carriers. Exploiting the topology induced quantum phenomena in such a material is challenging [9], [10]. In order to mitigate the challenges, the contribution from the bulk carriers are reduced by growing low-dimensional topological insulators (LDTIs). LDTIs are TIs that have at least one dimension at the nanoscale range. By reducing the dimension of TIs, their surface-to-volume ratio is increased which effectively increases the carrier contribution from the topological surface states. Indeed, LDTIs provide the opportunity to take advantage of every atomic layer to study the topology related phenomena [11]. LDTIs such as 1D (nanowires, nanoribbons) and 2D (nanoflakes, nanofilms) are grown either by top-down or bottom-up approaches. Bottom-up approach offers potentials and possibilities for producing LDTIs with less defects and more homogenous chemical composition. Chemical vapor deposition (CVD) and wet-chemical reactions are mostly used in the bottom-up approach to build up LDTIs from atom by atom or molecule by molecule to form nanowires or nanoflakes. In this study, we utilized CVD and wet chemical methods to synthesize 1D and 2D geometrical TIs, respectively. Fig 1.1(a) shows 5 atomic layers (top view) of $Bi_2Se_3$ TI whereas Figs. 1.1(b and c) show a single nanoflake and nanowire, respectively.

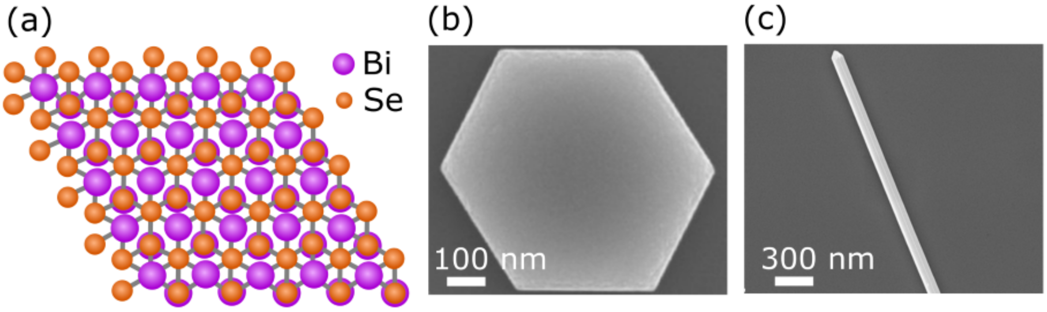

Figure 1.1: Examples of low-dimensional topological insulator. (a) Top view of 5 atomic layers of $Bi_2Se_3$. (b) Hexagonal nanoflake. Nanoflake is an example of a 2D material because one of its dimensions is in nanoscale range. (c) Nanowire. Nanowire has two of its dimensions in nanoscale range and therefore a 1D material

# Chapter 2

# Literature Review and Theoretical Background

## 2.1 Literature review – topological insulators

Coherent study and characterizing different phases of matter is one of the core objectives of condensed matter physics. The study of superconducting and magnetic phases of matter reveals that these phases (magnets and superconductors) spontaneously break the symmetries [12]. Is there order in the quantum ground state entanglement? And if yes, does this order break any symmetry? In order to explain the quantum Hall effect, the concept of topological order was introduced [13]. The quantum Hall state exhibits topological order and does not break any symmetries, rather it is robust against changes in the material parameters. The topological order is also found in a new phase of materials, the TIs. The discovery of TIs as a topological phase of material whose gapless edge $|e\rangle$ /surface states $|s\rangle$ are protected by time reversal symmetry are of particular importance. Like the integer quantum Hall state, the edge $|e\rangle$ /surface $|s\rangle$ states of TIs have gapless electronic states that are topologically protected and immune to backscattering by non-magnetic impurities. Previously in chapter one we defined TIs as materials with exotic metallic edge $|e\rangle$ /surface $|s\rangle$ states but with insulator bulk states. The metallic surface states $|s\rangle$ are associated with a 2D electron gas (2DEG) and hence the electronic wave functions of the system change when traversing from the valence band to the conduction band [14].

### 2.1.1 Historical perspective

In order to appreciate the physics of TIs, a brief discussion of the relevant historical background of TIs is important. In the conventional insulating state of condensed matter physics, due to the quantization of the energy of the atomic orbital (Fig. 2.1(a)), there is an energy gap separating the occupied electronic states from the unoccupied states (Fig. 2.1(b)) [15]. As theoretically predicted in 1974, the quantum Hall phase is another exotic insulating state [16]. In 1980, the experimental discovery of the quantum Hall effect in a high mobility 2D semiconductor, under strong magnetic fields, points to quantization of the Hall conductivity $\sigma_{xy}$ to integer multiples of $\frac{e^2}{h}$ at very low temperature [1] [17]. In such a system, the motion of electrons is in circular orbit (due to the perpendicular Lorentz force on electrons in the magnetic field), corresponding to an atomic orbital with quantized energy (Fig. 2.1(c)). Just like in an ordinary insulator, there is an energy gap separating the occupied and unoccupied states. At the edge of the quantum Hall phase, electrons propagate in the so-called skipping orbit [14] (i.e. electron motion is in one direction without quantized energies) (Fig. 2.1(c)). The energy as a function of momentum in such a system is shown in Fig. 2.1(d). In 1982, Thouless, Komoto, Nightingale, and den Nijs (TKNN) showed that in the quantum Hall system the k-space is mapped to a topological-nontrivial Hilbert space [13] and with an invariant topology $n$ such that $\sigma_{xy} = n\frac{e^2}{h}$. The TKNN invariant $n$ is called the winding number or Chern number and it is equivalent to the Berry phase of the Bloch wave function calculated around the Brillouin zone boundary divided by $2\pi$ (see section 2.1.2). The quantum Hall state exhibits topological order and hence is considered the first topological insulator [14]. The electrons in quantum Hall states are protected from impurity scattering and therefore there is no dissipation of energy in the form of heat. The quantum Hall effect occurs only when a strong magnetic field B is present and it is not *priori* clear how one can achieve the quantum Hall effect in the absence of a magnetic field $B$. In 2004, Kato *et al.* experimentally verified the appearance of transverse spin current in response to longitudinal electric field [18]. In 2005, the quantum spin Hall (QSH) insulator was proposed by Kane and Mele which are mainly two copies of the quantum Hall system [2]. In the QSH state (simplest 2D topological insulator), the role of the magnetic field is taken up by spin-orbit coupling (SOC). The SOC is the interaction between the spin of an electron and its orbital motion through space. Furthermore, the spin-orbit force is strong in atoms with a high atomic number because electrons in such atoms move at relativistic speed [2]. Electrons traversing through materials composed of high atomic numbers feel a strong spin and momentum dependent force that resembles a magnetic field. In 2D TIs, as predicted by Kane and Mele, the spin-up and spin-down electrons feel equal and opposite spin-orbit "magnetic fields" that are each in quantum Hall states (Fig. 2.2(a)) [2]. The existence of edge states $|e\rangle$ in which the spin-up and the spin-down electrons propagate in opposite directions, the Hall conductance is zero, because the two motions (spin-up/spin-down) cancel each other. Since the edge states $|e\rangle$ in 2D TIs (like the quantum Hall edge states) form a 1D conductor, the 2D TIs can conduct (Fig. 2.2(b)). The QSH edge states are protected from backscattering by time reversal symmetry (TRS) because TRS ensures the stability of the edge states $|e\rangle$. In 2007, König *et al.* observed the predicted edge conductance $\sigma_{xy}$ with quantization of $2\ \frac{e^2}{h}$ in a zero magnetic field when the chemical potential is tuned into the band gap [19]. As predicted, König *et al.* observed that the measured conductance is independent of the width of the sample. Furthermore, theorists observed that the topological classification of insulators can be extended to 3D systems [19] [20] [21]. In 2008, Hsieh *et al.* in an angle resolved photoemission spectroscopy (ARPES) experiment observed that Bismuth antimonide ($Bi_{1-x}Sb_x$) is a 3D TI [22] and their result was corroborated by the transport study conducted in 2009 by Taskin and Ando [23]. In a 3D TI, the direction of electron motion along the surface is determined by the spin direction which varies continuously as a function of propagation (Fig. 2.2(c and d)). The surface states $|s\rangle$ of a 3D TI are like half of a 2D conductor and additionally have a 2D metallic state where the spin direction is locked to the direction of propagation.

### 2.1.2 The Berry phase and curvature in electronic structure

Geometric phase angle running between 0 and $2\pi$ that is carried around a loop in its vector form is the Berry phase [24]. The Berry phase is a crucial concept in topological band

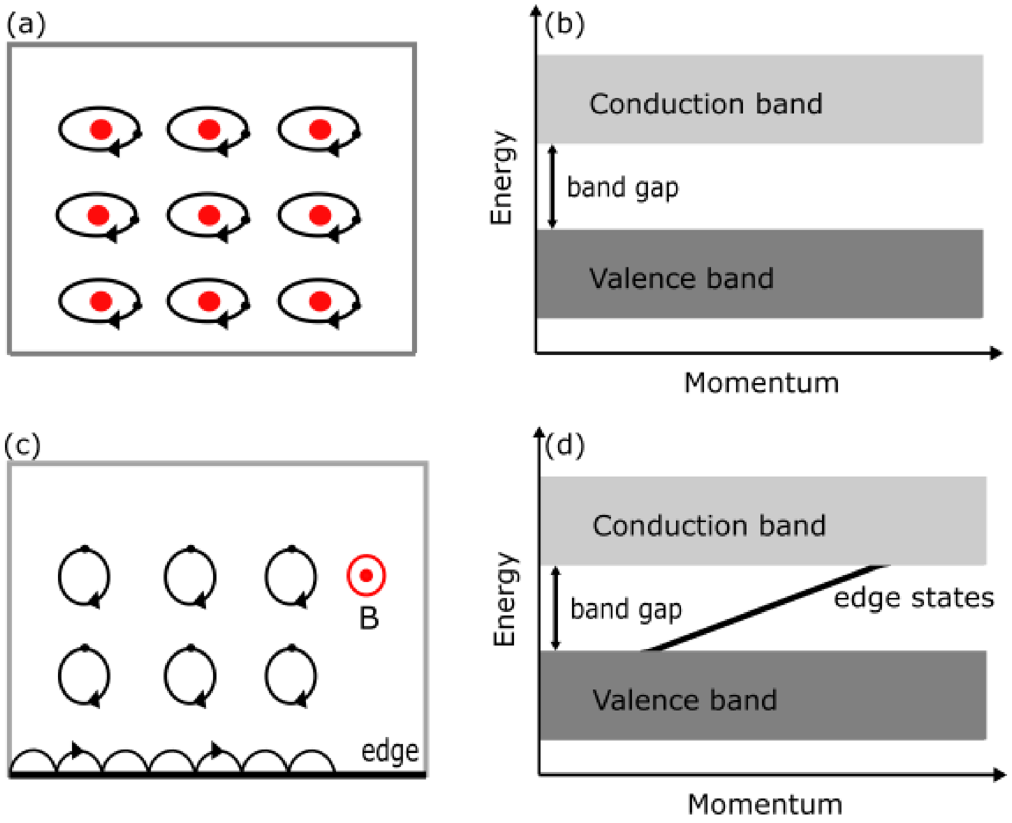

Figure 2.1: (a) Schematic diagram of the insulating state of condensed matter showing (b) the occupied and unoccupied electronic states separated by an energy gap. (c) The quantum hall effect showing the skipping orbits in the presence of magnetic field, B. The skipping orbits cause the one directional edge conduction in quantum hall devices. (d) The occupied and unoccupied electronic states showing the edge states. (Copyright [15]).

theory and plays a vital role in Bloch periodic systems where Bloch momenta are varied in closed paths by applying electric fields [25]. Consider a time varying Hamiltonian $H(R)$ in a loop which depends on parameters (R), say magnetic field, the adiabatic evolution of the system along the loop as the parameter $R(t)$ is varied slowly is given as [25]:

$$H(R)\,|n(R)\rangle = E_n(R)\,|n(R)\rangle \tag{2.1}$$

where $|n(R)\rangle$ is the eigenstates. The phase adiabatic evolution of the eigenstate is given as

$$|\Psi(t)\rangle = \exp^{-i\theta t}\,|n(R(t))\rangle \tag{2.2}$$

Solving eqn. 2.2 with schrödinger wave eqn. 2.3 we obtain eqn. 2.4

$$\hat{H}\,|\Psi\rangle = i\hbar\frac{d}{dt}\,|\Psi\rangle \tag{2.3}$$

$$\theta(t) = \frac{1}{\hbar}\int_0^L E_n(R(t^1))dt^1 - i\int_0^t \langle n(R(t^1))|\,\frac{d}{dt^1}\,|n(R(t^1))\rangle\,dt^1 \tag{2.4}$$

The first term on the RHS of eqn. 2.4 is the conventional dynamical phase and the second term is the Berry phase. From the second term, the Berry phase is "minus the complex phase of the product of inner products of the state vectors at neighboring points around

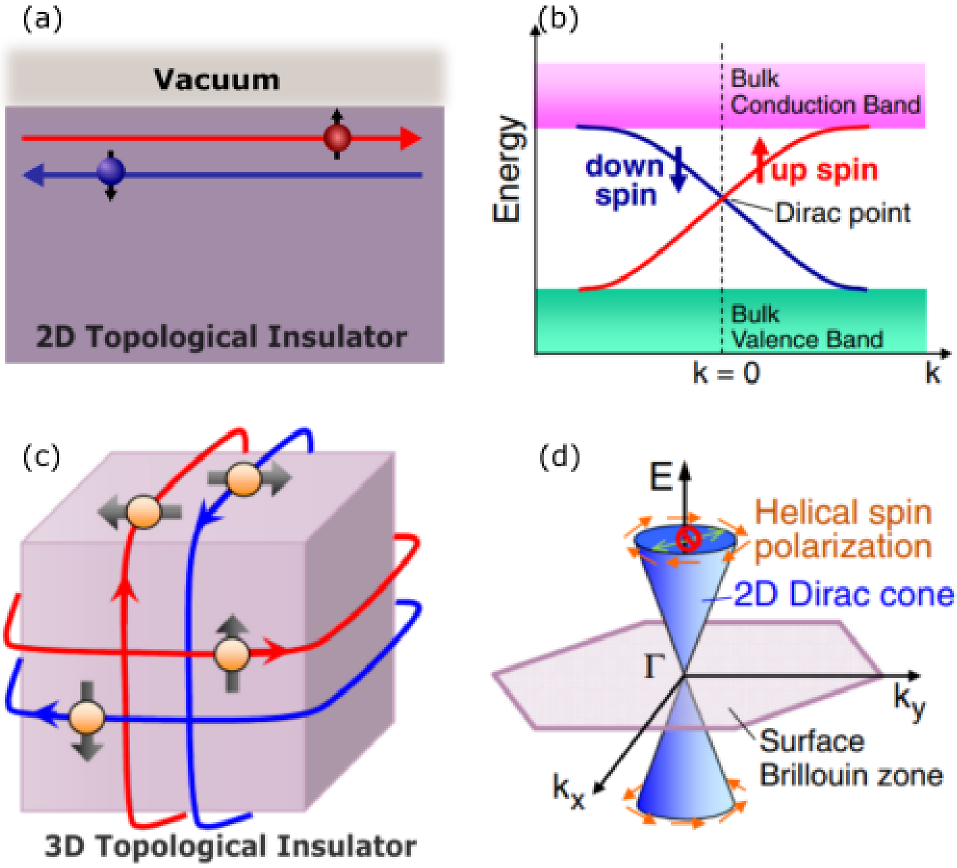

Figure 2.2: Edge and surface states of TIs with Dirac dispersions. (a) Schematic diagram of 2D TI showing the spin-up and spin-down electrons. (b) Energy dispersion of the spin non-degenerate edge states of the 2D TI forming a 1D Dirac cone. (c) Schematic diagram of 3D TI. (d) Energy dispersion of the spin non-degenerate surface state of a 3D TI forming a 2D Dirac cone. (Adapted with permission from JPSJ [1]).

the loop [26]. The second term could be re-written as a dot product integrated over a closed path

$$\Phi = i\int_0^t \langle n(R(t^1))|\,\frac{d}{dt^1}\,|n(R(t^1))\rangle\, dt^1 = \int_C \bar{dk}\cdot\bar{A} \tag{2.5}$$

$\bar{A} = i\,\langle n|\,\bar{\nabla}_k\,|n\rangle$ is the vector field defined over 2D surface.

**Stokes theorem**: Using Stokes theorem, eqn. 2.5 can be re-written as an integral over the surface of the closed path and the associated vector field is called the Berry curvature:

$$\Phi = \int_C \bar{dk}.\bar{A} = \int_S \bar{ds}\cdot\bar{\Omega} \tag{2.6}$$

where the Berry curvature $\bar{\Omega}$ in the vector field is $\bar{\Omega} = \bar{\nabla}\ \text{X}\ \bar{A}$. The Berry curvature moderates the paths of the electrons in the same way as magnets do, however unlike magnetic field, Berry curvature is defined over a momentum space [27].

Eqn. 2.5 is always real and with a value of 0 or $\pi$ depending on the sign of the integral [26].

**Chern theorem**: Using the Chern theorem in the limit of continuum, $\Phi$ computed on any closed 2D manifold S is quantized to be $2\pi$ multiplied by an integer.

$$\Phi = \int_S \bar{ds} \cdot \bar{\Omega} = 2\pi C \tag{2.7}$$

where C is the Chern number or topological invariant [28] [29]. $C = 0$ for a trivial insulator and $|C| = 1$ for a nontrivial insulator. A 1D topological nontrivial phase is characterized by $\Phi = \pi$, corresponding to edge states at the bulk band gap, whereas a trivial topology has $\Phi = 0$ and no edge states [28].

### 2.1.3 $Z_2$ Topological order

To understand many body phases with bulk energy gaps, the topological invariant of electronic states is a robust tool. We mentioned in the historic perspective that Hall conductance for non-interacting electron gas according to TKNN [13] is given as.

$$\sigma_{xy} = n\frac{e^2}{h} \tag{2.8}$$

where $n$ is a TKNN integer. Eqn. 2.8 is the origin of the topological invariant for the non-interacting integer quantum Hall effect [2] and distinguishes TI from a simple insulator. Hall conductivity violates time reversal symmetry (TRS) [2] therefore, TKNN integers are non-zero [30] when the TRS is lifted (existence of gapless edge states on the sample boundaries) but vanishes in the presence of TRS. At this point, we would like to emphasis that TRS plays a crucial role in the dynamics of the helical edge states [31] [32]. Even and odd numbers of pairs of helical states at each edge play a role in classifying topologies as trivial and nontrivial. For an even number of pairs, many body interactions or impurity scattering can open a gap at the edge and make the system topologically trivial (simple insulator). For an odd number of pairs, this cannot open a gap provided that TRS is not broken at the edge and hence the system is topologically nontrivial (topological insulator). Kane and Mele argued that the existence of spin-orbit interaction leads to the TRS invariant quantum spin Hall (QSH) state which has a bulk energy gap and a pair of gapless spin edge states on the boundary [33]. To support the idea that the QSH ground state is distinguishable from a simple insulator, the concept of $Z_2$ topological order that characterizes the TRS invariant system was introduced by Kane and Mele. There is a single $Z_2$ topological invariants that distinguishes a simple insulator from the QSH phase in 2D, whereas in 3D there are four $Z_2$ invariants [34] that distinguishes the ordinary insulator from weak TI (WTI) and strong TI (STI) [35]. STI are robust and lead to novel surface states (metallic) while WTI is destroyed by disorder [35]. WTI has an even number of Dirac points transversing the bulk band gap whereas in STI there are an odd number of Dirac points. The simplest TI would have one Dirac point transversing the bulk band gap. Some materials such as $Bi_2Se_3$, $Bi_2Te_3$, $Sb_2Te_3$ were predicted to have a single Dirac point and indeed experimental results confirmed the prediction [36] [37] [38].

### 2.1.4 Band inversion symmetry in TI

Unlike the realization of QSH in $Z_2$ topological order by [2], Bernevig, Hughes and Zhang (BHZ) theoretically presented an alternate route to realize QSH through band inversion which modifies the electronic state of such material [39]. The idea spans from the thickness of a quantum well of mercury telluride-cadmium telluride (HgTe-CdTe) semiconductor. In CdTe-HgTe-CdTe heterostructure, CdTe is the barrier material and HgTe is the well material [39]. Band inversion occurs at a certain thickness $d_c$ of the well material [39] which closes the gap at Dirac point to form topological nontrivial with helical edge states. The prediction was experimentally demonstrated in [19] [40]. The inversion of band at gamma point by HgTe (topological nontrivial) but not in CdTe (topological trivial) differentiates the two materials [41] [34] [42]. The band inversion in HgTe is because $\Gamma_6$ (s-type, doubly degenerate) appears below $\Gamma_8$ (p-type, j = 3/2 quadruply degenerate) [43] as shown in Fig. 2.3(b) unlike in CdTe shown in Fig. 2.3(a).

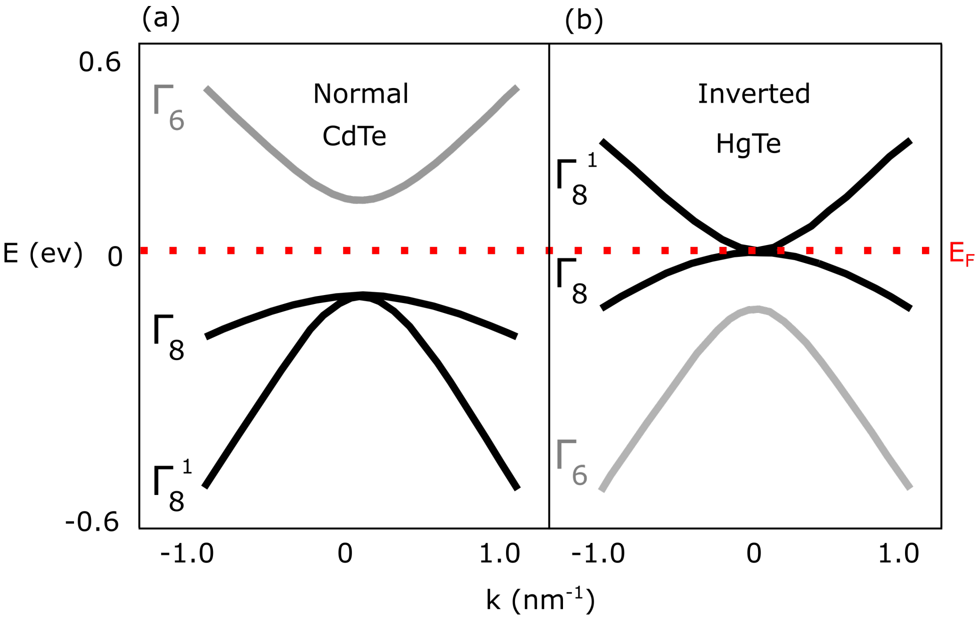

Figure 2.3: Bulk energy bands of HgTe and CdTe near the Γ point. $\Gamma_8^1$ is a light hole and $\Gamma_8$ is a heavy hole. (a) Normal energy band of CdTe (topological trivial). (b) Inverted energy band of HgTe (topological nontrivial). $\Gamma_6$ appears below $\Gamma_8$. The red horizontal dashed line is the Fermi level. (Adapted with permission from AAAS [39]).

The combination of $\Gamma_6$ and $\Gamma_8$ forms six basic atomic states per unit cell that combined into a six-component spinor [39]:

$$\Psi = (|\Gamma_6, 1/2\rangle, |\Gamma_6, -1/2\rangle, |\Gamma_8, 3/2\rangle, |\Gamma_8, 1/2\rangle, |\Gamma_8, -1/2\rangle, |\Gamma_8, -3/2\rangle) \tag{2.9}$$

By combining spin up and spin down (±) states reduce the six bands into three sub-bands E1, H1 and L1. The separation of L1 sub-bands from E1 and H1 reduced the consideration into an effective four band model. However we would like to mention that six band kane Hamiltonian has been used to explain band inversion [42] [41]. By considering symmetries, the effective Hamiltonian for E1 and H1 states is reduced to 2 x 2 subspace that takes the form of the (2+1)-dimensional Dirac Hamiltonian + $\epsilon(\omega)$ term [39].

$$H_{eff}(k) = \epsilon(\omega) + \begin{bmatrix} m(\omega) & A\pi^\dagger & 0 & 0 \\ A^*\pi & -m(k) & 0 & 0 \\ 0 & 0 & m(-k) & -A^*\pi \\ 0 & 0 & -A\pi^\dagger & -m(-k) \end{bmatrix} \tag{2.10}$$

where $\epsilon(k) = C - D(k_x^2 + k_y^2)$ and $m(k) = M - B(k_x^2 + k_y^2)$. B, C, and D are the expansion parameter. The Hamiltonian in eqn. 2.10 is block diagonal and related by the time reversal operation. The difference between E1 and H1 level at the Γ point is the mass (gap) parameter M. In band inversion, the level crossing occurs at a defined critical thickness $d_c$ of the HgTe (well). The plot of the energies of E1 and H1 sub-bands at in-plane momentum, k=0, as a function of HgTe thickness is shown in Fig. 2.4(b). The corresponding band dispersion is shown in Fig. 2.4(a). Fig. 2.4 shows that for thin HgTe (i.e d $< d_c$), the contribution of CdTe (barrier) dominates over HgTe (well) and $E(\Gamma_6) > E(\Gamma_8)$, we have a normal condition as shown in Fig. 2.3 (a). As the thickness of the well increases beyond the critical conduction, $d_c <$ d, the contribution of the well dominates and $E(\Gamma_8) > E(\Gamma_6)$, in this case we have an inverted condition (Fig. 2.3(b)). At d $= d_c$ band crossing region, the mass parameter M changes sign between the two sides of transition [39]. The foregoing discussion establishes the fact that the mass term is tuned by changing the thickness of the quantum well. At M = 0, gapless Dirac dispersion appears. From the calculation of the quantized Hall conductance in [44] and the number of edge states in 2D insulators, it is evident that pairs of helical edge states differ by 1 at each side of the critical thickness $d_c$ [39]. Thus one side of the transition is $Z_2$ odd and the other side is $Z_2$ even. The microscopic mechanism in CdTe-HgTe-CdTe heterostructure can be generalized to other 2D or 3D systems. 3D TI can be realized in an insulating system in which valence band and conduction band have opposite parity [34] and a band inversion (which is mediated by the strength of some parameters, such as spin orbit coupling (SOC)) and, of course, TRS is not lifted.

## 2.2 3D topological insulator ($Bi_2Se_3$)

In 3D TI, the spin of an electron is locked to its momentum at the surface (Fig. 2.2(d)) and it is immune, just like in 2D quantum well, to backscattering from non-magnetic impurities. The simplest 3D TI has one single gapless Dirac cone at Γ point (($K = 0$) *i.e.* the center of the bulk band gap) [35]. $Bi_2Se_3$ was predicted to be 3D STI by [45]. STI hosts potentials for realizing novel magnetic and electronic properties [46] [47] because of its unusual 2D edge states which may provide a route to spin-charge separation [48] [49]. *Ab initio* calculations [50] and experimental demonstrations using scanning tunnelling microscopy [51] and angle resolved photoemission spectroscopy (ARPES) [52] [53] [54] [55] confirm that $Bi_2Se_3$ is a STI and has a metallic surface state with a single Dirac cone (Fig. 2.5(a)) near the Γ point of the surface Brilloiun zone.

### 2.2.1 $Bi_2Se_3$ strong topological insulator (STI)

$Bi_2Se_3$ is a layered material with a bulk band gap of about 0.3 eV. It crystallizes in a rhombohedral crystal structure with space group $D^5_{3d}(R\bar{3}m)$ [56] [57] [58]. Its unit cell has five atoms and the atomic layers, $Se^1$-$Bi^1$-$Se^2$-$Bi^2$-$Se^3$, are covalently stacked along its c-axis to form a quintuple layer (Fig. 2.5(b)). The $Se^2$ site serves as the center of inversion and under an inversion operation, $Se^1$ changed to $Se^3$ and $Bi^1$ changed to $Bi^2$ [45].

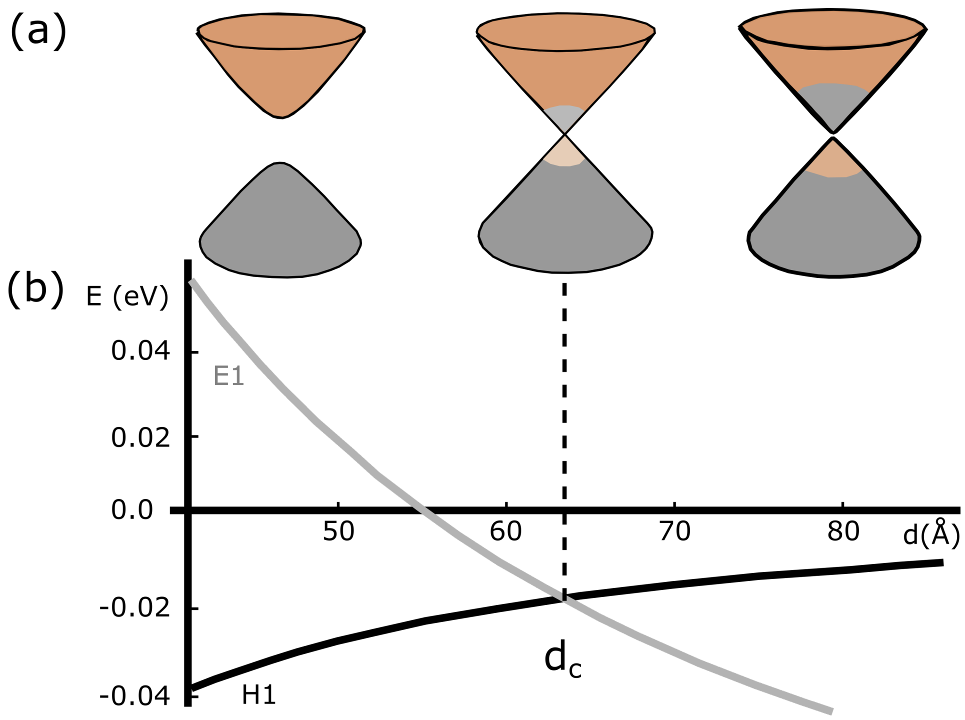

Figure 2.4: (a) Energy dispersion relations E$(k_x, k_y)$ of the E1 and H1 sub-bands at d = 40, 63.5, and 70 Å (from left to right). Colour coding indicates the symmetry type of the bands at that k point. At 40 Å, the conduction band is dominated by E1 and the valence band by H1. Near $d_c$, the states are evenly mixed. At 70 Å, the region near in-plane momentum $k_{||} = 0$ has exchanged their character (b) Energy of E1 (gray) and H1 (black) bands at $k_{||} = 0$ as a function of quantum well thickness d. (Adapted with permission from AAAS [39]).

Each quintuple layer is bonded to another by van der Waals forces which allows for easy cleaving of the layers. The five atoms in its primitive cell has 15 zone center phonon branches, 12 optical phonon and 3 acoustic modes according to group theory predictions. Out of the 12 optical phonon modes, 4 are symmetry infrared-active (2A$_{1u}$, 2E$_u$) and another 4 are symmetry Raman-active (2A$_{1g}$, 2E$_g$). The irreducible representation of Raman-active and infrared-active modes at the zone center phonon can be written as: $\Gamma = 2A_{1g} + 2E_g + 2A_{1u} + 2E_u$ [57]. Fig. 2.6(d) shows the schematic diagram of the bulk 3D Brillouin zone of $Bi_2Se_3$ and the 2D Brillouin zone of the projected (111) surface. The 4 symmetry Raman active and their vibration modes are shown in Fig. 2.5(c). E$_g$ modes are the in-plane and A$_{1g}$ are the out-of-plane vibration modes. Their corresponding Raman tensors are shown in eqn. 2.11 [57]. In this work, we detected 3 out of the 4 vibration modes.

$$A_{1g} = \begin{bmatrix} a & 0 & 0 \\ 0 & a & 0 \\ 0 & 0 & b \end{bmatrix}; \qquad E_g = \begin{bmatrix} 0 & -c & -d \\ -c & 0 & 0 \\ -d & 0 & b \end{bmatrix}, \quad \begin{bmatrix} c & 0 & 0 \\ 0 & -c & d \\ 0 & d & 0 \end{bmatrix} \tag{2.11}$$

The existence of metallic surface in $Bi_2Se_3$ was predicted by [45] through the *ab initio* calculations and found that the energy-momentum plot of the local density of states (LDOS) formed a single Dirac cone at the Γ point (Fig. 2.6(c)). Note that the imaginary part of the surface Green's function is the LDOS. Recall that spin orbit coupling (SOC) plays a vital role in TIs and more especially in the STI like $Bi_2Se_3$ system. Band structure calculation with and without SOC is shown in Figs. 2.6(a and b), respectively. Due to SOC effects, an inversion between conduction and valence bands was observed and such band inversion is lifted without SOC. The metallic surface state of $Bi_2Se_3$ TI is spin polarized and hosts quasi-relativistic or relativistic electrons depending on its mass [52] [59] [60]. Electron-phonon interaction at the metallic surface states of $Bi_2Se_3$ has been studied extensively with ARPES measurements [61] [62]. In a time-resolved ARPES (trARPES) study, the surface state dispersion oscillations were utilized to differentiate $A_{1g}$ optical phonon that couples to both the bulk band and surface band of $Bi_2Se_3$ [63] and hence distinguishing bulk and surface electron-phonon coupling in $Bi_2Se_3$.

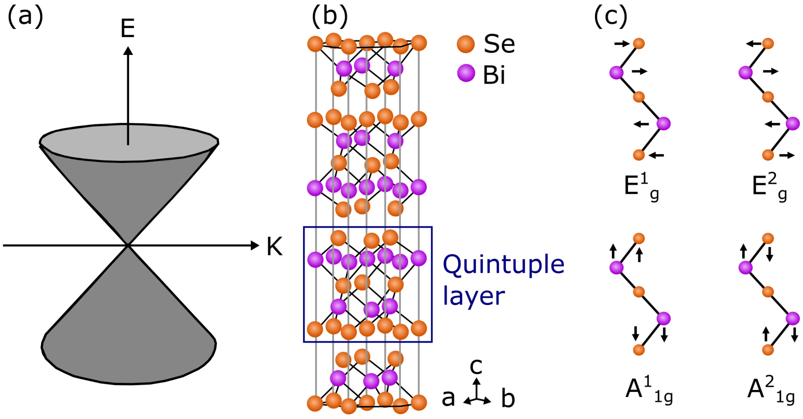

Figure 2.5: (a) Dispersion relation of the metallic surface state of $Bi_2Se_3$ TI. (b) Crystal structure of $Bi_2Se_3$ with the indicated quintuple layer. (c) The 4 symmetry Raman active vibration modes of $Bi_2Se_3$.

### 2.2.2 3D TI nanowire enclosed in a magnetic field

On the surface of 3D TI, the spin of an electron is locked perpendicular to its momentum and scattering by non-magnetic impurities is forbidden [64] [65] [66]. Recall that the relativistic dispersion relation of an electron with momentum p and rest mass m is given as [67] [68]:

$$E_{(p,m)} = c\sqrt{p^2 + m^2c^2} \tag{2.12}$$

for m ≈ 0 (relativistic), $E_{(pm)}$ = cp, linear dispersion relation which is associated to the metallic surface. The characteristic band dispersion of such a system is a Dirac cone [45] [69] (Fig. 2.7(a)). For a massive electron (non-relativistic), eqn. 2.12 leads to a parabolic dispersion relation with a gap that is dependent on the mass. The parabolic dispersion is associated to the bulk band. The unique property of 3D TI nanowire (1D) compared to geometrical 2D TI lies in the number of surfaces and the spin momentum locking at such surfaces. In TI of 2D geometry (nanofilms, nanoflakes or nanoribbons), there exist two surfaces (top and bottom) hosting the quasi-relativistic electrons. As the thickness of the films is reduced below 6 nm, due to quantum confinement effects, the insulating bulk band splits into sub-bands, the top and bottom surface hybridizes and results in a gapped surface state [70] [71].

In TI of 1D geometry (*i.e.* cylindrical nanowire), there exist one curved surface and

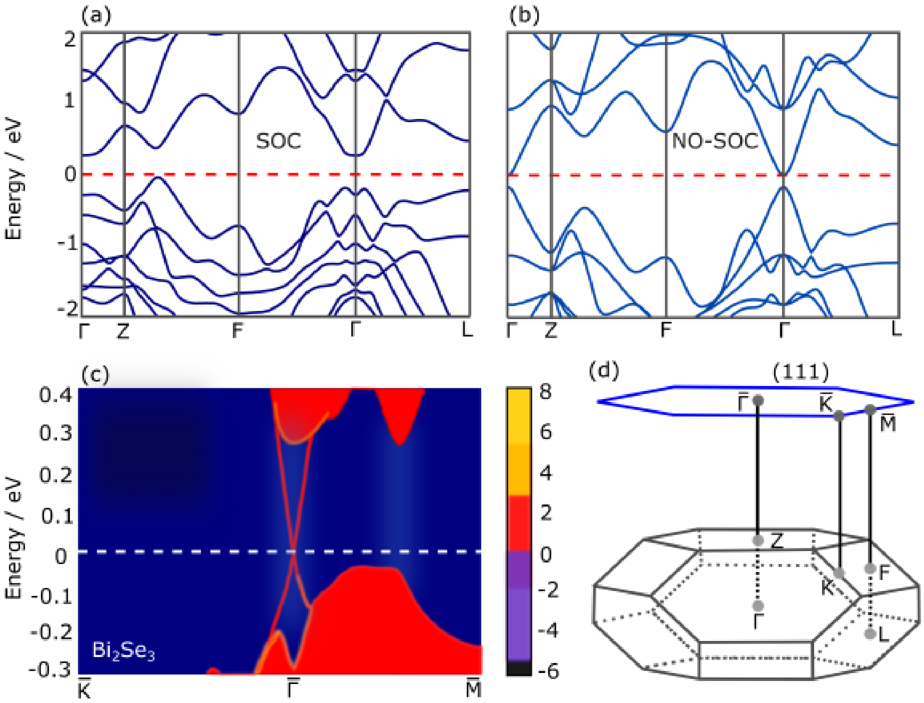

Figure 2.6: Calculated band structure for $Bi_2Se_3$ TI (a) with spin orbit coupling (SOC) and (b) without spin orbit coupling (NO-SOC). (c) Energy and momentum dependence of the local density of states (LDOS) for $Bi_2Se_3$. The surface state is clearly shown as the red lines at the $\Gamma$ point. (d) Schematic diagram of the bulk 3D Brillouin zone (BZ) of $Bi_2Se_3$ TI. The projected blue hexagonal shows (111) surface of the 2D BZ. (Adapted with permission from [45]).

the topological surface band splits into discrete 1D sub-bands [72] [73] [74] as the radius of the cylindrical nanowire is decreased. This quantization leads to gapped surface state at the Dirac point and the sub-band becomes doubly degenerate [74]. The electron spin in such a system is constrained in the tangent plane of the nanowire like in a closed loop (see section 2.1.2). The rotation of the electrons along the perimeter of the nanowire leads to a $\pi$-Berry's phase (see section 2.1.2).

The dispersion relation for 1D cylindrical nanowire in a magnetic field of flux ratio r is given as [74] [75] [76]:

$$E_l(k) = \pm\hbar\nu_F\sqrt{k^2 + \left(\frac{l-r}{R_w}\right)^2} \tag{2.13}$$

where $\nu_F$ is Fermi velocity, $R_w$ is the nanowire diameter, r is the flux ratio (r $= \Phi/\Phi_0$), $\Phi_0$ is the flux quantum and $l$ is the angular momentum quantum number with values of $\pm\frac{1}{2}$, $\pm\frac{3}{2}$, $\pm\frac{5}{2}$ and so on. Eqn. 2.13 is periodic in r and for $r = 0$, all branches of $E_l(k)$ are doubly degenerate [75] and opens a gap at the Dirac point. The degeneracy is lifted when $r \neq 0$. However, eqn. 2.13 does not explicitly contain the band gap term. Iorio *et al.* derived a dispersion relation containing the band gap term [72] [77] *i.e.*

$$E(k) = sC_2\sqrt{k^2 + (1+2m-2r)^2\tilde{\Delta}^2(R_0)} \tag{2.14}$$

where m is the quantum number (cylindrical symmetry confinement), the band gap $\Delta(R_0) = \frac{C_1}{R_0} = 2C_2\tilde{\Delta}(R_0)$, $C_1$ and $C_2$ are the interorbital and interspin coupling control, r is the magnetic flux ratio ($r = \Phi/\Phi_0$).

In the absence of a magnetic field, $r = 0$, a gap opens at the Dirac point and like eqn. 2.13, E(k) are doubly degenerate as shown in Fig. 2.7(b). The opening of the gap is ascribed to geometric effect ($\pi$-Berry phase) (see section 2.1.2) because the electron spins that encircling the Dirac cone by $2\pi$ acquires a $\pi$ phase shift. In the presence of a magnetic field applied longitudinally to the nanowire axis, the band gap $\Delta(R_0)$ is reduced. At $r = 0.5$, degeneracy is lifted and the gap closes at the Dirac point (Fig. 2.7(c)) because half flux quantum nullifies the effect of the Berry phase that induced gap opening [73] [78] [79] [72].

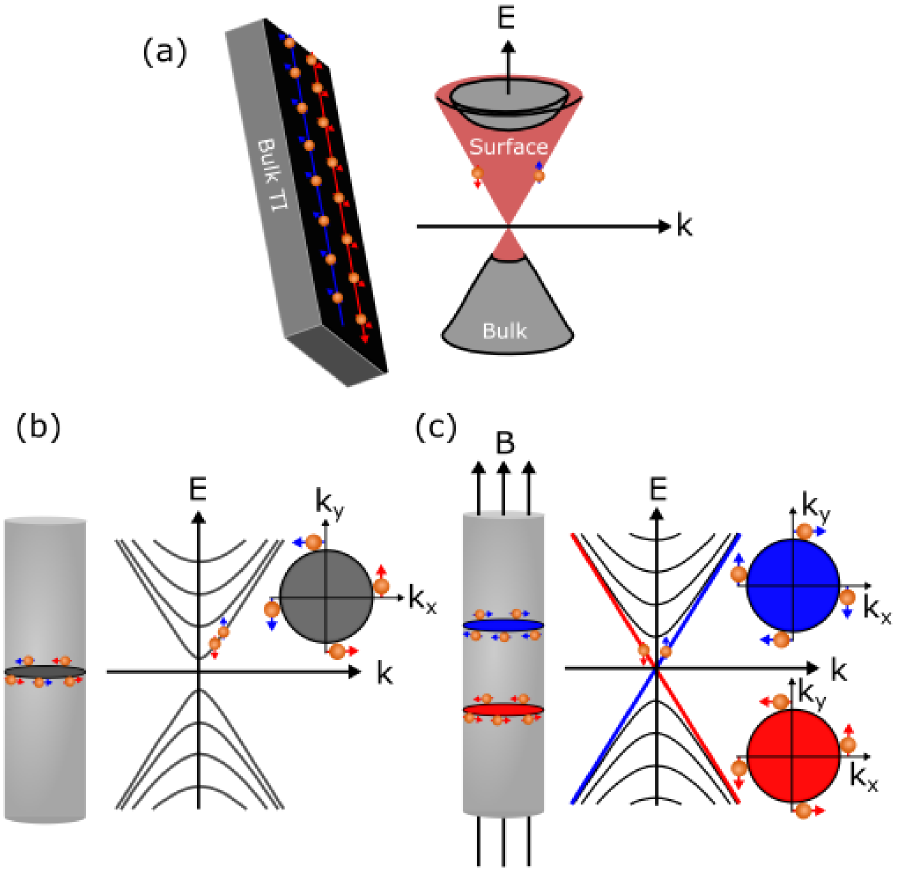

Figure 2.7: (a) Spin polarized metallic surface of bulk TI with the accompanied Dirac cone. (b) Degenerate state of $Bi_2Se_3$ NW showing the splitting of the surface state into sub-bands and opening of gap at the Dirac point. The inset shows a cross-section of the NW with (mix) spin configuration (c) Non-degenerate state of $Bi_2Se_3$ NW when magnetic field, B, is applied along the NW axis. The insets show a cross-section of the NW with (non-mix) spin configuration.

## 2.3 Inelastic light scattering and lattice dynamics

Light-matter interaction leads to some exciting phenomena which could be studied. It drives many systems [80] and helps in understanding some exotic properties of matter such as excitons, and collective oscillations. Through light-matter interactions we can derive the behaviour of electrons, phonons and electron-phonon couplings. Light matter interaction is a two photon process in which a photon is created and another photon is destroyed. The created photon (scattered light) can have the same energy with the destroyed photon (incident light) and in such a case it is called elastic (Raleigh) scattering. However, in inelastic scattering, the incident light has different energy compared with the scattered light and the difference in energy is used to excite the vibrational state in the system. This inelastic scattering was first discovered by C. V. Raman in 1928 [81] and it is now called Raman scattering.

### 2.3.1 Raman scattering

In Raman scattering, the created photon can have more (less) energy than the annihilated photon and it is referred to as anti-Stokes (Stokes). The difference in energy of the incident photon and the scattered photon called Raman shift ($\nu$) is represented as

$$\Delta\bar{\nu} = \bar{\nu}_0 - \bar{\nu} = \left(\frac{1}{\lambda_0} - \frac{1}{\lambda}\right) \cdot 10^7 cm^{-1} \tag{2.15}$$

where $\bar{\nu}_0 = \omega_0/2\pi c$ (wavenumber of the incident photon), $\bar{\nu} = \omega/2\pi c$ is the wavenumber of the scattered photon.

At room temperature, the intensity of Stokes is significantly higher than the intensity of anti-Stokes. Raman susceptibility of a medium is the probability that the incident photon is inelastically scattered by the medium and it is referred to as Raman cross-section [82]. Change in polarizability of the scattering medium makes its vibrational state to be Raman active [83]. The scattering intensity $I$ for each Raman active mode is given by $I(\omega) \propto |\tilde{e}_s \cdot R \cdot \tilde{e}_i|$ where $R$ is the Raman (3 x 3) tensor, $\tilde{e}_s$ and $\tilde{e}_i$ are the polarization of scattered and incident photons, respectively. The Raman spectroscopy probes the optical phonons at the Brillouin zone center where the momentum transfer $\tilde{q}$ $\approx$ 0 since the probing wavelengths are much longer than the lattice constant. $\tilde{q} = 2k_i$ and $k_i = 2\pi/\lambda$ and the distance between the Brillouin zone center to the zone boundary is $\pi/a$ (a = lattice constant) [84]. On the other hand, when the incident photon energy is close to one or more allowed electronic transitions, the intensity of the scattered photon is amplified unlike when the incident photon energy is not close to the allowed electronic transition [85]. The former is called resonance Raman and the latter is called ordinary Raman (non-resonance).

### 2.3.2 Theory of Raman scattering in crystals

In this section, we concentrate on the quantum mechanical approach of the Raman scattering process in conventional materials.

**Quantum mechanical approach**

The Hamiltonian ($\bar{H}$) describing the light-matter scattering consists of Hamiltonians for unperturbed $\bar{H}_0$ and perturbed $\bar{H}$(t≠0) systems. $\bar{H}$(t) is described by electron-phonon interaction $\bar{H}_{EP}$, photon-phonon interaction $\bar{H}_{PP}$ and photon-electron interaction $H_{PE}$ [86] [87]. $\bar{H}$ is given as:

$$\bar{H} = \bar{H}_0 + \bar{H}_{EP} + \bar{H}_{PP} + \bar{H}_{PE} \tag{2.16}$$

Let's consider the coupling of photon to electron described by the $\bar{H}_{PE}$ (which of course is the most significant process for Raman effect). The interaction of radiation field vector potential $\bar{A}$(r) with an electron of momentum operator $\bar{p}_j$ and position vector $\bar{r}_j$ for $\bar{p}_j \rightarrow \bar{p}_j$ + e$\bar{A}(\bar{r}_j)$ is described by $\bar{H}_{PE}$ as:

$$\bar{H}_{PE} = \frac{e^2}{2m_e}\sum_j \bar{A}(\bar{r}_j)\cdot\bar{A}(\bar{r}_j) + \frac{e}{m_e}\sum_j \bar{p}_j\cdot\bar{A}(\bar{r}_j) \tag{2.17}$$

where $m_e$ is the mass of electron and $e$ is the elementary charge. The first term in eqn. 2.17 is the A·A term and the second term is the p·A term. A·A has no resonance properties and contributes significantly if the initial and final states are the same. p·A contributes to scattering in second order matrix elements [88] and dominates when the incident photon energy is close to the transition energy from the initial $|i\rangle$ to the final $|f\rangle$ state which is the case for resonance Raman scattering. The components of the polarization tensor $\alpha_{\rho\sigma}$ representing a transition from the initial state $|i\rangle$ to a final state $|f\rangle$ through an intermediate state $|r\rangle$ are described by the Kramers-Heisenber-Dirac equation as [89] [90]:

$$(\alpha_{\rho\sigma})_{fi} = \sum_{r\neq i,f}\left(\frac{\langle f|\, P_\rho\, |r\rangle\, \langle r|\, P_\sigma\, |i\rangle}{\hbar\omega_{ri} - \hbar\omega_0 - i\Gamma_r} + \frac{\langle f|\, P_\sigma\, |r\rangle\, \langle r|\, P_\rho\, |i\rangle}{\hbar\omega_{rf} - \hbar\omega_0 - i\Gamma_r}\right) \tag{2.18}$$

where $\omega_{ri}$ is the transition frequency from $|i\rangle$ to $|r\rangle$, $\omega_{rf}$ is the transition frequency from $|r\rangle$ to $|f\rangle$, $\rho$ and $\sigma$ are the coordinates of the electric dipole operator. The transition probability from the ground state $|m, t\rangle$ to the excited state $|n, t\rangle$ is given by [88]:

$$P_{mn} = \frac{2\pi t}{\hbar}\delta(E_n - E_m)|\,\langle n|\, \bar{H}(t)\, |m\rangle\,|^2 \tag{2.19}$$

where $\bar{H}(t)$ is time dependent Hamiltonian. From eqn. 2.19, the transition probability per unit time t is written as:

$$P_{mn} = \frac{2\pi}{\hbar}\delta(E_n - E_m)|\,\langle n|\, \bar{H}(t)\, |m\rangle\,|^2 \tag{2.20}$$

The Raman cross section which represents the probability of coupling between a photon and investigated material is a function of polarizability of the material. The differential Raman cross section is proportional to the transition rate and it is given by

$$\frac{d^2\sigma}{d\omega d\Omega} = \frac{2\pi}{\hbar}\alpha(\hbar\omega_0)\sum_{n,m}\frac{e^{-\beta E_n}}{Z}|\,\langle n|\, \bar{H}(t)\, |m\rangle\,|^2\delta(E_n - E_m + \hbar\omega_0) \tag{2.21}$$

where Z is the partition function, $\hbar\omega_0$ is the incident photon energy, $\beta = 1/K_BT$, $\alpha(\hbar\omega_0)$ is the proportionality factor. Eqn. 2.21 is the Fermi's "Golden Rule". In the limit of $\bar{H}(t)$ being smaller that $H_0$, eqn. 2.21 can be rewritten as

$$\frac{d^2\sigma}{d\omega d\Omega} = -\frac{2\pi}{\hbar}\alpha(\hbar\omega_0)2(n(\omega) + 1)\Im(R(\omega + i\delta)) \tag{2.22}$$

$n(\omega)$ is the occupation function and $\Im(R(\omega + i\delta)$ is the imaginary part of the response function.

Recall that when the excitation photon energy is close to allowed electronic transition, the intensity of the scattered photon is amplified and it is called resonance Raman. The difference between ordinary and resonance Raman scattering is depicted visually in the

Feynman diagrams of the four photon Green's function [91] shown in Fig. 2.8.

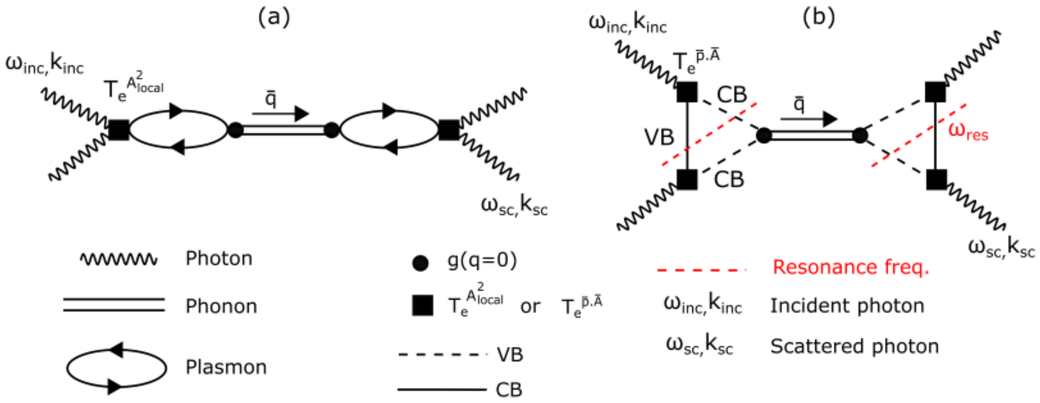

Figure 2.8: Feynman diagram of the four photon Green's function for (a) first non-order resonant for dominant inelastic light scattering at the surface state and (b) second order resonant interband inelastic light scattering in the bulk. VB and CB are the valence and conduction bands, respectively. Electron and hole line represent in (a) excitations within the Dirac cone and in (b) conduction and valence bands, respectively. The arrow above the phonon in (a) and (b) indicates the Stokes direction.

Fig. 2.8(a) shows the non-resonance Raman scattering process. The incoming laser $(\omega_{inc}, k_{inc})$ couples to the electronic system *via* $A^2_{local}$ matrix element and electron couples to phonon *via* $g(q = 0)$ term. The phonon (double horizontal lines) propagates in the direction of the arrow. The Raman scattering intensity for non-resonance processes can be approximated by [92] [88]

$$I^{nres}(\omega) = -Im[\bar{R}(\omega)] = -Im[(T_e^{A\cdot A})^2 g^2 \pi_0^2 D^0] \tag{2.23}$$

where $T_e^{A\cdot A}$ is the non-resonant term, $g$ is electron-phonon coupling constant, $D^0$ is the phonon propagator, $\pi_0$ is the polarization bubble and $\bar{R}(\omega)$ is the Raman response function. For resonance Raman scattering processes (Fig. 2.8(b)), the incoming laser $(\omega_{inc}, k_{inc})$ couples to the electronic system *via* $T_e^{\bar{p}\cdot\bar{A}}$ matrix element which is dependent on the incoming laser energy. The Raman scattering intensity for resonance processes can be approximated by [88]

$$I^{res}(\omega, \omega_{inc}) = -Im[\bar{R}(\omega, \omega_{inc})] = -Im[(T_e^{p\cdot A})^4 g^2 \pi_0(\omega_{inc})^2 D^0] \tag{2.24}$$

where $T_e^{p\cdot A}$ is the resonant term.

### 2.3.3 Phononic Raman scattering in topological insulator

The inelastic scattering in TIs is expected to differ from conventional materials due to the existence of conducting surface state and insulating bulk state hosting electrons that behave differently at the surface compared to the bulk of TI. We consider the metallic surface states hosting the spin textured electrons.

**Metallic surface states of TI**

From the Feynman diagrams (Fig. 2.8) and considering all bubbles contributing to the non-resonant matrix element, the Raman response function according to Bock *et al.* [93] is

$$\begin{aligned} R(\omega) &= -i\left[(iT_{A^2})^2(-\chi_{el}(\omega)) + (iT_{A^2})^2(ig_1)^2(-\chi_{el}^2(\omega))i\bar{G}(0,\omega)\right] \\ &= T_{A^2}^2\chi_{el}(\omega) - T_{A^2}^2(g_1)^2\chi_{el}^2(\omega)\bar{G}(0,\omega) \\ &= R_{el}(\omega) + R_{pho}(\omega) \end{aligned} \tag{2.25}$$

Now consider electronic susceptibility $\chi_{el}(\omega)$ to be

$$\chi_{el}(\omega) = \pi_{re} + i\pi_{im} \tag{2.26}$$

Phonon propagator that is renormalized by the low energy electronic susceptibility is

$$\bar{G}(0,\omega) = \frac{1}{2\bar{\Gamma}\omega + (\omega^2 - \bar{\omega_0}^2)} \tag{2.27}$$

with $\bar{\omega}_0^2 = \omega_0^2 + g_1^2\pi_{re}$ and $\bar{\Gamma}\omega = 2\Gamma\omega - g_1^2\pi_{im}$.

The contribution of the imaginary part of electronic susceptibility leads to a broadening of the phonon linewidth. Squaring the electronic susceptibility (eqn. 2.26), we obtain eqn. 2.28 which is the mixing of the real and imaginary part of electronic susceptibility with the imaginary part of the dressed phonon propagator.

$$\chi_{el}^2(\omega) = (\pi_{re} + i\pi_{im})^2 = \pi_{re}^2 - \pi_{im}^2 + 2i\pi_{re}\pi_{im} \tag{2.28}$$

The intensity associated with the mixing is given as [94]

$$\begin{aligned} I(\omega) = \eta(\omega,\omega_{inc},T)\Big(&-T_{A^2}^2\pi_{im} + \frac{T_{A^2}^2 g_1^2\bar{\Gamma}\omega}{(\bar{\Gamma}\omega)^2 + (\omega^2 - \bar{\omega}_0^2)^2} \\ &\left[\pi_{im}^2 - \pi_{re}^2 + 2\pi_{re}\pi_{im}\left(\frac{\omega^2 - \bar{\omega}_0^2}{\bar{\Gamma}\omega}\right)\right]\Big) \end{aligned} \tag{2.29}$$

By definition, Fano parameter $\bar{q}(\omega) = \pi_{im}(\omega)/\pi_{re}(\omega)$ and therefore we obtain a generalized Fano equation which utilizes exact phonon propagator see eqn. 2.30

$$\begin{aligned} I(\omega) = \eta(\omega,\omega_{inc},T)\Big(&-T_{A^2}^2\pi_{im} + \frac{T_{A^2}^2 g_1^2\bar{\Gamma}\omega\pi_{re}^2}{(\bar{\Gamma}\omega)^2 + (\omega^2 - \bar{\omega}_0^2)^2} \\ &\left[\bar{q}^2 - 1 + 2\bar{q}\left(\frac{\omega^2 - \bar{\omega}_0^2}{\bar{\Gamma}\omega}\right)\right]\Big) \end{aligned} \tag{2.30}$$

$\bar{q}$ which is the ratio of imaginary and real parts of the electronic susceptibility and it is dependent on the frequency. For an increasing imaginary (conversely decreasing real) part of electronic susceptibility, $\bar{q}$ becomes large and Fano eqn. 2.30 recovers to Lorentzian symmetric phonon line shape given as

$$I(\omega) = \eta(\omega,\omega_{inc},T)\left(-T_{A^2}^2\pi_{im} + \frac{T_{A^2}^2 g_1^2\bar{\Gamma}\omega\pi_{im}^2}{(\bar{\Gamma}\omega)^2 + (\omega^2 - \bar{\omega}_0^2)^2}\right) \tag{2.31}$$

For TIs, we obtain

$$I(\omega) = \eta(\omega, \omega_{inc}, T)\Big(-T^2_{A^2}\pi_{im} + \frac{T^2_{A^2} g_1^2 \bar{\Gamma}\omega\pi^2_{re}}{(\bar{\Gamma}\omega)^2 + (\omega^2 - \bar{\omega}_0^2)^2} \left[\bar{q}^2 - 1 + 2\bar{q}\left(\frac{\omega^2 - \bar{\omega}_0^2}{\bar{\Gamma}\omega}\right) + \frac{R}{\pi^2_{re}}\right]\Big) \tag{2.32}$$

Eqn. 2.32 is the Raman response of TI. $\frac{R}{\pi^2_{re}}$ is correction term for Fano parameter $\bar{q}$. Therefore in TIs both the low energy susceptibility and the ratio between resonant and non-resonant Raman scattering drive the phonon asymmetry. Schematic representation of coupling between discrete and continuum state is shown in Fig. 2.9

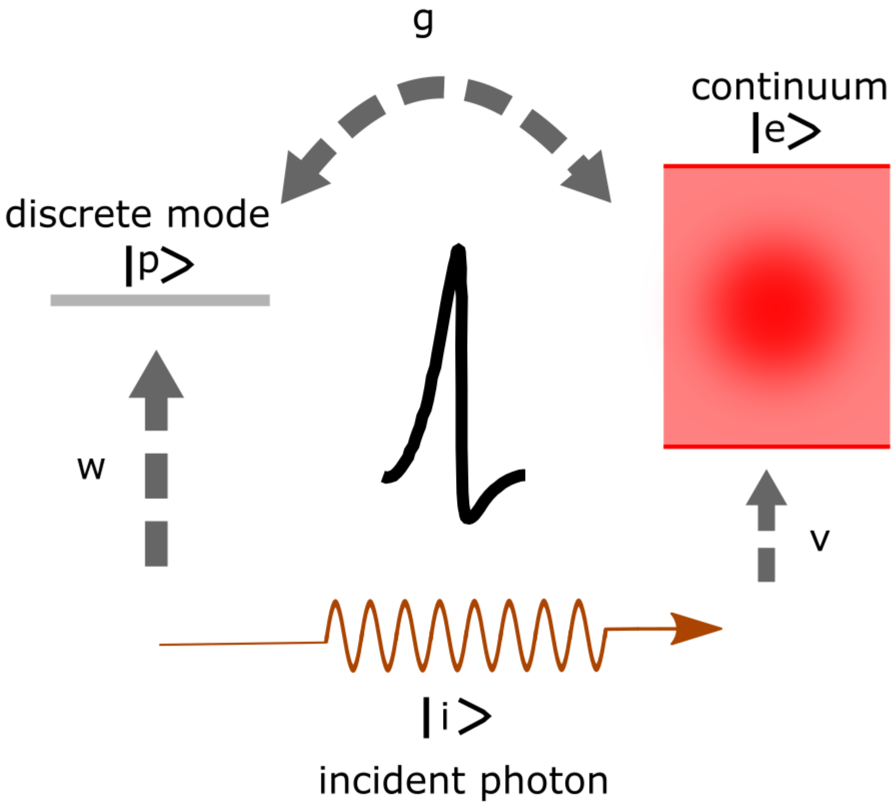

Figure 2.9: Schematic representation of discrete and continuum state interfering. An incident photon $|i\rangle$ excites the continuum $|e\rangle$ and discrete $|p\rangle$ states with coupling factor of v and w, respectively. $|e\rangle$ and $|p\rangle$ interact by a coupling strength g and the interaction results to Fano asymmetry shape.

## 2.4 Surface plasmons, carrier and hot carrier injection into the TI surface states

Charges can be transferred onto the $Bi_2Se_3$ TI, however only charges that are transferred to the surface (below the gap of 3D TI) have a possibility of retaining the Dirac particle-like features. We discuss two modes of charge transfers which we studied in this work, (a) carrier injection mediated by metal/TI interface (Fig. 2.10(a)) and (b) hot carrier injection by resonantly decayed surface plasmons (Fig. 2.10(b)).

### 2.4.1 Metal/TI interface

The carrier injection from metal/TI interface and more specifically from Au substrate to $Bi_2Se_3$ TI bulk and surface states was studied theoretically by Spataru and Leonard [95]. The transferred charges accumulate at the interface side of $Bi_2Se_3$ TI and cause band bending. For Au/$Bi_2Se_3$ TI interface, the TI bands can be shifted by ≈ 1 eV and thus locating the fermi level several hundreds of meVs above the conduction band edge [95]. The calculated spectral function with eqn. 2.33 projected on quintuplet layers and the associated density of states show that the spin momentum locking is maintained with minimal hybridization in such a system [95].

$$A_j(\vec{k}, E) = \sum_{n,i}^{i\epsilon QL_j} \omega^i_{n\vec{k}} \delta(E - \varepsilon_{n\vec{k}}) \tag{2.33}$$

where n, i, k, $\varepsilon_{n\vec{k}}$, and $\omega^i_{n\vec{k}}$ are the band index, atomic site index, crystal momentum, electron energy and site-projected electron wave function, respectively.

### 2.4.2 Localized surface plasmons

Plasmons are oscillations of free electrons in metals with a well defined frequency [96]. As the size of the metal is decreased below the wavelength of the exciting incident light, the associated electric field penetrates the metal and polarizes the conduction electrons [97]. The generated plasmons are localized at the surface of the nanoparticles (NPs) [98]. The localized surface plasmons (LSP) can be modeled as mass spring harmonic oscillator. The inertness and optical properties of gold NPs (Au NPs) made it an ideal candidate for localized surface plasmon generation and decay [97]. For a spherical Au NP, the extinction cross-section, $\sigma_{ext}$, is [96] [99]:

$$\sigma_{ext} = \frac{18\pi[\varepsilon_m(\lambda)]^{1.5}}{\lambda} V_{NP} \frac{Im[\varepsilon(\lambda)]}{[Re[\varepsilon] + 2\varepsilon_m(\lambda)]^2 + Im[\varepsilon(\lambda)]^2} \tag{2.34}$$

where $V_{NP}$ is the volume of NP, $\varepsilon_m$ is the dielectric constant of the non-absorbing ($Im[\varepsilon_{k,m,r}] = 0$) medium, and $\varepsilon = Re[\varepsilon(\omega)] + iIm[\varepsilon(\omega)]$ is the complex dielectric function that is frequency dependent. For maximum $\sigma_{ext}$, the LSP is excited at the frequency where $Re[\varepsilon_{NP}(\omega)] \approx -\chi\varepsilon_m(\omega)$ called Fröhlich condition.

**Decay of LSP**
The decay of LSP is guided by the total relaxation rate Γ which is proportional to the surface plasmon resonance (SPR) bandwidth represented as [97]:

$$\Gamma = \Gamma_{nr} + \omega^2\Gamma_r \tag{2.35}$$

The first term in eqn. 2.35 is for non-radiative decay and the second term is for radiative decay which depends on the SPR frequency. Non-radiative decay (*via* Landau damping) is accompanied by the emission of hot electrons and holes. It can occur through inter-band transition from d-band to s-band leading to a generation of low energy hot electrons in s-band and high energy hot holes in d-band or intra-band transition from sp-band to empty sp-band above the Fermi level [100] [101] [102]. In inter-band transition, Studies on non-radiative decay of surface plasmons can be found in [103] [104] [105] [106].

**Injection into topological surface states**

The injection of carriers from the plasmonic metal into the topological surface states was modeled theoretically based on density matrix formalism. The density of generated hot carriers is given by eqn. 2.36 [107] and that of the injected carriers into the surface state of 3D TI along the x-axis is given by eqn. 2.37 [107]. Recall that only carriers that are injected at the metallic surface states (*i.e.* below the bulk gap of 3D TI) could retain spin polarized behaviour. Due to spin momentum locking of a single particle Dirac state in reciprocal space, only hot electrons (with tangential momentum direction) which have closely overlapping spin components to the Dirac states are injected into the 3D surface states [107].

$$\delta\rho_k = \frac{2}{(2\pi)^3}\frac{1}{\hbar\omega}k_r^2|\Omega_{k,q}|^2\frac{m}{\hbar^2 q}\log\left(\frac{k_f}{k-q}\right)\Theta(k-k_F) \tag{2.36}$$

where $\Theta(k-k_F)$, $k_r$, q, $L_y$ and $k_F$ are the Heavyside step function, wave vector, momentum, length of $Bi_2Se_3$ sample along the y direction and Fermi wave vector, respectively. $\Omega_{k,q}$ is the excitation rate that describes the number of carriers generated per second.

$$\delta\eta = \frac{\delta\rho_k}{2}\frac{V}{N}\frac{E_F^{3/2}}{[(E_F+e\phi)^{3/2}-E_F^{3/2}]}\frac{1}{L_y\hbar\nu_F}e\varphi_b \tag{2.37}$$

where $\nu_F \approx 6 \times 10^5$ m/s is the Fermi velocity for $Bi_2Se_3$, $E_F$ is Fermi energy, V/N $\approx$ $10^{-22}$ $cm^3$.

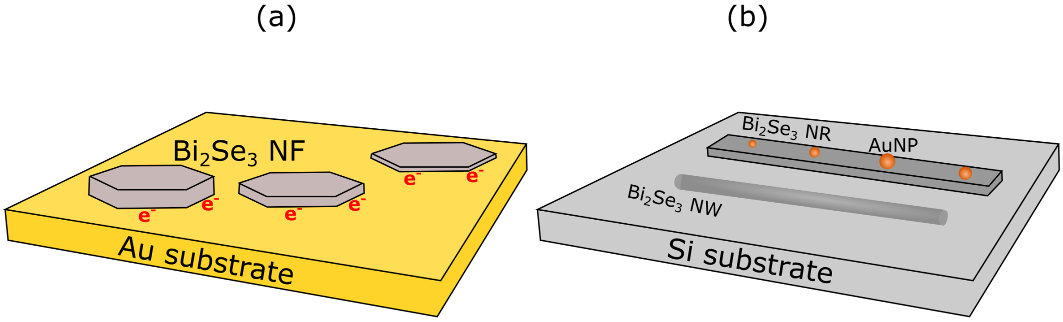

Figure 2.10: Schematic representation of (a) interface and (b) hot carrier injection into $Bi_2Se_3$ TI. The injected carriers at the metallic surface states are spin polarized and are immune to non-magnetic backscattering.

# Chapter 3

# Experimental Techniques

In this chapter, we will present the growth of $Bi_2Se_3$ nanoflakes (NFs), nanoribbons (NRs) and nanowires (NWs). We will examine the micro-Raman set-up, photolithography process of contatcing the samples, and electrical transport measurement. Sample preparations and brief discussions of different characterization techniques used in this work will be discussed.

## 3.1 Synthesis methods

This section will dwell on synthesis methods used to fabricate the samples. $Bi_2Se_3$ NWs and NRs were fabricated in an oven by the chemical vapour deposition (CVD) method. $Bi_2Se_3$ NFs were fabricated using a wet chemical polyol (WCP) method.

### 3.1.1 Chemical vapour deposition method

Chemical vapour deposition (CVD) is an attractive and widely used fabrication method to fabricate high quality monocrystalline, polycrystalline and amorphous nanostructure materials on different substrates. In this work, we used the CVD method to grow high quality monocrystalline $Bi_2Se_3$ NWs and NRs on silicon ⟨100⟩ substrates. Fig. 3.1 shows the schematic diagram of the CVD.

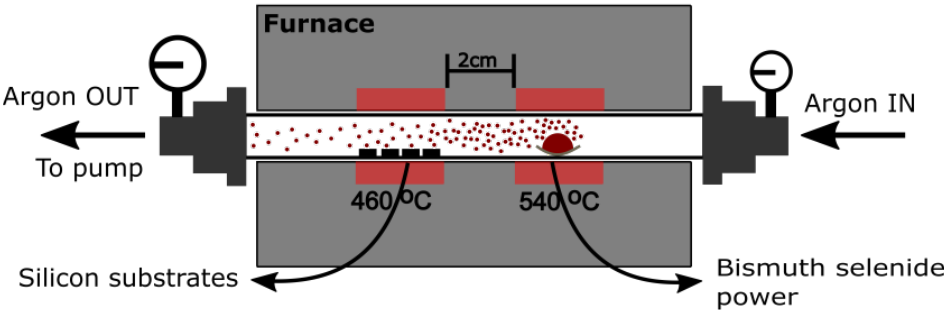

Figure 3.1: Schematic diagram of chemical vapour deposition (CVD) showing the upstream ($540^oC$) and downstream ($460^oC$) temperatures.

### Growth of $Bi_2Se_3$ nanoribbons and nanowires

NRs and NWs of $Bi_2Se_3$ were grown in an oven and we followed a general approach in CVD [108] [11] [9] with full optimization for the growth process. The furnace is made up of two heating zones, the downstream and the upstream. During synthesis, the downstream and the upstream were heated to 440 $^oC$ and 540 $^oC$, respectively. The growth mechanism is by vapour liquid solid (VLS) process in which gold (Au) catalyst activates the reaction. The eutectic composition of Au:$Bi_2Se_3$ lowers the melting temperature of the Au alloy, thereby allowing the alloy to melt and subsequently reaching saturation point from which crystal growth can occur. The general procedures for synthesizing $Bi_2Se_3$ NRs and NWs in an oven are summarized as below:

(a) **Preparation of the silicon substrates**
Silicon substrates were cleaned in Piranha solution and rinsed multiple times in deionized water in order to remove dirt.

(b) **Functionalizing the silicon substrates**
Silicon substrates were functionalized with 0.1 % w/v aqueous poly-L-lysine to enhance the attachment of gold nanoparticles to the substrates.

(c) **Coating the substrates with gold nanoparticles**
The substrates were dipped inside a colloid solution of gold nanoparticle (AuNPs) (50 nm diameter) for 5s.

(d) **Growth of the $Bi_2Se_3$ nanostructures**
0.2g of granular $Bi_2Se_3$ was placed in an alumina boat and loaded at the upstream zone of the furnace. Si substrates coated with AuNPs were loaded at the downstream zone of the furnace. The tube was pumped to a pressure of 40 mTorr, and flushed multiple times with ultrapure argon gas to minimize oxygen contamination in the 2.5 cm diameter quartz tube. The downstream and upstream zones were heated to their various temperatures in 1 hour. The carrier gas flow rate, the pressure and reaction time were set to 30 standard cubic centimeters per minute (sccm), 780 mTorr, and 1 hour, respectively (Fig. 3.1). In order to provide a selenium environment and to protect the surface of the $Bi_2Se_3$, after the reaction, the argon flow was systematically switched off and the system was allowed to cool down to room temperature within 2.5 h. (Figs. 4.5 and 4.12 in Chapter 4 for the result).

(e) **Tuning the growth parameters**
In order to obtain nanostructures of different sizes and shapes, the growth parameters such as the Argon flow rate, the pressure in the quartz tube and/or growth temperature were tuned.

## 3.1.2 Wet-chemical polyol method

The synthesis of $Bi_2Se_3$ nanoflakes follows a standard wet-chemical method [109] [110]. The chemicals used for the synthesis include Bismuth (III) nitrate ($Bi(NO_3) * 5H_2O$, 98 % Sigma Aldrich) as source of Bismuth (Bi), Sodium selenite ($Na_2SeO_3$, 99 % Sigma Aldrich) as source of Selenium, polyvinylpyrrolidone (PVP, $C_6H_9NO$, 55.000M, Sigma Aldrich) as a reducing agent/growth surface stabilizer and ethylene glycol (EG, $C_2H_6O_2$, 99.5 %, ROTH, JT Baker) as a solvent medium for the synthesis. The synthesis process involves dissolving 0.66 g PVP (55K), 0.30 g $Bi(NO_3) * 5H_2O$, and 0.15 g $Na_2SeO_3$ in 30 mL EG at 60 $^oC$. The solution was transferred into a three-neck flask which is connected to a water cooled reflux (Fig. 3.2). The stirring was done with a teflon bar at 450 revolution per minute (rpm). The reaction temperature and time were 190 $^oC$ and 120 minutes, respectively. The first process in the reaction is that EG reacts with $O_2$ to form glycolaldehyde [111], which acts as a reducing agent for the precursor. Bi plates, hexagons and Se needle are formed as a parallel side product [109] [110]. After a certain time, $Bi_2Se_3$ nucleates and grows into nanoflakes. The solution changes from transparent to a stable homogeneous black liquid. After the reaction, the solution is allowed to cool down to room temperature. The product of the reaction is washed with acetone and isopropanol in a centrifuge and stored in isopropanol [109] [110]. see Fig. 4.1 in Chapter 4 for the results.

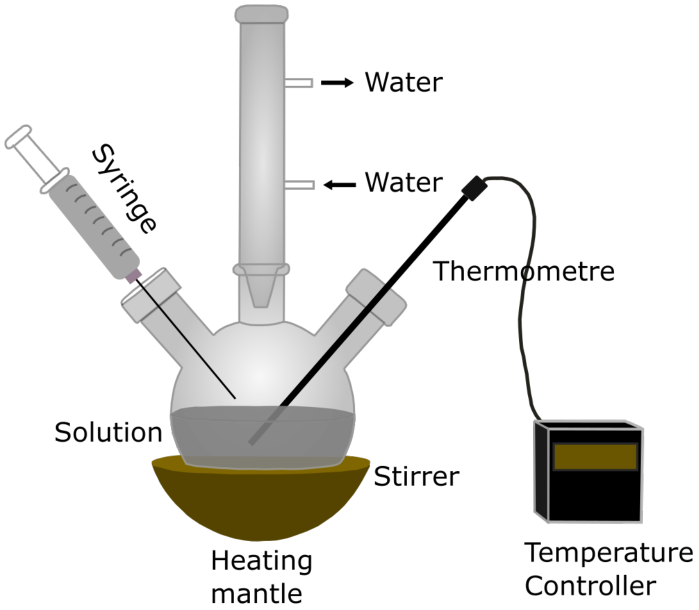

Figure 3.2: Schematic diagram of the wet chemical set-up. (Adapted with permission from [112]).

### Drop Casting the $Bi_2Se_3$ nanoflakes on the finder grid and decorating individual $Bi_2Se_3$ nanoribbons with AuNPs

The solution containing the nanoflakes was drop-cast on finder grid substrates and the isopropanol was allowed to evaporate. The finder grid substrates (gold sputtered and silicon) were marked such that individual nanoflakes could be identified and measured. 10 µL of dispersed AuNPs in water was drop-cast on the individual nanoribbons and dried before measurement. As mentioned earlier in section 3.1, individual nanoribbons were transferred to the custom-made 100 µm x 100 µm silicon finder grid with the aid of a micro-manipulator.

## 3.2 Raman spectroscopy

The Raman data were acquired at the Center for Free Electron Laser Science (CFEL) in Hamburg using a micro-Raman set-up that is coupled to the Ultimate Triple 3 (UT-3) [113].

### 3.2.1 The Ultimate Triple 3

This is a triple-grating, fully achromatic, deep ultraviolet (UV) to near-infrared (IR) spectrometer [113]. The UT-3 is designed such that the image aberration is minimized by using on-and off- axis parabolic mirrors. The Raman signal is collected with a reflective entrance objective of numerical aperture 0.5. A strong stray light rejection with high resolution in the UV and IR region is achieved by the use of elliptical mirrors [113]. The whole set up is located in a controlled cleanroom. For long term stability, the controlled temperature and relative humidity are kept at 22 $^oC \pm 0.5\ ^oC$ and 40 % ± 3 %, respectively. UT-3 uses two Tsunami Ti:Sapphire laser systems (3950-X1BB, Spectra Physics Lasers Inc., California) to achieve a wide range of incident wavelengths. This is realized by the use of either second, third or fourth harmonic generation (Spectra Physics Lasers Inc., California). The green Millennia Pro Xs 10sJS and Millenia eV diode laser (Spectra Physics Lasers Inc., California) are used as the pump lasers. The auto correlator (APE GmbH, Berlin) was used to determine the pulse width of the laser and it is about 1 ps. The schematic diagram of the UT-3 is shown in Fig. 3.3

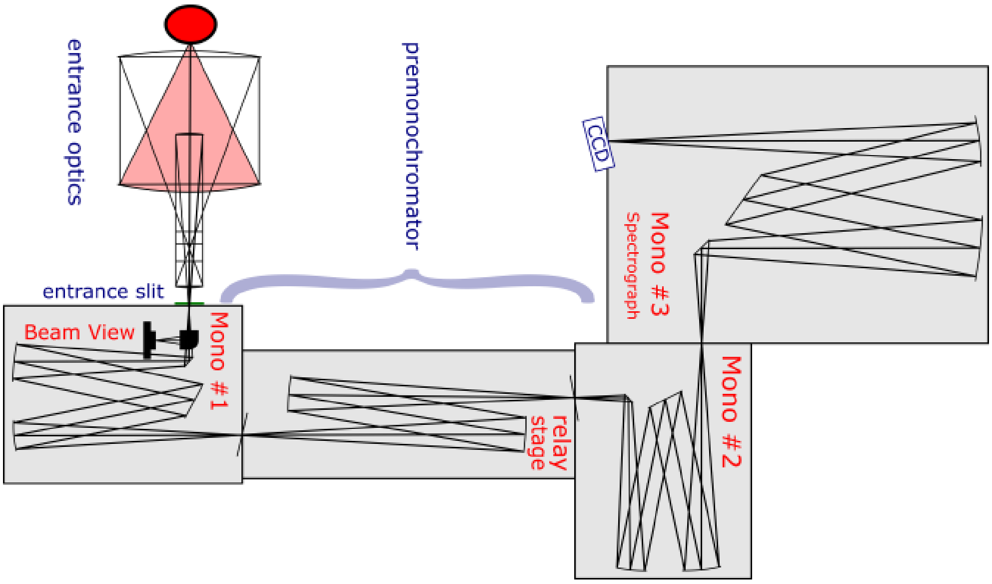

Figure 3.3: Schematic diagram of the UT-3 showing the entrance optics, which focuses the light into the pre-monochromator (Mono1, relay stage and Mono2). The light is spectrally resolved in Mono3 in order to achieve a strong stray light rejection with high resolution. (Adapted from [113]).

### 3.2.2 Micro-Raman

A custom made micro-Raman with beam spot diameter in the range of 211 nm ± 3 nm - 400 nm ± 5 nm, depending on laser wavelength, was developed by us [92] [114]. We used the micro-Raman to resolve different diameters of gold nanoparticles on the $Bi_2Se_3$ nanoribbons and nanoflakes down to 39 nm and were able to conduct detailed Raman study on a single nanowire, nanoribbon and nanoflake. The custom made micro-Raman was mounted on an aluminum support to ensure stability of the set-up. The set-up was mounted on a translation stage which allows for x, y, and z translational degrees of freedom. The incoming laser light was guided through a spatial filter, and focused on the sample by an infinitely corrected microscope objective 50X Mitutoyo Plan Apo HR (NA = 0.75) or 50X Mitutoyo Plan Apo (NA = 0.5). With the aid of the focusing objective, IC50 (Olympus, Japan), the scattered light from the sample was focused on the entrance optics (EO) of the UT-3 spectrometer. At the back of the construction is the white light source QTH10/M (Thorlabs, USA) which is in-coupled into the beam path by a beam splitter BS064 (Thorlabs, USA) with 70 % reflection and 30 % transmission. The white light and the probe laser light were focused on the sample: switching between light microscope and the Raman mode is controlled by a motorized mirror. The reflected light is focused on the CCD camera by tube lens when the mirror is driven out. The scattered Raman light is focused onto the UT-3 spectrometer axis when the mirror is driven in. The CCD camera specification is as follows: 5 M pixel CCD chip DFK37BUX264 (The Imagine Source, USA), 3.45 µm × 3.45 µm pixel size, 50X magnification. The image size per pixel is approximately 70 nm. The computer aided design (CAD) drawing of the micro-Raman set up is shown in Fig. 3.4 [114].

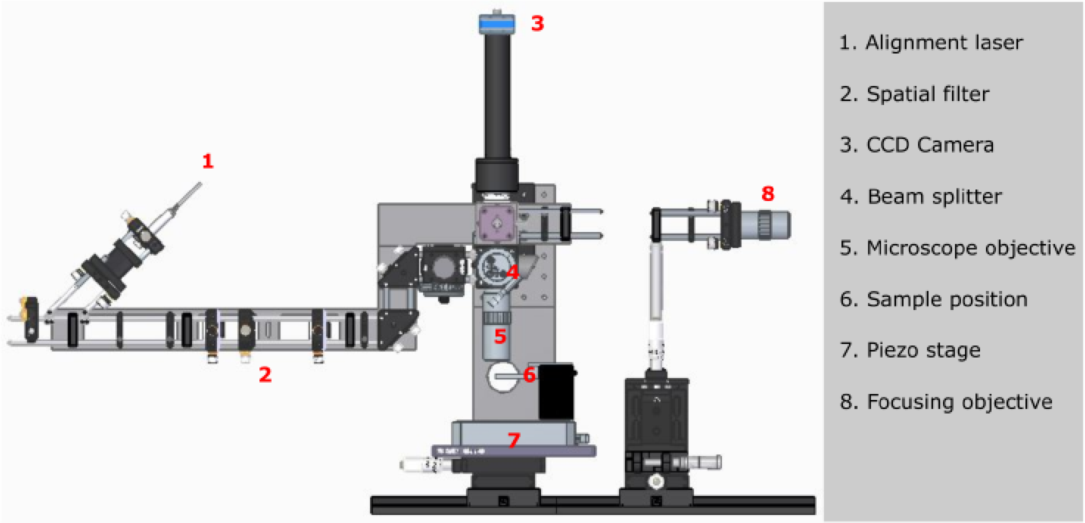

Figure 3.4: CAD drawing of the micro-Raman set-up. The incoming laser beam enters the spatial filter and it is focused on the sample by an infinity corrected microscope objective. The scattered light from the sample is redirected and focused on a CCD camera through the entrance optics of UT-3. (Figure taken from [115]).

### 3.2.3 Beam path in the micro-Raman

The schematic diagram of the micro-Raman is shown in Fig. 3.5. The beam path of the monochromatic laser light i.e. red laser (633 nm), is shown as a red arrow. The incoming red laser enters the spatial filter through the wave plate ($\lambda/2$) as shown at the left hand-side of the diagram. The first lens, with 25 mm focal length, focuses the laser light into a 25 µm pinhole. With the aid of the second lens, of 75 mm focal length, the beam is widened to a diameter of about 12 mm. The widened beam is guided through two $45^o$ mirrors on to the first beam splitter (BS1), which reflects 70 % and transmits 30 %, and then to the second beam splitter (BS2), which reflects 10 % and transmits 90 % of the monochromatic laser beam. The monochromatic laser light is then focused on the sample by microscope objective (MO) (Mitutoyo Japan, 50X objective, NA = 0.75/0.5). Note that the sample is mounted on top of a multi-axis piezo scanner P-517 (PI, Germany), which is operated by an E-710.3CD controller (PI, Germany) for precise positioning of the sample, laser spot and scanning of the samples during measurements [92] [114]. The Raman signal (shown in rainbow color), together with the reflected light, were focused on the entrance objective (EO) of the UT-3 using an objective IC50 (Olympus, Japan).

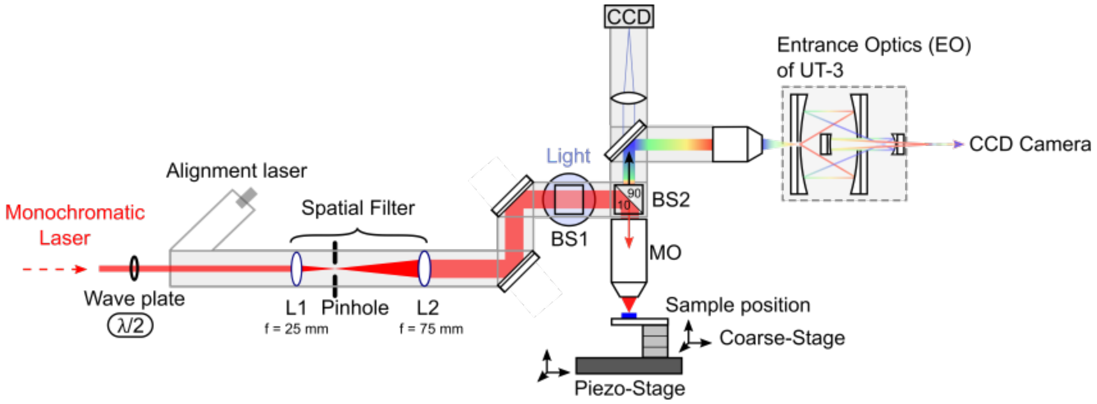

Figure 3.5: Schematic diagram of beam path in the micro-Raman set-up. The incoming monochromatic laser light passes through the wave plate ($\lambda/2$) and enters the spatial filter. The spatial filter is made up of a 25 mm lens, 20 µm pinhole and then a 75 mm lens. To modify the beam height, a periscope is used. The beam passes through a beam splitter (BS) (reflect 10 % and transmission 90 %) and is focused on the sample by the 50X objective of numerical aperture (NA) (0.75 or 0.50). The scattered light passes through the BS and it is directed at $90^o$ by a motorized mirror to Olympus objective (NA=0.4). The Olympus objective focuses the signal to the entrance optics of the UT-3. (Figure adapted from [92]).

### 3.2.4 Raman study

The study on $Bi_2Se_3$ NWs was conducted with a green laser (532 nm wavelength) whereas the measurements on $Bi_2Se_3$ NRs and NFs were conducted with a red laser, (633 nm wavelength) except for the Resonance study. The resonance study was conducted on NRs and NFs and the following lasers were used (a) red laser, 633 nm wavelength (Gas, 05-LHP-123-496 HeNe), (b) yellow laser, 594 nm wavelength (Diode, OBIS 594LS 1233468), (c) light green laser, 560 nm wavelength (Diode, OBIS 561LS 1223779) and (d) green laser, 532 nm wavelength (Diode, Millenia Pro 10sJS). The nanoscopic beam spot size enabled us to precisely place the beam on the sample during measurements. The power on the sample was measured with a power meter (PM160, Thorlabs, USA). The maximum laser power at the sample during measurements depended on the laser wavelength and Mitutoyo objective lens used. Typically, the power at the sample was less than 50 $\mu$W. The beam spot diameter (full width at half maximum (FWHM)) was around 200 nm - 550 nm depending on the laser wavelength and the microscope objective used. In order to determine the beam spot size, the laser spot was focused on a bare <111> silicon

substrate and the image of the beam spot was recorded. The intensity cut in different directions through the 2D image of the laser spot was obtained and fitted with a Gaussian profile. Fig. 3.6(b) shows an exemplary line cut through the 2D image obtained with 633 nm wavelength and the corresponding FWHM is shown in Fig. 3.6(a). For more detail of the line cut of various wavelengths, (see section 2.1 of Appendix B).
For a typical Raman measurement, the spectra were acquired in back-scattering configuration while employing Porto notation configuration (Fig. 3.6(c and d)) [116] [117]. All measurements were acquired in parallel configuration except for polarization dependence study where perpendicular configuration was used (Fig. 3.6(d)). The acquisition time for the study depended on whether we were measuring the nanoflakes or nanowires/nanoribbons. To exclude laser heating of the samples, the laser power on the sample was kept at low values depending on the laser wavelength used. Note that several pre-test measurements were carried out before the actual measurement.

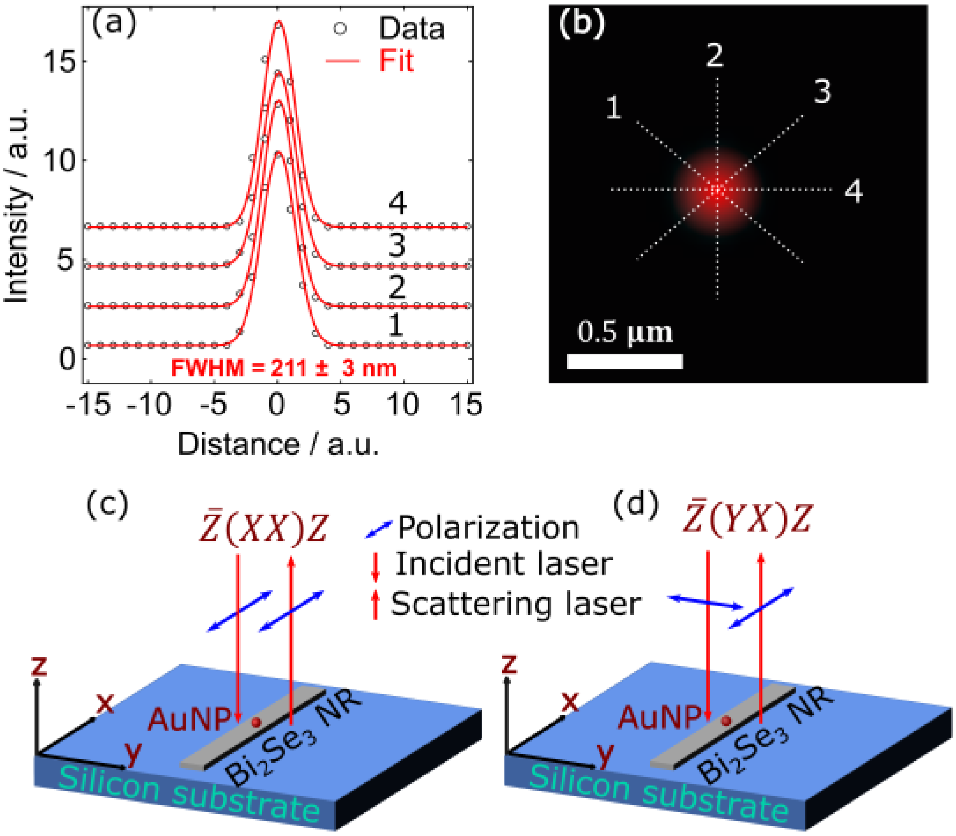

Figure 3.6: Beam spot size and Porto configuration. (a) Gaussian fit of the intensity profile from (b) in four different directions. (b) Intensity cut from 2D image of red laser spot. Porto configuration showing the parallel (c) and perpendicular (d) polarization of the incident and scattered light. Adapted from [118].

### 3.2.5 Magnetic field dependent Raman measurements

Magnetic field dependence was conducted on our sample during Raman study. In order to achieve this, a custom made aluminum construction was designed to hold two bar magnets each of 500 mT. The bar magnets were used to create fields along the long axis of the Bi$_2$Se$_3$ nanowires. Adjustable screws were used to adjust the distance between the bar magnets to about 7 mm apart [115]. The magnetic field at the sample position is determined using a Hall effect sensor GM05 (Hirst Magnetic Instruments Ltd., UK). For magnetic field dependence Raman study, the $Bi_2Se_3$ nanowire was aligned parallel to both the magnetic field of the two bar magnets, and the polarization of the laser light. The measurement sequence was (a) measuring a sample in the construction without the magnetic field, (b) switching on the magnetic field and repeating the measurement, (c) turning off the magnetic field and repeating the measurement. After that, the sample was removed and another sample was used and the sequence was repeated.

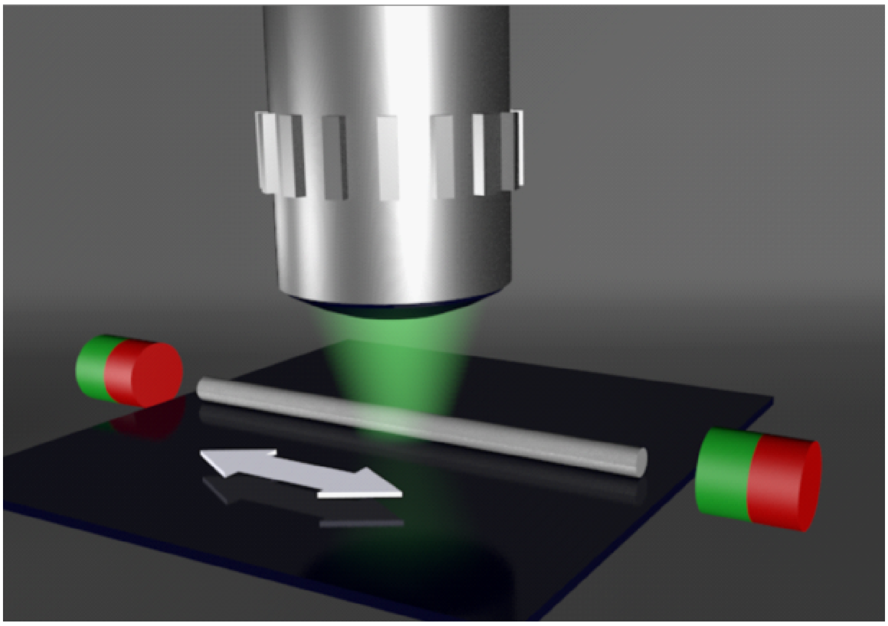

Figure 3.7: Sketch of the Raman study when the magnetic field is applied along the long axis of the wire. The 532 nm laser is focused on the NW and magnetic fluxes are created in NWs by two permanent magnets along the axis. The white double head arrow is the scan direction. Taken from [115].

## 3.3 Sample Characterization

In this section, we discuss various characterization techniques used in characterizing our samples. Techniques such as scanning electron microscopy (SEM), transmission electron microscopy (TEM), high resolution transmission electron microscopy (HRTEM), selected area electron diffraction (SAED), energy filtered transmission electron microscopy (EFTEM), electron energy loss spectroscopy (EELS), energy dispersive x-ray spectroscopy (EDX), and atomic force microscopy (AFM) were used to investigate our samples.

### 3.3.1 Atomic force microscopy

A commercially available atomic force microscopy (AFM) (Q-scope 250 model) was used to determine the shape and height (thickness) of the samples. The AFM has a 40 µm x 40 µm scan head, a lateral resolution of 0.6 nm, and a vertical resolution of 0.05 nm. In the measurement condition, the cantilever is scanned along the x -axis (horizontal scan) and it is in intermittent contact mode. The data acquired in the AFM were analyzed with

Gwyddion and ImageJ software and the results obtained with the AFM are presented and discussed in chapter 4 (results and discussion).

### 3.3.2 Scanning electron microscopy

A commercially available field effect scanning electron microscopy (FESEM) (ZEISS ΣIGMA) was used to determine the position and size of the AuNPs on the nanostructures. For bright resolution images, an acceleration voltage was set between 1kV - 8kV. Depending on the nanostructure under study, the in-lens detector for secondary electrons with a working distance of about 3 mm and a magnification of between 50, 000 - 120, 000 was used.

### 3.3.3 Transmission electron microscopy

TEM was used to determine the crystallinity and the growth direction of the samples. The TEM study was conducted with a JEOL JEM-2100 with 200 kV acceleration voltage and a LaB6 cathode. Samples were transferred to carbon coated CU TEM grids from the Si substrate and pre-characterized with SEM before TEM study. Multiple samples were studied with TEM, high resolution transmission electron microscopy (HRTEM) and selected area electron diffraction (SAED). The shells of the samples were studied with energy filtered transmission electron microscopy (EFTEM) and electron energy loss spectroscopy (EELS)(FEI Tecnai F30 $G^2$ STwin). The results are presented and discussed in chapter 4.

### 3.3.4 Energy dispersive x-ray spectroscopy

EDX was used to determine the stoichiometry of the samples. Both the SEM and TEM were equipped with a nitrogen cooled X-Max 50 detector (Oxford). This allowed for the in-situ characterization of the stoichiometry of the samples during SEM and TEM study.

## 3.4 Magneto-transport study

In this section, we outline processes involved in magneto-transport measurements of the samples. Sequentially the process involves: designing the markers and the electrode pattern, photolithographic patterning of markers on the substrate, transferring nanowires onto the marked substrate, spin coating the substrate with photoresist, writing the electrodes on the sample, developing the pattern, etching the nanowire, contacting the nanowire with metal electrodes, wire bonding the electrodes and electrical-transport measurement.

### 3.4.1 Device pattern design

The design that can be printed on the sample could be designed in any chip design environment. In our case, we used K-layout. The K-layout design contains the marker and the electrodes. For precise contact on the nanowire, the markers are first printed on the silicon (Si) substrate (note Si substrate is covered with 300 nm $SiO_2$ layer) and nanowires transferred to the markers before the electrodes are written on the sample.

### 3.4.2 Photolithography patterning

The µPG 101 Micro pattern generator from Heidelberg Instrument was used to print the design on the Si substrate Fig. 3.8(e). Before printing the design on the Si substrate, various processes for cleaning and depositing positive photoresist were carried out. A Si wafer was cleaned with acetone, isopropanol, deionized water, dried with nitrogen and baked at 115 $^oC$ for 60 s. 30 µL of positive photoresist (S1813, Rohm and Haas electronic materials LLC) was dropped on the substrate and initially spun at 500 rpm (revolutions per minute) for 5 s and then at 4000 rpm for 30 s and pre-baked at 115 $^oC$ for 60 s before exposing it to µPG 101 laser printer to print either the markers or the contact electrodes. The exposure dosage was 15 mW, 50/60 %, x4. The exposed pattern was developed with microposit MF-319 developer (Dow Europe GmBH, c/o DSP Germany), gold coated in a sputtering chamber and the unexposed photoresist was removed with remover mr-Rem 400 (micro resist technology GmbH) at 60 $^oC$ to expose the device markers or the electrodes. Note that all the photolithography processes were conducted in a cleanroom under yellow light illumination.

### 3.4.3 Transfer of the nanoribbons and nanowires

A custom-made x,y,z - positioner micro-manipulator was used to transfer the nanoribbons and nanowires to the Si substrate (Fig. 3.8(b)). For Raman study, the nanostructures were transferred to the 225 fields of 100 µm x 100 µm custom-made silicon finder grid. For electrical transport study, the nanowire was transferred to the design marker before repeating the process for the electrode contact. The positioner has 51 mm long tungsten picoprobe tips (T-4-10) with a wire shaft diameter of 10 µm, a point radius <0.1 µm and a tip length of 3.3 mm. Fig. 3.8(f) shows the picoprobe tip with the attached nanowires.

### 3.4.4 Etching of the nanowire

Argon etching of the nanowire was carried out at room temperature in the reactive ion etching system ICP-RIE (SI 500, Sentech instrument GmBH). The etching was done in order to remove photoresist residues as well the native oxide layer on the nanowire. After etching, the nanowire was quickly transferred into the Physical Vapour Deposition system (PLS 500, Balzers Pfeiffer) in order to make metal contact on the exposed surface and to reduce the oxidation of the nanowire surface. Note that etching the nanowire occurred immediately after developing the device (containing nanowire), just before the metal contact.

### 3.4.5 Wire bonding

The Si substrate was mounted on a puck and electrically connected to the terminals of the puck. The puck is about 2 cm in diameter and contains large areas that are specifically designed to bond thin aluminum wires on the areas. The thin aluminum wires were bonded from the four electrodes (channel pads) on the device containing the nanowire, onto the four terminals (channel pads) of the puck (viz I-, V-, V+, I+) (Fig. 3.8(d)) by a wire bonder system (TPT wire bonder). In this way, the wire is connected to the circuit of the puck and the puck is electronically connected to the Dynacool (physical measurement system).

### 3.4.6 Electrical transport measurement

Electrical measurement was conducted in a physical property measurement system (PPMS) Dynacool (Quantum Design) (Fig. 3.8(a)). The Dynacool is equipped with a cryostat that can cool the sample down to 2 K and can apply a magnetic field between ± 9T. The resistance measurements were performed in the helium atmosphere in a 4-point configuration Fig. 3.8(c) and 4.6(c)(in Chapter 4) using lock-in techniques with the applied current $I$ and measured voltage $V$. Note that before mounting the puck in the Dynacool, 2-probe and 4-probe room temperature resistance measurement was performed on the device with source measurement unit (Rohde & Schwarz, 6241A) to verify the contacts.

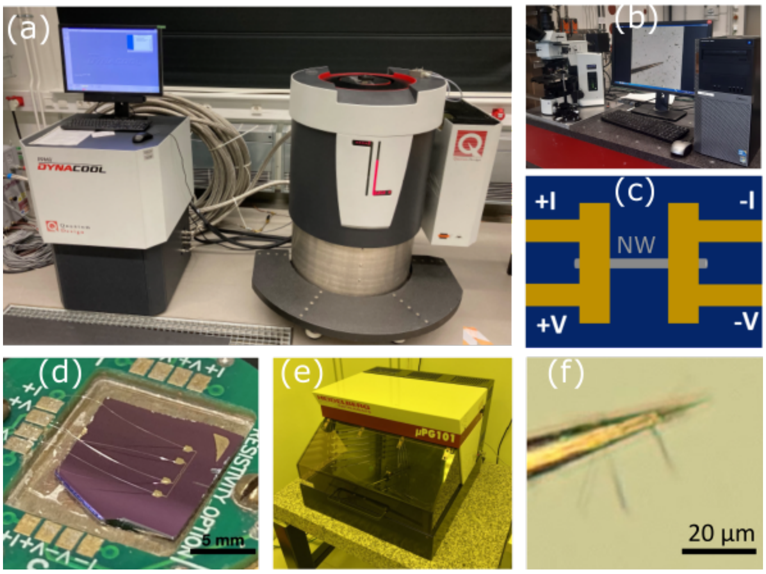

Figure 3.8: (a) Set-up of PPMS dynacool used for the magnetotransport measurement. [119] (b) Micro-manipulator set. Magnified image of the picoprobe tip with the attached NWs is shown in (f). (c) Schematic diagram of the device. Four electrode terminals of current and voltage are shown in yellow colour. The contacted NW is represented in grey colour. (d) Magnified image of the device mounted on the puck and electrically bonded. (e) Image of the laser writer (µPG 101 Micro pattern generator).

# Chapter 4

# Results and Discussions

The results are presented in three different sections namely: (1) carrier injection from gold substrates into the topological insulator $Bi_2Se_3$ nanoflakes, (2) quantum confinement of the spin Berry phase on 1D topological surfaces of $Bi_2Se_3$ nanowires and (3) plasmonic hot carrier injection into topological insulator $Bi_2Se_3$ nanoribbons. In each case, detailed characterization results which validate the quality of our samples are presented in chronological order.The position of the Fermi energy was estimated with the results from the electrical magneto-transport measurements. The results of Raman spectroscopic studies on $Bi_2Se_3$ nanoflakes, nanoribbons and nanowires are outlined and critically evaluated. Furthermore, the interactions of photons, plasmons, electrons and phonons are elucidated from the Raman spectra.

## 4.1 Carrier injection from gold substrates into the topological insulator $Bi_2Se_3$ nanoflakes

In this section, we present the results of the electron-phonon coupling, interface enhancement and phonon renormalization at the $Bi_2Se_3$ nanoflake/gold substrate interface. We utilize Raman scattering to study the dependency of the nanoflake thickness on the electron-phonon coupling at the $Bi_2Se_3$/gold interface. The effect of carrier injection from gold substrate at the interface and how it modified the band structure of $Bi_2Se_3$ nanoflakes in the first few quintuple layers is discussed. We first examine the quality of the synthesized $Bi_2Se_3$ nanoflakes by conducting various characterization processes outlined in chapter three.

### 4.1.1 AFM, SEM, TEM, HRTEM and SAED Characterization of the nanoflakes

The as-grown nanoflakes dispersed in isopropanol solution were drop-cast onto silicon and gold substrates for further studies. Fig. 4.1(a) shows a representative AFM image of the synthesized nanoflakes. The height profile of the nanoflake in Fig. 4.1(a) is shown in Fig. 4.1(d) with an average size of 12 nm. Note that the average size of the synthesized nanoflakes is 8 QL (quintuple layer) [120] [121] [110]. The thickness of each QL of $Bi_2Se_3$ is $\approx 1$ nm [122] and the measured nanoflakes were carefully analyzed since the height of the nanoflakes plays an important role in the carrier injection at the metal/TI interface. EDX shows that the grown samples have the correct stoichiometry i.e. Bi:Se

(2:3) [121] [120] [109].

Fig. 4.1(b) shows a representative SEM image of the synthesized nanoflakes. During the growth process, the solution changes from transparent to a stable homogeneous black liquid [120] [109]. The synthesized nanoflakes are mostly hexagonal in shape, while a few of the nanoflakes show truncated trigonal shape as shown in Fig. 4.1(b).

To elucidate the crystallinity, morphology and growth direction of the synthesized nanoflakes, we performed a detailed TEM characterization. Fig. 4.1(c) clearly shows the hexagonal shape of an exemplary nanoflake. The high-resolution TEM (HRTEM) image of the nanoflakes is shown in Fig. 4.1(e) and indicates that the nanoflakes have single crystalline quality. The lattice spacing was determined from the HRTEM to be 0.22 nm as shown in Fig. 4.1(e) and it is in agreement with the $11\bar{2}0$ spacing in the ab-plane [56] [123]. In order to determine the growth direction of the nanoflake, the SAED pattern was taken from the sample in the [001] zone axis and the result indicates that the growth is in $\langle 110 \rangle$ directions as shown in Fig. 4.1(f). Indexing the bright reflections in the SAED pattern of Fig. 4.1(f), $R\bar{3}m/D^5_{3d}$ space group was obtained [122] [56] [57]. Apart from the bright reflections, weak reflections (marked in blue circles) were observed and attributed to selenium vacancies (superlattice) [109].

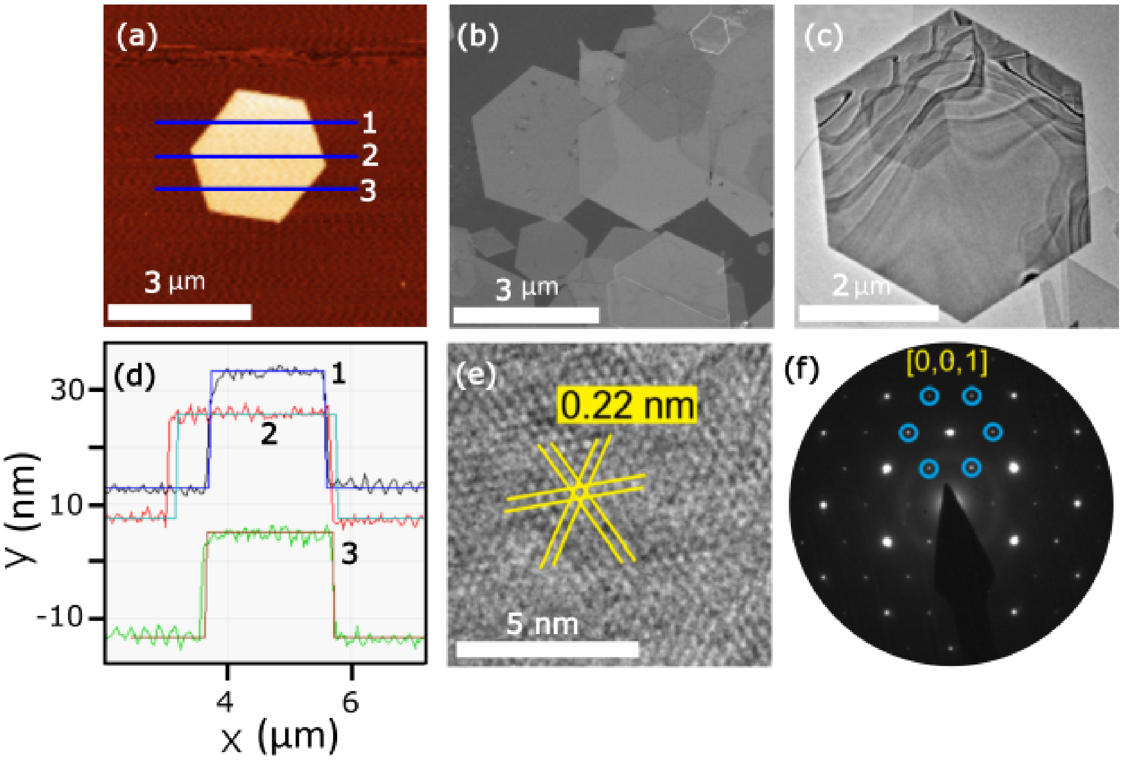

Figure 4.1: AFM, SEM, TEM and HRTEM images of grown NFs. (a) AFM image of 15 nm thick NF as determined by the height profile shown in (d). (b) SEM images of NFs showing hexagonal and truncated triangular shapes. (c) An exemplary TEM image of NF. (e) HRTEM image of NF, lattice spacings of 0.22 nm was obtained as shown in yellow lines. (f) SAED pattern of NF shows orientation along [001]. The observed weak reflections marked in blue circles are attributed to superlattice. (Adapted with permission from APS [120]).

### 4.1.2 Thickness dependence Raman study of $Bi_2Se_3$ nanoflakes

We earlier discussed band structure, crystalline structure, and Raman modes of $Bi_2Se_3$ (for details see section 2.2.1). Here we present the result of Raman spectroscopy study on thickness dependence of $Bi_2Se_3$ nanoflakes (NFs) on gold (Au) substrate. The thickness of the NFs studied is between 7 nm to 13 nm. We established a relationship between the optical contrast and the thickness of the NFs.The optical contrast was determined by calculating the average greyscale value of the NFs compared to the surrounding Au substrate. For thin NFs, we found that the optical contrast is proportional to the thickness of the NFs (for details, see section 4.1 on Appendix B). The calculated optical contrast for the studied NFs and corresponding thickness is shown in Fig. 4.2(e - j). The optical contrast of 31.51, 39.48, 42.38, 42.83, 44.83, 56.18 has corresponding thickness of 7.90 $\pm$ 1.0, 8.97 $\pm$ 0.6, 9.80 $\pm$ 1.3, 10.10 $\pm$ 0.8, 9.92 $\pm$ 0.8, 12.56 $\pm$ 1.4, respectively. All data were corrected for the spectral response of the instrument [113]. Fig. 4.2 shows the Raman spectra for the 6 NFs studied with 633 nm excitation wavelength. 633 nm corresponds to the energy of interband transition in $Bi_2Se_3$ [45] [124]. From the Raman spectra of NFs of thickness greater than 12 nm, we can assign the three distinct phonon modes to $A^1_{1g}$, $E^2_g$ and $A^2_{1g}$ symmetry [57] [125] [126] [127]. As the thickness of the NFs is decreased below 10 nm, we found strong renormalization in the $A^1_{1g}$ and $A^2_{1g}$ phonon modes and splitting of the $E^2_g$ phonon mode into two peaks. This shows that the three modes are sensitive to NF thickness. For a careful line shape analysis, the $E_g$ modes were fitted with simplified Lorentzian (eqn. 4.1) and the $A_{1g}$ modes with simplified Fano (eqn. 4.2) [128].

$$L(\omega) = I_0 \frac{\omega\Gamma}{(\omega^2 - \omega_0^2)^2 + (\Gamma\omega)^2} \tag{4.1}$$

$$F(\omega) = I_0 \frac{(q + (\frac{\omega-\omega_0}{\Gamma}))^2}{1 + (\frac{\omega-\omega_0}{\Gamma})^2} \tag{4.2}$$

where $I_0$, q, $\omega$, $\omega_0$, and $\Gamma$ represent the intensity, Fano parameter, scattering frequency, phonon frequency, and FWHM, respectively. Fig. 4.2(c) shows the full width at half maximum (FWHM) as a function of NF thickness. We observe broadening of the $A^1_{1g}$ and $A^2_{1g}$ modes as the NF thickness is decreased. The $A^1_{1g}$ mode broadens from 5 $cm^{-1}$ to 12 $cm^{-1}$ and the $A^2_{1g}$ mode broadens from 9 $cm^{-1}$ to 13 $cm^{-1}$ as the thickness is decreased from about 13 nm down to 8nm. This peak broadening (decrease of the phonon lifetime) of the $Bi_2Se_3$ modes is attributed to a strong electron-phonon coupling [129]. The broadening of the $A^1_{1g}$ and $A^2_{1g}$ modes is accompanied by a strong decrease in the Fano parameter, q (Fig. 4.2(d)). The Fano parameter is the ratio between imaginary and real parts of the electronic susceptibility. This implies the interference between discrete phonon states and low-energy electronic degrees of freedom, [130] and it determines the asymmetry of the profile and hence electron-phonon coupling strength [129]. The smaller the q, the stronger the effective interference between electrons and phonons due to an increased contribution of the imaginary part of the electronic susceptibility. We reveal that q decreases with thickness of the NF, which indicates that the electron-photon interaction is stronger for thin NFs (Fig. 4.2(d)). Furthermore, the plot of the frequency as a function of the NF thickness is shown in Fig. 4.2(d). We found softening of the $A^1_{1g}$ mode by 3 $cm^{-1}$ and hardening of the $A^2_{1g}$ mode by 2.6 $cm^{-1}$. The phonon frequency is renormalized by the real part of an electronic susceptibility [93] [120] [110], therefore, softening of the $A^1_{1g}$ mode can be explained as coupling to a positive real part and the hardening of the $A^2_{1g}$ mode as coupling to a negative real part of the electric susceptibility [110]. Considering the signs of q for $A^1_{1g}$ and $A^2_{1g}$ modes, it is clear that the coupling of these modes to the electronic susceptibility occur at the frequency range between 60 $cm^{-1}$ - 130 $cm^{-1}$ [110]. We observe the splitting of the $E^2_g$ mode as a function of NF thickness as shown in Fig. 4.2(b). The $E^2_g$ mode splits into two on the low energy side of the bulk $E^2_g$ mode and the emerging new mode is related to a surface vibrational mode [110]. Perturbing the surface crystalline symmetry results in reduction of the bulk point group symmetry $D^d_3$ to the surface point group $C^v_3$ [131] [132]. This surface point group contains irreducible representations that include infrared (IR) active bulk phonons that transform to Raman active upon the breaking of inversion symmetry at the surface [110]. The mode around 124 $cm^{-1}$ can be assigned to the in-plane bulk IR mode of $E^2_u$ symmetry [57] and this assignment is supported by the polarization dependence study (for details, see section 4.3 on Appendix B). This mode has been observed in both thin and bulk $Bi_2Se_3$ at temperatures of 80 K and 13 K respectively [133] [132] [127].

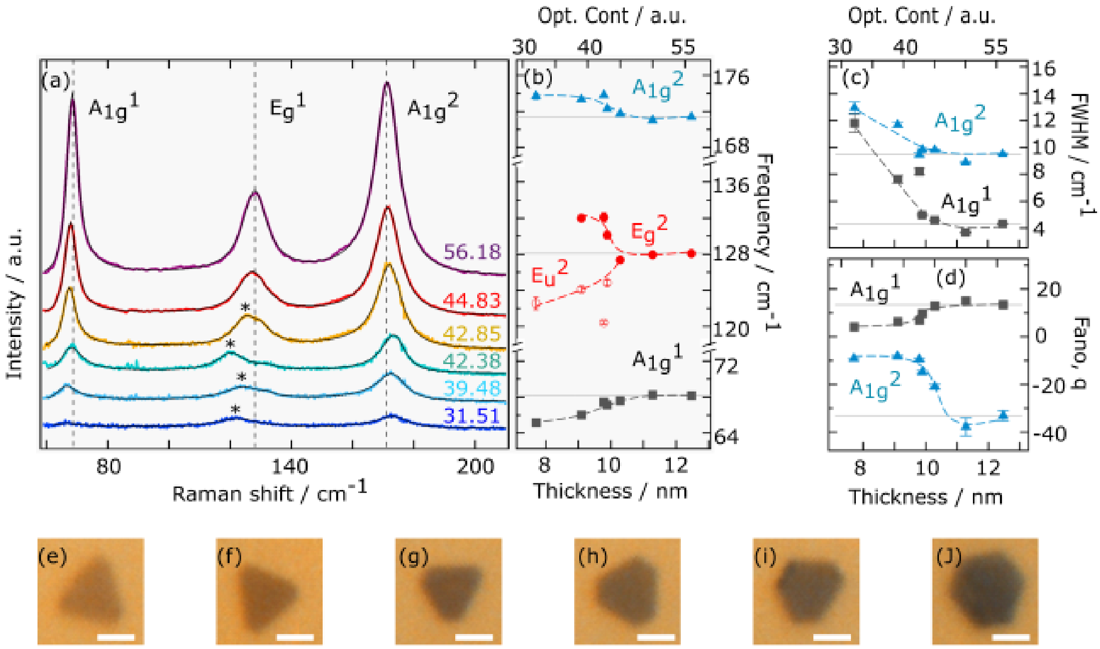

Figure 4.2: Thickness dependent phonon renormalization in $Bi_2Se_3$ on Au substrate. (a) Raman spectra of NFs with thicknesses from 7.7 nm - 12.5 nm corresponding to optical contrast (OC) of 31.51 - 56.18. The vertical dashed lines represent the $A^1_{1g}$,$E^2_g$ and $A^2_{1g}$ modes and correspond to the modes of bulk $Bi_2Se_3$. The developing IR mode is marked by asterisks. The OC are given next to the spectra. (b) Frequency as a function of NF thickness. Frequency is renormalized with decreasing NF thickness. (c) Broadening of FWHM with decreasing NF thickness. (d) Fano parameter as a function of NF thickness. Grey horizontal lines in (b - d) represent reference value obtained from the thickest NF. Dashed lines are guide to the eye. (e - j) Microscope images of the studied NFs in (a) and corresponding to OC of 31.51 - 56.18 respectively. (Reprinted with permission from [110]).

### 4.1.3 Resonance Raman study of $Bi_2Se_3$ nanoflakes

In order to determine in- and off-resonance behaviour of the phonons in $Bi_2Se_3$ as well as the injected carriers from the gold substrate, we conducted resonance Raman study on silicon (Si) and Au substrates. We used excitation wavelengths of 532 nm, 560 nm, 594 nm, 633 nm, and 705 nm. Fig. 4.3(a) shows the Raman spectra of single $Bi_2Se_3$ NFs on Si and Au substrates at different excitation wavelengths. The dotted lines represent measurements on Si substrate while the solid lines represent measurement on Au substrate. We can assign the two distinct phonon modes to $E_g^2$ and $A_{1g}^2$ symmetry as previously. All data were corrected for the spectral response of the instrument, scattering volume and the dielectric properties of $Bi_2Se_3$ (for details, see section 3.2 on Appendix B) [113] and fitted by Lorentzian. The plot of phonon susceptibility as a function of excitation wavelength is shown in Fig. 4.3(b). Tuning the excitation wavelength into resonance of the NFs, we reveal the strongest phonon susceptibility at 633 nm corresponding to 1.96 eV. Recall that 633 nm corresponds to interband transitions in $Bi_2Se_3$ and has been reported previously [58] [124] [134] [135]. For the NFs on Si substrate, when tuning the excitation wavelength into resonance, we obtain signal enhancement by a factor of 10. The bulk reference shown in Fig. 4.3(b) has weak signal enhancement in comparison with the NFs [129]. Measuring equivalent NFs on Au substrate, we show signal enhancement by a factor of 50 when tuning excitation wavelength into resonance [110]. This is because the injected carriers from Au substrate into the NFs increase the number of available electrons for resonant interband transition and hence increase the enhanced Raman response function. The susceptibility enhancement which is the ratio of the peak phonon intensity for NF on Au substrate to the comparable NF on Si substrate measured at the same excitation wavelength (i.e. $E = X^{Au}/X^{Si}$) is shown in Fig. 4.3(c). The susceptibility enhancement increases with increasing excitation wavelength. Note that the strongest susceptibility enhancement, which is approximately 20-fold is found at slightly above the resonance wavelength. The intensity ratio $E_g^2/A_{1g}^2$ as a function of the wavelength is shown in Fig. 4.3(d). Our result shows that $A_{1g}^2$ mode is more sensitive to the resonant wavelength than the $E_g^2$ for NFs on Si and Au substrates. This indicates that resonance is intrinsic to the $Bi_2Se_3$ [110].

### 4.1.4 Carrier injection and electron-phonon interaction in $Bi_2Se_3$ nanoflakes

The strong renormalization of the phonons in our system (NFs/Au contact) is a result of enhanced electron-phonon interactions that is associated with Au substrate injecting electrons into $Bi_2Se_3$ NFs. Spataru *et al.*, predicted the injection of carriers from gold into $Bi_2Se_3$, which leads to substantial band bending and accumulation of free electrons on the interface side of the contacted NF [95]. Substantial phonon renormalization, i.e. softening of $A_{1g}^1$ mode of up to 3 $cm^{-1}$ and hardening of $A_{1g}^2$ mode of up to 2.6 $cm^{-1}$, distinguishes our observed carrier injection from the so called phonon confinement model of out-of-plane vibrations observed by Zhang *et al.* [129]. Zhang *et al.* studied $Bi_2Se_3$ NFs on Si substrate and observed softening of $A_{1g}^1$ mode by 1.2 $cm^{-1}$ when thickness of NF is decreased from 13 nm to 8 nm [129]. Further, our observed changes in Fano parameter and FWHM strongly support a low-energy electronic susceptibility. Fig. 4.4(e) shows a model of carrier injection and charge accumulation at the interface side of the contacted NFs. The accumulated charges yield an electric field across the NF due to the insulating bulk and hence the electric field in combination with the induced band bending effect enhances the Raman scattering cross section [110]. Fig. 4.4(c) shows the phonon intensity as a function of NF thickness. The phonon intensity is corrected for the scattering volume. We find a thickness dependence of all three phonon modes, with the intensities increasing with thickness. Our result reveals strongest phonon renormalization at thicknesses below 10 nm which indicates strong electron-phonon coupling. Moreover,

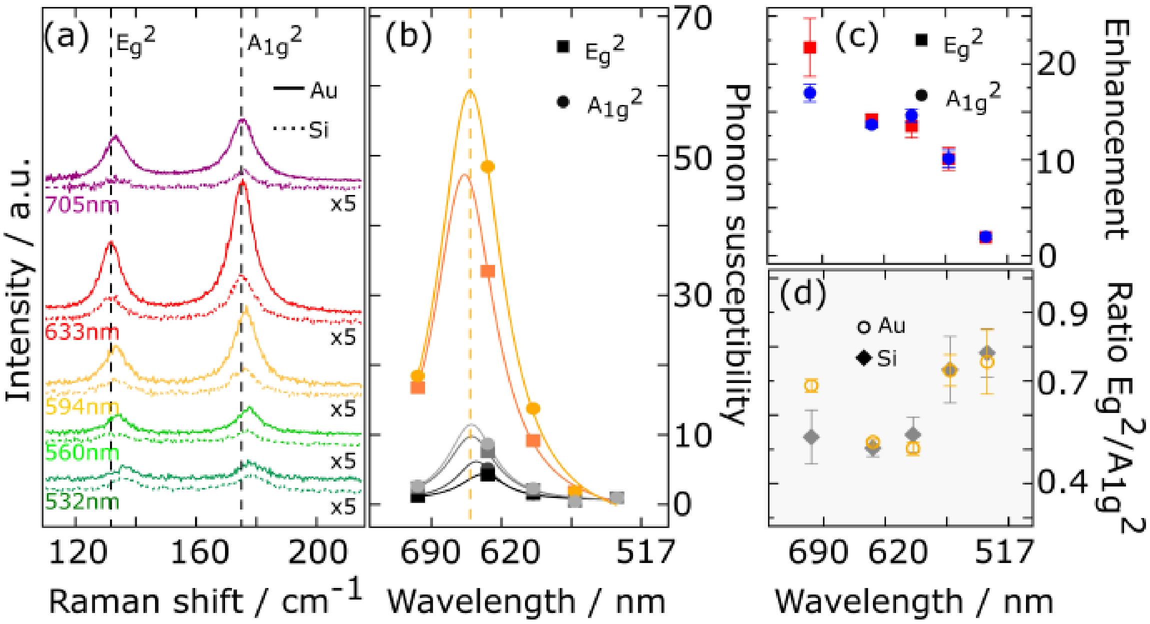

Figure 4.3: Resonance Raman studies of $Bi_2Se_3$ NFs/bulk on Au and Si substrates. (a) The spectra acquired at different excitation wavelengths (532 - 705 nm). Dashed vertical lines are the phonon modes ($E_g^2$ and $A_{1g}^2$). Si and Au substrates are represented by the dotted and solid lines. Spectra from measurement on Si substrate is scaled by a factor of 5. (b) Phonon susceptibilities as a function of excitation wavelength. The susceptibility is normalized to the value at 532 nm. Resonance profiles of the $E_g^2$ (squares) and $A_{1g}^2$ (circles). The solid lines are the Lorentzian fit to the data. Yellow, grey and black symbols represent the spectra from NF on Au, Si substrates and the spectra from bulk $Bi_2Se_3$ respectively. The vertical dashed line is the resonance frequency. (c) Enhancement between the NF Raman signal on gold and silicon substrates at the corresponding wavelength of the $E_g^2$ (squares) and $A_{1g}^2$ (circles) phonons. (d) Susceptibility ratios of the $E_g^2$ and $A_{1g}^2$ for the NFs on Au (open circles) and Si (grey diamonds) substrates. (Reprinted with permission from [110]).

as the thickness increases beyond 10 nm, we find a step increase of the phonon intensity. In Fig. 4.4(d) we show the band bending effects predicted by Spataru *et al.* for $Bi_2Se_3$ on Au substrate. The injected carriers populate the bulk conduction bands and lead to a downward band bending by 1 eV changing the electronic band structure to a depth of 5 nm from the interface [95]. Further, it is evident that reducing the thickness of the NF, will also reduce the contribution from the insulating bulk region primarily because of the band bending mediated by the carrier injection at the interface. For a thin NF, the band bending effects tune the bulk conduction band out of resonance condition, thereby suppressing the interband transition [110]. This leads to weak Raman susceptibility in thin NFs (with thickness less than 10 nm). In order to explain the electron-phonon interactions, the phonon linewidth can be used to estimate the coupling strength of the electron-phonon coupling [93]. The renormalized width of the phonon is given by

$$gc_2 = \sqrt{|2\bar{\Gamma}\omega_0 - 2\Gamma_0\omega_0|} \tag{4.3}$$

where $\omega_0$ and $\Gamma_0$ are frequency and width of the phonon before renormalization. $\bar{\Gamma}$ is the renormalized width of the phonon. $c_2$ is proportional to the imaginary part of the electronic susceptibility $\pi_1$ and g is a variable that hints at the electron-phonon coupling. Recall that the imaginary part of the electronic susceptibility determines the electronic background which is necessary for Fano interference. If there is no change in the electronics background then $c_2$ is constant and g determines the electron-phonon coupling. Indeed our result shows that there is no change in the Bose corrected electronic background after subtraction of the phonons as shown in Fig. 4.4(b) and therefore we applied eqn. 4.3 to determine the dependence of g on electron-phonon coupling as a function of NF thickness. Fig. 4.4(a) reveals that electron-phonon coupling is enhanced at the same critical thickness at which the phonon frequency is drastically reduced, thus demonstrating the band bending effects [110].

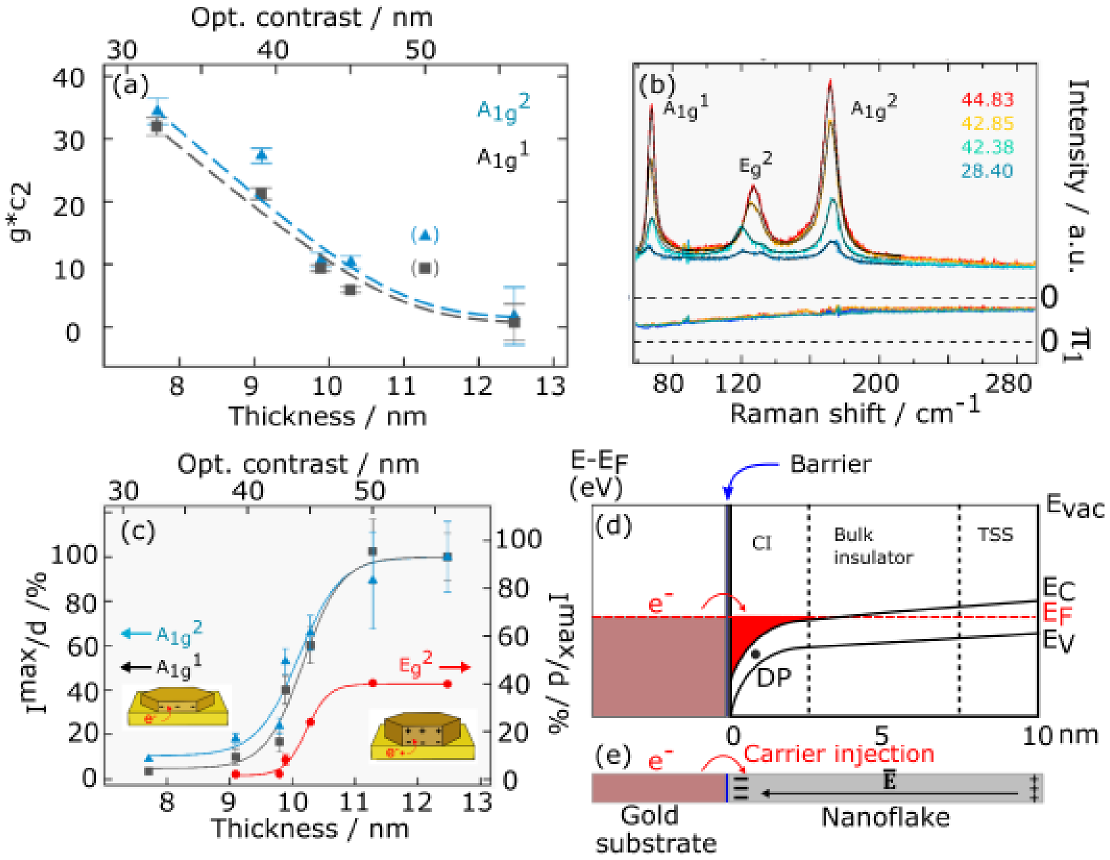

Figure 4.4: Phonon renormalizations and Raman intensity enhancement induced by carrier injection. (a) Electron-phonon coupling strength as a function of NF thickness. (b) Raman spectra of $Bi_2Se_3$ NFs with varying thickness (OCs) and their Bose corrected extracted background corresponding to the imaginary part of a low energy electronic susceptibility. (c) Raman intensity as a function of NF thickness. The intensities were corrected for the scattering volume and normalized to the value of the thickest NF. The insets represent the NF model. (d) The model of the band bending effects adapted from Spataru et al., thick NF has band bending effects localized at the contacted surface while thin NF has band bending effects across the entire NF. Three regions are observed, (i) the strongly bent contact surface, (ii) the bulk insulator region and (iii) the top surface in contact with the vacuum. The black dot represents the position of the Dirac point. Ec, EF, EV are the conduction band edge, the Fermi level and the valence band edge, respectively. (e) Schematic diagram of charge injection from gold substrate into the contacted $Bi_2Se_3$ surface and appearance of an electric field across a thick NF. (Reprinted with permission from [110]).

# Publication 1:
# Carrier injection observed by interface-enhanced Raman scattering from topological insulators on gold substrates

Sarah Scheitz, Tomke Eva Glier, Christian Nweze, Malte van Heek, Isa Moch, Robert Zierold, Robert Blick, Nils Huse, and Michael Ruebhausen.

ACS: Applied Materials & Interfaces - JULY 2022
https://doi.org/10.1021/acsami.2c04380

Reprinted with permission from ACS Appl. Mater. Interfaces 2022, 14, 28, 32625–32633.

ACS APPLIED MATERIALS & INTERFACES

www.acsami.org Research Article

# Carrier Injection Observed by Interface-Enhanced Raman Scattering from Topological Insulators on Gold Substrates

Sarah Scheitz,* Tomke Eva Glier, Christian Nweze, Malte van Heek, Isa Moch, Robert Zierold, Robert Blick, Nils Huse, and Michael Rübhausen*

Cite This: *ACS Appl. Mater. Interfaces* 2022, 14, 32625−32633 Read Online

ACCESS | Metrics & More | Article Recommendations | Supporting Information

**ABSTRACT:** The electron-phonon interaction at the interface between topological insulator (TI), namely, $Bi_2Se_3$ and $Bi_2Te_3$ two-dimensional (2D) nanoflakes, to a gold substrate as a function of TI flake thickness is studied by means of Raman scattering. We reveal the presence of interface-enhanced Raman scattering and a strong phonon renormalization induced by carriers injected from the gold substrate to the topological surface in contact. We derive the change of the electron-phonon coupling showing a nearly linear behavior as a function of layer thickness. The strongly nonlinear change of the Raman scattering cross section as a function of flake thickness can be associated with band bending effects at the metal-TI interface. Our results provide spectroscopic evidence for a strongly modified band structure in the first few quintuple layers of $Bi_2Se_3$ and $Bi_2Te_3$ in contact with gold.

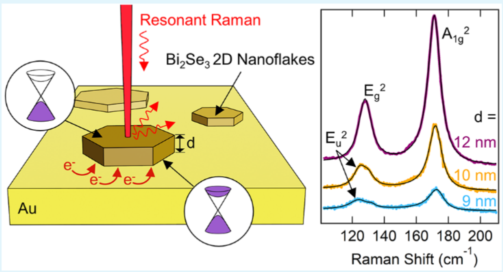

**KEYWORDS:** *topological insulator gold contact, $Bi_2Se_3$, $Bi_2Te_3$, Raman spectroscopy, carrier injection, band bending, electron-phonon coupling*

## 1. INTRODUCTION

Spin-polarized surface states hosting quasi-relativistic electrons are a key characteristic of topological insulator (TI) nanostructures.[1,2] Most importantly, novel, robust, and highly conductive electronic channels can form at interfaces between systems with different topological character. These surface states are topologically protected by time-reversal symmetry and are the result of a strong spin-orbit coupling (SOC) term in the Hamiltonian. Due to the spin-momentum locking of the topological surface states (TSS) leading to reduced back-scattering and high carrier mobilities, TIs have become promising candidates for spin-transfer torque memory devices,[3−6] high-performance photodetectors,[7] and fiber lasers.[8] At interfaces of systems with different topological character, one would expect that the TSS are robust.[1,9] Yet, the response of the TSS to a contact or substrate is critical for the development of electronic devices with consequences for their applications. Furthermore, the relevance of topological physics depends on the Fermi-level position at the interfaces due to possible charge transfer across the interface.[10] Even though detailed theoretical predictions on the metal-TI band structure exist,[11] these obscured interfaces are rarely studied. Especially the contact to gold is of high interest in TI-based devices.[7,12,13] Important representatives for three-dimensional TIs are $Bi_2Se_3$ and $Bi_2Te_3$ featuring a single Dirac Cone in the Brillouin zone center with different bulk band gaps.[14] The narrow-gap semiconductor $Bi_2Se_3$ is one of the most intensively studied three-dimensional (3D) TIs due to its comparably large bulk band gap of 0.3 eV with the Dirac point positioned within the bulk band gap.[15,16] In contrast, the band gap of 0.16 eV in $Bi_2Te_3$ is substantially smaller and the Dirac point is shifted close to the valence band.[17,18] Despite many studies on the electronic properties of $Bi_2Se_3$ and $Bi_2Te_3$ by means of transport measurements,[19−22] only a very limited number of studies exist that explicitly focus on the local properties of the Au-TI interface. The interface chemistry between gold and $Bi_2Se_3$ has been studied both theoretically[11] and experimentally,[23,24] revealing chemical inertness and no hybridization with the TSS. However, ab initio calculations have predicted the injection of carriers into the TI leading to substantial band bending at the Au-TI interface of about 1 eV.[11] Often the metal-to-insulator contact is not directly accessible for experiments that study the topological state from the side of the vacuum. However, Raman scattering on thin flakes has already been proven to be a valuable tool to reveal quasi-

**Received:** March 10, 2022
**Accepted:** June 30, 2022
**Published:** July 11, 2022

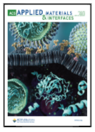

ACS Publications

https://doi.org/10.1021/acsami.2c04380

relativistic electrons and their interactions with phonons of the TSS.[25−27] Note that Raman scattering is a contact-free, local, and direct measurement of the interface properties. Furthermore, Raman spectroscopy is a volume scattering technique and allows us to study TSS that are not directly accessible or covered, which is the main challenge for highly surface-sensitive techniques like angle-resolved photoemission spectroscopy (ARPES)[21] and scanning tunneling spectroscopy (STS).[28] In particular, Raman spectroscopy allows for understanding the interplay between electronic degrees of freedom and the lattice.

In this paper, we study the interface between a gold substrate and topological insulator nanoflakes (NFs) of $Bi_2Se_3$ and $Bi_2Te_3$ of varying thickness by employing spatially resolved high-resolution Raman scattering. Tuning the thickness of the NFs allows for controlling (a) the bulk contribution, which is used to identify contributions originating from the surface, and (b) the effective charge transfer from the substrate. We investigate the changes in the electronic susceptibility of the NFs and its influence on the phonon line shapes as a function of the NF's thickness and optical contrast, thereby identifying carrier injection at the interface. We discuss the implications of band bending on the observed Raman spectra and determine the changes in the electron-phonon interaction as a function of NF thickness.

## 2. EXPERIMENTAL SECTION

$Bi_2Se_3$ and $Bi_2Te_3$ NFs were synthesized using a wet-chemical polyol method, which is described in detail in ref26 and the Supporting Information (SI-Section 1). The single crystallinity, growth direction, and correct stoichiometry were thoroughly verified using transmission electron microscopy (TEM), selected area electron diffraction (SAED), and energy-dispersive X-ray spectroscopy (EDX), respectively.[26] For the investigation of individual NFs, the dispersed flakes were drop-cast onto silicon and gold substrates and their thicknesses were determined using atomic force microscopy (AFM) (see SI-Section 4). Raman measurements on individual NFs were acquired employing a custom-made micro-Raman setup[29,30] creating diffraction-limited laser spot diameters varying between 211 to 398 nm depending on wavelength (see SI-Section 2). All spectra were collected in an effective backscattering configuration with the polarization configuration $z(xx)\bar{z}$ denoted in Porto notation.[31] The micro-Raman setup enables the use of various excitation wavelengths in the visible range of 400−700 nm. Details on the used laser sources and data treatment are given in SI-Sections 2 and 3. Due to the low thermal conductivity of both $Bi_2Se_3$ and $Bi_2Te_3$,[32] extensive prestudies on laser powers and integration times were conducted to determine appropriate measurement configurations that exclude laser heating effects on the Raman spectra. With the employed conditions, we ensure damage-free measurements (see SI-Section 2.2). We found that for a 633 nm excitation wavelength with a spot diameter of 211 nm, a power of 40 $\mu$W (leading to a power density of 114 kW/cm$^2$ on the sample) results in low noise Raman signals without damaging the NFs. The spectra were acquired while scanning over the NF surfaces by about 2−4 $\mu$m$^2$. All data have been normalized to power and integration time and are corrected for the spectral response of the instrument.[29]

## 3. RESULTS AND DISCUSSION

**3.1. Resonance Raman Study on $Bi_2Se_3$.** We first investigate $Bi_2Se_3$ NFs on gold and silicon substrates as a function of wavelength to determine the Raman resonance profile. By measuring under resonant conditions, the collected Raman signal of individual NFs is increased by an order of magnitude, which enables higher accuracy in the data analysis of NFs differing by only a few nanometers in thickness. Figure 1a shows the collected Raman spectra of single $Bi_2Se_3$ NFs on silicon and gold for excitation wavelengths of 532, 560, 594, 633, and 705 nm. For all NFs, regardless of the substrate, the characteristic bulk phonon modes of $E_g^2$ and $A_{1g}^2$ symmetry were identified.[33,34] In Figure 1b, we show the peak susceptibilities extracted from Lorentzian fits for both phonons for all incident photon energies. To obtain the resonance behavior, we have corrected the peak intensities for the dielectric properties of $Bi_2Se_3$ as well as the scattering volume

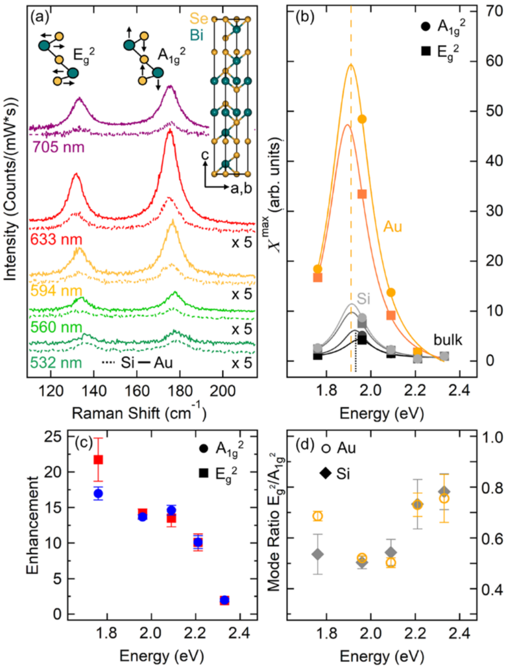

**Figure 1.** Resonance studies on $Bi_2Se_3$. NF Raman signal on gold compared to silicon substrates and a bulk single crystal. (a) Comparison of Raman spectra from single NFs on silicon (dotted) and sputtered gold substrate (solid) for different excitation wavelengths as indicated. The thicknesses of the NFs are given in Table S4 in the SI. All spectra are normalized to laser power as well as integration time and are displayed with an offset for clarity. The measurements on silicon substrates are all multiplied by a factor of 5. The insets show the crystal structure of a conventional $Bi_2Se_3$ unit cell and the atomic displacement vectors for the two observed phonon modes. (b) Resonance profiles of the $E_g^2$ (squares) and $A_{1g}^2$ (circles) phonon susceptibilities as a function of energy corresponding to the excitation wavelength shown in (a). Gray and yellow markers correspond to the spectra of the NFs on silicon and gold substrate, respectively. Lorentzian fits are given as solid lines for the NFs on Au and Si. Black markers show the resonance behavior of a $Bi_2Se_3$ bulk sample. Values are normalized to 532 nm (2.33 eV). The dashed and dotted lines indicate the resonance frequency of the NFs on Au and bulk sample, respectively. (c) Enhancement between the NF Raman signal on gold and silicon at the corresponding energy of the $E_g^2$ (squares) and $A_{1g}^2$ (circles) phonons. (d) Susceptibility ratios of the $E_g^2$ to $A_{1g}^2$ modes for the NFs on Si (gray diamonds) and Au (yellow open circles).

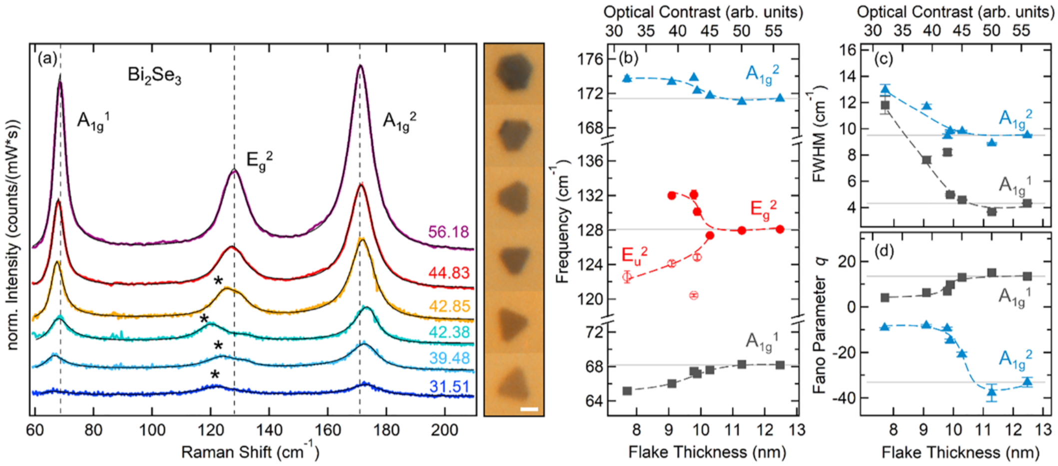

**Figure 2.** Phonon renormalization in $Bi_2Se_3$ NFs with varying thickness on the same gold substrate. (a) Raman spectra of six individual NFs with decreasing thicknesses from 12.5 nm (OC = 56.18) to 7.7 nm (OC = 31.51) (see Table S5 in the SI). Corresponding microscope images of the measured NFs are shown to the right of the spectra. The scale bar is 2 μm. In the diagram, the three main phonon modes $A_{1g}^1$, $E_g^2$, and $A_{1g}^2$ of $Bi_2Se_3$ are labeled as well as a growing IR mode marked by asterisks. Vertical dashed lines are given as a guide to the eye and correspond to the mode frequencies for the thickest NF. The optical contrasts of the NFs are given next to their corresponding spectra. Renormalization of (b) mode frequencies, (c) FWHM, and (d) extracted Fano parameters with NF thickness. Dashed lines are a guide to the eye. For reference, phonon frequencies, FWHM, and Fano parameters measured from the thickest NF are given as solid gray lines in (b−d).

of each measured NF. Details on the correction factors used to obtain the Raman susceptibilities are given in SI-Section 3.2. Already on the silicon substrate, we obtain a signal increase by a factor of 10 when tuning the excitation wavelength into resonance. For a reference bulk sample, a similar but weaker resonance is observed (see Figure 1b). This resonance of $Bi_2Se_3$ has been previously reported[35,36] and is generally assigned to a resonant interband transition.[37,38] However, for the measurements on gold substrate, a substantially larger signal is obtained for all wavelengths in comparison with the silicon substrate. Furthermore, we observe an enhanced resonance profile on gold with a signal increase by a factor of 50 when tuning the excitation energy into the red. Note that the Raman susceptibility of the bulk sample is significantly smaller than the NF susceptibilities, an effect that has been observed before for $Bi_2Se_3$ and $Bi_2Te_3$ thin-film samples.[27,39] Due to the penetration depth of around 9 nm in the visible spectra range (see SI-Figure S2c), the bulk and NF samples actually yield similar scattering volumes. Yet, the thin NFs show a strongly enhanced Raman response, which we discuss in the final part of this study. Figure 1b clearly indicates a sharp resonance of the phonons in the $Bi_2Se_3$ NFs on the gold substrate at 633 nm corresponding to 1.96 eV. The resonance profiles for bulk samples and NFs on silicon and gold were fitted by a Lorentzian profile. They exhibit similar resonance positions at 1.94 ± 0.06 eV (bulk) and 1.91 ± 0.03 eV (NFs), both of which are close to the 1.96 eV (633 nm) excitation line. By comparing the peak susceptibilities of the silicon and gold measurements, we determine an increasing enhancement for both phonons on the gold substrate, $E = X^{Au}/X^{Si}$, which is shown in Figure 1c. The enhancement on the gold substrate is increasing when tuning the incident photon energy to smaller energies. The strongest relative signal enhancement by a factor of ~20 is found for 1.76 eV, which is at slightly lower energies compared to the resonance position at 1.90 eV. We further observe a change in the relative susceptibilities of the $E_g^2$ to the $A_{1g}^2$ modes when approaching the resonance as shown in Figure 1d. The $A_{1g}^2$ mode shows a stronger enhancement around the resonant excitation energy, which results in a decreasing susceptibility ratio of $E_g^2$ to $A_{1g}^2$. This trend is observed for NFs on both, silicon and gold substrates. Our observations of identical resonance profiles and mode ratios for NFs on silicon and gold show that the resonance is intrinsic to the $Bi_2Se_3$ NFs. The enhanced $Bi_2Se_3$ resonance on Au provides first indications that the conditions for a resonant interband transition are changed. We show in the final part of this work how the interband transitions are affected by band bending effects as a possible consequence of carrier injection from the gold substrate. Carriers injected into the bottom NF side in contact with gold increase the number of available electrons for resonant interband transitions and lead to an enhanced Raman response. This view is also supported by changes in the resonance positions in the NF samples compared to the bulk, where the occupation of bands responsible for the resonant transitions leads to a slight change in resonance energy. All further measurements have been conducted under resonant conditions with an excitation wavelength of 633 nm.

**3.2. Thickness Dependence of $Bi_2Se_3$ and $Bi_2Te_3$ NFs on Au.** In Figure 2, we study the thickness dependence of the Raman signal from $Bi_2Se_3$ NFs on the same gold substrate. Figure 2a shows selected Raman spectra of $Bi_2Se_3$ NFs with decreasing thicknesses from 12.5 to 7.7 nm. The change in NF thickness of only a few nanometers is already apparent in optical microscope images, where the optical contrast (OC) of the NFs changes drastically with thickness. The OC is defined by the ratio of the averaged greyscale values on the NF compared to the values on the gold substrate (see SI-Section 4.1). NFs with thicknesses above 12 nm appear dark on the gold substrate with OCs above 50, whereas the OC decreases

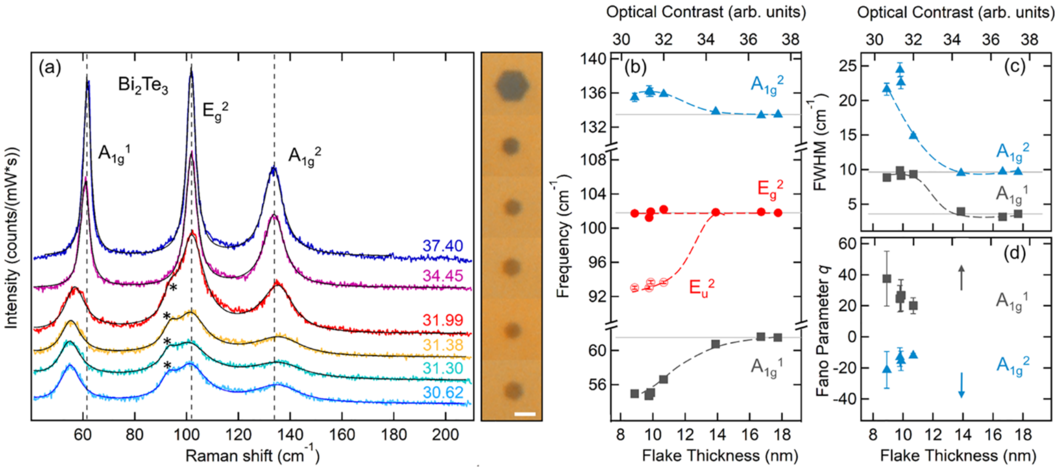

**Figure 3.** Phonon renormalization in $Bi_2Te_3$ NFs with varying thickness on the same gold substrate. (a) Raman spectra of six individual NFs with decreasing thicknesses from 17.7 nm (OC = 37.40) to 8.9 nm (OD = 30.62) (see Table S5 in the SI). Corresponding microscope images of the measured NFs are shown to the right of the spectra. The scale bar is 2 μm. In the diagram, the three main phonon modes $A_{1g}^1$, $E_g^2$, and $A_{1g}^2$ of $Bi_2Te_3$ are labeled as well as a growing IR mode marked by asterisks. Dashed lines are given as a guide to the eye and correspond to the mode frequencies for the thickest NF. Renormalization of (b) mode frequencies, (c) FWHM, and (d) Fano parameter with NF thickness. Dashed lines are a guide to the eye. For reference, phonon frequencies and FWHM measured from the thickest NF are given as solid gray lines in (b,c). In (d), the Fano parameters for A modes in thick NFs ($d > 14$ nm), which obtained very high values due to their symmetrical line shape, are indicated by arrows.

for thinner NFs of around 8 nm down to a value of 32. Indeed, in this range of thicknesses, the OC is directly proportional to the NF thickness as shown in the SI-Section 4.1, thus allowing for a direct experimental control of the NF thickness in the Raman measurement. For $Bi_2Se_3$ NFs with high OCs above 50 (corresponding to $d > 12$ nm), Raman spectra show the three well-known bulk phonons of $A_{1g}^1$ (63.18 ± 0.02 cm$^{-1}$), $E_g^2$ (123.08.18 ± 0.04 cm$^{-1}$), and $A_{1g}^2$ (166.41 ± 0.02 cm$^{-1}$) symmetries,[33] with the frequencies obtained for the thickest NF given in parentheses. Intriguingly, for thinner NFs close to a critical OC of 45 ($d < 10$ nm), the three bulk phonons experience a strong renormalization. In particular, with decreasing OC, the $A_{1g}$ modes are shifted in frequency and the E-mode splits into a double peak feature. Furthermore, for the lowest OC, we observe a substantial decrease in Raman intensity that we cannot exclusively attribute to the decreased thickness of the NF.

By fitting the $E_g$ modes with Lorentzian and the $A_{1g}$ modes with Fano profiles, we show in Figure 2b the extracted mode frequencies that reveal a softening of the low-energy $A_{1g}^1$ mode by 3 cm$^{-1}$ and a hardening of the $A_{1g}^2$ mode by 2.6 cm$^{-1}$ in the investigated range of NF thicknesses. This frequency renormalization is accompanied by an increase of the full width at half-maximum (FWHM) by 8 and 4 cm$^{-1}$, respectively, as shown in Figure 2c. Moreover, for thin NFs on gold, the bulk $E_g^2$ phonon splits into two modes. The split low-energy mode separates from the $E_g^2$ bulk mode by about 10 cm$^{-1}$, as shown in Figure 2b. The emerging phonon on the low-energy side of the bulk $E_g^2$ phonon in NFs with low thicknesses is related to a surface vibrational mode. At the surface, the crystalline symmetry is perturbed, which results in a reduction of the bulk point group symmetry $D_3^d$ to the surface point group $C_3^v$.[40,41] The $C_3^v$ point group contains irreducible representations that include infrared (IR) active bulk phonons, which become Raman-active upon the breaking of inversion symmetry at the surface. For $Bi_2Se_3$, the mode around 124 cm$^{-1}$ can be assigned to the in-plane bulk IR mode of $E_u^2$ symmetry.[33] This surface mode has been observed for bulk samples at very low temperatures <13 K[25,41] and thin-film samples below 9 nm thickness at 80 K.[42] We have confirmed the E-symmetry of the emerging surface vibrational mode by conducting Raman measurements with parallel (xx) and crossed (xy) polarization. A thorough analysis of the symmetry is given in the SI-Section 4.3. The significant thickness dependence of the $A_{1g}$ modes becomes further apparent when analyzing the line shape of the phonons. For the $A_{1g}$ modes, we find an asymmetric Fano profile yielding information on the electron-phonon coupling. This line shape encodes a coupling of discrete phonon states to electronic degrees of freedom in the system.[43] The Fano parameter $q$ determines the asymmetry of the profile, where the negative or positive sign of $q$ specifies whether the electronic susceptibility constructively interferes with the phonon on its low- or high-energy side, respectively. In agreement with the observed renormalizations of mode frequencies and FWHM, we find a strong decrease in the Fano parameter for NFs below an OC of 45 and corresponding thickness below 10 nm, as shown in Figure 2d. This observation shows the presence of a low-energy electronic susceptibility interacting with the phonons. Since the phonon frequency is renormalized by the real part of an electronic susceptibility,[26,44] the softening of the $A_{1g}^1$ mode can be explained by coupling to a positive real part and the hardening of the $A_{1g}^2$ mode by coupling to a negative real part of the electric susceptibility. Furthermore, taking the opposite signs of the Fano parameter $q$ for the two $A_{1g}$ modes into account, this spectral behavior indicates the coupling of these modes to an electronic susceptibility in a frequency range between 60 and 130 cm$^{-1}$.

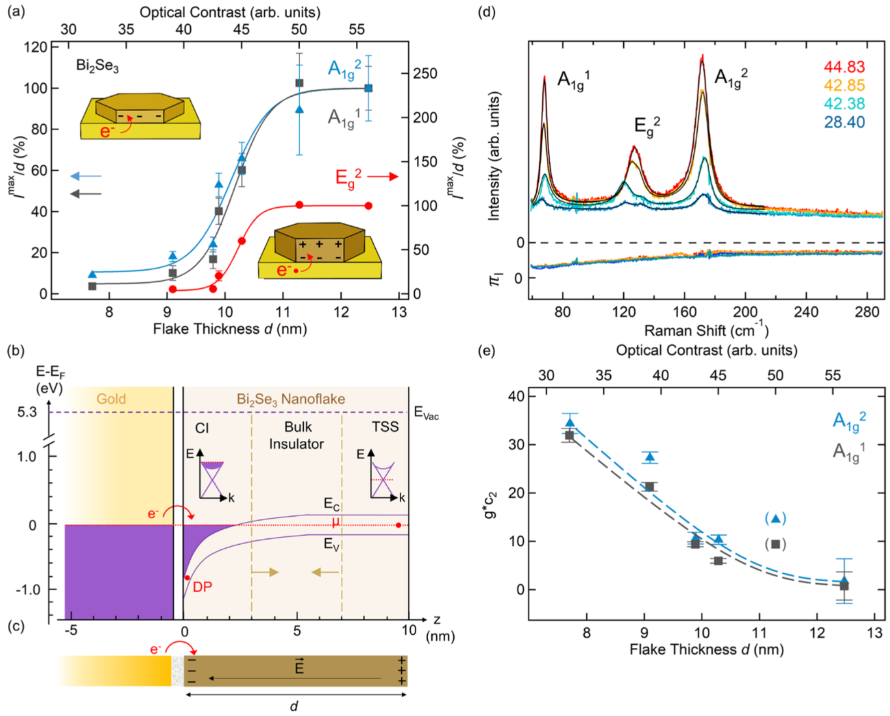

**Figure 4.** Carrier injection-induced Raman enhancement and phonon renormalizations. (a) Scattering volume-corrected intensities of the three measured phonon modes in $Bi_2Se_3$ as a function of NF thickness. Intensities were normalized to the value of the thickest NF. The right axis corresponds to the $E_g^2$ intensities. The insets show a model of a thin NF with band bending effects across the entire NF (left) and a thick NF with band bending localized to the bottom surface (right). (b) Model of the band structure for a contacted $Bi_2Se_3$ NF on gold with values for the band bending potential according to ref11. Bulk bands experience downward bending due to carrier injection (CI) into the contacted surface. Three different regions in the NF are indicated by vertical dashed lines corresponding to the strongly bent contact surface, the bulk insulator region, and the top surface with the native topological surface state (TSS) in contact with air. The relative position of the Dirac point (DP) for the bottom and top TSS are marked as red dots. Top insets illustrate the relative Fermi position in the top and bottom Dirac Cone. (c) Illustration of charge injection from gold into the contacted $Bi_2Se_3$ surface and development of an electric field across a thick NF. (d) Raman spectra of $Bi_2Se_3$ NFs with varying OCs and their Bose-corrected extracted background corresponding to the imaginary part of a low-energy electronic susceptibility. (e) Electron-phonon coupling strength determined from line width renormalization with dashed lines as a guide to the eye.

In Figure 3, we present data from the equivalent experiment on the 3D TI $Bi_2Te_3$, which exhibits a smaller bulk band gap of 0.16 eV. The OC of $Bi_2Te_3$ NFs is also proportional to the NF thickness, as shown in SI-Section 4.1. The thickness-dependent Raman measurements on gold for $Bi_2Te_3$ NFs from around 18 to 9 nm are presented in Figure 3a. For all NFs, the bulk Raman modes of $A_{1g}^1$ (61.53 ± 0.03 cm$^{-1}$), $E_g^2$ (101.80 ± 0.02 cm$^{-1}$), and $A_{1g}^2$ (133.49 ± 0.11 cm$^{-1}$) symmetries are detected with frequencies of the thickest measured NF given in parentheses. In comparison with $Bi_2Se_3$, the Raman modes of $Bi_2Te_3$ are shifted to lower frequencies due to the higher mass of Te atoms compared to Se atoms.[33] When evaluating the Raman spectra as a function of NF thickness, the phonons show a behavior similar to $Bi_2Se_3$ with respect to phonon renormalizations as the NFs get thinner. For NFs with OCs below 34, we find strong deviations in frequency, FWHM, and Fano parameter from the Raman spectra of thicker NFs. Namely, a stronger softening by 6.9 cm$^{-1}$ compared to $Bi_2Se_3$ and a comparable hardening by 3 cm$^{-1}$ of the respective $A_{1g}^1$ and $A_{1g}^2$ phonon modes as shown in Figure 3b is observed. We find increasing FWHMs by about 6 and 13 cm$^{-1}$, respectively, which is accompanied by a decreased Fano parameter for thin NFs (Figure 3c,d), indicating incipient electron-phonon interactions also in these thin $Bi_2Te_3$ NFs. In particular, a similar mode splitting of the $E_g^2$ mode is clearly apparent. In $Bi_2Te_3$, the split emerging mode at 93.5 cm$^{-1}$ can again be assigned to the bulk IR-active $E_u^2$ mode[33] (see SI-Section 4.3). This surface mode has been experimentally observed at room temperature in thin-film samples and nanoplates with thicknesses below 7 nm[45−47] as well as in films of drop-cast NFs below 100 K.[26]

### 3.3. Interface-Enhanced Raman Scattering by Carrier Injection.

Our observation of strong renormalizations of the phonons in metal-contacted TIs is a result of an enhanced electron-phonon interaction that can be associated with carrier injection and corresponding band bending at the contacted side of the NF as we will detail below. In comparison, Zhang et al. have measured $Bi_2Se_3$ NFs of differing thicknesses placed on silicon substrates and observed a much weaker frequency shift in the $A_{1g}^1$ phonon of only 1.2 cm$^{-1}$ for decreasing NF thicknesses between 13 and 8 nm.[34] This was assigned to a phenomenological phonon confinement model of the out-of-plane vibrations leading to a relaxed bulk Raman selection rule ($q = 0$). However, our measurements on NFs placed on gold reveal a substantially stronger renormalization for the $A_{1g}^1$ mode of up to 3 $cm^{-1}$ for $Bi_2Se_3$ and even 5.8 $cm^{-1}$ for $Bi_2Te_3$ NFs in the same thickness range. Hence, the strong redshifts of the $A_{1g}^1$ modes and especially the blueshifts of the $A_{1g}^2$ modes cannot only be attributed to a confined phonon state. Furthermore, the observation of concomitant changes in the line width and Fano parameter hint very strongly toward the presence of a low-energy electronic susceptibility. Ab initio calculations have predicted the injection of carriers from gold into $Bi_2Se_3$, leading to a substantial band bending[11] and accumulation of free carriers on the interface side of the contacted NF. The charge accumulation yields an electric field across the NF due to the insulating bulk as illustrated in Figure 4c. This leads to the conclusion that the build-up field in combination with the induced band bending effect enhances the Raman scattering cross section in contrast to the weaker signal obtained from NFs on Si (see Figure 1b). The strong interface enhancement induced by carrier injection is further supported by the observation of the usually weak bulk IR modes in both $Bi_2Se_3$ and $Bi_2Te_3$. Additionally, the presence of free carriers injected in the bottom side of the NFs explains both the thickness-dependent phonon renormalizations and intensities. In Figure 4a, we show the dependence of the $Bi_2Se_3$ phonon mode intensities corrected for the NF scattering volume as a function of NF thickness. We find a stronger thickness dependence of the Raman intensities than anticipated by the linear change in scattering volume. For thicker NFs, an enhanced Raman signal is observed that quickly collapses below a critical thickness of about 10 nm. In this range of thinner NFs, we also observe the strongest phonon renormalization indicating a strongly enhanced electron-phonon interaction. In Figure 4b, we schematically display the band bending effects predicted by Spataru et al.[11] for $Bi_2Se_3$ on gold. The injected carriers at the contacted NF surface lead to a downward bending by 1 eV changing the electronic band structure to a depth of 5 nm from the interface of the Au film and the NF[11] and populating the bulk conduction bands. With decreasing NF thickness, this carrier injection reduces the insulating bulk region until the band bending reaches across the entire NF as illustrated in Figure 4b. For thick NFs ($d > 11$ nm), the electronic band structure meets the conditions of resonant interband transitions leading to strong Raman susceptibilities. The scattering volume-corrected intensities for thicker NFs are, therefore, constant. However, with decreasing NF thicknesses below $d < 10$ nm, the band bending quickly leads to tuning out of the resonance conditions in accordance with the drastically reduced Raman signal by more than 80% when reducing the NF thickness from 11 to 9 nm. The scattering volume-corrected intensities for the three phonon modes are readily fit by a sigmoidal function revealing a critical thickness of 10.2 ± 0.2 nm, as shown in Figure 4a. For the sake of clarity, we have depicted a native $Bi_2Se_3$ in Figure 4b with the Fermi level positioned in the center of the bulk band gap at the uncontacted side. However, it is known that the surface of $Bi_2Se_3$ samples is typically *n*-doped after sample preparation due to electron doping by local Se vacancies.[48] The accumulated charges induce a downward band bending similarly to a gold substrate, typically reaching ~2 nm below the surface and leading to the formation of trivial surface states.[49−51] For a 10 nm thick NF, this would give an effective bulk contribution of 6 nm, which is further modified by the strong band bending effects induced by the Au substrate. Hence, only a small region inside an NF would contribute to the resonant Raman scattering signal, which explains the abruptly decreasing Raman intensity for NFs thinner than 10 nm that is caused by tuning the bulk conduction bands out of resonance.

### 3.4. Electron-Phonon Interaction.

The growing contribution of injected carriers for decreasing NF thicknesses is further mirrored in the continuous phonon renormalizations. The additional free carriers provide a low-energy electronic susceptibility that couples to the lattice. The resulting electron-phonon interaction can be derived from the phonon self-energy effects,[44] in particular the change of the widths of the phonon line shape can be used to estimate the change in the electron-phonon interaction. The change in the width of the phonon is given by

$$gc_2 = \sqrt{|2\tilde{\Gamma}\omega_0 - 2\Gamma_0\omega_0|} \tag{1}$$

where $\omega_0$ and $\Gamma_0$ are the native frequency and not renormalized width of the phonon, $\tilde{\Gamma}$ is the renormalized width, and $C_2$ is proportional to the imaginary part of the electronic susceptibility $\pi_I$. It is only possible to derive a quantity that is proportional to the electron-phonon coupling $g$, and its changes can be derived only if the imaginary part of the electronic susceptibility $\pi_I$ is constant. However, $\pi_I$ also determines the electronic background required for the Fano interference. Therefore, we study the changes in the observed electronic susceptibility, i.e., the Bose-corrected background after subtraction of the phonons in Figure 4d. Indeed, we find no changes in the electronic susceptibility, strongly suggesting that $c_2$ is indeed constant. Accordingly, we can apply eq 1 to derive the change of the electron-phonon coupling as a function of NF thickness, as shown in Figure 4e. We find that the electron-phonon coupling is enhanced at the same critical thickness at which the phonon intensity is reduced, demonstrating that both observations can be related to the band bending effects. For $Bi_2Te_3$ with a reduced bulk band gap and a similar electron affinity of 5.3 eV,[52] one would expect analogous band bending and qualitatively identical effects on Raman enhancement, which is indeed the case as shown in the SI-Section 4.5. This provides evidence that the observed effects seem to be intrinsic for topological insulators of this class of materials.

## 4. CONCLUSIONS

In conclusion, we have studied the interface between a gold substrate and 2D nanoflakes (NFs) of the topological insulators $Bi_2Se_3$ and $Bi_2Te_3$ as a function of NF thickness by means of Raman scattering under resonant excitation with 633 nm. By reducing the thickness of the NFs an increasing surface contribution becomes apparent in the detection of the bulk IR $E_u^2$ mode in both $Bi_2Se_3$ and $Bi_2Te_3$ at room temperature. We reveal the presence of interface-enhanced Raman scattering and strong phonon renormalization induced by carriers injected from the gold substrate to the TI NF in contact. This carrier injection results in band bending, which leads to the formation of an intrinsic field enhancement for NFs thicker than 11 nm. In turn, the charge accumulation at the contacted side of the NF yields strong phonon renormalization for thinner NFs due to an enhanced electron-phonon coupling and simultaneous reduction of the resonant Raman conditions. The abrupt reduction in Raman intensity and incipient phonon renormalizations at a transition thickness of 10.5 nm show the implications of band bending effects. This creates a fundamental understanding of TI/gold contacts that should be considered for TI applications and experiments in the ultrathin limit. Our results outline the capability of Raman spectroscopy to study the carrier injection and subsequent electron-phonon interaction in obscured interfaces between a TI and metal contact and pave the way for further investigations on different TI/metal contacts.

## ■ ASSOCIATED CONTENT

### Supporting Information

The Supporting Information is available free of charge at https://pubs.acs.org/doi/10.1021/acsami.2c04380.

> Sample preparation; Raman setup; data treatment; correction factors for resonance Raman study; quantification of NF optical contrast; influence of NF lateral dimensions; symmetry properties of phonons; estimated carrier density in $Bi_2Se_3$; interface enhancement of $Bi_2Te_3$ NFs on gold, and ellipsometry data of Au substrate (PDF)

## ■ AUTHOR INFORMATION

### Corresponding Authors

**Sarah Scheitz** − *Institut für Nanostruktur- und Festkörperphysik, Center for Free Electron Laser Science (CFEL), Universität Hamburg, 22761 Hamburg, Germany;* orcid.org/0000-0002-0305-5512; Email: sscheitz@physnet.uni-hamburg.de

**Michael Rübhausen** − *Institut für Nanostruktur- und Festkörperphysik, Center for Free Electron Laser Science (CFEL), Universität Hamburg, 22761 Hamburg, Germany;* Email: mruebhau@physnet.uni-hamburg.de

### Authors

**Tomke Eva Glier** − *Institut für Nanostruktur- und Festkörperphysik, Center for Free Electron Laser Science (CFEL), Universität Hamburg, 22761 Hamburg, Germany;* orcid.org/0000-0001-8943-1509

**Christian Nweze** − *Institut für Nanostruktur- und Festkörperphysik, Center for Free Electron Laser Science (CFEL), Universität Hamburg, 22761 Hamburg, Germany;* orcid.org/0000-0002-4569-4902

**Malte van Heek** − *Institut für Nanostruktur- und Festkörperphysik, Center for Free Electron Laser Science (CFEL), Universität Hamburg, 22761 Hamburg, Germany*

**Isa Moch** − *Institut für Nanostruktur- und Festkörperphysik, Center for Free Electron Laser Science (CFEL), Universität Hamburg, 22761 Hamburg, Germany*

**Robert Zierold** − *Institut für Nanostruktur- und Festkörperphysik, Center for Hybrid Nanostructures (CHyN), Universität Hamburg, Hamburg 22761, Germany;* orcid.org/0000-0003-0292-0970

**Robert Blick** − *Institut für Nanostruktur- und Festkörperphysik, Center for Hybrid Nanostructures (CHyN), Universität Hamburg, Hamburg 22761, Germany*

**Nils Huse** − *Institut für Nanostruktur- und Festkörperphysik, Center for Free Electron Laser Science (CFEL), Universität Hamburg, 22761 Hamburg, Germany;* orcid.org/0000-0002-3281-7600

Complete contact information is available at: https://pubs.acs.org/10.1021/acsami.2c04380

### Notes

The authors declare no competing financial interest.

## ■ ACKNOWLEDGMENTS

The authors thank Stephan Martens for the support on ellipsometry measurements.

## ■ ABBREVIATIONS

TI, topological insulator
SOC, spin−orbit coupling
TSS, topological surface states
NF, nanoflake
TEM, transmission electron microscopy
SAED, selected area electron diffraction
EDX, energy-dispersive X-ray spectroscopy
AFM, atomic force microscopy
OC, optical contrast
FWHM, full width at half-maximum
IR, infrared
DP, Dirac point

## ■ REFERENCES

(1) Hasan, M. Z.; Kane, C. L. Colloquium: Topological Insulators. *Rev. Mod. Phys.* **2010**, *82*, 3045−3067.

(2) Qi, X. L.; Zhang, S. C. Topological Insulators and Superconductors. *Rev. Mod. Phys.* **2011**, *83*, 1057−1110.

(3) Mellnik, A. R.; Lee, J. S.; Richardella, A.; Grab, J. L.; Mintun, P. J.; Fischer, M. H.; Vaezi, A.; Manchon, A.; Kim, E.-A.; Samarth, N.; Ralph, D. C. Spin-Transfer Torque Generated by a Topological Insulator. *Nature* **2014**, *511*, 449−451.

(4) Fan, Y.; Upadhyaya, P.; Kou, X.; Lang, M.; Takei, S.; Wang, Z.; Tang, J.; He, L.; Chang, L.-T.; Montazeri, M.; Yu, G.; Jiang, W.; Nie, T.; Schwartz, R. N.; Tserkovnyak, Y.; Wang, K. L. Magnetization Switching through Giant Spin−Orbit Torque in a Magnetically Doped Topological Insulator Heterostructure. *Nat. Mater.* **2014**, *13*, 699−704.

(5) Jamali, M.; Lee, J. S.; Jeong, J. S.; Mahfouzi, F.; Lv, Y.; Zhao, Z.; Nikolić, B. K.; Mkhoyan, K. A.; Samarth, N.; Wang, J.-P. Giant Spin Pumping and Inverse Spin Hall Effect in the Presence of Surface and Bulk Spin−Orbit Coupling of Topological Insulator $Bi_2Se_3$. *Nano Lett.* **2015**, *15*, 7126−7132.

(6) Pesin, D.; MacDonald, A. H. Spintronics and Pseudospintronics in Graphene and Topological Insulators. *Nat. Mater.* **2012**, *11*, 409−416.

(7) Zhang, H.; Zhang, X.; Liu, C.; Lee, S.-T.; Jie, J. High-Responsivity, High-Detectivity, Ultrafast Topological Insulator $Bi_2Se_3$/Silicon Heterostructure Broadband Photodetectors. *ACS Nano* **2016**, *10*, 5113−5122.

(8) Zhao, C.; Zou, Y.; Chen, Y.; Wang, Z.; Lu, S.; Zhang, H.; Wen, S.; Tang, D. Wavelength-Tunable Picosecond Soliton Fiber Laser with Topological Insulator: $Bi_2Se_3$ as a Mode Locker. *Opt. Express* **2012**, *20*, 27888−27895.

(9) Kane, C. L.; Mele, E. J. Z2 Topological Order and the Quantum Spin Hall Effect. *Phys. Rev. Lett.* **2005**, *95*, No. 146802.

(10) Kondou, K.; Yoshimi, R.; Tsukazaki, A.; Fukuma, Y.; Matsuno, J.; Takahashi, K. S.; Kawasaki, M.; Tokura, Y.; Otani, Y. Fermi-Level-Dependent Charge-to-Spin Current Conversion by Dirac Surface States of Topological Insulators. *Nat. Phys.* **2016**, *12*, 1027−1031.

(11) Spataru, C. D.; Léonard, F. Fermi-Level Pinning, Charge Transfer, and Relaxation of Spin-Momentum Locking at Metal Contacts to Topological Insulators. *Phys. Rev. B* **2014**, *90*, No. 085115.

(12) Yeh, Y. C.; Ho, P. H.; Wen, C. Y.; Shu, G. J.; Sankar, R.; Chou, F. C.; Chen, C. W. Growth of the $Bi_2Se_3$ Surface Oxide for Metal-Semiconductor-Metal Device Applications. *J. Phys. Chem. C* **2016**, *120*, 3314−3318.

(13) Litvinov, V. *Magnetism in Topological Insulators*; Springer, 2020. https://doi.org/10.1007/978-3-030-12053-5.

(14) Zhang, H.; Liu, C. X.; Qi, X. L.; Dai, X.; Fang, Z.; Zhang, S. C. Topological Insulators in $Bi_2Se_3$, $Bi_2Te_3$ and $Sb_2Te_3$ with a Single Dirac Cone on the Surface. *Nat. Phys.* **2009**, *5*, 438−442.

(15) Hsieh, D.; Xia, Y.; Qian, D.; Wray, L.; Dil, J. H.; Meier, F.; Osterwalder, J.; Patthey, L.; Checkelsky, J. G.; Ong, N. P.; Fedorov, A. V.; Lin, H.; Bansil, A.; Grauer, D.; Hor, Y. S.; Cava, R. J.; Hasan, M. Z. A Tunable Topological Insulator in the Spin Helical Dirac Transport Regime. *Nature* **2009**, *460*, 1101−1105.

(16) Xia, Y.; Qian, D.; Hsieh, D.; Wray, L.; Pal, A.; Lin, H.; Bansil, A.; Grauer, D.; Hor, Y. S.; Cava, R. J.; Hasan, M. Z. Observation of a Large-Gap Topological-Insulator Class with a Single Dirac Cone on the Surface. *Nat. Phys.* **2009**, *5*, 398−402.

(17) Chen, Y. L.; Analytis, J. G.; Chu, J.-H.; Liu, Z. K.; et al. Experimental Realization of a Three-Dimensional Topological Insulator, $Bi_2Te_3$. *Science* **2009**, *325*, 178−181.

(18) Hsieh, D.; Xia, Y.; Qian, D.; Wray, L.; Meier, F.; Dil, J. H.; Osterwalder, J.; Patthey, L.; Fedorov, A. V.; Lin, H.; Bansil, A.; Grauer, D.; Hor, Y. S.; Cava, R. J.; Hasan, M. Z. Observation of Time-Reversal-Protected Single-Dirac-Cone Topological-Insulator States in $Bi_2Te_3$ and $Sb_2Te_3$. *Phys. Rev. Lett.* **2009**, *103*, No. 146401.

(19) Steinberg, H.; Gardner, D. R.; Lee, Y. S.; Jarillo-Herrero, P. Surface State Transport and Ambipolar Electric Field Effect in $Bi_2Se_3$ Nanodevices. *Nano Lett.* **2010**, *10*, 5032−5036.

(20) Chiatti, O.; Riha, C.; Lawrenz, D.; Busch, M.; Dusari, S.; Sánchez-Barriga, J.; Mogilatenko, A.; Yashina, L. V.; Valencia, S.; Ünal, A. A.; Rader, O.; Fischer, S. F. 2D Layered Transport Properties from Topological Insulator $Bi_2Se_3$ Single Crystals and Micro Flakes. *Sci. Rep.* **2016**, *6*, No. 27483.

(21) Hoefer, K.; Becker, C.; Rata, D.; Swanson, J.; Thalmeier, P.; Tjeng, L. H. Intrinsic Conduction through Topological Surface States of Insulating $Bi_2Te_3$ Epitaxial Thin Films. *Proc. Natl. Acad. Sci. U.S.A.* **2014**, *111*, 14979−14984.

(22) Qu, D. X.; Hor, Y. S.; Xiong, J.; Cava, R. J.; Ong, N. P. Quantum Oscillations and Hall Anomaly of Surface States in the Topological Insulator $Bi_2Te_3$. *Science* **2010**, *329*, 821−824.

(23) Fanetti, M.; Mikulska, I.; Ferfolja, K.; Moras, P.; Sheverdyaeva, P. M.; Panighel, M.; Lodi-Rizzini, A.; Píš, I.; Nappini, S.; Valant, M.; Gardonio, S. Growth, Morphology and Stability of Au in Contact with the $Bi_2Se_3$(0 0 0 1) Surface. *Appl. Surf. Sci.* **2019**, *471*, 753−758.

(24) Walsh, L. A.; Smyth, C. M.; Barton, A. T.; Wang, Q.; Che, Z.; Yue, R.; Kim, J.; Kim, M. J.; Wallace, R. M.; Hinkle, C. L. Interface Chemistry of Contact Metals and Ferromagnets on the Topological Insulator $Bi_2Se_3$. *J. Phys. Chem. C* **2017**, *121*, 23551−23563.

(25) Gnezdilov, V.; Pashkevich, Y. G.; Berger, H.; Pomjakushina, E.; Conder, K.; Lemmens, P. Helical Fluctuations in the Raman Response of the Topological Insulator $Bi_2Se_3$. *Phys. Rev. B* **2011**, *84*, No. 195118.

(26) Buchenau, S.; Scheitz, S.; Sethi, A.; Slimak, J. E.; Glier, T. E.; Das, P. K.; Dankwort, T.; Akinsinde, L.; Kienle, L.; Rusydi, A.; Ulrich, C.; Cooper, S. L.; Rübhausen, M. Temperature and Magnetic Field Dependent Raman Study of Electron-Phonon Interactions in Thin Films of $Bi_2Se_3$ and $Bi_2Te_3$ Nanoflakes. *Phys. Rev. B* **2020**, *101*, No. 245431.

(27) Zhang, J.; Peng, Z.; Soni, A.; Zhao, Y.; Xiong, Y.; Peng, B.; Wang, J.; Dresselhaus, M. S.; Xiong, Q. Raman Spectroscopy of Few-Quintuple Layer Topological Insulator $Bi_2Se_3$ nanoplatelets. *Nano Lett.* **2011**, *11*, 2407−2414.

(28) Mann, C.; West, D.; Miotkowski, I.; Chen, Y. P.; Zhang, S.; Shih, C. K. Mapping the 3D Surface Potential in $Bi_2Se_3$. *Nat. Commun.* **2013**, *4*, No. 2277.

(29) Schulz, B.; Bäckström, J.; Budelmann, D.; Maeser, R.; Rübhausen, M.; Klein, M. V.; Schoeffel, E.; Mihill, A.; Yoon, S. Fully Reflective Deep Ultraviolet to near Infrared Spectrometer and Entrance Optics for Resonance Raman Spectroscopy. *Rev. Sci. Instrum.* **2005**, *76*, No. 073107.

(30) Glier, T. E. *Applications of Functional One-Dimensional Nanostructures Studied by Light Scattering Dissertation*; Universität Hamburg, 2021.

(31) Arguello, C. A.; Rousseau, D. L.; Porto, S. P. S. First-Order Raman Effect in Wurtzite-Type Crystals. *Phys. Rev.* **1969**, *181*, 1351−1363.

(32) Majumdar, A. Thermoelectricity in Semiconductor Nanostructures. *Science* **2004**, *303*, 777−778.

(33) Richter, W.; Becker, C. R. A Raman and Far-Infrared Investigation of Phonons in the Rhombohedral $V_2$-$VI_3$ Compounds. *Phys. Status Solidi (b)* **1977**, *84*, 619−628.

(34) Zhang, J.; Peng, Z.; Soni, A.; Zhao, Y.; Xiong, Y.; Peng, B.; Wang, J.; Dresselhaus, M. S.; Xiong, Q. Raman Spectroscopy of Few-Quintuple Layer Topological Insulator $Bi_2Se_3$ Nanoplatelets. *Nano Lett.* **2011**, *11*, 2407−2414.

(35) Shahil, K. M. F.; Hossain, M. Z.; Goyal, V.; Balandin, A. A. Micro-Raman Spectroscopy of Mechanically Exfoliated Few-Quintuple Layers of $Bi_2Te_3$, $Bi_2Se_3$, and $Sb_2Te_3$ Materials. *J. Appl. Phys.* **2012**, *111*, No. 054305.

(36) Humlíček, J.; Hemzal, D.; Dubroka, A.; Caha, O.; Steiner, H.; Bauer, G.; Springholz, G. Raman and Interband Optical Spectra of Epitaxial Layers of the Topological Insulators $Bi_2Te_3$ and $Bi_2Se_3$ on $BaF_2$ substrates. *Phys. Scr.* **2014**, *T162*, No. 014007.

(37) Mishra, S. K.; Satpathy, S.; Jepsen, O. Electronic Structure and Thermoelectric Properties of Bismuth Telluride and Bismuth Selenide. *J. Phys.: Condens. Matter* **1997**, *9*, 461−470.

(38) Sharma, Y.; Srivastava, P.; Dashora, A.; Vadkhiya, L.; Bhayani, M. K.; Jain, R.; Jani, A. R.; Ahuja, B. L. Electronic Structure, Optical Properties and Compton Profiles of $Bi_2S_3$ and $Bi_2Se_3$. *Solid State Sci.* **2012**, *14*, 241−249.

(39) Shahil, K. M. F.; Hossain, M. Z.; Teweldebrhan, D.; Balandin, A. A. Crystal Symmetry Breaking in Few-Quintuple $Bi_2Te_3$ Films: Applications in Nanometrology of Topological Insulators. *Appl. Phys. Lett.* **2010**, *96*, No. 153103.

(40) Li, J.; Tu, J. J.; Birman, J. L. Symmetry Predicted Transitions in 3D Topological Insulators. *Solid State Commun.* **2013**, *163*, 11−14.

(41) Kung, H. H.; Salehi, M.; Boulares, I.; Kemper, A. F.; Koirala, N.; Brahlek, M.; Lošt'ák, P.; Uher, C.; Merlin, R.; Wang, X.; Cheong, S. W.; Oh, S.; Blumberg, G. Surface Vibrational Modes of the Topological Insulator $Bi_2Se_3$ Observed by Raman Spectroscopy. *Phys. Rev. B* **2017**, *95*, No. 245406.

(42) Eddrief, M.; Atkinson, P.; Etgens, V.; Jusserand, B. Low-Temperature Raman Fingerprints for Few-Quintuple Layer Topological Insulator $Bi_2Se_3$ films Epitaxied on GaAs. *Nanotechnology* **2014**, *25*, No. 245701.

(43) Fano, U. Effects of Configuration Interaction on Intensities and Phase Shifts. *Phys. Rev.* **1961**, *124*, 1866−1878.

(44) Bock, A.; Ostertun, S.; Sharma, R. D.; Rübhausen, M.; Subke, K. O.; Rieck, C. T. Anomalous Self-Energy Effects of the $B_{1g}$ Phonon in $Y_{1-x}(Pr, Ca)_XBa_2Cu_3O_7$ Films. *Phys. Rev. B* **1999**, *60*, 3532−3537.

(45) Wang, C.; Zhu, X.; Nilsson, L.; Wen, J.; Wang, G.; Shan, X.; Zhang, Q.; Zhang, S.; Jia, J.; Xue, Q. In Situ Raman Spectroscopy of Topological Insulator $Bi_2Te_3$ Films with Varying Thickness. *Nano Res.* **2013**, *6*, 688−692.

(46) He, R.; Wang, Z.; Qiu, R. L. J.; Delaney, C.; Beck, B.; Kidd, T. E.; Chancey, C. C.; Gao, X. P. A. Observation of Infrared-Active Modes in Raman Scattering from Topological Insulator Nanoplates. *Nanotechnology* **2012**, *23*, No. 455703.

(47) Yuan, J.; Zhao, M.; Yu, W.; Lu, Y.; Chen, C.; Xu, M.; Li, S.; Loh, K. P.; Bao, Q. Raman Spectroscopy of Two-Dimensional $Bi_2Te_xSe_{3-x}$ Platelets Produced by Solvothermal Method. *Materials* **2015**, *8*, 5007−5017.

(48) Hor, Y. S.; Richardella, A.; Roushan, P.; Xia, Y.; Checkelsky, J. G.; Yazdani, A.; Hasan, M. Z.; Ong, N. P.; Cava, R. J. p-type $Bi_2Se_3$ for topological insulator and low-temperature thermoelectric applications. *Phys. Rev. B* **2009**, *79*, No. 195208.

## 4.2 Quantum confinement of the spin Berry Phase on 1D topological surfaces of $Bi_2Se_3$ nanowires

In this section, we present the results of the geometrical crossover from 2D to 1D in TI $Bi_2Se_3$ nanowires and how the geometrical crossover results in a new state with a Spin Berry Phase (SPB). We show how reduction in the radius of $Bi_2Se_3$ nanowire results in surface-enhanced Raman scattering (SERS) and the quenching of the SERS with the magnetic field applied along the long axis of the nanowire. In order to validate the quality of the grown nanowires, we first present the characterization results.

### 4.2.1 AFM, SEM, TEM, EDX, HRTEM and SAED Characterization of the circular nanowires

Fig. 4.5 shows the AFM, SEM, EDX and HR-TEM of the synthesized $Bi_2Se_3$ nanowires. Before the characterization, the wires were transferred onto Si substrates and TEM grid with the aid of a custom-made micro-manipulator. The synthesized nanowires have diameters ranging from 20 nm to 800 nm and with lengths from 5 µm to 35 µm [115]. Fig. 4.5(a-b) shows an exemplary AFM image of the synthesized nanowire. The radius of the nanowire is 105 nm and Fig. 4.5(b) shows the circular cross section of the nanowire. SEM images of nanowires of radius 100 nm and 175 nm are shown in Fig. 4.5(c-d) respectively. The observed curve surface supports the circular cross section of the nanowires.
To confirm single crystallinity and morphology of the synthesized nanowires, detailed TEM, HRTEM and SAED characterization were performed on the nanowires. Fig. 4.5(e) shows the TEM image of $Bi_2Se_3$ nanowire with 37.5 nm radius. It is clearly observed from Fig. 4.5(e) that the nanowire was covered with a thin (approximately 1.5 nm) amorphous oxide shell which protects the surface of the topological insulator nanowires from oxidation (unlike in nanoflakes where the polymer (PVP) provides protection to the surface). The correct stoichiometry of the grown nanowires is determined with the TEM-EDX. Fig. 4.5(g) shows an exemplary EDX spectra acquired from a single nanowire and on average, the ratio of Bi to Se is observed to be 0.613 (i.e 38 atm% Bi and 62 atm% Se). The observed Cu peak came from the Cu TEM grid. Furthermore, the HRTEM image of nanowire with a diameter of 42 nm shows clearly the stacking of quintuple layers with a spacing of 0.95 nm as shown in Fig. 4.5(h) and it is in agreement with the thickness of 1 QL of $Bi_2Se_3$ [129]. The HRTEM image of Fig. 4.5(f) shows that the nanowires have lattice spacing of 0.21 nm which is in agreement with previous reports [136] [137]. HRTEM in combination with the SAED confirms that the grown nanowires are single crystalline in $Bi_2Se_3$ $R\bar{3}m$ structure as shown in Fig. 4.5(i). The growth is found to be perpendicular to c-axis direction along the $[11\bar{2}0]$ (Fig. 4.5(i)), in agreement with previous growth mechanisms [108] [9]. Fast Fourier transform (FFT) shown in Fig. 4.5(j) shows hexagonal symmetry due to the orientation along [0001] and confirms the growth direction of the nanowires.

### 4.2.2 Determination of carrier concentration in $Bi_2Se_3$ nanowire

To determine the carrier concentration of the NW, we conducted magneto-transport study on the NW. For magneto-transport measurement, contacts are applied to a NW with the aid of a photolithographic process as described in chapter three. Fig. 4.6(a and b) are the SEM images of a NW with a chromium-contact pattern. The diameter of the NW

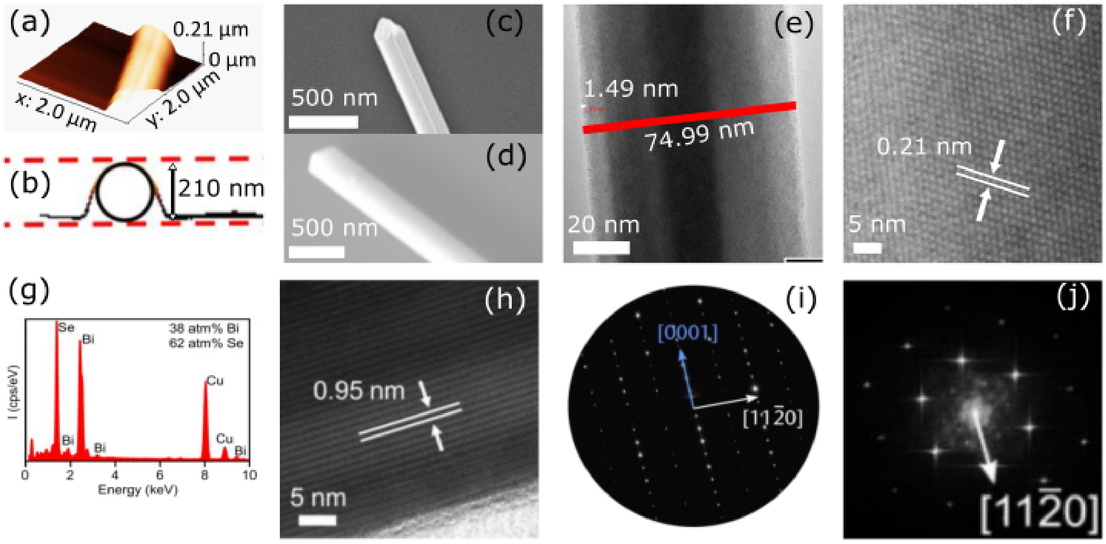

Figure 4.5: AFM, SEM, EDX, TEM and HRTEM of the grown NWs. (a) AFM image of 105 nm radius NW with a circular cross-section shown in (b). (c) and (d) SEM images of NW of radius 100 nm, and 175.5 nm NWs, respectively. (e) TEM image of 37.5 nm NW radius. The 1.5 nm amorphous oxide shell covering the surface of the NW is visible in the TEM image. (f) HRTEM image of a NW, lattice spacings were clearly resolved. (g) Exemplary EDX from the NW shows correct stoichiometry of Bi:Se (2:3). The Cu peak is from the TEM copper grid. (h) HRTEM image of nanowire with a radius of 21 nm reveals the stacking of each quintuple layer with a thickness of about 0.95 nm. (i) Selected area electron diffraction (SAED) pattern shows that the NW growth is perpendicular to the c-axis. (j) Fast Fourier transform (FFT) shows the hexagonal symmertry of the NW due to the orientation along [0001]. (Adapted from [115]).

is 260 nm as can be seen in Fig. 4.6(b). The configuration for measuring the resistance along the long axis of the NW i.e. $R_{XX}$ and the magnetic field B applied perpendicular to the NW is shown in Fig. 4.6(c). Temperature dependent electrical measurements are displayed in Fig. 4.6(d). The NW shows metallic behaviour as the resistance decreases with decreasing temperature. We recall that in TI NW, the surface is metallic with an insulating bulk and therefore decreasing size of the NW gives a higher surface to volume ratio which in turn leads to higher total electrical conductivity [138] [139].

I - V characteristic of the contact at different temperatures confirms ohmic contact as shown in Fig. 4.7(a). Note that surface states in NWs can be investigated by utilizing magnetoresistance (MR) oscillations such as Shubnikov-de Haas and Weak-Anti-Localization (WAL) effect. The MR as a function of magnetic fields (in the low-field limit) that are applied perpendicular to the nanowire axis and the current direction at different temperatures is shown in Fig. 4.7(b). Our results show the WAL which decreases with increasing temperatures. WAL is a common tool to verify the existence of Dirac states and strong spin-orbit coupling in TIs [140] [141] [142]. From the magneto-transport data, a polynomial fit (representing smooth bulk background) was subtracted to expose MR oscillations. Fig. 4.7(c) shows the oscillating MR as a function of $\frac{1}{B}$ in the high-field limit. The vertical lines represent the minima (Landau level, $n$) which can be indexed [142]. The MR oscillations in 2D systems are periodic in $\frac{1}{B}$ such that the minima (Landau level) is constant and this gives rise to a linear dependence between the index and the inverse magnetic field [143] [140].

$$n_{2D} = \frac{1}{B}\left(\frac{k_F^2\hbar}{2e}\right) - \gamma \tag{4.4}$$

$$n_{2D} = \frac{k_F^2}{2\pi} \tag{4.5}$$

where B, n, e, $k_F$, and $\gamma$ are magentic field, index level, electron charge, Fermi wave vector and y-axis intercept. Furthermore, the 1D Landau level can be expressed as

$$n_{1D} = \frac{1}{B}\left(\frac{k_F^2\hbar}{2e}\right)\left(\frac{1}{\sqrt{1-\left(\frac{\hbar k_F}{erB}\right)}}\right) - \gamma \tag{4.6}$$

where r is the radius of the NW. At large value of r, eqn. 4.6 reduces to eqn. 4.4. Fig. 4.7(d) is the graph of the index plot as a function of the inverse magnetic field. Two regions can be identified in the graph i.e. the high field (1D) and the low field (2D) regions in accordance with eqns. 4.6 and 4.4. From eqns. 4.6 and 4.4, we can derive the Fermi wave vector, $k_F = (1.24 \pm 0.42)$ x $10^{-2}$Å$^{-1}$. From the Fermi wave vector, the effective carrier concentration $n$ of the measured NW was estimated to be 4.9 x $10^{11} cm^{-1}$ [115]. The low carrier concentration of NW shows that we are indeed dealing with Dirac states which in effect supports our observation of the spin Berry phase as can be seen later in this section.

### 4.2.3 Geometrical crossover from 2D to 1D in TI $Bi_2Se_3$ nanowires

Raman spectra as a function of nanowire (NW) radius is shown in Fig. 4.8(a). Recall that the distinct phonon modes can be assigned to $A^2_{1g}$ and $E^2_g$ modes. The spectra show a gradual disappearance, reappearance and decrease of the Raman signal as the radius of the NW is steadily decreased from about 200 nm down to about 20 nm. The Raman signal obtained from a geometrical 2D NF is comparable to the Raman signal from NW of radius 206 nm (Fig. 4.8(a)) and of course the 206 nm radius NW could be considered as a 2D or bulk limit [115]. By decreasing the radius of the NW from 200 nm to 100 nm, the corresponding Raman signal decreases to around 100 nm, when the Raman signal completely disappears. This is associated with the decreased scattering volume of the NW. As the radius of the NW is decreased beyond 100 nm, the Raman signal reappears again and peaks at about 30 nm NW radius. This clearly shows crossover from 2D to 1D behaviour [115]. As we mentioned earlier, the line shape of the Raman spectra can be modeled either with eqn. 4.2 or eqn. 4.1. Fig. 4.8(b) shows the mode difference as a function of NW radius and we show that $A^2_{1g}$ and $E^2_g$ modes are approaching each other as the NW radius is decreased. The mode difference of 2.42 $cm^{-1}$ (0.3 meV) is obtained as the NW radius is decreased from 206 nm down to 21 nm. This phonon renormalization shows the existence of interaction between discrete and continuous states. The scattering volume corrected intensity which is normalized to the intensity of the 206 nm radius NW is shown in Figs. 4.8(c and d). The result shows that the susceptibility enhancement of both $A^2_{1g}$ and $E^2_g$ modes are NW radius dependent with the intensity of $A^2_{1g}$ and $E^2_g$ modes peaking at about 28 nm and 20 nm, respectively [115]. Figs. 4.9(a and b) show exemplary spectra fitted with Lorentzian and Fano, respectively, for comparison. In order to extract the Fano parameter q, Raman spectra are fitted with Fano (eqn. 4.2) and in the limit of low signal intensity due to small scattering volume, it is unfortunately not

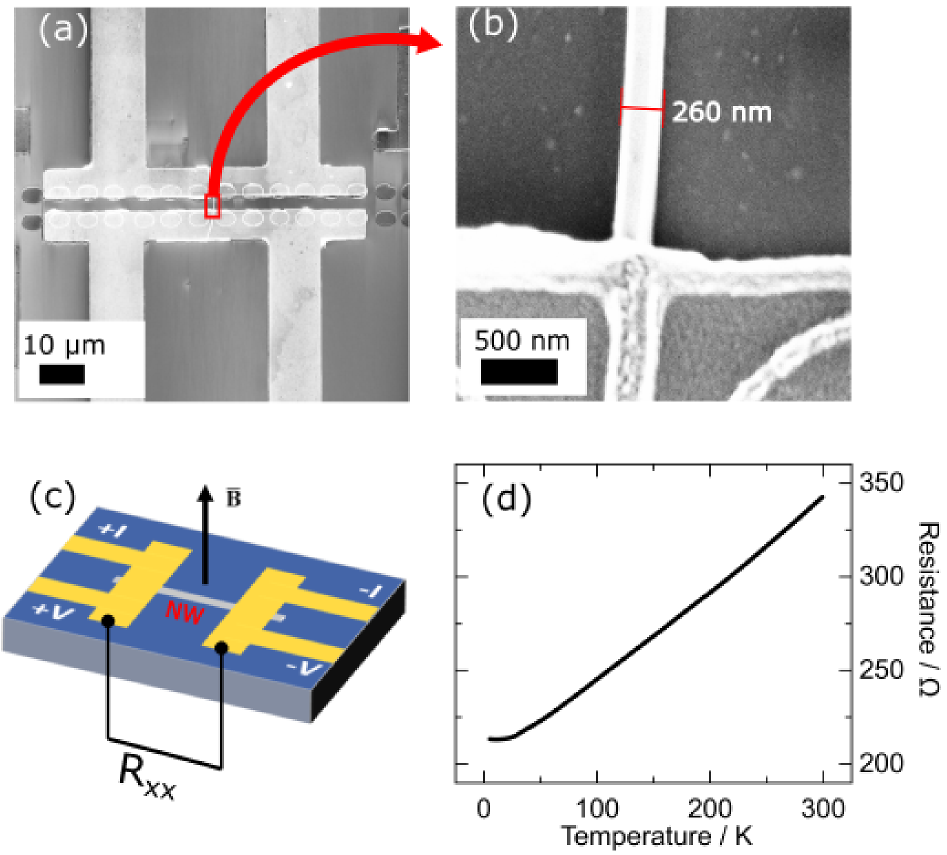

Figure 4.6: Device for magnetotransport studies. (a-b) SEM images of the device containing 130 nm radius nanowire. The nanowire is connected to the chromium (Cr) contacts as shown in (b). (c) Schematic diagram of the device showing four terminals, the direction of the magnetic field (B) and the $R_{xx}$ for determining Shubnikov-de Haas oscillation. (d) Resistance as a function of temperature measured during cool down. (Adapted from [115]).

reasonable to fit the spectra with Fano. From Fig. 4.9(b), we found that the 206 nm NW has Fano parameters of −67 and +109 for $E_g^2$ mode and $A_{1g}^2$ mode, respectively. Again, we found phonon width of the 206 nm NW to be 5.07 and 6.20 for $E_g^2$ mode and $A_{1g}^2$ mode, respectively (see SI 6 of Appendix C for details of the fit parameters). For NW of radius 25 nm, we found broadening of the phonon width as well as decreased Fano parameter. The phonon linewidth of 5.5 and 6.98 were obtained for $E_g^2$ mode and $A_{1g}^2$ mode, respectively and the Fano parameter of −10.30 was obtained for $E_g^2$ mode. The broadening of the phonon linewidth is expected due to electron-phonon interaction that can be derived from the phonon self-energy effects [88] [93]. Our result shows that the 206 nm NW, which we earlier stated as 2D limit, shows sharp and symmetric phonon modes whereas the 25 nm NW, which is 1D geometry, shows broad and asymmetric phonon modes [115].

### Quenching of surface-enhanced Raman scattering with magnetic field

Fig. 4.9(c and d) show the Raman spectra obtained when the magnetic field is switched off and on. The magnetic field is applied along the long axis of the NW. The study was conducted on two different NWs of radii 31 nm and 45 nm. In each case, we applied a magnetic field of 80 mT resulting in a different flux ratio (r) which is dependent on the

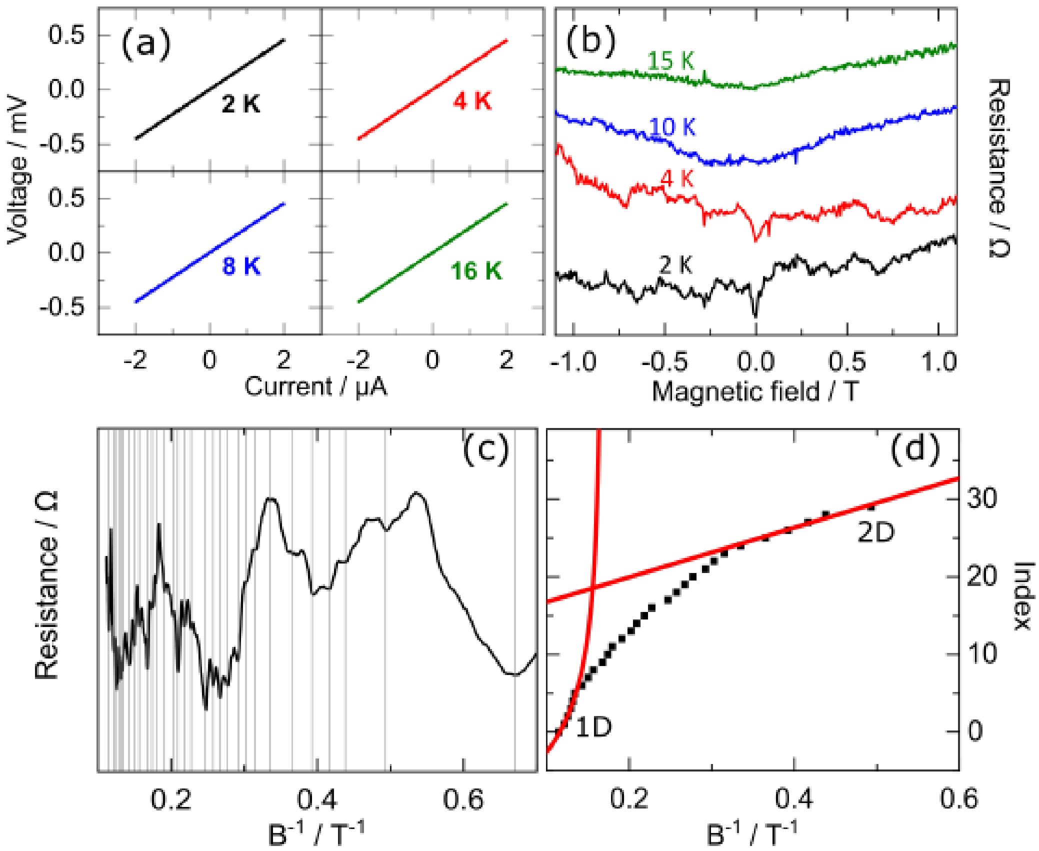

Figure 4.7: Magnetoresistance (MR) studies on nanowire of radius 130 nm. (a) I - V characteristic of the nanowire at 2, 4, 8 and 16 K. The result shows ohmic contacts. (b) MR in the low field limit showing the weak ant-localization (WAL) effect at 2 and 4 K. (c) Oscillating MR obtained after subtracting the polynomial bulk from the raw data at 4 K. The position of the minima is marked with grey vertical lines. (d) Index plot of the minima $n$ as a function of inverse magnetic field $B^{-1}$. The red solid lines are the fit to the data at high and low magnetic fields. (Taken from [115]).

radius of the NW [72]. The predicted critical value to quench the SERS is half a flux quantum [72] which corresponds to 165 mT and 350 mT for NW of radii 45 nm and 31 nm, respectively [115]. Our experimental result shows a total quench of the SERS on the two studied NWs when a magnetic field of 80 mT is applied along the axis of the NWs. Again, the signal re-appears when the magnetic field is turned off (Fig. 4.9(c and d)). Our model in the next section explains the quenching and reappearance of the Raman signal on turning the magnetic field on and off. This behaviour, according to our model, clearly reveals the existence of spin Berry phase in 1D topological insulator surface states.

### 4.2.4 The model and result interpretation

The surface to volume ratio of topological insulators (TIs), and of course other materials, increases with decreasing diameter. By reducing the radius of cylindrical TI nanowires (NWs), charge density at its surface increases [72] and can couple to the photon field and enhance the Raman response of TIs. As can be seen from the plasmonic study in the next section, surface enhanced Raman scattering (SERS) shows Raman enhancements by $10^2$ to $10^9$ -fold if the frequency of the photon is at resonance with the frequency of the surface

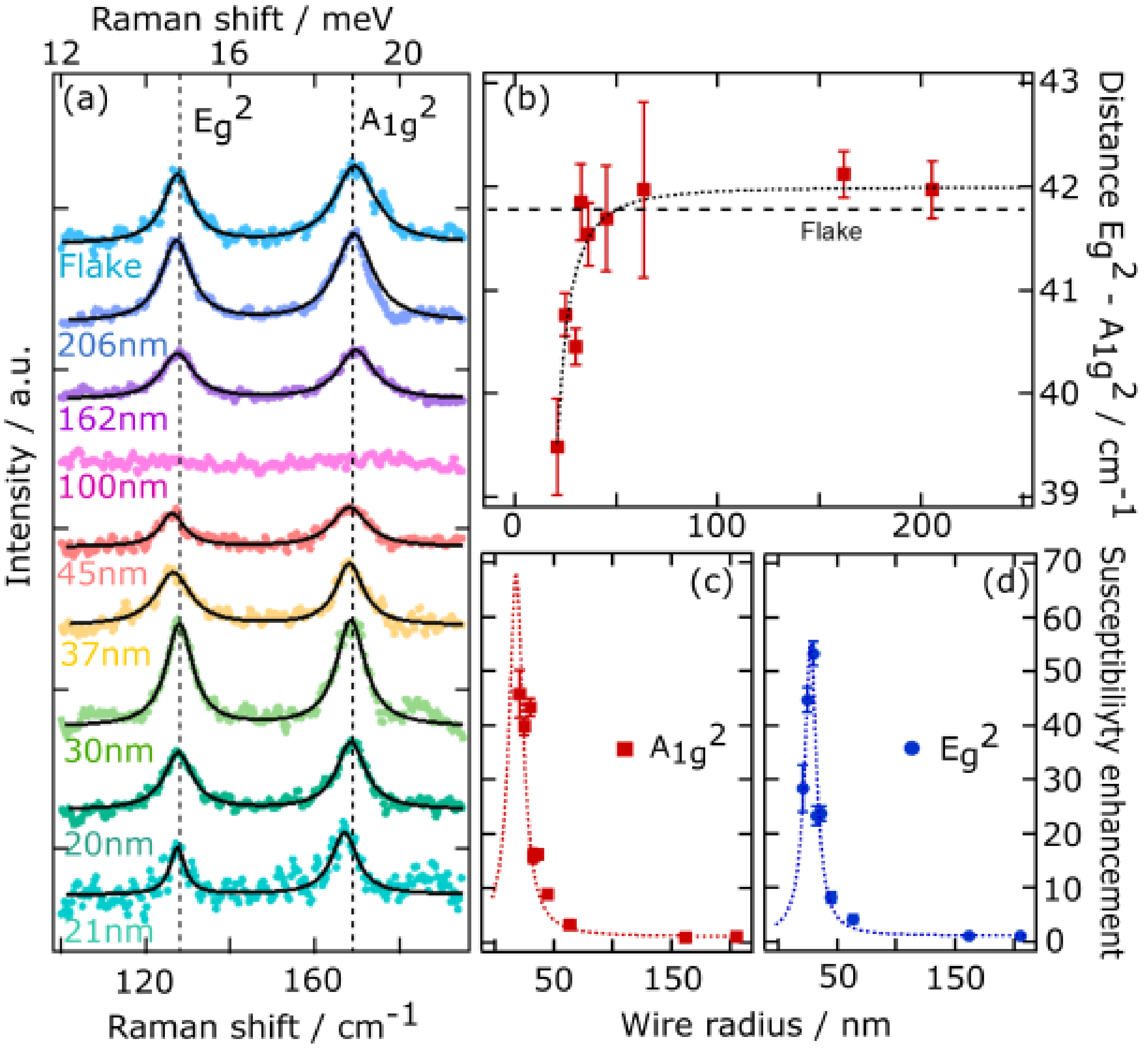

Figure 4.8: Raman studies on cylindrical nanowires of different radii. (a) Raman spectra of $Bi_2Se_3$ nanowires of radii from 206 to 21 nm, including reference $Bi_2Se_3$ NF with thickness of 10 nm. The two dashed vertical lines are the $E_g^2$ and $A_{1g}^2$ modes. The result shows variation of Raman intensity with nanowire radius. (b) Energy difference ($E_g^2$ - $A_{1g}^2$) as a function of nanowire radius. The dashed horizontal line is the energy difference obtained from reference NF. Raman susceptibility as a function of nanowire radius for (c) $A_{1g}^2$ mode and for (d) $E_g^2$ mode. The susceptibilities were corrected for the scattering volume and normalized to the susceptibility at 206 nm. The red and blue dotted profile are the Lorentzian guide to the eye with maximum radius at 28 nm and 18 nm for $E_g^2$ mode and $A_{1g}^2$ mode, respectively. (Taken from [115]).

plasmons [144] [145]. We consider a non-resonant process, since frequency of the photons and that of plasmons differs, coupled with the fact that our observed enhancement is less than $10^2$ -fold. The Feynman diagram representing four photon Green's function [91] for non-resonant Raman scattering is shown in Fig. 4.10 (see section 2.3.1 for details).

Photons excite plasmons and the excited plasmons couple to the low energy phonons and these low energy phonons get enhanced. Therefore phonons can act as local probes for the plasmons. Understandably, the energies of the phonons in $Bi_2Se_3$ TI, in this case, $E_g^2$ and $A_{1g}^2$ are expected to be in the range of the energy scale of plasmons in the 1D confined surface state [115] [72] and the highest effect is expected when the frequency of

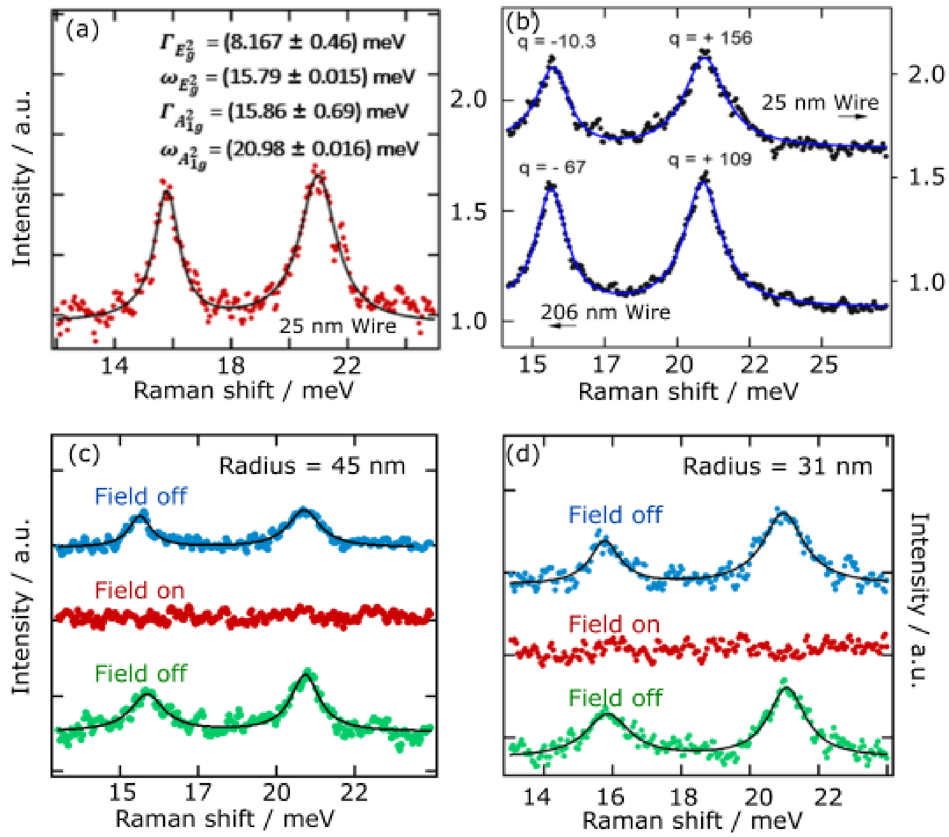

Figure 4.9: Raman studies on two different nanowires in the presence and absence of magnetic field. Exemplary Raman spectra fitted with (a) Lorentzian and (b) Fano profiles. Raman spectra acquired in the ON (blue and green markers) and OFF (red marker) magnetic field for (c) 45 nm and (d) 31 nm nanowire radii. (Adapted from [115]).

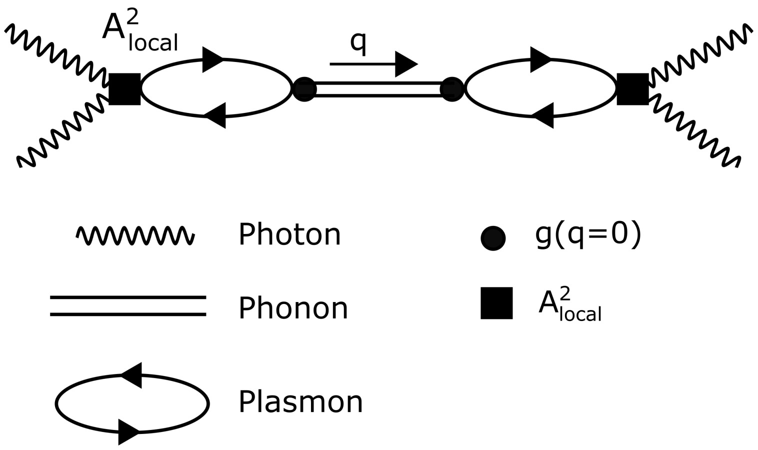

Figure 4.10: Feynman diagram of the four photon (wavy lines) Green's function for non-resonant Raman process. The polarization bubble represents the plasmons and the two horizontal solid lines represent the phonon propagator. The arrow on the phonon propagator represents the Stokes direction. The vertices, solid square and circles, represent the photon-electron and electron-phonon coupling respectively.

the phonons matches that of the plasmons. The interaction between the plasmon and the phonon is expected to change the phonon frequency [146] [93] and indeed we observed frequency shift in our experiment (Fig. 4.8(b)). In other to model the plasmon-phonon interaction considering that plasmons in TI NW depend on the radius of the NW [72], we follow the plasmonic dispersion relation in magnetic field and it is given as

$$\epsilon_{k,m,r}(R_0) = \pm C_2\sqrt{k^2 + (1+2m-2r)^2\tilde{\Delta}(R_0)} \tag{4.7}$$

where k, m, $\tilde{\Delta}(R_0)$, and r are the momentum, sub-band quantum number, band gap (as a function of radius), and magnetic flux ratio (ratio of applied magnetic field to quantum flux $(\hbar/2e)$), respectively. The band gap $\tilde{\Delta}(R_0)$ is inversely proportional to the radius of NW as in eqn. 4.8

$$\tilde{\Delta}(R_0) = \frac{C_1}{C_2}\frac{1}{2R_0} = \frac{\alpha}{d} \tag{4.8}$$

where $C_1$, $C_2$, $R_0$ and d represent inter-spin coupling, inter-orbit coupling, radius of NW, and diameter of NW, respectively.

To model plasmon dispersion relation in TI NW as a function of the NW radius, we take m = 0 (assuming first sub-band is occupied), k = 0.0005 Å$^{-1}$ (compatible with the average photon momentum transferred to the electrons along the wire axis [115] [72]), $C_1 = C_2 = C = 3.33eV$Å(to ensure particle-hole symmetry) we obtained $\alpha = 0.866$ and therefore $C_1 = 2.88$ eVÅ. From eqn. 4.7 we plot the dispersion relation $\epsilon_{k,m,r}$ as a function of NW radius $R_0$ at different magnetic flux ratio r as shown in Fig. 4.11(a). From the plot, we can deduce that the dispersion relation is sensitive to the applied magnetic field and also to the radius of the NW. The plasmonic dispersion is completely quenched when the magnetic flux ratio is 0.5 as predicted by [72]. The value 0.5 (or its multiple) corresponds to a magnetic flux shift of $\pi$ which cancels the $\pi$ spin Berry's phase [73]. NWs of radius above 50 nm have a negligible effect on the dispersion relation as shown in Fig. 4.11(a). Dashed horizontal lines represent the phonon energies for $E_g^2$ and $A_{1g}^2$. The phonon energies of $E_g^2$ and $A_{1g}^2$ modes match the plasmonic excitation energies when the radius of the NWs are 28 nm and 18 nm, respectively. This supports our experimental result (Fig. 4.8(c and d)).

Consider the Feynman diagram i.e. Fig. 4.10, the local field enhancement is represented as $A_{local}^2$ and estimated to be of the order 10 $A^2$ ($A^2$ being the first order non-resonant term of the light-matter interaction). The plasmonic susceptibility can be written as [147]

$$\chi_{Plas}(R_0) = \frac{1}{\omega^2 - (2\epsilon_{k,m,r}(R_0))^2 + 2i\frac{\epsilon_{k,m,r}(R_0)}{\tau_k}} = \chi_{Plas}^{Re} + \chi_{Plas}^{Im} \tag{4.9}$$

where $R_0$, $\epsilon_{k,m,r}$, $\tau_k$ present the NW radius, electron dispersion relation and plasmonic life time respectively. Note that $\chi_{Plas}^2(R_0)$ would always be real.

From the Feynman diagram in Fig. 4.10, plasmon couples to phonon by means of coupling constant g. Since TI properties are dominated by the center of the Brillouin Zone (BZ) [115] we utilize a Raman probe at $k = q \approx 0$ limit. The phonon susceptibility (propagator) is given by

$$\chi_{Phon}(\omega_0, \Gamma) = \frac{1}{\omega^2 - \omega_0^2 + 2i\Gamma} \tag{4.10}$$

The Feynman diagram in Fig. 4.10 can be approximated as the product of eqn. 4.9 squared and eqn. 4.10 multiply by effective coupling constant $|A_{local}^2/A^2|g^2$ as shown in eqn. 4.11

$$I(\omega, R_0) = -Im\left(\left|\frac{A^2_{local}}{A^2}\right|^2 g^2\chi^2_{Plas}(R_0)\chi_{Phon}\right) \tag{4.11}$$

Eqns. 4.7 and 4.9 produced an identical dispersion relation shown in Fig. 4.11(a) when the $\omega_0$ and $\Gamma$ are fixed at the values obtained from Lorentizian fitting of the reference nanoflake (4.9(a)). The only unknown parameter is the plasmon lifetime $\tau_k$ and we estimated the $\tau_k$ to be 500 ps [115]. From eqn. 4.11, we calculated the Raman intensity of $E^2_g$ and $A^2_{1g}$ modes at zero (0) magnetic field for different NW radii. Fig. 4.11(b) shows the plot of the calculated Raman intensity as a function of Raman shift for different wire radius. The result shows that the Raman intensity for $E^2_g$ mode peaks at 25 nm NW radius whereas the Raman intensity for $A^2_{1g}$ mode peaks at 20 nm NW radius in conformity with the experimental results. Fig. 4.11(f) shows the susceptibility enhancement as a function of wire radius for experimental and calculated values. It is evident that our calculation can reproduce the experimental results by considering a single plasmonic mode that obeys the dispersion relation of eqn. 4.9. We performed the same calculation with eqn. 4.11 on 30 nm NW radius and applied a magnetic flux of 0.13. Fig. 4.11(c) shows the reduction of the Raman intensities of $E^2_g$ and $A^2_{1g}$ modes in the presence of the magnetic field. The intensity of $E^2_g$ mode is nearly suppressed but that of $A^2_{1g}$ mode was reduced by a factor of 0.4 and interestingly, we could not find any sign of $A^2_{1g}$ mode in our experiment (Fig. 4.9). The complete quenching of $E^2_g$ and $A^2_{1g}$ modes intensity by the magnetic field clearly supports the presence of the SBP in 1D quantum confined TIs [115].

In order to explain the reason why the intensity of $E^2_g$ and $A^2_{1g}$ modes peaks at 25 nm and 20 nm NW radii, respectively, we will plot the graph of $\chi^2_{Plas}(R_0)$ i.e. square of eqn. 4.9. Fig. 4.11(d) is the plot of plasmonic susceptibility squared as a function of Raman shift for different NW radii in the absence of a magnetic field. Note that the plasmonic susceptibility is corrected for the scattering volume i.e. by scaling with $R^2_0$. The vertical black dashed lines represent $E^2_g$ and $A^2_{1g}$ modes. The plot shows the diameter dependent Raman matrix element and the plasmon energy of 25 nm radius wire matches the phonon energy of $E^2_g$ mode and therefore the energy of plasmon in the wire of radius 25 nm is in resonance with th $E^2_g$ mode. Furthermore, for $A^2_{1g}$ mode, the plasmon energy matches the phonon energy for a wire of radius less than 40 nm. These results are in conformity with our experimental results shown in Fig. 4.8(c and d). Again, for 25 nm radius wire, we calculated the effect of the magnetic field (applied along the axis of the wire) on the plasmon energy as shown in Fig. 4.11(e). The result shows that the plasmonic susceptibility is shifting in energy with the impact of such shift increasing with the magnetic flux and hence reduces the interference between phonon and plasmon susceptibilities leading to quenching of the phonon intensities [115]. Our experimental results, together with the simulation results show that application of a magnetic field along the wire axis suppresses the phonon intensities and hence unambiguous proof of the existence of the $\pi$ spin Berry phase at the TI surface state as theoretically studied [72] [79] [78].

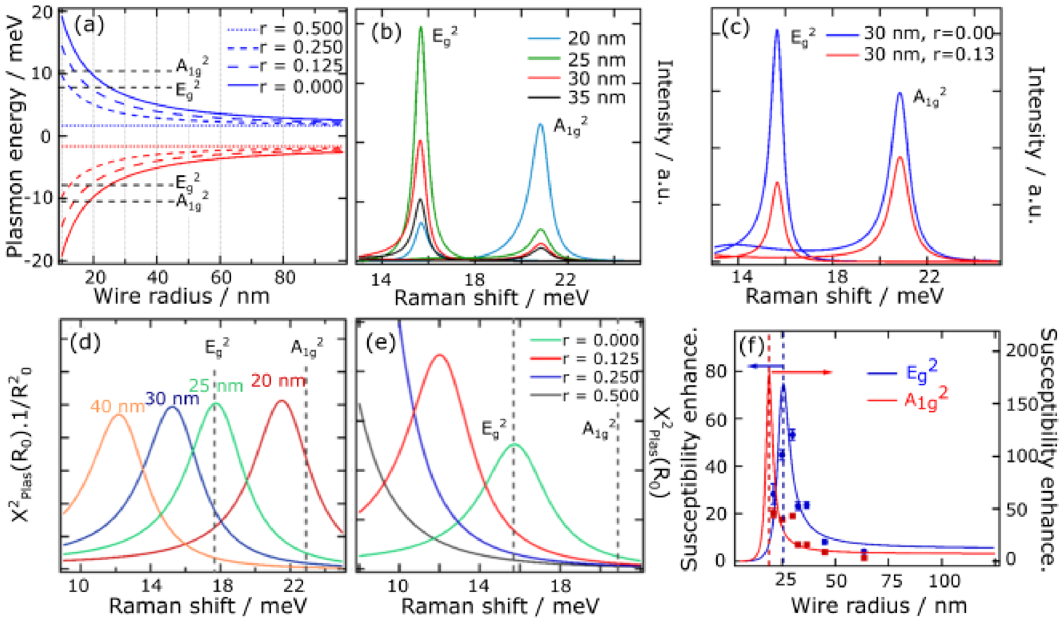

Figure 4.11: Simulation of the Raman data: (a) Dispersion relation ($\epsilon_{k,m,r}(R_0)$) as a function of cylindrical nanowire radius for m=0 (first sub band), k=0.0005 Å$^{-1}$, $\alpha = 0.866$, flux ratios r = 0.0 to 0.5. The phonon energies are represented by the dashed horizontal lines. in the absence of a magnetic field, the gap opens and surface plasmons interact with the phonons and subsequently enhances the Raman matrix element. (b) Nanowire radius dependent on the intensity of Raman signal (non-resonant SERS of the 1D TI). By decreasing the radius of nanowires, $E_g^2$ mode goes into resonance before $A_{1g}^1$ mode. (c) Raman spectra as a function of magnetic field. Magnetic field suppresses the modes differently. Plasmonic susceptibility as a function of (d) nanowire radius and (e) magnetic flux ratio. (f) Simulated (solid line) and experimental data (markers) of the susceptibility enhancement as a function of nanowire radius. The susceptibilities were normalized to the value at 206 nm radius wire. (Figures adapted from [115]).

# Paper 1:
# Quantum Confinement of the Spin Berry Phase on 1D Topological Surfaces of Single $Bi_2Se_3$ Nanowires

Christian Nweze, Tomke Eva Glier, Sarah Scheitz, Lea Westphal, Florian Biebl, Soeren Buchenau, Lewis O. Akinsinde, Niklas Kohlmann, Lorenz Kienle, Isabel Gonzalez Diazplacio, Robert Froemter, Robert Zierold, Robert Blick, Nils Huse, and Michael Ruebhausen.

# Quantum Confinement of the Spin Berry Phase on 1D Topological Surfaces of Single $Bi_2Se_3$ Nanowires

*Christian Nweze*[*‡1], *Tomke E. Glier*[*‡1], *Sarah Scheitz*[1], *Lea Westphal*[1], *Florian Biebl*[1], *Sören Buchenau*[1], *Lewis O. Akinsinde*[1,2], *Niklas Kohlmann*[2], *Lorenz Kienle*[2], *Isabel González Díaz-Placio*[3], *Robert Frömter*[3], *Robert Zierold*[3], *Robert Blick*[3], *Nils Huse*[3], *and Michael Rübhausen*[*‡1]

[1] Institut für Nanostruktur- und Festkörperphysik, Center for Free Electron Laser Science (CFEL), Universität Hamburg, Luruper Chaussee 149, 22761, Hamburg, Germany

[2] Institute for Materials Science, Faculty of Engineering, Kiel University, Kaiserstrasse 2, 24143 Kiel, Germany

[3] Institut für Nanostruktur- und Festkörperphysik, Center for Hybrid Nanostructures (CHyN), Universität Hamburg, Luruper Chaussee 149, 22761, Hamburg, Germany

KEYWORDS: Topological Insulator, Surface Enhanced Raman Scattering, Spin-Berry Phase; Magnetic Field, One-Dimensional, Micro-Raman Spectroscopy

Topological insulators (TIs) exhibit unconventional quantum phases that can be tuned by external quantum confinements. The geometrical crossover from 2D to 1D in a TI results in a novel state with a Spin Berry Phase (SBP). We use Raman scattering on single crystalline $Bi_2Se_3$-TI nanowires to track the geometrical crossover from quasi 2D to quasi 1D. It is marked by the sudden appearance of plasmonic surface-enhanced Raman scattering (SERS) in nanowires below 100 nm diameter. A magnetic field applied along the wire axis results in a quenched SERS, providing clear evidence that spin-polarized plasmonic excitations of the SBP dominate the electronic excitation spectrum.

Topological insulators (TIs) exhibit Dirac cones, segments of nearly linear dispersion, where both dispersion branches have opposite spin orientation.[1–3] The spin-polarized bands make TIs interesting candidates for many applications such as room-temperature spintronics, quantum computing, and thermoelectric generators.[4] Experimental studies report on the investigation of electrical transport properties from nano-ribbons.[5–11] TIs offer an exciting avenue to study physical anomalies and unconventional states in matter.[6] In particular, geometric quantum confinement leads to exciting effects. For instance, morphing a 3D TI such a $Bi_2Se_3$ into a 1D cylinder leads to a splitting of the 2D conical Dirac band structure of the SS into 1D discrete subbands.[12,13] As a consequence, 1D plasmonic bands are formed with gaps in the electronic excitation spectrum due to self-interference of the electronic wave functions around the cylinder perimeter. These gaps are inversely proportional to the wire diameter.[12,14] Electronic bands of the TI are spin-polarized and consequently a Spin Berry Phase (SBP) is formed. The application of a magnetic field along the wire axis adds an additional phase shift to the electronic wave function yielding a high sensitivity to small magnetic fluxes and as a consequence the restoration of the Dirac cone for magnetic fields of the order of a single flux quantum.[12,14,15]

In 3D TIs with planar geometry, such as 2D-flakes and thin films, optical studies of plasmons have provided a deep insight into their electronic structure.[16–22] Raman scattering on TIs has revealed the thickness-dependent quantum confinement of phonons in $Bi_2Se_3$ flakes and thin films.[20–23] Plasmonic excitations at surfaces can enhance the Raman scattering cross-section by surface-enhanced Raman scattering (SERS).[24,25] Thus, Raman scattering is a powerful tool to study the low-energy excitation spectrum, which is determined by novel plasmonic states, and to understand the coupling between spin, charge, and lattice degrees of freedom in TIs.

Low-energy 1D plasmonic excitations of TIs have an energy scale of the order of 10 meV.[12,13] Direct absorption measurements of the plasmonic excitations will fail, as these low energies correspond to electromagnetic wavelengths of more than 100 µm exceeding the nanowire diameter by far. In this letter, we report on the study of single nanowires in a diameter range suitable to study the geometrical crossover from 2D to 1D TI SS and provide evidence for the presence of a SBP in nanowires with a diameter below 100 nm. We have designed a micro-Raman setup[26] that uses a circular diffraction limited spot with a diameter of (544 ± 13) nm within a magnetic field provided by two permanent magnets (Fig. 1(a) and (b), see SI 4). The heating of the wire even for powers of 140 µW from a 532 nm diode laser, was mitigated by scanning along the nanowire axis (see Fig. 1(a)). We have synthesized circular $Bi_2Se_3$ nanowires with lengths from 5 µm to 35 µm (see Fig. 1(d)-(f)) and diameters ranging from 22 nm to 800 nm (see SI 2). $Bi_2Se_3$ nanowires with diameters down to 42 nm together with the laser focus were observed in the custom-made optical microscope, enabling a precise control of the scanning procedure (see Fig. 1(d)). The cylindrical shape of the nanowires is demonstrated by scanning electron microscopy (SEM) and atomic force microscopy (AFM) images (Fig. 1(e) and (f), see SI 2). High-resolution transmission electron microscopy (HRTEM) confirms the single crystallinity of the wires and a 1D wire growth perpendicular to c-axis direction along the [11-20] axis (Fig. 1(c)) in agreement with previous growth mechanisms.[8,27] The wires exhibit an amorphous oxide shell as can be seen in Fig. 1(c), which is also evident in energy filtered TEM maps of the Oxygen-K edge (see lower inset and SI 2). Energy-dispersive X-ray spectroscopy (EDX) studies shown in the SI (SI 2) support the 2:3 (Bi:Se) stoichiometry. The wire, its quintuple layers, and orientation during the experiment are shown in Fig. 1(b) with the c-axis being perpendicular to the wire axis. We expect a Raman spectrum of phonons that is essentially comparable to that of a conventional 2D-flake of $Bi_2Se_3$.[23,28] Magneto-transport measurements on devices as shown in Fig. 1(g) obtained from a 260 nm diameter wire reveal the presence of metallic SS. Weak anti-localization effects prove the strong spin-orbit coupling, which is prerequisite for the band inversion and the formation of Dirac-like SS. The measurements show a magnetic field-dependent crossover between 2D- and 1D-electrical transport in agreement with previous observations.[29–31] From the transport measurements the Fermi vectors can be estimated to be $k_F = (1.24 \pm 0.42) \cdot 10^{-2}$ Å$^{-1}$ leading to an effective carrier concentration $n = (k_F)^2/2\pi = 4.9 \cdot 10^{11}$ cm$^{-2}$ in good agreement with the 2:3 stoichiometry. More details are given in SI 8.

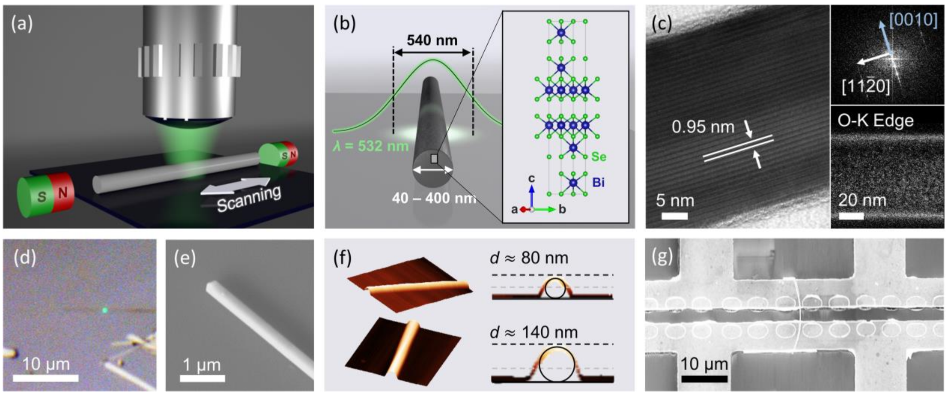

**Figure 1.** Experimental setup and sample characterization: (a) Sketch of the experimental Raman setup. A 532 nm diode laser beam is focused on a single $Bi_2Se_3$ nanowire. The scan direction along the wire axis is shown (white arrow). A magnetic field can be applied along the wire axis. (b) Schematic illustration of the quintuple layers and the wire growth in relation to the Raman experiments. (c) HRTEM micrograph of a wire (42 nm diameter). The wire is viewed along [2-1-10] showing the quintuple layer stacking. The FFT shown in the upper inset reveals a growth direction of [11-20] orthogonal to the c-axis. The lower inset presents an exemplary EFTEM elemental map of the O-K edge at 530 eV. (d) Microscopy image of a wire with 73 nm diameter and the laser spot (green). (e) SEM image of a 316 nm wire. (f) Cross-sections as determined by AFM on wires with 80 nm and 140 nm diameter, respectively. The shapes are approximated by circles. (g) Device for transport measurements. The SEM image shows the 260 nm wire connected to the Cr contacts.

The results of the Raman measurements as a function of nanowire diameter are shown in Fig. 2. In Fig. 2(a) we observe the $E^2_g$- and $A^2_{1g}$-modes of the $Bi_2Se_3$ phonons characteristic for the structure building quintuple layers.[32] The measurements of the 2D flake and the 411 nm nanowire show nearly identical phonon modes, which is in agreement with the stacking of the quintuple layers perpendicular to the wire elongation. The observed Raman intensity decreases proportional to the square of the wire diameter reflecting the decreased scattering volume. Finally, at around 200 nm, the signal strength of the nanowires is lost. Four nanowires with diameters between 180 nm and 225 nm were measured confirming this result. Surprisingly, the intensity of the Raman signal from wires smaller than 100 nm starts to increase again, peaking around 60 nm. This observation marks a clear crossover from a 2D to a 1D behaviour. In order to model the contributing phonons, the line shape can be described by Lorentz- or Fano-profiles.[33–36] The details of the line shape analysis are given in SI 6. For the sake of clarity, we fit Lorentz-profiles to the phonons. In Fig. 2(b) we plot the energy difference between the $E^2_g$- and $A^2_{1g}$-modes, which is reduced by about 0.3 meV as the wire diameter is decreased. The simultaneous changes in intensity and relative phonon position point clearly towards the interaction of the phonon with an electronic mode that is characteristic for a 1D confined TI (see SI 7). The intensities of the $E^2_g$- and $A^2_{1g}$-modes divided by the square of the wire diameter and normalized to the susceptibility of the 411 nm wire are plotted in Fig. 2(c) and (d). While the $E^2_g$-mode intensity peaks at a wire diameter of 55 nm the $A^2_{1g}$-modes intensity continues to rise indicating that the highest intensity of the $A^2_{1g}$-mode occurs below 40 nm. These results suggest a coupling of these phonons to an electronic low-energy excitation with an excitation energy depending on the diameter of the wire.

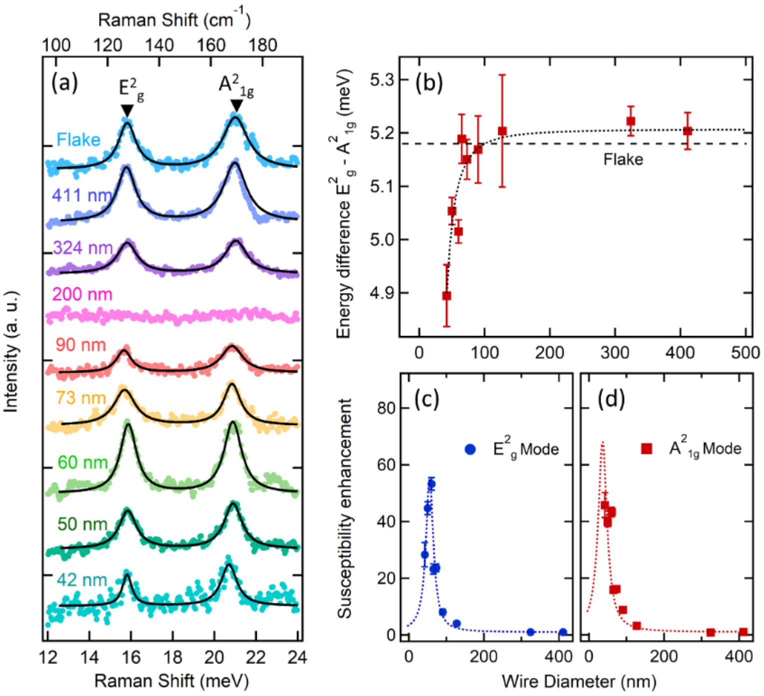

**Figure 2.** Experimental Raman data: (a) Raman spectra of $Bi_2Se_3$ nanowires with diameters from 411 nm to 42 nm, as well as from a $Bi_2Se_3$ flake with a thickness of 10 nm. (b) Energy difference between the $E^2_g$- and the $A^2_{1g}$-modes as function of wire diameter. The dashed line guides the eye. (c) Raman susceptibility of the $E^2_g$-mode and (d) Raman susceptibility of the $A^2_{1g}$-mode as function of wire diameter. Curves were normalized to their respective susceptibilities at 411 nm. A Lorentzian with a maximum at a wire diameter of 55 nm models the $E^2_g$-mode susceptibility. (d) A Lorentzian with a maximum at 36 nm was added as guide to the eye.

For circular 3D TIs, surface charges build up with decreasing wire diameter.[12] The resulting electric field can couple to the photon field in Raman scattering. Surface enhanced Raman scattering (SERS) shows Raman enhancements between $10^2$ and $10^9$ in resonance with surface plasmons of metallic nanoparticles.[24,25] Since the frequency of the optical photons and the frequency of the plasmons in TIs are expected to be different by two orders of magnitude, we adopt a non-resonant picture of the Raman process. This assumption is supported by the fact that the spectra in the 1D regime reveal the same contributing phonons that are present in the 2D limit, suggesting that a local field enhancement effect amplifies the conventional response. This mechanism is pictorially shown in Fig. 3(a). For 3D TI SS that are confined in 1D a photon excites plasmons and the phonons coupling to them get enhanced. In this context, the phonons act as low-energy probe of the electronic excitation spectrum. The energies of the $E^2{}_g$-mode and the $A^2{}_{1g}$-mode are 15.6 meV and 20.86 meV matching the expected energy scale of the plasmon in the 1D confined SS.[12] The largest effect is expected when the energy of the plasmon matches the phonon energy. Note, the same plasmon that is responsible for the enhancement of the Raman process also interacts with the phonon so that we would expect changes in the phonon frequencies as observed in Fig. 2(b). As shown in SI 6, the $E_g{}^2$-mode exhibits a distinctive enhancement of the Fano-parameter at smaller NW diameter concomitantly with an enhanced width (broadening) and shift in mode frequency (hardening) clearly indicating the presence of a novel low-energy mode.[33–35]

A novel quasi-particle excitation in an unconventional quantum state reveals itself by its dispersion relation. Experimentally, one would vary the momentum to probe the dispersion relation. However, the plasmonic dispersion relation depends strongly on the wire diameter. Therefore, our study on single nanowires as a function of wire diameter is suitable to track the dispersion of electronic excitations in the SBP. The dispersion relation of electronic states of a 1D cylinder in a magnetic field is given by[12,37],

$$\varepsilon_{k,m,r}(R_0) = \pm C_2\sqrt{k^2 + (1 + 2m - 2r)^2\,\tilde{\Delta}^2(R_0)} \quad , \tag{1}$$

with a gap opening in the electronic excitation spectrum that is inversely proportional to the wire diameter

$$\tilde{\Delta}(R_0) = \frac{C_1}{C_2}\frac{1}{2R_0} = \frac{\alpha}{d} \quad . \tag{2}$$

$C_1$ and $C_2$ are the inter-spin and inter-orbital coupling constants. $R_0$ and $d$ are the radius and diameter of the wire, respectively. $k$ is the momentum, $m$ is the sub-band quantum number, and $r$ is the magnetic flux ratio along the wire axis in units of an elementary flux quantum. We take the following values. $m = 0$ assuming that only one sub-band is occupied. This is motivated by the 2:3 stoichiometry (see EDX analysis in SI 2) and transport studies (see SI 8). $k = 0.0005$ Å$^{-1}$ is compatible with the averaged photon momentum transferred to the electrons along the wire axis. From Ref. [12] one obtains $C_2 = C_1 = 3.33$ eV Å. However, we have obtained $\alpha = 0.866$ leading to $C_1 = 2.88$ eV Å. With these parameters, we plot the electronic energies of the first sub-band as a function of wire diameter in Fig. 3(b). The energies of the $E^2_g$- and $A^2_{1g}$-phonons are marked by straight lines. Two essential conclusions can be made: Firstly, the impact of the cylindrical quantum confinement becomes relevant for wire diameters below 100 nm and, secondly, the energies of $E^2_g$-mode and the $A^2_{1g}$-mode match the excitation energies of the 1D plasmon at slightly different wire diameters of 55 nm and 36 nm, respectively. Both observations are well in line with the key findings in our experiment (Fig. 2(c) and (d)), strongly suggesting that the phonons couple to the photons by means of the electronic SS of the cylindrical TI. Note, with increasing magnetic flux parallel to the NW axis, it is possible to quench these plasmonic excitations, which vanish for a fractional magnetic flux quantum of $r = 0.5$.[12] Since the topological properties are dominated by the centre of the Brillouin Zone and as we apply a $q \approx 0$ Raman probe, we will evaluate the Feynman diagram in the $k = q \approx 0$ limit. From the Feynman diagram shown in Fig. 3(a)[38] we obtain:

$$I(\omega, R_0) = -\mathrm{Im}\left[M_0^2\, \chi_{\mathrm{Plas}}^2(R_0)\, \chi_{\mathrm{Phon}}\right] \;, \tag{3}$$

where $M_0^2 = \left|\frac{A_{\mathrm{local}}^2}{A^2}\right|^2 g^2$, with $A^2$ being the first order non-resonant term of the light-matter interaction to a free electronic particle and $g$ being the electron-phonon coupling constant. $A_{\mathrm{local}}^2$ is representing the local field enhancement, which we estimate to be of the order of 10 $A^2$. The plasmonic susceptibility depends now critically on $R_0$ due to the dispersion relation (equation (1)). The real and imaginary parts of the plasmonic susceptibility can be modelled by[39]

$$\chi_{\mathrm{Plas}}(R_0) = \frac{1}{\omega^2 - \left(2\varepsilon_{k,m,r}(R_0)\right)^2 + 2i\,\frac{\varepsilon_{k,m,r}(R_0)}{\tau_k}} \;, \tag{4}$$

with $\tau_k$ being the plasmon lifetime. The phonon susceptibility is given by

$$\chi_{\mathrm{Phon}}(\omega_0, \Gamma) = \frac{1}{\omega^2 - \omega_0^2 + 2i\Gamma} \;. \tag{5}$$

The observed Raman intensity depends on the radius of a nanowire *via* the dispersion relation (equation (1)) in the susceptibility of the 1D-plasmon. The required input parameters were fixed in the following way. The bare phonon frequencies $\omega_0$ and damping constants $\Gamma$ for both phonons were taken from the 2D limit, i.e. fits to the phonon spectrum of the flake. The dispersion in equation (4) was identical to the one shown in Fig. 3(b). The only unknown parameter is the plasmon lifetime. It determines the width of the resonance as a function of wire diameter. For the calculations shown in Fig. 3(c) we have assumed an interaction of both phonons with one and the same plasmonic excitation and an estimated plasmon lifetime of 500 ps. When comparing Fig. 2(c) and (d) with Fig. 3(d), it is evident that our simplified calculation can reproduce the experimentally derived different resonance behaviours of the $E^2_g$- and $A^2_{1g}$-modes by considering a single plasmonic mode that obeys the dispersion relation of equation (1) with $m = 0$ and $r = 0$ (for more details see SI 7).

If these plasmons originate from the proposed SBP they should be very sensitive to the application of even small magnetic fields, as indicated by the sensitivity of the dispersion (equation (1)) to an applied magnetic field (see Fig. 3(b)). The critical value is half a flux quantum.[12] For wires of 90 nm and 62 nm diameter this corresponds to magnetic fields of about 165 mT and 350 mT, respectively. We have applied a field in axial geometry as outlined in Fig. 1(a). The results are shown for a 62 nm wire in Fig. 3(e) with a field of 80 mT corresponding to $r = 0.13$ in equation (1). The effect was reproduced for a wire with a diameter of 90 nm (see SI 4). The SERS is completely quenched with an applied magnetic field and recovers to the original results without field. This behaviour is even more dramatic than anticipated by our model. The calculation in Fig. 3(f), performed with the same parameters as the calculations in Fig. 3(c), would indicate a strongly suppressed $E^2_g$-mode but only a 40 % suppression on the high energy $A^2_{1g}$-mode. Yet, we could not find any sign of the $A^2_{1g}$-mode in magnetic field measurements on wires with diameters of 62 nm and 90 nm. The extraordinarily strong magnetic field suppression clearly supports the presence of the SBP in 1D quantum confined TIs. Furthermore, the strong dependence suggest that magnetic fields applied along the wire axis influence parameters such as the ratio $\alpha$ indicating changed inter-spin or inter-orbital coupling constants.

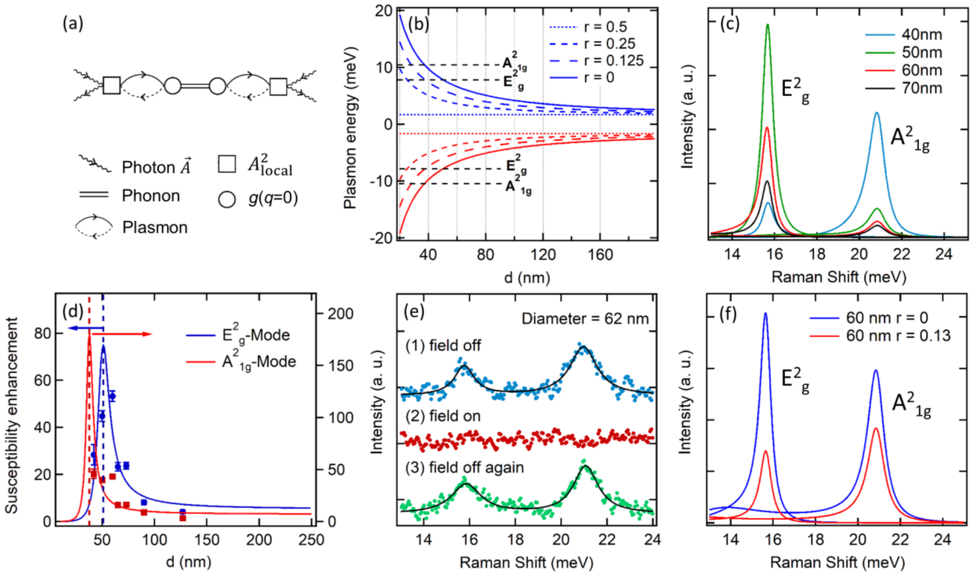

**Figure 3.** Simulation of the Raman data: (a) Feynman diagram showing the Raman process for phonons. (b) Dispersion $\varepsilon_{k,m,r}(R_0)$ for $m = 0$ (first sub band) of a cylindrical nanowire for finite momentum $k = 0.0005$ Å$^{-1}$ as a function of wire diameter with $\alpha = 0.866$ and ratios $r$ of the magnetic flux quantum ($r = 0$ to r = 0.5). Dashed straight lines mark the phonon energies. As the gap opens, the surface plasmons interact with the phonons and enhance the observed Raman phonon intensities. (c) Calculated non-resonant SERS of the 1D TI nanowires for different wire diameters. The $E^2_g$-mode at 15.6 meV goes into resonance for larger wire diameters as compared to the $A^2_{1g}$-mode at 20.86 meV. (d) Calculated (solid line) and experimentally observed (markers) susceptibility enhancement of the $E^2_g$- and $A^2_{1g}$-mode. The Raman susceptibilities were normalized to the susceptibilities at 411 nm. (e) Experimental Raman spectra of a 62 nm

wire without, with, and again without magnetic field of 80 mT (see SI 4). (f) Simulated Raman spectra as a function of magnetic field.

In conclusion, we have shown the geometrical crossover from a 2D to 1D confined topologically protected SS below a critical nanowire diameter of about 100 nm. The 1D TI SS exhibits SERS that is strongly dependent on the diameter of the nanowires. We attribute these effects to novel spin-polarized plasmonic excitations within the SBP. We support this assignment by the observed SERS signal and the signal quenching induced by very small magnetic fluxes along the wire axis. The basic features of our experiments could be understood by modelling the coupling between spin-polarized 1D plasmons of the TI with the phonons. The 1D plasmons obey the expected dispersion relation and the only free parameters used in our model are $\alpha$ and $\tau$ representing the ratio between inter-spin to inter-orbital coupling strengths and the plasmon lifetime, respectively. Thus, we have provided clear evidence that spin-polarized plasmonic excitations of the SBP dominate the electronic excitation spectrum and we have established a new route to study low-energy excitation spectrum of 1D TI nanowires by means of Raman scattering.

## ASSOCIATED CONTENT

**Supporting Information**. PDF is available divided into the following sections: $Bi_2Se_3$ nanowire synthesis (SI 1); Sample characterization (SI 2); Raman measurements (SI 3); Magnetic field dependent Raman measurements (SI 4); Data analysis (SI 5); Line shape analysis (SI 6); Calculation (SI 7); Nanowires and magnetic-transport measurements (SI 8).

AUTHOR INFORMATION

## Corresponding Author

* C.N.: cnweze@physnet.uni-hamburg.de, T.E.G.: tglier@physnet.uni-hamburg.de, M.R.: ruebhausen@physnet.uni-hamburg.de

## Author Contributions

Design of the study: M.R., C.N., T.E.G.; Oven CVD: C.N. L.A. S.B.; Sample synthesis and fabrication: C.N.; Raman setup: M.R., T.E.G., L.W., F.B.; Raman measurements: T.E.G., L.W., S.S., C.N., M.R.; SEM/EDX: R.F., C.N., N.H., S.S.; TEM/EDX: N.K., C.N., L.K., L.A.; AFM: S.S., F.B., C.N.; Transport measurements, device fabrication, and analysis: R.Z., R.B., I.G.D.-P., C.N., S.B.; Theory and simulation: M.R. and T.E.G.; Writing of the manuscript: M.R., T.E.G., C.N., N.H., with input from all co-authors. ‡These authors contributed equally.

## Funding Sources

We acknowledge financial support via HGF/DESY and DFG 773/8-1 (M.R.) and KI 1263/17-1 (L.K.). C.N. is Funded by Tertiary Education Trust Fund (TETFund) Abuja, Nigeria, through Nnamdi Azikiwe University, Awka, Nigeria under Academic Staff Training and Development Programme.

ACKNOWLEDGMENT

The authors thank Dirk Manske (MPI Stuttgart), Andrivo Rusydi (NUS), and Lance Cooper (UIUC) for productive discussions. We acknowledge the Siemens PLM Software for using Solid Edge 2020.

ABBREVIATIONS

AFM, atomic force microscopy; EFTEM, energy filtered TEM; FFT, fast Fourier transformation; SBP, Spin Berry Phase; SEM, scanning electron microscopy; SERS, surface enhanced Raman scattering; SS, surface states; TEM, transmission electron microscopy; HRTEM, high resolution TEM; TI, topological insulator.

REFERENCES

(1) Fu, L.; Kane, C. L.; Mele, E. J. Topological Insulators in Three Dimensions. *Phys. Rev. Lett.* **2007**, *98* (10), 106803. https://doi.org/10.1103/PhysRevLett.98.106803.

(2) Fu, L.; Kane, C. L. Topological Insulators with Inversion Symmetry. *Phys. Rev. B* **2007**, *76* (4), 045302. https://doi.org/10.1103/PhysRevB.76.045302.

(3) Qi, X.-L.; Zhang, S.-C. Topological Insulators and Superconductors. *Rev. Mod. Phys.* **2011**, *83* (4), 1057–1110. https://doi.org/10.1103/RevModPhys.83.1057.

(4) Eibl, O.; Nielsch, K.; Peranio, N.; Völklein, F. *Thermoelectric Bi2Te3 Nanomaterials*; Eibl, O., Nielsch, K., Peranio, N., Völklein, F., Eds.; Wiley-VCH Verlag GmbH & Co. KGaA: Weinheim, Germany, 2015. https://doi.org/10.1002/9783527672608.

(5) Dufouleur, J.; Veyrat, L.; Teichgraeber, A.; Neuhaus, S.; Nowka, C.; Hampel, S.; Cayssol, J.; Schumann, J.; Eichler, B.; Schmidt, O.; et al. Quasi-Ballistic Transport of Dirac Fermions in a Bi2Se3 Nanowire. *Phys. Rev. Lett.* **2012**, *110* (18), 186806. https://doi.org/10.1103/PhysRevLett.110.186806.

(6) Gooth, J.; Niemann, A. C.; Meng, T.; Grushin, A. G.; Landsteiner, K.; Gotsmann, B.; Menges, F.; Schmidt, M.; Shekhar, C.; Süß, V.; et al. Experimental Signatures of the Mixed

Axial–Gravitational Anomaly in the Weyl Semimetal NbP. *Nature* **2017**, *547* (7663), 324–327. https://doi.org/10.1038/nature23005.

(7) Peng, H.; Lai, K.; Kong, D.; Meister, S.; Chen, Y.; Qi, X.-L.; Zhang, S.-C.; Shen, Z.-X.; Cui, Y. Aharonov–Bohm Interference in Topological Insulator Nanoribbons. *Nat. Mater.* **2010**, *9* (3), 225–229. https://doi.org/10.1038/nmat2609.

(8) Kong, D.; Randel, J. C.; Peng, H.; Cha, J. J.; Meister, S.; Lai, K.; Chen, Y.; Shen, Z.-X.; Manoharan, H. C.; Cui, Y. Topological Insulator Nanowires and Nanoribbons. *Nano Lett.* **2010**, *10* (1), 329–333. https://doi.org/10.1021/nl903663a.

(9) Hong, S. S.; Zhang, Y.; Cha, J. J.; Qi, X.-L.; Cui, Y. One-Dimensional Helical Transport in Topological Insulator Nanowire Interferometers. *Nano Lett.* **2014**, *14* (5), 2815–2821. https://doi.org/10.1021/nl500822g.

(10) Zhang, K.; Pan, H.; Wei, Z.; Zhang, M.; Song, F.; Wang, X.; Zhang, R. Synthesis and Magnetotransport Properties of Bi2Te3 Nanowires. *Chinese Phys. B* **2017**, *26* (9), 096101. https://doi.org/10.1088/1674-1056/26/9/096101.

(11) Bardarson, J. H.; Brouwer, P. W.; Moore, J. E. Aharonov-Bohm Oscillations in Disordered Topological Insulator Nanowires. *Phys. Rev. Lett.* **2010**. https://doi.org/10.1103/PhysRevLett.105.156803.

(12) Iorio, P.; Perroni, C. A.; Cataudella, V. Plasmons in Topological Insulator Cylindrical Nanowires. *Phys. Rev. B* **2017**, *95* (23), 235420. https://doi.org/10.1103/PhysRevB.95.235420.

(13) Imura, K.-I.; Takane, Y.; Tanaka, A. Spin Berry Phase in Anisotropic Topological Insulators. *Phys. Rev. B* **2011**, *84* (19), 195406. https://doi.org/10.1103/PhysRevB.84.195406.

(14) Iorio, P.; Perroni, C. A.; Cataudella, V. Quantum Interference Effects in Bi2Se3 Topological Insulator Nanowires with Variable Cross-Section Lengths. *Eur. Phys. J. B* **2016**, *89* (4), 97. https://doi.org/10.1140/epjb/e2016-70041-7.

(15) Shi, L.-K.; Lou, W.-K. Surface States of Bi2Se3 Nanowires in the Presence of Perpendicular Magnetic Fields. *Chinese Phys. Lett.* **2014**, *31* (6), 067304. https://doi.org/10.1088/0256-307X/31/6/067304.

(16) Zhang, H.; Liu, C.-X.; Qi, X.-L.; Dai, X.; Fang, Z.; Zhang, S.-C. Topological Insulators in Bi2Se3, Bi2Te3 and Sb2Te3 with a Single Dirac Cone on the Surface. *Nat. Phys.* **2009**, *5* (6), 438–442. https://doi.org/10.1038/nphys1270.

(17) Fei, Z.; Andreev, G. O.; Bao, W.; Zhang, L. M.; McLeod, A. S.; Wang, C.; Stewart, M. K.; Zhao, Z.; Dominguez, G.; Thiemens, M.; et al. Infrared Nanoscopy of Dirac Plasmons at the Graphene–SiO2 Interface. *Nano Lett.* **2011**, *11* (11), 4701–4705. https://doi.org/10.1021/nl202362d.

(18) Lai, Y.-P.; Lin, I.-T.; Wu, K.-H.; Liu, J.-M. Plasmonics in Topological Insulators. *Nanomater. Nanotechnol.* **2014**, *4* (1), 13. https://doi.org/10.5772/58558.

(19) Autore, M.; Engelkamp, H.; D'Apuzzo, F.; Gaspare, A. Di; Pietro, P. Di; Vecchio, I. Lo; Brahlek, M.; Koirala, N.; Oh, S.; Lupi, S. Observation of Magnetoplasmons in Bi2Se3 Topological Insulator. *ACS Photonics* **2015**, *2* (9), 1231–1235.

https://doi.org/10.1021/acsphotonics.5b00036.

(20) Glinka, Y. D.; Babakiray, S.; Lederman, D. Plasmon-Enhanced Electron-Phonon Coupling in Dirac Surface States of the Thin-Film Topological Insulator Bi2Se3. *J. Appl. Phys.* **2015**, *118* (13), 135713. https://doi.org/10.1063/1.4932667.

(21) Shahil, K. M. F.; Hossain, M. Z.; Goyal, V.; Balandin, A. A. Micro-Raman Spectroscopy of Mechanically Exfoliated Few-Quintuple Layers of Bi2Te3, Bi2Se3, and Sb2Te3 Materials. *J. Appl. Phys.* **2012**, *111* (5), 054305. https://doi.org/10.1063/1.3690913.

(22) Eddrief, M.; Atkinson, P.; Etgens, V.; Jusserand, B. Low-Temperature Raman Fingerprints for Few-Quintuple Layer Topological Insulator Bi2Se3 Films Epitaxied on GaAs. *Nanotechnology* **2014**, *25* (24), 245701. https://doi.org/10.1088/0957-4484/25/24/245701.

(23) Zhang, J.; Peng, Z.; Soni, A.; Zhao, Y.; Xiong, Y.; Peng, B.; Wang, J.; Dresselhaus, M. S.; Xiong, Q. Raman Spectroscopy of Few-Quintuple Layer Topological Insulator Bi2Se3 Nanoplatelets. *Nano Lett.* **2011**, *11* (6), 2407–2414. https://doi.org/10.1021/nl200773n.

(24) Lee, S. J.; Guan, Z.; Xu, H.; Moskovits, M. Surface-Enhanced Raman Spectroscopy and Nanogeometry: The Plasmonic Origin of SERS. *J. Phys. Chem. C* **2007**, *111* (49), 17985–17988. https://doi.org/10.1021/jp077422g.

(25) Santoro, G.; Yu, S.; Schwartzkopf, M.; Zhang, P.; Koyiloth Vayalil, S.; Risch, J. F. H.; Rübhausen, M. A.; Hernández, M.; Domingo, C.; Roth, S. V. Silver Substrates for Surface Enhanced Raman Scattering: Correlation between Nanostructure and Raman Scattering Enhancement. *Appl. Phys. Lett.* **2014**, *104* (24), 243107. https://doi.org/10.1063/1.4884423.

(26) Schulz, B.; Bäckström, J.; Budelmann, D.; Maeser, R.; Rübhausen, M.; Klein, M. V.; Schoeffel, E.; Mihill, A.; Yoon, S. Fully Reflective Deep Ultraviolet to near Infrared Spectrometer and Entrance Optics for Resonance Raman Spectroscopy. *Rev. Sci. Instrum.* **2005**, *76* (7), 073107. https://doi.org/10.1063/1.1946985.

(27) Yan, Y.; Liao, Z.-M.; Zhou, Y.-B.; Wu, H.-C.; Bie, Y.-Q.; Chen, J.-J.; Meng, J.; Wu, X.-S.; Yu, D.-P. Synthesis and Quantum Transport Properties of Bi2Se3 Topological Insulator Nanostructures. *Sci. Rep.* **2013**, *3* (1), 1264. https://doi.org/10.1038/srep01264.

(28) Buchenau, S.; Akinsinde, L. O.; Zocher, M.; Rukser, D.; Schürmann, U.; Kienle, L.; Grimm-Lebsanft, B.; Rübhausen, M. Scalable Polyol Synthesis for Few Quintuple Layer Thin and Ultra High Aspect Ratio Bi2Se3 Structures. *Solid State Commun.* **2018**, *281*, 49–52. https://doi.org/10.1016/j.ssc.2018.07.003.

(29) Buchenau, S.; Sergelius, P.; Wiegand, C.; Bäßler, S.; Zierold, R.; Shin, H. S.; Rübhausen, M.; Gooth, J.; Nielsch, K. Symmetry Breaking of the Surface Mediated Quantum Hall Effect in Bi2Se3 Nanoplates Using Fe3O4 Substrates. *2D Mater.* **2017**, *4* (1), 015044. https://doi.org/10.1088/2053-1583/aa525e.

(30) Bäßler, S.; Hamdou, B.; Sergelius, P.; Michel, A.-K.; Zierold, R.; Reith, H.; Gooth, J.; Nielsch, K. One-Dimensional Edge Transport on the Surface of Cylindrical Bi x Te 3−y Se y Nanowires in Transverse Magnetic Fields. *Appl. Phys. Lett.* **2015**, *107* (18), 181602. https://doi.org/10.1063/1.4935244.

(31) Hamdou, B.; Gooth, J.; Dorn, A.; Pippel, E.; Nielsch, K. Aharonov-Bohm Oscillations and Weak Antilocalization in Topological Insulator Sb 2 Te 3 Nanowires. *Appl. Phys. Lett.*

**2013**, *102* (22), 223110. https://doi.org/10.1063/1.4809826.

(32) Richter, W.; Becker, C. R. A Raman and Far-Infrared Investigation of Phonons in the Rhombohedral V2–VI3 Compounds Bi2Te3, Bi2Se3, Sb2Te3 and Bi2(Te1−xSex)3 (0 <x < 1), (Bi1−ySby)2Te3 (0 <y < 1). *Phys. Status Solidi* **1977**, *84* (2), 619–628. https://doi.org/10.1002/pssb.2220840226.

(33) Bock, A.; Ostertun, S.; Das Sharma, R.; Rübhausen, M.; Subke, K.-O.; Rieck, C. T. Anomalous Self-Energy Effects of the B1g Phonon in Y1-x(Pr,Ca)XBa2Cu3O7 Films. *Phys. Rev. B* **1999**, *60* (5), 3532–3537. https://doi.org/10.1103/PhysRevB.60.3532.

(34) Chen, X. K.; Altendorf, E.; Irwin, J. C.; Liang, R.; Hardy, W. N. Oxygen-Concentration Dependence of the Raman Continua in YBa2Cu3Oy Single Crystals. *Phys. Rev. B* **1993**, *48* (14), 10530–10536. https://doi.org/10.1103/PhysRevB.48.10530.

(35) Friedl, B.; Thomsen, C.; Cardona, M. Determination of the Superconducting Gap in RBa2Cu3O7−δ. *Phys. Rev. Lett.* **1990**, *65* (7), 915–918. https://doi.org/10.1103/PhysRevLett.65.915.

(36) Cooper, S. L.; Klein, M. V. Light Scattering Studies of the Low Frequency Excitation Spectra of High Temperature Superconductors. *Comments Cond. Mat. Phys* **1990**, *15* (2), 99–124. https://doi.org/10.1007/978-3-662-04221-2_6.

(37) Bechstedt, F. *Many-Body Approach to Electronic Excitations - Concepts and Applications*; 2015. https://doi.org/10.1007/978-3-662-44593-8_19.

(38) Kawabata, A. Green Function Theory of Raman Scattering. *J. Phys. Soc. Japan* **1971**, *30*

(1), 68–85. https://doi.org/10.1143/JPSJ.30.68.

(39) Mattuck, R. D. *A Guide to Feynman Diagrams in the Many-Body Problem*; 1967.

Table of Contents:

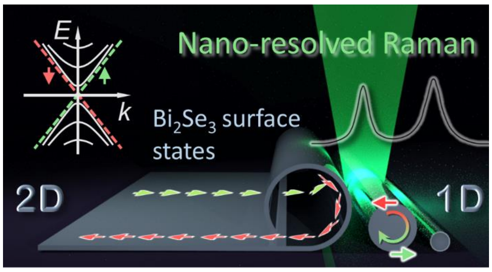

## 4.3 Plasmonic hot carrier injection into topological insulator $Bi_2Se_3$ nanoribbons

In this section, we present the result of our study on manipulating the electronic surface states of $Bi_2Se_3$ TI with a single AuNP and how the phonon modes in $Bi_2Se_3$ are used to locally probe the modified relativistic surface state of $Bi_2Se_3$. We will discuss the interplay between the resonantly excited plasmons in AuNP and the electronic surface states of single crystalline $Bi_2Se_3$ nanoribbons (NRs). In order to validate the quality of our samples, we will first present the characterization results.

### 4.3.1 AFM, SEM and EDX results

AFM is used to determine the thickness of the NRs. Fig. 4.12(a) shows an exemplary AFM image of the studied NR and one can clearly see a single AuNP attached to it. The profile through the NR (dashed blue line) shown in Fig. 4.12(c) shows that the thickness of the NR is 47 nm. SEM was used to determine the position of the attached AuNP and to further confirm the width of the NRs. Fig. 4.12(e - l) show SEM images of two different NRs and on each of them, different sizes of AuNPs were attached. EDX was conducted to determine the stoichiometry of the grown sample. Fig. 4.12(b) shows an exemplary spectra acquired from the NRs. This shows atm% of Bismuth and Selenium to be 39 and 61, respectively, which represent the correct stoichiometry i.e. $Bi : Se = 2 : 3$. The result of the polarization study which validates the crystallinity of the NRs is presented in "polarization dependence study" of Appendix D. Fig. 4.12(d) shows the TEM image and the average absorbance of the polydisperse AuNP used in this work. For more information on the synthesis and characterization of AuNP see [148].

### 4.3.2 Resonance Raman study on AuNP attached on nanoribbons

The spectra acquired from a single NR decorated with different sizes of AuNP at different excitation wavelengths is shown in Fig. 4.13. In Figs. 4.13(a - c) the NR is attached with a 108-nm AuNP , a 141-nm AuNP and Off_AuNP (i.e. bare NR). The spectra were corrected for the scattering and the spectra response of the instrument [113] and are fitted with the generalized Fano eqn. 4.12 (see section 2.3.3 for details)

$$I(\omega, T=0) = y + \frac{\bar{A}\bar{\Gamma}\omega}{(\bar{\Gamma}\omega)^2 + (\omega^2 - \bar{\omega}_0^2)^2}[\bar{q}^2 - 1 + 2\bar{q}\frac{(\omega^2 - \bar{\omega}_0^2)}{\bar{\Gamma}\omega}] \tag{4.12}$$

with

$$y = -T_{A^2}^2 \pi_{im} \tag{4.13}$$

$$\bar{A} = -T_{A^2}^2 g_1^2 \pi_{re}^2 \tag{4.14}$$

As previously, the two distinct phonon modes are assigned to $E_g^2$ and $A_{1g}^2$ symmetry. We mentioned earlier in section 4.1.3 that when tuning the excitation wavelength into the interband transitions of $Bi_2Se_3$, the Raman signals are enhanced. For the 100 nm thick NR studied, we found that tuning the excitation wavelength into resonance when measuring on the bare nanoribbon (from 532 nm to 633 nm), the Raman signal of $E_g^2$ and $A_{1g}^2$ modes (red symbols) increases by a factor of 11 and 20 respectively (Fig. 4.13(d)).

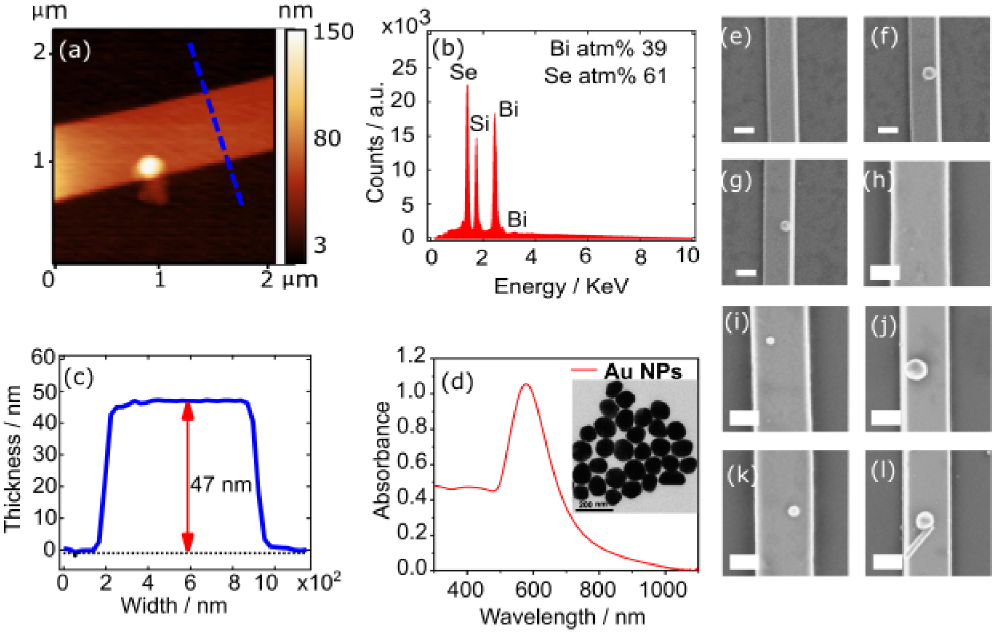

Figure 4.12: (a) An exemplary AFM image of $Bi_2Se_3$ nanoribbon with attached AuNP. (c) The profile from the blue dashed line (in (a)) shows the thickness of 47 nm. (b) An exemplary EDX spectra from na single $Bi_2Se_3$ nanoribbon showing correct stoichiometry. The Silicon peak emanated from the Si substrate. (d) Absorbance of AuNPs as a function of wavelength. The inset is the TEM image of the AuNPs. (e-l) show the SEM images of two $Bi_2Se_3$ nanoribbons decorated with different sizes of AuNPs. Each scale bar represents a length of 200 nm. (Adapted with permission from [118]).

Again, tuning the excitation wavelength into resonance when measuring on the 141-nm AuNP, the Raman signal is increased by a factor of 40 and 98 for $E_g^2$ and $A_{1g}^2$ modes (black symbols), respectively. This enhancement is attributed to hot carrier injection into the $Bi_2Se_3$ TI. Weinhold *et al.* observed a similar behaviour in graphene [8]. Interestingly, tuning the excitation wavelength into resonance when measuring on the 108-nm AuNP, the Raman signal is increased by a factor of more than 160 and 350 for $E_g^2$ and $A_{1g}^2$ modes (blue symbols), respectively. This strongly enhanced Raman signal in 108-nm AuNP is explained as the excitation wavelength (633 nm) and is in resonance range to the surface plasmon energy of 108-nm AuNP [149] [150] [151]. The results show that the presence of AuNP on the $Bi_2Se_3$ TI surface enhances the Raman signal and opens the opportunity to control the local electronic properties of the TI by different sizes of AuNP [118].

### 4.3.3 Scan related hot carrier injection into the surface states of topological insulator

Fig. 4.14(a) shows the Raman spectra acquired when scanning along a 76.3 nm NR decorated with a single 120 nm AuNP. The scan direction (white arrow) and polarization of the laser light (red arrow) is shown by the SEM image of Fig. 4.14(e). The spectra were fitted with eqn. 4.12. We scanned from +900 nm to −900 nm with the AuNP at position 0 nm and we reveal the strongest Raman susceptibility enhancement when measuring at the On_AuNP position. We obtained susceptibility enhancement factors of 19, 18 and 41 for $A_{1g}^1$, $E_g^2$, $A_{1g}^2$, respectively Fig. 4.14(d). The normalized frequency as a function of the

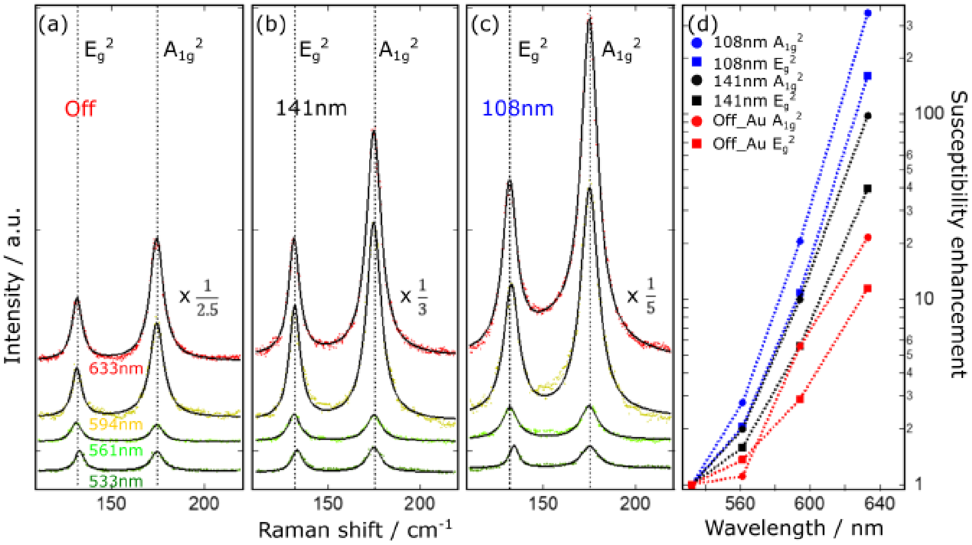

Figure 4.13: Resonance Raman spectra of a single $Bi_2Se_3$ nanoribbon with different sizes of AuNPs (a) Off_AuNP (bare TI), (b) 141-nm AuNP and (c) 108-nm AuNP. The Raman spectra taken with 633, 594, 561 and 532 excitation wavelengths are shown in red, yellow, light green, and green, respectively. The data obtained form 633 nm wavelength of Off_AuNP, 141-nm and 108-nm is scaled down by 2.5, 3, and 5, respectively. The dotted vertical lines represent $A_{1g}^2$ and $E_g^2$ phonon modes. (d) Phonon susceptibility as a function of wavelengths. The $A_{1g}^2$ and $E_g^2$ phonon modes are represented with square and circle markers, respectively while the blue, black, and red symbols represent 108-nm AuNP, 141-nm AuNP and Off_AuNP positions, respectively. (Figure adapted with permission from [118]).

distance from the AuNP is shown in Fig. 4.14(b). The frequency was normalized to the value at the position 0 nm (On_AuNP position). The result shows that the frequencies of $A_{1g}^1$ and $A_{1g}^2$ are sensitive to the position of the AuNP and are strongly renormalized when scanning across the AuNP. The scan related normalization of the phonon modes has been observed in graphene and attributed to the coupling of the optical modes with hot electrons transferred from resonantly excited AuNPs plasmons [8]. Furthermore, we observed the broadening (decrease of the phonon lifetime) of the normalized full width at half maximum (FWHM) as we scanned across the AuNP (Fig. 4.14(c)). This broadening of the three phonon modes has been reported in $Bi_2Se_3$ NFs and attributed to strong electron-phonon coupling [129]. We reveal that the Fano parameter $\bar{q}$ has a lower value when measuring at the On_AuNP position than at the Off_AuNP position Fig. 4.14(f). $\bar{q}$ implies the interference between discrete phonon states and low-energy electronic degrees of freedom [130] [118]. The smaller the $\bar{q}$ the stronger the effective interference between electrons and phonons due to an increased contribution of the imaginary part of the electronics susceptibility [118]. The lower value of $\bar{q}$ at the On_AuNP position indicates that the electron-phonon interaction is strong.

### 4.3.4 Gold nanoparticle size dependent Raman study

Fig. 4.15(a) shows the Raman spectra acquired from 90 nm thick NR decorated with 39, 50, 120 and 147 nm size AuNPs. The spectra were fitted with eqn. 4.12. The distinct phonon modes are the $A_{1g}^1$, $E_g^2$ and $A_{1g}^2$ symmetry as previously assigned. We

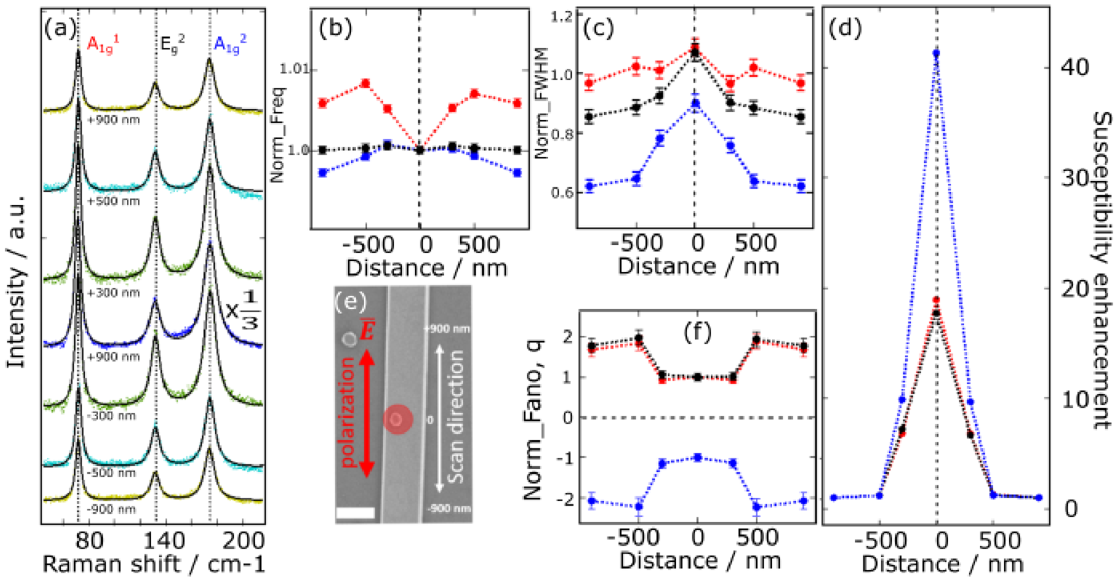

Figure 4.14: Raman studies of a single $Bi_2Se_3$ nanoribbon in the vicinity of AuNP. (a) Raman spectra acquired from 76.3 nm thick nanoribbon of width 400 nm and decorated with a single AuNP of size 120 nm. The spectra were acquired when scanning across the AuNP from +900 nm to -900 nm (The AuNP is at position 0nm). The dotted vertical lines represent the position of the phonon modes. (b) Normalized frequency, (c) Normalized FWHM, (d) Susceptibility enhancement and (f) Normalized Fano parameter, $\bar{q}$ as a function of distance from AuNP. All data normalized to the value at On-AuNP position. (e) SEM image of the studied nanoribbon with the AuNP attached to the surface. The red and white arrows represent the polarization of the incident laser and scan direction, respectively. (Figure taken with permission from [118]).

observe renormalization of the $A_{1g}^2$ mode mostly in 39 nm and 50 nm AuNPs as shown in Fig. 4.15(b). The observed hardening of the $A_{1g}^2$ mode originates from the interaction of the phonon modes with the real part of the low energy electronics susceptibility of the hot carriers from plasmonic AuNPs [118]. Renormalization of phonon modes in periodic arrays of nanoribbons of $Bi_2Se_3$ has been observed previously [152] [153]. Fig. 4.15(c) shows the normalized Fano parameter $\bar{q}$ as a function of AuNP size. We stated earlier that $\bar{q}$ measures the interference between the phonon states and electronic degrees of freedom and this results in an asymmetric Fano profile that is dependent on AuNP size. Our result shows no noticeable dependence of FWHM on the AuNP size as shown in Fig. 4.15(d).

### 4.3.5 Plasmonic decay and hot carrier injection

Raman intensity enhancement, phonon renormalization and peak broadening in the distinct phonon modes observed in our results can be explained in the scheme, Fig. 4.16. Metal/TI interface is associated with a band bending region as a result of carrier injection [95]. This region has a dimension of about 3 - 5 nm and it is obscured by the AuNP (blue shaded area) Fig. 4.16(a). Photon irradiation on the AuNP generates excitation of collective free carrier oscillations at the surface of AuNP (i.e. surface plasmons). The excited plasmons in resonance with the incident light field leads to a confinement of the incident light field [154] [118]. The resonantly excited plasmons decay non-radiatively by generation of hot carriers as shown in Fig. 4.16(c). The surface states conduction band

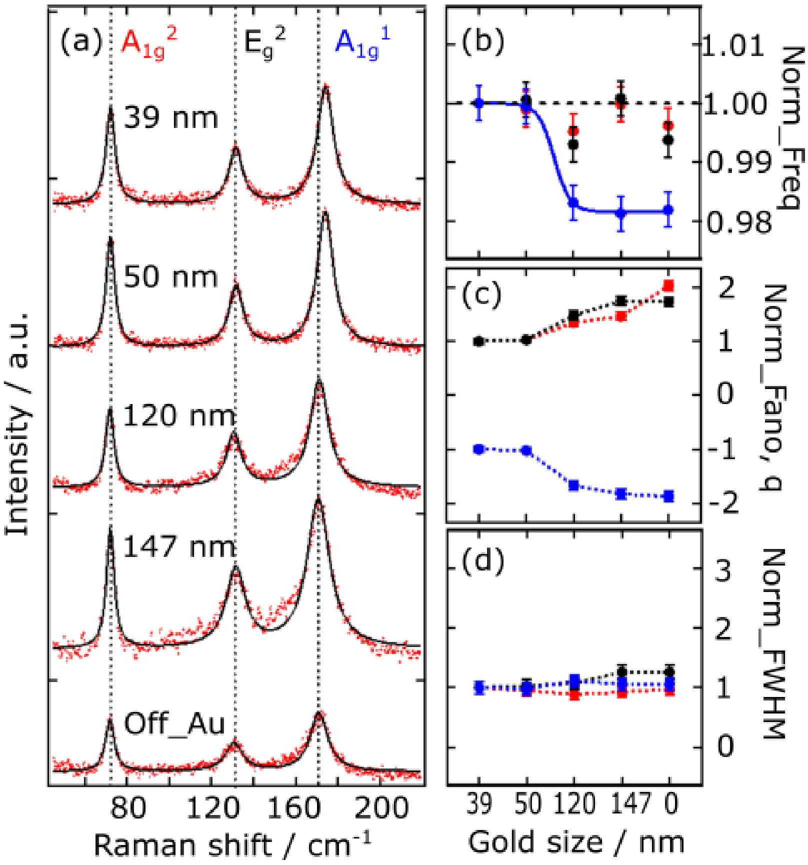

Figure 4.15: Raman studies of a single $Bi_2Se_3$ decorated with different sizes of AuNPs. (a) Raman spectra acquired from 90.1 nm thick nanoribbon of width 292 nm and decorated with four different AuNPs of sizes 39, 50, 120, and 147 nm. The dotted vertical lines represent the phonon mods of the bare TI. (b) Frequency, (c) Fano parameter, (d) FWHM as a function of AuNP diameter. All normalized to the value at 39 nm position. (Figure taken with permission from [118]).

(CB) and valence band (VB) are represented by the black linear dispersion lines whereas the grey parabolic curves represent the bulk. The dotted red horizontal line represents the Fermi energy of the bare TI and the blue curve at the bottom of the surface state CB represents the hot electrons injected from the resonantly decayed surface plasmons into the upper dirac cone. Detailed reports on the injection of hot electrons from resonantly decayed plasmons into the CBs of semiconductors can be found in ref. [155] [156] [157]. From the diagram, one can see that low energy phonons cannot interfere with the bulk electrons provided that the Fermi surface lies between the bulk CB and VB. However, low-energy phonons can interact with the quasi-relativistic electrons that populate the surface state of the TI. Fig. 4.16(b) shows the $\bar{q}$ as a function of the wavelength measured at bare TI and On-AuNP positions. The blue, black and red symbols represent the $\bar{q}$ when measuring on the 108-AuNP, 141-AuNP and bare TI, respectively. Our results show that the $\bar{q}$ has no significant dependence when measuring on bare TI, whereas measuring on 108-nm AuNP and 141-nm AuNP the $\bar{q}$ shows a dependence on excitation wavelength. $\bar{q}$ measures the interaction between electronic susceptibility and phonon. The fact that $\bar{q}$ is constant in bare TI and strongly wavelength dependent on AuNP positions, supports a hot carrier injection mechanism [118]. Therefore the scheme in Fig. 4.16(c) supports our observations. Recall that when measuring on 108-nm AuNP, we observed strong signal enhancement by a factor of 350. This can be explained as double-resonance behaviour. The band structure calculations for Bi$_2$Se$_3$ show that Bi$_2$Se$_3$ has interband transition energy of 2.0 eV [124] [45]. The 633 nm excitation wavelength (1.96 eV) that generated the surface plasmons in the 108-nm AuNP is simultaneously in resonance with the plasmon frequency of the 108-nm AuNP and also in resonance with the interband transition in Bi$_2$Se$_3$ [118]. This double resonance enhances the hot carrier transfer and consequently the Raman matrix element.

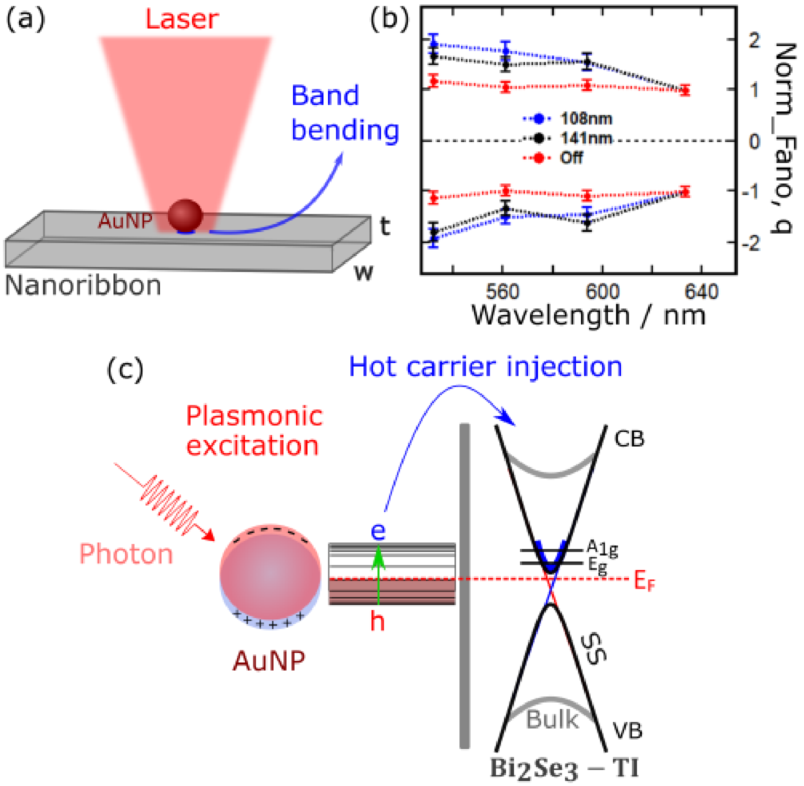

Figure 4.16: Schematic illustration of plasmon decay and hot electron injection. (a) TI nanoribbon decorates with AuNP. The blue area is the band bending region (this region is about 3n m and it is covered by the laser spot). (b) Fano parameter, $\bar{q}$ as a function of wavelength for the bare TI (red symbol), 141-nm AuNP (black symbol) and 108-nm AuNP (blue symbol) position. All normalized to the value at 633 nm wavelength. (c) Schematic representation of hot carrier in TI. The decayed plasmon injects electrons into the surface states Dirac cone(blue parabola). The grey parabola and the black linear dispersion are the bulk and surface electronic bands. The red dotted horizontal line is the Fermi energy of the bare TI. CB and VB are the conduction band and the valence band. (Figure taken with permission from [118]).

# Publication 2:
# Plasmonic Hot Carrier Injection from Single Gold Nanoparticles into Topological Insulator $Bi_2Se_3$ Nanoribbons

Christian Nweze, Tomke E. Glier, Mika Rerrer, Sarah Scheitz, Yalan Huang, Robert Zierold, Robert Blick, Wolfgang J. Parak, Nils Huse, and Michael Rübhausen.

RSC: Nanoscale - November 2022
DOI https://doi.org/10.1039/D2NR05212A

Reprinted with permission from C. Nweze, T. E. Glier, M. Rerrer, S. Scheitz, Y. Huang, R. Zierold, R. Blick, W. J. Parak, N. Huse and M. Rübhausen, Nanoscale, 2022, Advance Article , DOI: 10.1039/D2NR05212A.

Nanoscale

ROYAL SOCIETY OF CHEMISTRY

PAPER

View Article Online
View Journal

Check for updates

**Cite this:** DOI: 10.1039/d2nr05212a

# Plasmonic hot carrier injection from single gold nanoparticles into topological insulator $Bi_2Se_3$ nanoribbons†

Christian Nweze, *[a] Tomke E. Glier, [a] Mika Rerrer,[a] Sarah Scheitz,[a]
Yalan Huang,[b] Robert Zierold, [b] Robert Blick,[b] Wolfgang J. Parak, [b]
Nils Huse [b] and Michael Rübhausen*[a]

Received 21st September 2022,
Accepted 14th November 2022

DOI: 10.1039/d2nr05212a

rsc.li/nanoscale

Plasmonic gold nanoparticles injecting hot carriers into the topological insulator (TI) interface of $Bi_2Se_3$ nanoribbons are studied by resonant Raman spectroscopy. We resolve the impact of individual gold particles with sizes ranging from 140 nm down to less than 40 nm on the topological surface states of the nanoribbons. In resonance at 1.96 eV (633 nm), we find distinct phonon renormalization in the $E_g{}^2$- and $A_{1g}{}^2$-modes that can be associated with plasmonic hot carrier injection. The phonon modes are strongly enhanced by a factor of 350 when tuning the excitation wavelengths into interband transition and in resonance with the surface plasmon of gold nanoparticles. At 633 nm wavelength, a plasmonic enhancement factor of 18 is observed indicating a contribution of hot carriers injected from the gold nanoparticles into the TI interface. Raman studies as a function of gold nanoparticle size reveal the strongest hot carrier injection for particles with size of 108 nm in agreement with the resonance energy of its surface plasmon. Hot carrier injection opens the opportunity to locally control the electronic properties of the TI by metal nanoparticles attached to the surface of nanoribbons.

## Introduction

Topological insulators (TIs) are a new set of quantum materials with conducting surface states and an insulating bulk.[1] The surface states of TIs have gapless electronic states that are protected by time reversal symmetry.[2–4] These surface states host quasi-relativistic electrons[2,5] and are immune to backscattering by nonmagnetic impurities due to strong spin–orbit coupling.[2,6] TIs with their spin-textured surface states find applications in quantum computing, spintronics, photonics, fibre lasers, and optoelectronic devices.[7–10] Bismuth selenide ($Bi_2Se_3$) is considered an ideal candidate for realizing intriguing phenomena associated with TIs due to its surface state band structure of Dirac-like linear dispersion with a bulk energy band gap of about 0.3 eV, which is significantly larger than the room temperature energy scale of around 25 meV.[6,11] Moreover, the Dirac point of $Bi_2Se_3$ is supposed to be within the bulk bandgap and not buried in the bulk bands as in bismuth telluride ($Bi_2Te_3$) and antimony telluride ($Sb_2Te_3$). Device applications requiring Dirac materials demand detailed understanding of the role of contacts and carrier injection in controlling their relativistic surface states.[8,12] The interface between the conducting surface states of $Bi_2Se_3$ and metals has been theoretically studied.[13,14] Most of these theories are concerned with the generation of hot plasmonic carriers and their injection into the semiconductors interface and molecular surfaces.[15,16] Remarkably, contacting the surface of $Bi_2Se_3$ with gold thin films does not destroy the spin-momentum locking in $Bi_2Se_3$.[13] Gold nanoparticles (AuNPs) have a large number of delocalized electrons, which can interact with electromagnetic fields to generate surface plasmons[17] which exhibit a large absorption cross section that has been exploited to enhance and trap light.[15] The resonantly excited surface plasmons change the optical properties of AuNPs drastically and can decay non-radiatively into hot electron–hole pairs.[12,18] In graphene-based devices, hot electron–hole pairs increase local electron densities and generate photocurrents.[19,20] The local manipulation of relativistic quantum states of nanostructures with AuNPs is an emerging research field[8,21,22] and in this fashion, the surface states of $Bi_2Se_3$ can be engineered

---

[a] *Institut für Nanostruktur- und Festkörperphysik, Centre for Free Electron Laser Science (CFEL), Universität Hamburg, Luruper Chaussee 149, 22761 Hamburg, Germany. E-mail: cnweze@physnet.uni-hamburg.de, mruebhau@physnet.uni-hamburg.de*

[b] *Institut für Nanostruktur- und Festkörperphysik, Centre for Hybrid Nanostructures (CHyN), Universität Hamburg, Luruper Chaussee 149, 22761 Hamburg, Germany*

† Electronic supplementary information (ESI) available: Additional information on the $Bi_2Se_3$ nanoribbon synthesis and Au nanoparticle synthesis, transfer of ribbons, drop casting of AuNPs, AFM, EDX, and SEM image, polarization dependence study. See DOI: **https://doi.org/10.1039/d2nr05212a**

into future device requirements by locally manipulating the electronic band structure in nanostructures.[23] The hot photoinjected electrons interact with the relativistic quantum states of TIs and couple to the surface phonon modes.[15] Micro-Raman spectroscopy with a high local resolution of about 200 nm enables the investigation of the local electronic properties by probing the phonons on sample scales of less than 400 nm. Furthermore, controlling the interaction of the surface states with hot photoinjected electrons by means of an electromagnetic field opens the opportunity to control the local electronic properties of TIs optically. Spatially resolved micro-Raman spectroscopy is as an excellent tool for simultaneously studying the generation of electron–hole pairs and detection of the corresponding electron–phonon interaction.[12]

In this work, we probe the local area around AuNPs which are not easily accessible in the electrical transport measurement. We locally manipulate the electronic structure of 1D nanostructures (nanoribbons) of $Bi_2Se_3$ with single AuNPs and use the phonon modes in $Bi_2Se_3$ as local probes of the modified relativistic surface state. The interplay between the electronic surface states of a single crystalline $Bi_2Se_3$ nanoribbon and resonantly excited plasmons in a AuNP is studied by micro-Raman spectroscopy with spatial resolution of 211 nm (see Fig. S7 in the ESI(F)† for details). Different sizes of AuNPs on the same $Bi_2Se_3$ nanoribbon were employed to locally manipulate the electronic band structure. We scan across single AuNPs deposited on a $Bi_2Se_3$ nanoribbon in order to determine the changes in electron–phonon interactions as a function of distance from the respective AuNP and reveal the phonon self-energy effect due to electrons injected into the relativistic surface state.

## Results and discussion

$Bi_2Se_3$ with its layered, rhombohedral crystal structure belongs to the space group ($R\bar{3}m/D_{3d}^5$).[6,24–26] Its structure consists of five atomic layers, Se–Bi–Se–Bi–Se, that are covalently stacked along its *c*-axis to form a quintuple layer with a thickness of ∼1 nm. The unit cell of $Bi_2Se_3$ contains three quintuple layers and each quintuple layer is bound to neighbouring quintuple layers by van der Waals forces. Group theory predicts the five atoms in the primitive cell of $Bi_2Se_3$ to have 15 zone-centre phonon branches, 3 acoustic and 12 optical phonon modes. Of the 12 optical modes, 4 are symmetry Raman-active ($2A_{1g}$, $2E_g$) and 4 are symmetry infrared-active ($2A_{1u}$, $2E_u$). The irreducible representations for the zone-centre phonon can be written as: $\Gamma = 2E_g + 2A_{1g} + 2E_u + 2A_{1u}$ [1].[25] The Raman tensors and their corresponding atomic displacements of the Raman-active modes in $Bi_2Se_3$ are shown in Fig. S6 (in the ESI(E)).† The correct stoichiometry (2 : 3 (Bi : Se)) of the nanoribbons is confirmed by SEM-EDX (see Fig. S4 in the ESI(D)†). SEM and AFM studies shown in the inset (Fig. 1 and 3) and the ESI† support the reported width and thickness of the nanoribbons, respectively (Fig. S5 in the ESI(D)†).

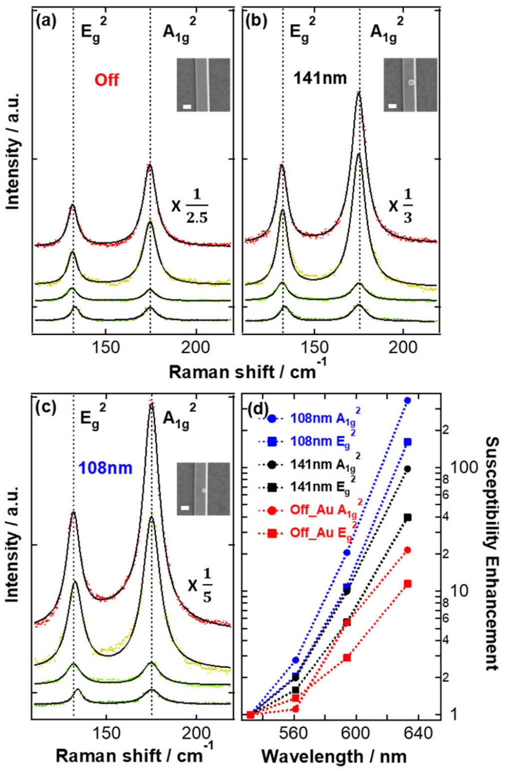

**Fig. 1** Resonance Raman spectra of a single $Bi_2Se_3$ nanoribbon with a thickness of 100 nm and width of 210 nm decorated with gold nanoparticles (AuNPs) of the following diameters: (a) Off_AuNP, *i.e.* spectrum recorded far away from any AuNP, (b) 141 nm, and (c) 108 nm. The Raman spectra taken with 633, 594, 561, and 533 nm are shown in red, yellow, light green, and green, respectively. The solid black line represents the fit to the data and the dashed vertical lines represent the positions of the respective $E_g^2$ and $A_{1g}^2$-modes in the $Bi_2Se_3$ nanoribbon taken with 633 nm. The data obtained for 633 nm excitation of the 108 nm AuNP, the 141 nm AuNP, and Off_AuNPs is divided by 5, 3 and 2.5, respectively, as indicated in panels (a–c). The insets in panels (a–c) show the SEM images of the studied sample area. Each scale bar represents a length of 200 nm (d) Phonon susceptibilities as a function of excitation wavelengths normalized to the phonon susceptibility at 532 nm. The blue, black, and red markers correspond to the measurements on 108 nm AuNP, 141 nm AuNP, and Off_AuNP respectively. Square and circle markers correspond to $E_g^2$ and $A_{1g}^2$-modes, respectively.

The in- and off-resonance study of a single $Bi_2Se_3$ nanoribbon decorated with AuNPs is shown in Fig. 1. Fig. 1(a–c) shows the Raman spectra of a single $Bi_2Se_3$ nanoribbon decorated with a 108 nm AuNP, a 141 nm AuNP, and Off_AuNP in the laser focus (=Off_AuNP, *i.e.* spectrum recorded far away from any AuNP) at different excitation wavelengths. We can assign the two distinct phonon modes to $E_g^2$ and $A_{1g}^2$ symmetry[27–29] and the assignment is supported by the Raman tensor in Fig. S6(a) (ESI)† as well as the polarization-dependent data in Fig. S8 (ESI†). The spectra were fitted with eqn (1) ("Generalized Fano equation").[30]

$$I(\omega,\, T=0) \propto y + \frac{\bar{A}\bar{\Gamma}\omega}{(\bar{\Gamma}\omega)^2 + (\omega^2 - \bar{\omega}_0{}^2)^2}\left[\bar{q}^2 - 1 + 2\bar{q}\frac{(\omega^2 - \bar{\omega}_0{}^2)}{\bar{\Gamma}\omega}\right] \tag{1}$$

with

$$y = -T_{A^2}{}^2 \pi_{\mathrm{im}}$$

$$\bar{A} = -T_{A^2}{}^2 g^2 \pi_{\mathrm{re}}{}^2$$

where $\bar{A}$, $y$, $\bar{q}$, $\omega_0$, $\bar{\Gamma}$, $g$ and $T$ represent the amplitude, electronics background, ratio between imaginary and real parts of the electronic susceptibility, frequency, width of phonon line, electron–phonon coupling, and electron–photon coupling, respectively. $\pi_{\mathrm{im}}$ and $\pi_{\mathrm{re}}$ are the imaginary and real part of electronic susceptibility while $A^2$ is the non-resonant matrix element.[53] All data were corrected for the scattering volume and the spectral response of the instrument.[31] Fig. 1(d) shows the relative phonon susceptibilities of 108 nm AuNP, 141 nm AuNP, and Off_AuNP as a function of the excitation wavelength $\lambda$. The phonon susceptibilities were normalized to the susceptibility at 532 nm wavelength. The circle and square markers correspond to the $A_{1g}{}^2$ and the $E_g{}^2$ mode, respectively. As we tune the excitation wavelength into resonance of the nanoribbon (from 532 nm to 633 nm), the Raman signal increases by a factor of 20 for the $A_{1g}{}^2$ mode and a factor of 11 for the $E_g{}^2$ mode (red symbols) in the Off_Au position. This resonance has been reported previously and it is attributed to interband transitions in $Bi_2Se_3$.[26,32–34] We observe that tuning the excitation wavelength into resonance when measuring on the 141 nm AuNP results in a further increase in the Raman signal by a factor of 98 for $A_{1g}{}^2$ mode and a factor of 40 for the $E_g{}^2$ mode (black symbols). We attribute the enhancement of the Raman signal to the hot carrier injection into the $Bi_2Se_3$ TI. Our reference measurements on silicon substrate decorated with AuNPs support our attribute (see Fig. S10 in the ESI(I)†). A similar behaviour has been observed in graphene.[12] Surprisingly, measuring on 108 nm AuNP results in a signal enhancement factor of more than 350 for the $A_{1g}{}^2$ mode and a factor of 160 for the $E_g{}^2$ mode (blue symbol). The plasmonic enhancement factor at 633 nm excitation wavelength on 141 nm and 108 nm AuNP is 5 and 18 for $A_{1g}{}^2$ mode, respectively and the corresponding plasmonic enhancement factor for $E_g{}^2$ mode is 3.6 and 15, respectively. Note that without the capping layer on AuNP, we would expect stronger hot carrier injection.[54,55] The Raman spectra in Fig. 1 were measured on the same $Bi_2Se_3$ nanoribbon with the differently sized AuNPs spaced more than 2.2 μm apart from each other. Hot carriers are efficiently excited when the localized surface plasmon (LSP) of AuNP is in resonance with the excitation wavelength.[35] By means of Landau damping, the excited hot carriers decay non-radiatively into hot electron–hole pairs.[36] Note that non-radiative decay can occur either through intraband excitations within the sp (conduction) band above the Fermi level or through interband transition from d-band to s-band.[37,38] The density of generated hot carriers and excitation rate in metallic surface plasmons was theoretically studied by Paudel *et al.*[14] and it was observed that the density of the generated hot carriers scales with the square of the excitation rate.[14] The data in Fig. 1 reveals the strongest hot carrier injection into the $Bi_2Se_3$ nanoribbon by 108 nm AuNP which can be explained by the resonance energy of its surface plasmon in the red wavelength range.[39–41] We show that the presence of AuNPs, more especially AuNP whose LSP is in resonance with the excitation wavelength, on $Bi_2Se_3$ strongly enhances the Raman signal and thus opens an opportunity to control the local electronic properties of the TI by different sizes of AuNP. Furthermore, we conducted measurements in the vicinity of an AuNP with 633 nm excitation wavelength as shown in Fig. 2. We scanned across a single AuNP on a $Bi_2Se_3$ nanoribbon from −900 to +900 nm with the AuNP at 0 nm (Fig. 2(b)).

Fig. 2(a) shows the Raman spectra while moving the focus of the laser beam away from the AuNP, *i.e.* scanning along the nanoribbon. We can assign the three distinct phonon modes to $A_{1g}{}^1$, $E_g{}^2$, and $A_{1g}{}^2$ symmetry. All three modes show strong characteristic enhancements in the vicinity of the AuNP and the enhancement decays when moving the focus of the laser beam away from the AuNP. Fig. 2(b) shows the SEM image of the measured sample. The scan direction is depicted by the white double-headed arrow. The polarization of the laser is along the long axis of the $Bi_2Se_3$ nanoribbon as shown by the double-headed red arrow. The phonon modes were fitted with the generalized Fano line shape described by eqn (1). Fig. 2(c) displays the normalized Fano parameter, $\bar{q}$ as a function of distance from the AuNP. The Fano parameter $\bar{q}$ implies the interference between discrete phonon states and low-energy electronic degrees of freedom.[42] The smaller the $\bar{q}$, the stronger the effective interference between electrons and phonons due to an increased contribution of the imaginary part of the electronics susceptibility. We reveal that $\bar{q}$ is smaller for On_Au position than Off_Au position. This indicates that the electron–phonon interaction is much stronger when measuring at the On_Au position than measuring at the Off_Au position. Fig. 2(d) shows the normalized full width at half maximum (FWHM) as a function of the distance from the AuNP. We observe broadening of the three phonon modes as we scan towards the AuNP due to high density of hot electrons, in the vicinity of AuNP, which interact with the phonons. The density of the hot carriers injected into the $Bi_2Se_3$ TI at the AuNP/TI interface decreases with the distance from the AuNP. This is corroborated by the small value of Fano parameter $\bar{q}$ for On_Au position and the ratio between the FWHM of $A_{1g}{}^2/A_{1g}{}^1$ ($E_g{}^2/A_{1g}{}^1$) mode that increases from 1.77 (1.60) to 2.28 (1.83) at the AuNP position (see Fig. S9 in the ESI(H)†). Such a decrease of the phonon lifetime (peak broadening) of the $Bi_2Se_3$ modes has been observed previously and attributed to a strong electron–phonon coupling.[6] Our observation of high density of hot electrons near the AuNP and a reduced one away from AuNP is supported by the theoretical study of carrier distribution on

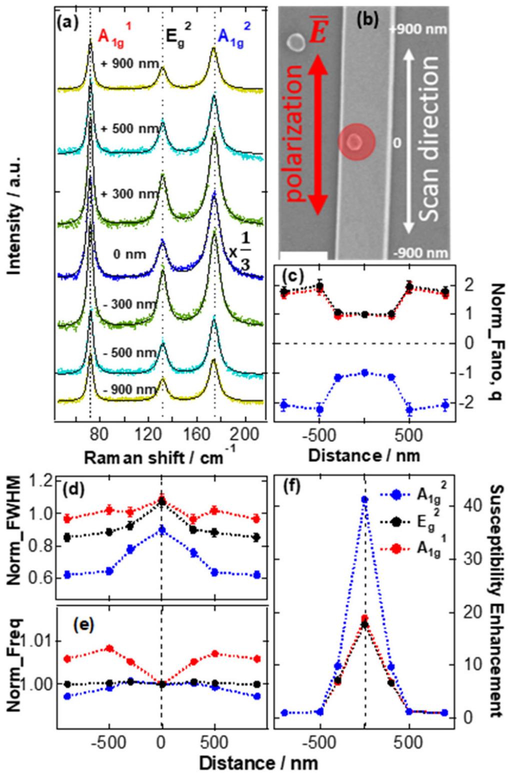

Fig. 2 Raman studies of single $Bi_2Se_3$ nanoribbon in the vicinity of AuNP with 633 nm excitation wavelength. (a) Raman spectra of $Bi_2Se_3$ nanoribbon of thickness 76.3 nm and width 400 nm and decorated with a single 120 nm AuNP. The spectra were collected scanning across the nanoribbon in different distance to the AuNP from −900 to +900 nm as shown in (a). The black vertical dashed lines represent the positions of $A_{1g}^1$, $E_g^2$ and $A_{1g}^2$ modes of the bare nanoribbon. The data obtained at the AuNP position is divided by 3 as indicated in the panel (a). (b) SEM image of the studied nanoribbon with the AuNP. The red and white arrows represent the polarization of the laser and the scan direction. (c) Fano parameter, $\tilde{q}$, (d) Norm_FWHM (normalized full width at half maximum), (e) Norm_Freq (normalized frequency) and (f) susceptibility enhancement as a function of the distance from the AuNP. All normalized to the value at the On_AuNP (0 nm) position. The vertical and horizontal dashed lines represent guide to the eye.

the surface of the $Bi_2Se_3$ TI at different length scales after the hot carrier injection by Paudel *et al.*[14] Furthermore, we observe phonon renormalization of the $A_{1g}^1$ and $A_{1g}^2$ modes when scanning across the AuNP (Fig. 2(e)). The scan-related renormalization of the phonon modes has been observed in graphene and attributed to the coupling of the optical phonon modes at specific wave vectors with hot electrons transferred upon resonant excitation of AuNPs plasmons.[12] Fig. 2(f) reveals the Raman susceptibility enhancement when scanning across the AuNP. The Raman susceptibility enhancement factor of 19, 18, and 41, for $A_{1g}^1$, $E_g^2$, and $A_{1g}^2$ modes, respectively, is obtained when measuring at the On_AuNP position. In short, the observed Raman susceptibility enhancement shows that the presence of AuNPs enhances the Raman scattering by injection of hot electrons from the AuNP into $Bi_2Se_3$.

In Fig. 3 we present the study of four different sizes of AuNPs on a single $Bi_2Se_3$ nanoribbon. The Raman spectra are shown in Fig. 3(a). The insets are the SEM images of 39, 50, 120, and 147 nm size AuNPs and each scale bar represents a length of 100 nm. The spectra were fitted with the generalized Fano eqn (1). Line shape analysis of the Raman spectra reveals an asymmetric Fano profile depending on the diameter of the AuNP (Fig. 3(b)). We like to recall that the Fano parameter $\tilde{q}$ measures the interference between the phonon states and electronic degrees of freedom. We further observe a hardening of the $A_{1g}^2$ mode mostly in 39 and 50 nm AuNPs (Fig. 3(c)) as indicated by the blue shift in this mode. The frequency shift originates from the interaction of phonon mode with the real part of the low energy electronic susceptibility of the injected hot carriers from plasmonic AuNPs. The mutual interaction of plasmons with phonons leads to phonon renormalization. This renormalization of phonon modes is the result of interactions of the phonons with surface plasmon polaritons.

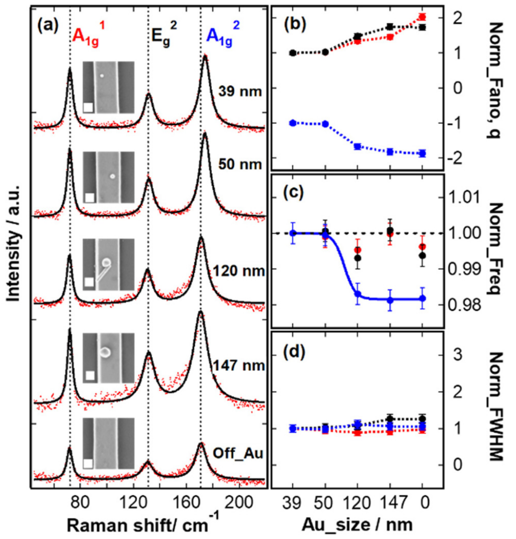

Fig. 3 Raman studies of a single $Bi_2Se_3$ nanoribbon decorated with AuNPs of different sizes. (a) Raman spectra of a $Bi_2Se_3$ nanoribbon with thickness of 90.1 nm and width of 292 nm and decorated with four different AuNPs of sizes 39, 50, 120, and 147 nm. The insets in (a) show the SEM images. Each scale bar represents a length of 100 nm. The black vertical dashed lines indicate the positions of $A_{1g}^1$, $E_g^2$ and $A_{1g}^2$ modes without AuNPs present. (b) Fano parameter $\tilde{q}$ (c) Frequency and (d) FWHM as a function of the AuNP diameter. All plotted line-width parameters are normalized to the value of the 39 nm AuNP. The horizontal dashed line represents a guide to the eye.

Similar effects have been reported previously in the periodic arrays of ribbons of $Bi_2Se_3$.[43,44] In Fig. 3(d), we show the normalized FWHM as a function of the diameter of AuNPs. Our result shows no noticeable dependence of FWHM on the size of AuNPs.

## Plasmonic decay and hot electron transfer

Fig. 4a shows the schematic illustration of the measured $Bi_2Se_3$ nanoribbon. The blue shaded area beneath the AuNP indicates the region of band bending which is associated with the metal/TI interface,[13] note that this region has a dimension of only 3–5 nm and its lateral extent is governed by the size of the AuNP. The phonon enhancement and renormalization in our results are explained in the scheme in Fig. 4c. Laser irradiation on the AuNP leads to excitation of collective free carrier oscillations at its surface, *i.e.*, surface plasmons. The generated plasmons in resonance with the incident light field lead to a confinement of the incident light field.[45] The resonantly excited plasmons decay non-radiatively by generation of hot carriers as depicted in Fig. 4(c). The density of the generated hot carriers decreases at some distance away from the AuNP. The grey parabolic dispersion lines represent the $Bi_2Se_3$ bulk conduction band (CB) and valence band (VB) while the black linear dispersion lines represent the surface states' CB and VB. The black thick horizontal lines represent the energy levels of the low energy phonons. The red dash line represents the Fermi energy ($E_F$) for the bare TI. The resonantly decayed plasmons inject hot electrons into the CB (the upper Dirac cone) of the TI. There have been detailed reports on the extraction of hot charge carriers from the resonantly excited plasmons into the CBs of semiconductors.[16,19,46] The transferred hot electrons populate states on the thick blue parabola in Fig. 4(c). The schematic diagram illustrates that low-energy phonons cannot interfere with the bulk electrons provided that the Fermi surface lies between the bulk CB and VB. Conversely, low-energy phonons can couple to the quasi-relativistic electrons that populate the surface states of the TI. This picture supports our observation of the coupling between the electronic degrees of freedom and the phonon states evidenced by the phonon renormalization in the vicinity of the AuNPs as explained earlier. Fig. 4(b) shows the dependence of Fano parameter $\bar{q}$ on the excitation wavelength λ when measuring on the 108 nm AuNP (blue symbol) and 141 nm AuNP (black symbol). Fig. 4(b) further shows that measuring on the bare TI (red symbol), the Fano parameter $\bar{q}$ has no significant dependence on the excitation wavelength. The Fano parameter represents a measure of the electronic susceptibility interacting with a phonon. The fact that this parameter is constant in the bulk but strongly wavelength dependent for the AuNPs, strongly supports a hot carrier injection mechanism. Furthermore, our observation of the strong signal enhancement by a factor of 350 on the 108 nm AuNP can be explained as double-resonance behaviour: the band structure calculations for $Bi_2Se_3$ show an interband transition energy of 2.0 eV.[11,32] The 633 nm excitation wavelength (1.96 eV) that generated the surface plasmons in the 108 nm AuNP is simultaneously in resonance with the plasmon frequency of the 108 nm AuNP and also in resonance with the interband transition in $Bi_2Se_3$. This double resonance enhances hot electron transfer and consequently, the Raman scattering cross-section.

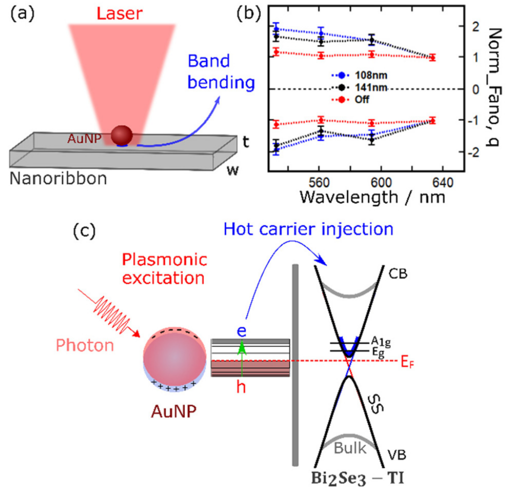

**Fig. 4** (a) Schematic illustration of the TI nanoribbon decorated with a AuNP. The blue shaded area indicates the region of band bending (note that the band bended region is covered by the AuNP), the laser spot covers predominantly areas in the vicinity of the AuNP (t = thickness and w = width of the nanoribbon). (b) Fano parameter $\bar{q}$ as a function of the excitation wavelength for the bare TI (red marker), 141 nm AuNP (black marker), and 108 nm AuNP (blue marker) position. All normalized to the value at 633 nm wavelength. The horizontal dashed line represents a guide to the eye. (c) The scheme for the hot carrier injection in TI. The resonantly excited plasmons of a AuNP decay by injecting hot electrons into the conduction band of TI. The grey parabolic dispersion represents the conduction band (CB) and the valence band (VB) of bulk TI. The surface state (SS) is represented by the black linear dispersion. The red dashed horizontal line represents the Fermi energy ($E_F$) of the bare TI. The black thick horizontal lines represent the phonons. The phonons lie in the SS of the linear dispersion and interact with the injected electrons (thick blue parabola).

## Conclusions

We have studied photoinduced doping of the topological insulator $Bi_2Se_3$ surface states by means of hot electrons generated from the decayed surface plasmons of AuNPs by nanoscopic Raman spectroscopy. We showed that the lattice dynamics in $Bi_2Se_3$ are modified in the vicinity of a gold nanoparticle. By tuning the excitation wavelength into double resonance with the plasmon frequency and interband transition in $Bi_2Se_3$, we reveal the strongest enhancement of the phonon modes by a factor of 350. Our result shows strong electron–phonon interactions and phonon renormalization induced by hot-carrier injection from the resonantly excited plasmons into the electronic surface states of the $Bi_2Se_3$. Our study provides a fundamental understanding of the interaction between electrons and phonons on the nanoscale. This insight opens the opportunity to locally investigate and control a variety of active optoelectronic and optical properties.

## Methods

Single crystalline $Bi_2Se_3$ nanoribbons were grown in a two-heating zone furnace *via* chemical vapor deposition (CVD). The furnace was equipped with a quartz tube of diameter 2.5 cm. $Bi_2Se_3$ nanoribbons were grown on silicon ⟨100⟩ substrates with a native oxide ($SiO_2$) layer. We followed the general approach in CVD method[47–49] with full optimization for growth of $Bi_2Se_3$ nanoribbons (see the ESI(A)† about the experimental procedure). A custom-made $x$, $y$, $z$ – positioner micro-manipulator was used to transfer the nanoribbons to a custom-made silicon finder grid with 225 fields of 100 μm × 100 μm. Atomic force microscopy (AFM) was utilized to measure the thickness (height) and width of the nanoribbons. Scanning electron microscope (SEM) was used to determine the position and size of the AuNPs. Energy dispersive X-ray spectroscopy (EDX) was employed to investigate the stoichiometry of the nanoribbons. The nanoribbons were decorated with single gold nanoparticles of different sizes before the Raman measurement (see ESI(C)†). For this a polydisperse solution of AuNPs with mean diameter of 96 nm was used,[50] which comprise a range of different AuNP diameters (see the ESI(B)† about the synthesis and characterization of the AuNPs). By using SEM AuNPs of different size on the nanoribbons could be selected for measurements. All nanoribbons were characterized before and after the Raman study. Raman scattering spectroscopy of AuNP decorated single nanoribbons was carried out at room temperature with a custom-made piezo-controlled micro-Raman set-up.[31,51] The spatial resolution of the micro-Raman is 211 nm at 633 nm excitation wavelength. The measurements were carried out in back-scattering configuration while employing Porto notation $\bar{Z}(XX)Z$ configuration.[52] In all measurements, the polarization of the laser is parallel to the $c$-axis of the wire (except for polarization studies with indicated polarizations) (see the ESI(G)† about the Polarization dependence study). In order to exclude laser heating of the samples, the laser power on the sample surface was kept below 50 μW.

## Abbreviations

| | |
|---|---|
| AuNPs | Gold nanoparticles |
| Tis | Topological insulators |
| LSP | Localized surface plasmon |
| CVD | Chemical vapor deposition |
| SEM | Scanning electron microscopy |
| AFM | Atomic force microscopy |
| EDX | Energy dispersive X-ray |
| VB | Valence band |
| CB | Conduction band |
| FWHM | Full width at half maximum |
| $Bi_2Se_3$ | Bismuth selenide |

## Author contributions

The manuscript was written through contributions of all authors. All authors have given approval to the final version of the manuscript.

## Conflicts of interest

There are no conflicts to declare.

## Acknowledgements

We thank Robert Frömter for discussions on electron microscopy. Yalan Huang is supported by the Chinese Scholarship Council (CSC). Parts of this project were supported by the Cluster of Excellence 'Advanced Imaging of Matter' of the Deutsche Forschungsgemeinschaft (DFG) – EXC 2056 – project ID 390715994.

## References

1 Y. Ando, Topological insulator materials, *J. Phys. Soc. Jpn.*, 2013, **82**, 1020011–10200132, DOI: **10.7566/JPSJ.82.102001**.

2 M. Z. Hasan and C. L. Kane, Colloquium: Topological insulators, *Rev. Mod. Phys.*, 2010, **82**, 3045–3067, DOI: **10.1103/RevModPhys.82.3045**.

3 C. L. Kane and E. J. Mele, Z2 topological order and the quantum spin hall effect, *Phys. Rev. Lett.*, 2005, **95**, 1468021–1468024, DOI: **10.1103/PhysRevLett.95.146802**.

4 B. A. Bernevig, T. L. Hughes and S. C. Zhang, Quantum Spin Hall Effect and Topological Phase Transition in HgTe Quantum Wells, *Science*, 2006, **314**, 1757–1761, DOI: **10.1126/science.1133734**.

5 X. L. Qi and S. C. Zhang, Topological insulators and superconductors, *Rev. Mod. Phys.*, 2011, **83**, 1057–1110, DOI: **10.1103/RevModPhys.83.1057**.

6 J. Zhang, Z. Peng, A. Soni, Y. Zhao, Y. Xion, B. Peng, J. Wang, M. S. Dresselhaus and Q. Xiong, Raman spectroscopy of few-quintuple layer topological insulator $Bi_2Se_3$ nanoplatelets, *Nano Lett.*, 2011, **11**, 2407–2414, DOI: **10.1021/nl200773n**.

7 V. Sacksteder, T. Ohtsuki and K. Kobayashi, Modification and control of topological insulator surface states using surface disorder, *Phys. Rev. Appl.*, 2015, **3**, 0640061–0640067, DOI: **10.1103/PhysRevApplied.3.064006**.

8 M. K. Ranjuna and J. Balakrishnan, Investigating the thermal transport in gold decorated graphene by opto-thermal Raman technique, *Nanotechnology*, 2022, **33**, 1857061–1857069, DOI: **10.1088/1361-6528/ac45c2**.

9 C. Zhao, Y. Zou, Y. Chen, Z. Wang, S. Lu, H. Zhang, S. Wen and D. Tang, Wavelength-tunable picosecond soliton fiber laser with Topological Insulator: $Bi_2Se_3$ as a mode locker "Mode-locked fiber lasers based on a saturable absorber incorporating carbon nanotubes, *J. Opt. Soc. Am.*, 2012, **20**, 27888–27895, DOI: **10.1364/OE.20.027888**.

10 W. Zhao, L. Chen, Z. Yue, Z. Li, D. Cortie, M. Fuhrer and X. Wang, Quantum oscillations of robust topological surface states up to 50 K in thick bulk-insulating topological insulator, *npj Quantum Mater.*, 2019, **4**, 1–6, DOI: **10.1038/s41535-019-0195-7**.

11 H. Zhang, C. X. Liu, X. L. Qi, X. Dai, Z. Fang and S. C. Zhang, Topological insulators in $Bi_2Se_3$, $Bi_2Te_3$ and $Sb_2Te_3$ with a single Dirac cone on the surface, *Nat. Phys.*, 2019, **5**, 438–442, DOI: **10.1038/nphys1270**.

12 M. Weinhold, S. Chatterjee and P. J. Klar, Modifying graphene's lattice dynamics by hot-electron injection from single gold nanoparticles, *Commun. Phys.*, 2019, **2**, 1–10, DOI: **10.1038/s42005-019-0115-y**.

13 C. D. Spataru and F. Léonard, Fermi-level pinning, charge transfer, and relaxation of spin-momentum locking at metal contacts to topological insulators, *Phys. Rev. B: Condens. Matter Mater. Phys.*, 2014, **90**, 0851151–0851156, DOI: **10.1103/PhysRevB.90.085115**.

14 H. P. Paudel, V. Apalkov, X. Sun and M. I. Stockman, Plasmon-induced hot carrier transfer to the surface of three-dimensional topological insulators, *Phys. Rev. B*, 2018, **98**, 0754281–0754287, DOI: **10.1103/PhysRevB.98.075428**.

15 A. O. Govorov, H. Zhang and Y. K. Gun'Ko, Theory of photoinjection of hot plasmonic carriers from metal nanostructures into semiconductors and surface molecules, *J. Phys. Chem. C*, 2013, **117**, 16616–16631, DOI: **10.1021/jp405430m**.

16 M. W. Knight, Y. Wang, A. S. Urban, A. Sobhani, B. Y. Zheng, P. Nordlander and N. J. Halas, Embedding Plasmonic Nanostructure Diodes Enhances Hot Electron Emission, *ACS Nano Lett.*, 2013, **13**, 1687–1692, DOI: **10.1021/nl400196z**.

17 V. Amendola, R. Pilot, M. Frasconi, O. M. Maragò and M. A. Iatì, Surface plasmon resonance in gold nanoparticles: A review, *J. Phys.: Condens. Matter*, 2017, **29**, 2030021–20300249, DOI: **10.1088/1361-648X/aa60f3**.

18 L. D. Landau, On the vibration of the electronic plasma, *J. Phys.*, 1946, **10**, 25–34.

19 Z. Fang, Y. Wang, Z. Liu, A. Schlather, P. M. Ajayan, F. H. L. Koppens, P. Nordlander and N. J. Halas, Plasmon-induced doping of graphene, *ACS Nano*, 2012, **6**, 10222–10228, DOI: **10.1021/nn304028b**.

20 Z. Fang, Z. Liu, Y. Wang, P. M. Ajayan, P. Nordlander and N. J. Halas, Graphene-antenna sandwich photodetector, *Nano Lett.*, 2012, **12**, 3808–3813, DOI: **10.1021/nl301774e**.

21 A. Scandurra, F. Ruffino, M. Censabella, A. Terrasi and M. G. Grimaldi, Dewetted Gold Nanostructures onto Exfoliated Graphene Paper as High Efficient Glucose Sensor, *Nanomaterials*, 2019, **9**, 1794–1799, DOI: **10.3390/nano9121794**.

22 A. Singh, G. Sharma, B. P. Singh and P. Vasa, Charge-Induced Lattice Compression in Monolayer $MoS_2$, *J. Phys. Chem. C*, 2019, **123**, 17943–17950, DOI: **10.1021/acs.jpcc.9b02308**.

23 C. Z. Chang, P. Tang, X. Feng, K. Li, X. Ma, W. Duan, K. He and Q. Xue, Band Engineering of Dirac Surface States in Topological-Insulator-Based van der Waals Heterostructures, *Phys. Rev. Lett.*, 2015, **115**, 1368011–1368015, DOI: **10.1103/PhysRevLett.115.136801**.

24 B. Irfan, S. Sahoo, A. Gaur, M. Ahmadi, M. Guine, R. Katiyar and R. Chatterjee, Temperature dependent Raman scattering studies of three-dimensional topological insulators $Bi_2Se_3$, *J. Appl. Phys.*, 2014, **115**, 1735061–1735067, DOI: **10.1063/1.4871860**.

25 W. Richter, H. Koi-Iler and C. R. Becker, A Raman and Far-Infrared Investigation of Phonons in the Rhombohedra1 V2–V13 Compounds BigTe3, Bi2Se3, Sb2Tea and Bi2 (Te14Sea)3 (0 < *x* < l), (Bil,Sbv)2Te3 (0 < *y* < 1), *Phys. Status Solidi B*, 1977, **84**, 619–628 **https://onlinelibrary.wiley.com/doi/abs/10.1002/pssb.2220840226**.

26 K. M. F. Shahil, M. Z. Hossain, V. Goyal and A. A. Balandin, Micro-Raman spectroscopy of mechanically exfoliated few-quintuple layers of Bi2Te3, Bi2Se3, and Sb2Te3 materials, *J. Appl. Phys.*, 2012, **111**, 0543051–0543058, DOI: **10.1063/1.3690913**.

27 H. Li, H. Peng, W. Dang, L. Yu and Z. Liu, Topological insulator nanostructures: Materials synthesis, Raman spectroscopy, and transport properties, *Front. Phys.*, 2012, **7**, 208–217, DOI: **10.1007/s11467-011-0199-7**.

28 Y. Zhao, X. Luo, J. Zhang, J. Wu, X. Bal, M. Wang, J. Jia, H. Peng, Z. Liu, S. Quek and Q. Xiong, Interlayer vibrational modes in few-quintuple-layer Bi2Te3 and Bi2Se3 two-dimensional crystals: Raman spectroscopy and first-principles studies, *Phys. Rev. B: Condens. Matter Mater. Phys.*, 2014, **90**, 2454281–24542811, DOI: **10.1103/PhysRevB.90.245428**.

29 M. Eddrief, P. Atkinson, V. Etgens and J. Bernard, Low-temperature Raman fingerprints for few-quintuple layer topological insulator Bi2Se3 films epitaxied on GaAs, *Nanotechnology*, 2014, **25**, 2457011–2457018 **https://iopscience.iop.org/article/10.1088/0957-4484/25/24/245701/meta**.

30 T. E. Glier, S. Scheitz, C. Nweze and M. Ruebhausen, Inelastic light scattering to study electron-phonon interactions in Topological Insulators" Unpublished.

31 B. Schulz, J. Baeckstroem, D. Budelmann, R. Maeser and M. Ruebhausen, Fully reflective deep ultraviolet to near infrared spectrometer and entrance optics for resonance Raman spectroscopy, *Rev. Sci. Instrum.*, 2005, **76**, 0731071–07310713, DOI: **10.1063/1.1946985**.

32 P. Sharma, R. Sharma, V. Awana, T. Narayanan, B. Gupta, N. Vashistha, L. Tyagi and M. Kumar, Low-temperature

ultrafast optical probing of topological bismuth selenide, *J. Alloys Compd.*, 2021, **886**, 1612351–1612359, DOI: **10.1016/j.jallcom.2021.161235**.

33 M. Eddrief, F. Vidal and B. Gallas, Optical properties of Bi2Se3: From bulk to ultrathin films, *J. Phys. D: Appl. Phys.*, 2016, **49**, 5053041–5053010, DOI: **10.1088/0022-3727/49/50/505304**.

34 Y. Sharma, P. Srivastava, A. Dashora, L. Vadkhiya, M. Bhayani, R. Jain, A. Jani and B. Ahuja, Electronic structure, optical properties and Compton profiles of $Bi_2S_3$ and $Bi_2Se_3$, *Solid State Sci.*, 2012, **14**, 241–249, DOI: **10.1016/j.solidstatesciences.2011.11.025**.

35 M. L. Brongersma, N. J. Halas and P. Nordlander, Plasmon-induced hot carrier science and technology, *Nat. Nanotechnol.*, 2015, **10**, 25–34, DOI: **10.1038/nnano.2014.311**.

36 X. Li, D. Xiao and Z. Zhang, Landau damping of quantum plasmons in metal nanostructures, *New J. Phys.*, 2013, **15**, 0230111–02301115, DOI: **10.1088/1367-2630/15/2/023011**.

37 E. Minutella, F. Schulz and H. Lange, Excitation-dependence of plasmon-induced hot electrons in gold nanoparticles, *J. Phys. Chem. Lett.*, 2017, **8**, 4925–4929, DOI: **10.1021/acs.jpclett.7b02043**.

38 C. Clavero, Plasmon-induced hot-electron generation at nanoparticle/metal-oxide interfaces for photovoltaic and photocatalytic devices, *Nat. Photonics*, 2014, **8**, 95–103, DOI: **10.1038/nphoton.2013.238**.

39 Y. Francescato, V. Giannini and A. M. Stefan, Plasmonic Systems Unveiled by Fano Resonances, *ACS Nano*, 2012, **6**, 1830–1838, DOI: **10.1021/nn2050533**.

40 S. Link and M. A. El-Sayed, Shape and size dependence of radiative, non-radiative and photothermal properties of gold nanocrystals, *Int. Rev. Phys. Chem.*, 2000, **19**, 409–453, DOI: **10.1080/01442350050034180**.

41 H. S. Kim and D. Y. Lee, Near-infrared-responsive cancer photothermal and photodynamic therapy using gold nanoparticles, *Polymers*, 2018, **10**, 9611–96114, DOI: **10.3390/POLYM10090961**.

42 U. Fano, Effects of Configuration Interaction on Intensities and Phase Shifts, *Phys. Rev.*, 1961, **124**, 1866–1878, DOI: **10.1103/PhysRev.124.1866**.

43 P. di Pietro, M. Ortolani, O. Limaj, A. Di Gaspare, V. Giliberti, F. Giorgianni, M. Brahlek, N. Bansal, N. Koirala, S. Oh, P. Calvani and S. Lupi, Observation of Dirac plasmons in a topological insulator, *Nat. Nanotechnol.*, 2013, **8**, 556–560, DOI: **10.1038/nnano.2013.134**.

44 Y. Deshko, L. Krusin-Elbaum, V. Menon, A. Khanikaev and J. Trevino, Surface plasmon polaritons in topological insulator nano-films and superlattices, *Opt. Express*, 2016, **24**, 7398–7410, DOI: **10.1364/oe.24.007398**.

45 K. A. Willets and R. P. van Duyne, Localized surface plasmon resonance spectroscopy and sensing, *Annu. Rev. Phys. Chem.*, 2007, **58**, 267–297, DOI: **10.1146/annurev.physchem.58.032806.104607**.

46 P. Singhal and H. N. Ghosh, Hot Charge Carrier Extraction from Semiconductor Quantum Dots, *J. Phys. Chem. C*, 2018, **122**, 17586–17600, DOI: **10.1021/acs.jpcc.8b03980**.

47 H. Peng, K. Lai, D. Kong, S. Meister, Y. Chen, X. Qi, S. Zhang, Z. Shen and Y. Cui, Aharonov-Bohm interference in topological insulator nanoribbons, *Nat. Mater.*, 2010, **9**, 225–229, DOI: **10.1038/nmat2609**.

48 D. Kong, J. Randel, H. Peng, J. Cha, S. Meister, K. Lai, Y. Chen, Z. Shen, H. Manoharan and Y. Cui, Topological insulator nanowires and nanoribbons, *Nano Lett.*, 2010, **10**, 329–333, DOI: **10.1021/nl903663a**.

49 Y. Yan, Z. Liao, Y. Zhou, H. Wu, Y. Bie, J. Chen, J. Meng, X. Wu and D. Yu, Synthesis and quantum transport properties of Bi2Se3 topological insulator nanostructures, *Sci. Rep.*, 2013, **3**, 12641–11645, DOI: **10.1038/srep01264**.

50 J. Hühn, C. Carrillo-Carrion, M. Soliman, C. Pfeiffer, D. Valdeperez, A. Masood, I. Chakraborty, L. Zhu, M. Gallego, Z. Yue, M. Carril, N. Feliu, A. Escudero, A. Alkilany, B. Pelaz, P. Pino and W. Parak, Selected standard protocols for the synthesis, phase transfer, and characterization of inorganic colloidal nanoparticles, *Chem. Mater.*, 2017, **29**, 399–461, DOI: **10.1021/acs.chemmater.6b04738**.

51 T. E. Glier, *Applications of Functional One-Dimensional Nanostructures Studied by Light Scattering*, University of Hamburg, 2021.

52 T. C. Damen, S. P. Porto and B. Tell, Raman Effect in Zinc Oxide, *J. Phys. Chem. Solids*, 1966, **142**, 570–574, DOI: **10.1103/PhysRev.142.570**.

53 A. Bock, S. Ostertun, R. Das Sharma, M. Rübhausen, K. O. Subke and C. T. Rieck, Anomalous self-energy effects of the B1g phonon in Y1-x(Pr,Ca)xBa2Cu3O7 films, *Phys. Rev. B: Condens. Matter Mater. Phys.*, 1999, 3532–3537, DOI: **10.1103/PhysRevB.60.3532**.

54 H. Lee, S. Yoon, J. Jo, B. Jeon, T. Hyeon, K. An and J. Y. Park, Enhanced hot electron generation by inverse metal oxide interfaces on catalytic nanodiode, *Faraday Discuss.*, 2019, **214**, 353, DOI: **10.1039/C8FD00136G**.

55 J. Y. Park, H. Lee, J. R. Renzas, Y. Zhang and G. A. Somorjai, Probing hot electron flow generated on pt nanoparticles with Au/$TiO_2$ schottky diodes during catalytic CO oxidation, *Nano Lett.*, 2008, **8**, 2388, DOI: **10.1021/nl8012456**.

# Chapter 5

# Summary, Conclusion and Outlook

## 5.1 Summary

We investigated lattice dynamics and phononic processes in single crystalline $Bi_2Se_3$ topological insulator (TI) nanowires (NWs), nanoribbons (NRs) and nanoflakes (NFs). High quality $Bi_2Se_3$ NWs, NRs and NFs were synthesized by the wet chemical polyol method and in the oven by the vapour liquid solid (VLS) process. We determined the quality of the $Bi_2Se_3$ TI materials by characterizing them with atomic force microscopy (AFM), scanning electron microscopy (SEM), energy dispersive x-ray spectroscopy (EDX), transmission electron microscopy (TEM), high resolution TEM (HRTEM), and selected area electron diffraction (SAED). The AFM/SEM/TEM images show cylindrical NWs, NRs and hexagonal/truncated triangular NFs. SEM-EDX and TEM-EDX show correct stoichiometry (i.e. Bi:Se (2:3)). HRTEM and SAED reveal a quintuple layer thickness of 0.95 nm and single crystallinity with growth direction perpendicular to the c-axis of the $Bi_2Se_3$ nanostructures. Magnetotransport measurements were carried out on the NW and from the Shubnikov-de Haas oscillations we calculated the carrier concentration and the position of the Fermi level in the NW. The result shows a low doping range (4.9 x $10^{11}$ $cm^{-1}$) for the effective stoichiometry.

By means of micro-Raman spectroscopy of beam spot size down to 211 nm we studied carrier injection into the topological surface states of $Bi_2Se_3$ NFs, geometrical crossover from 2D to 1D in topological insulator $Bi_2Se_3$ NWs and plasmonic hot carrier injection into the topological surface states of $Bi_2Se_3$ NRs.

**Carrier injection into the topological surface states of $Bi_2Se_3$ NFs**
10 µL of $Bi_2Se_3$ NFs in isopropanol was drop-cast on marked Au and Si substrates. The isopropanol was allowed to evaporate leaving behind the NFs. Different thicknesses of the NFs were identified with the aid of AFM and were measured with micro-Raman. The laser power on the sample depended on the excitation wavelength used and generally was kept below 40 µW for a 633 nm wavelength of beam spot size 211 ± 3 nm resulting in power density of 114 $kW/cm^2$. The measurements were conducted while scanning over the NF by about 3 $µm^2$. Resonance and thickness dependent Raman studies were performed on the NFs on Au substrate and compared with that on Si substrate. The result shows the presence of interface-enhanced Raman scattering, strong phonon enhancement (by a factor of 50) and renormalization (softening of $A^1_{1g}$ mode by 3 $cm^{-1}$ and hardening of $A^2_{1g}$ mode by 2.6 $cm^{-1}$) as a result of carriers injected into the surface states of the

contacted NF side from the Au substrate. Fig. 5.1(c and d) show the schematic diagram of carrier injection into the $Bi_2Se_3$ surface states. The result also reveals significant peak broadening (by about 8 $cm^{-1}$ for $A^1_{1g}$ mode and 4 $cm^{-1}$ for $A^2_{1g}$ mode) with the associated decreasing Fano parameter $\bar{q}$ as the thickness of the NF is decreased. $\bar{q}$ determines the electron-phonon coupling strength and implies the interaction between low energy electronic degrees of freedom with the discrete phonon state. The fact that $A^1_{1g}$ mode softens and $A^2_{1g}$ hardens means that $A^1_{1g}$ mode interacts with the positive real part of electronics susceptibility whereas $A^2_{1g}$ interacts with the negative real part of electronics susceptibility.

**Geometrical crossover from 2D to 1D in topological insulator $Bi_2Se_3$ NWs**
Single NWs of different radii were transferred to the marked Si substrate with the aid of a custom made micro-manipulator. The radius was determined with the AFM and SEM before the Raman study. Micro-Raman spectroscopy was conducted with a green laser (532 nm wavelength) of beam spot size 544 ± 13 nm. The laser power on the sample surface was kept less than 140 µW. To avoid sample damage, Raman spectra were acquired while scanning along the NW axis with a speed of about 250 nm/s. A NW radius dependent Raman study was conducted. The result shows that the Raman intensity decreases with decreasing NW radius (i.e. reduction of scattering volume of the NW) and the signal intensity appears to vanish around 50 nm radius. Further decrease of the NW radius results in the appearance of a Raman signal that peaks at about 30 nm radius. We attributed the behaviour to crossover from 2D limit to 1D in TI and it is characterized by the sudden appearance of plasmonic surface-enhanced Raman scattering (SERS). Furthermore, on application of the magnetic field along the NW axis as depicted in Fig. 5.1(a), we observed quenching of the surface enhanced Raman signal (SERS). This shows that spin-polarized plasmonic excitation of the spin Berry phase dominates over the electronic excitation spectrum. We simulated our observation following non-resonant Raman scattering since the observed enhancement is less than a factor of 100 and also since the frequency of phonon and that of plasmons is assumed to differ. By considering plasmonic dispersion relation in the magnetic field and the plasmonic susceptibility from four photon Green's function, we show that a magnetic field (flux ratio $\approx 0.5$) along the wire axis suppresses the phonon intensities (as shown in Fig. 5.1(b)) and therefore, unambiguous proof of the existence of the $\pi$ spin Berry phase at the TI surface states.

**Hot carrier injection into topological surface states of $Bi_2Se_3$ NRs.**
We conducted micro-Raman spectroscopy on single crystalline NRs decorated with single AuNP of different sizes. NRs were transferred onto a marked Si substrate before Raman study. We performed resonance Raman study on bare NRs and on NRs decorated with different sizes of AuNPs. We carried out a scan study around the vicinity of 120 nm AuNP. In all the studies, the laser power was kept below 50 $\mu$W and Raman spectra were acquired in 20 mins. The results show that on tuning the excitation wavelength into resonant frequency while measuring on the bare NR, we obtained an enhancement of the signal with a factor of 11 and 20 for $E^2_g$ and $A^2_{1g}$ modes, respectively. Measuring on the same NR but at a position containing 141 nm AuNP, we obtained an enhancement factor of 40 and 98 for $E^2_g$ and $A^2_{1g}$ modes, respectively. The enhancement is attributed to hot carrier injection into the $Bi_2Se_3$ TI (Fig. 5.1(e)). A similar behaviour was observed by Weinhold *et al.* in graphene. Furthermore, we obtained a maximum enhancement factor of 160 and 350 for $E^2_g$ and $A^2_{1g}$ modes, respectively, when measuring on a position containing 108 nm AuNP. We attribute this behaviour to hot carrier injection occurring

at resonance range of surface plasmons. The 633 nm excitation wavelength that produced the maximum enhancement is in resonance range to the surface plasmon energy of 108 nm AuNP. The result acquired when scanning across the 120 nm NR shows strong renormalization and broadening of the phonon modes. The out-of-plane vibrations of the phonon modes show more sensitivity when approaching AuNP. The renormalization of the modes is attributed to the coupling of the optical modes to hot electrons transferred from resonantly excited AuNP plasmons and the broadening of the phonon modes is attributed to strong electron-phonon interactions. Results of the AuNP size dependent study reveal renormalization of the $A_{1g}^2$ mode mostly in 39 nm and 50 nm AuNP. The observed hardening of the $A_{1g}^2$ mode is a result of the interaction of the phonon mode with the real part of the low energy electronics susceptibility of the hot carriers from plasmonic AuNP.

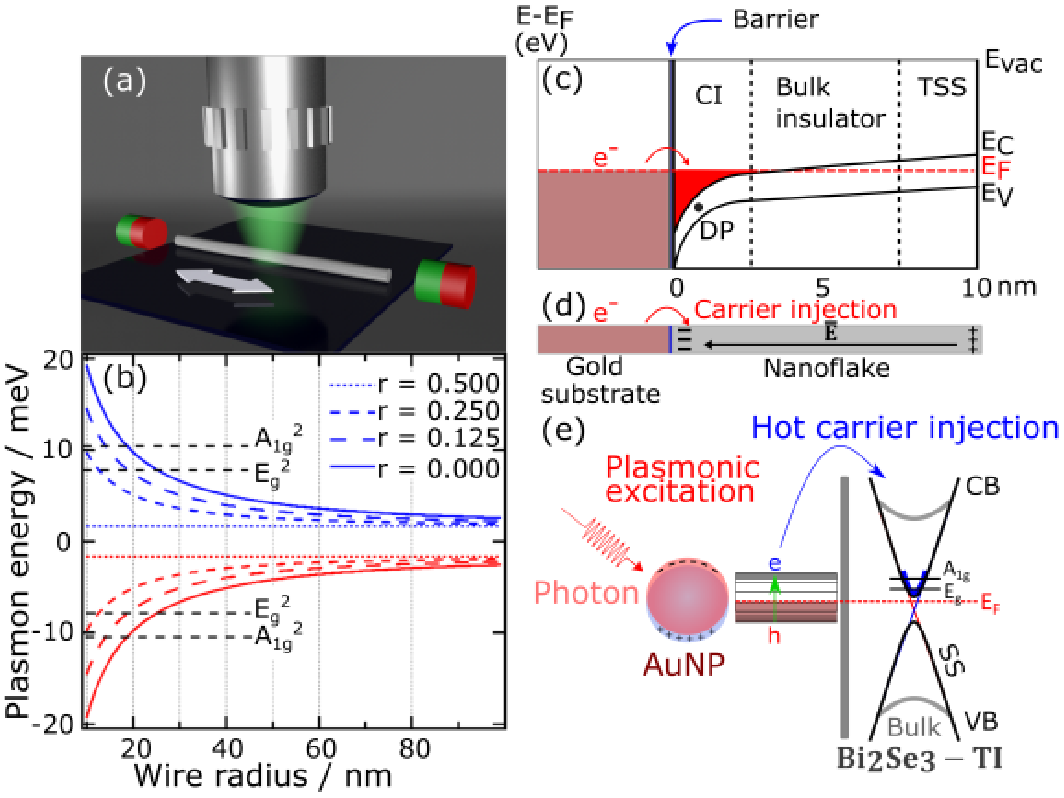

Figure 5.1: (a) Sketch of SPB experimental set-up.(b) Simulated plasmon energy as a function of magnetic fluxes. Schematic representation of (c and d) carrier injection and (e) plasmonic hot carrier injection into the topological surface states of $Bi_2Se_3$ TI. (Figure adapted with permissions from [115] [110] [118]).

.

## 5.2 Conclusion

We studied the phonon dynamics in topological insulators of $Bi_2Se_3$ NWs, NRs and NFs by means of Raman scattering. We found the effect of thickness of NRs or radius of NWs on the phonon mode intensity. For the NWs, we have shown that reducing the radius of the NW results in a crossover from 2D to 1D confined topological protected surface states. Below 50 nm radius, we observed the appearance of SERS on 1D TI surface states and we attributed the effects to the novel spin-polarized plasmonic excitations within the spin Berry phase. A magnetic field applied along the axis of the NW completely quenched the SERS. Our simulations and experimental results provided evidence that in TI NWs of smaller radius, spin polarized plasmonic excitation of the SBP dominates the electronic excitation spectrum. We established and distinguished between hot carrier and carrier injection at the TI surface states. We showed that, in NFs drop-cast on Au substrate, doping by carrier injection dominates and it is characterized by strong phonon enhancement by a factor of 50. Significant broadening and renormalization of the modes is a result of strong electron-phonon interaction mediated by carrier injection from Au substrate into the NF surface states. The injected carrier at the contacted region of the NF causes a band bending effect which enhances the field locally. At NF thickness below 10.5 nm, an increasing surface contribution becomes apparent in the detection of the bulk infra red (IR) $E_u^2$ mode. The injected carrier causes reduction of the resonant Raman condition and subsequently decreased the Raman intensity. On the other hand, by tuning the excitation wavelength into double resonance while measuring on NR decorated with AuNP, we reveal that doping by hot carrier injection dominates. The associated phonon enhancement factor of more than 350 was obtained. We showed that phonon dynamics in TI is modified by the attached AuNP. Our results provide a fundamental understanding of the electron-phonon interactions and the capability of studying this interaction at the interface which is not easily accessible by other measuring techniques.

## 5.3 Outlook

Understanding fundamental interactions between quasi-relativistic electron-phonon coupling in submicron range is a key factor in realizing predicted exotic properties of Dirac materials including TIs. The interaction between phonon and low energy electronic susceptibility at nanoscale will open the opportunity to manipulate, control and investigate optoelectronic properties of Dirac materials. To systematically study the disappearance of the SERS, systematic application of external magnetic fluxes is required. Low surface doping and hence the position of Fermi energy in TIs plays a vital role in enhancing interference between the spin Berry phase and the magnetic field and therefore tuning the position of the Fermi level is expected to affect the plasmon dispersion and spectral weight of TIs [72]. To achieve this, *in situ* Raman measurement and electric field induced Fermi level tuning/modulation is necessary. The surface states of TIs are spin polarized and we manipulated it with AuNP (non-magnetic); however, it would be interesting to manipulate the spin-polarized state with magnetic nanoparticles. "Electro-magneto-phononic" in which the lattice vibrations of materials depend on both the direction of the applied magnetic field and the direction of current is expected to open opportunities for fundamental understanding of 1D plasmonic relations. Transient plasmonic decay from resonantly excited surface plasmons on TI and the associated electron-phonon interaction within the vicinity of the plasmonic AuNP is an interesting outlook and 2D NF is a candidate for the study.

# Chapter 6

# Acknowledgments and Bibliography

## 6.1 Acknowledgments

For everything, there is always a time (Ecclesiastes 3:1). This is the time to appreciate and acknowledge each and every one that made this work a success. I am thankful with praise to God for "the life" to embark on this work and his peace which surpasses all understanding (Philippians 4:6).

**Supervision:** From the very first acceptance and invitation to come over to Germany for an excellent research and collaboration, to providing an enabling environment for scientific discussions, academic supervision and research, I am grateful to **Prof. Dr. Michael. A. Rübhausen**. Thank you for sponsoring my photolithographic training in Dresden, for the opportunity given to me to work independently, for all the useful discussions, for supporting my quest for knowledge and for academic development.
From scientific discussions to understanding peculiarities of international students, you are always willing to support. Thank you **Prof. Dr. Nils Huse** for opening your hands for academic activities, for the SEM and for being my second supervisor and reviewer.

**Dispution committee members:** I am grateful to **Prof. Dr. Wolfgang J. Parak, Prof. Dr. Daniela Pfannkuche and Dr. Robert Zierold**. For accepting to be members of my disputation committee. I am thankful to **Prof. Dr. Daniela Pfannkuche** for chairing the committee.

**Group members:** Thank you **Dr. Gerd Neuber** and **Dr. Benjamin. R. Grimm-Lebsanft** for being the postdocs incharge when I joined the group. Special thanks to **Dr. Tomke. E. Glier**, your time in the lab is filled with excitement. Looking back at our SBP experiment, our tip-toeing into the lab, magic fingers and for sure by now, you might have learnt a lot about Igbo culture. I look forward to more exciting research and scientific advancement. Not forgetting the coffee, story time! Thank you Tomke.
It is very unlikely to forget all the lab experience and late hour office work with **Sarah Scheitz**. Thank you Sarah for the various scientific discussions and collaborations. Coffee break with Sarah is a good avenue to mix science with family discussions, future projections and work life balance. Thank you **Dr. Melissa Teubner** for not forgetting my birthday and always willing to know how my day is going especially within my first year in Germany. Thank you **Florian Biebl** and **Dieter Rukser** for the first optics lab experience in Hamburg. On the same hand, I thank **Sören Buchenau** for the office

discussions and viewing science from multi-dimensions. **Sören** I look forward to someday for a vacation to Nigeria or any other country in Africa as you have wished. Thank you **Isa Moch, Malte van Heek and Lea Westphal** for your excellent support. **Mika Rerrer**, I appreciate your time and energy in the course of measurement. You devoted a lot of time and energy in identifying the positions of the gold nanoparticles at the SEM. Thank you Mika for your curiosity. Thank you **Stephanie Baer** for your support in administrative processes. I wouldn't have comfortably found my way around Hamburg on my first day of arrival. You have got excellent communication skills and were able to support all the bureaucratic work before and after my arrival to Hamburg. I specially thank you, **Dr. Ing. Lewis Akinsinde** for all the support and contacts in the early days of the VLS set-up.

**Collaboration/cooperation:** Thank you **Prof. Robert Blick** for utilizing research facilities in your group. I appreciate **Dr. Robert Zierold** for all the scientific support, discussions and advice. You provided all the necessary contact for the training in Dresden. I sincerely thank you for the magneto-transport study of the samples. Together with **Isabel Gonzalez Diaz-Placio**, the magneto-transport measurement was accomplished. Thank you **Dr. Heiko Reith** and **Dennis Hofmann** from Leibniz-Institut für Festkörper- und Werkstoffforschung (IFW) Dresden for the workshop. Thank you **Dr. Robert Frömter** for the SEM and your scientific input. I thank **Prof. Dr. Lorenz Kienle** and **Niklas Kohlmann** from Christian Albrechts-Universität Kiel for the TEM studies.

**Graduate school:** I am very grateful to **Pier Helmholtz Graduate School (PHGS)** for all the support, training and sponsorships. I acknowledge your sponsorship especially for my summer school in Spain.

**Proofreaders:** Many special thanks to **Dr. Madeleine Resühr** and **Dr. Jens Resühr** for taking out time to proofread through this piece of work and the translations involved. I appreciate your encouragement and support. I am also grateful to Gosife's Godparent, **Madeleine Herring**. You spent hours with me going through each line of the thesis while at the same time finding out time to play with G.G. Madeleines I am very grateful.

**Family and friends:** I am grateful to all my family members and friends for your prayers and support. I am also thankful to **Jörg Scharwies, Bridget Scharwies and Patrick Scharwies**, for all the support, encouragement and taking out time with Gosife during the course of this work.
**Gosife Nweze**, thank you for your understanding. I know, I might not have given you enough time as you might wish to have, however your laughter keeps the work going.
Let me specifically and specially thank the first lady of my kingdom and my wife, **Nuel Ejimone-Nweze**. Your criticism, encouragement, opinion, organization, care and above all your love keep this work going. I am not unmindful of all the time you were awake waiting for me to come back. Thank you for your lovely understanding and for being a perfect mother to Gosife.

On a final note, I apologize to a good number of people I could not mention and who positively influenced this work in one way or another. I am thankful for your support, care and love towards the completion of this work. **Thank you.**

# Bibliography

[1] Y. Ando, "Topological insulator materials," *Journal of the Physical Society of Japan*, vol. 82, no. 10, p. 102001, 2013.

[2] C. L. Kane and E. J. Mele, "Z 2 topological order and the quantum spin hall effect," *Physical review letters*, vol. 95, no. 14, p. 146802, 2005.

[3] L. Fu and C. L. Kane, "Superconducting proximity effect and majorana fermions at the surface of a topological insulator," *Physical review letters*, vol. 100, no. 9, p. 096407, 2008.

[4] A. P. Schnyder, S. Ryu, A. Furusaki, and A. W. Ludwig, "Classification of topological insulators and superconductors in three spatial dimensions," *Physical Review B*, vol. 78, no. 19, p. 195125, 2008.

[5] A. M. Essin, J. E. Moore, and D. Vanderbilt, "Magnetoelectric polarizability and axion electrodynamics in crystalline insulators," *Physical review letters*, vol. 102, no. 14, p. 146805, 2009.

[6] V. Sacksteder, T. Ohtsuki, and K. Kobayashi, "Modification and control of topological insulator surface states using surface disorder," *Physical Review Applied*, vol. 3, no. 6, p. 064006, 2015.

[7] M. Kim, Z. Jacob, and J. Rho, "Recent advances in 2d, 3d and higher-order topological photonics," *Light: Science & Applications*, vol. 9, no. 1, pp. 1–30, 2020.

[8] M. Weinhold, S. Chatterjee, and P. J. Klar, "Modifying graphene's lattice dynamics by hot-electron injection from single gold nanoparticles," *Communications Physics*, vol. 2, no. 1, pp. 1–10, 2019.

[9] D. Kong, J. C. Randel, H. Peng, J. J. Cha, S. Meister, K. Lai, Y. Chen, Z.-X. Shen, H. C. Manoharan, and Y. Cui, "Topological insulator nanowires and nanoribbons," *Nano letters*, vol. 10, no. 1, pp. 329–333, 2010.

[10] F. Xiu, L. He, Y. Wang, L. Cheng, L.-T. Chang, M. Lang, G. Huang, X. Kou, Y. Zhou, X. Jiang *et al.*, "Manipulating surface states in topological insulator nanoribbons," *Nature nanotechnology*, vol. 6, no. 4, pp. 216–221, 2011.

[11] H. Peng, K. Lai, D. Kong, S. Meister, Y. Chen, X.-L. Qi, S.-C. Zhang, Z.-X. Shen, and Y. Cui, "Aharonov–bohm interference in topological insulator nanoribbons," *Nature materials*, vol. 9, no. 3, pp. 225–229, 2010.

[12] M. Franz and L. Molenkamp, Eds., *Topological Insulators*, 1st ed. Elsevier, 2013, vol. 6.

[13] D. J. Thouless, M. Kohmoto, M. N. Nightingale, and M. den Nijs, “Quantized hall conductance in a two-dimensional periodic potential,” *Physical Review Letters*, vol. 49, pp. 405–408, 4 1982.

[14] P. D. Pietro, *Optical Properties of Bismuth-Based Topological Insulators.* Springer International Publishing, 2014.

[15] C. Kane and J. Moore, “Topological insulators,” *Physics World*, vol. 24, pp. 32–36, 2 2011.

[16] T. Ando and Y. Uemura, “Theory of quantum transport in a two-dimensional electron system under magnetic fields. i. characteristics of level broadening and transport under strong fields,” *Journal of the Physical Society of Japan*, vol. 36, pp. 959–967, 4 1974.

[17] K. v. Klitzing, G. Dorda, and M. Pepper, “New method for high-accuracy determination of the fine-structure constant based on quantized hall resistance,” *Physical Review Letters*, vol. 45, pp. 494–497, 8 1980.

[18] Y. K. Kato, R. C. Myers, A. C. Gossard, and D. D. Awschalom, “Observation of the spin hall effect in semiconductors,” *science*, vol. 306, no. 5703, pp. 1910–1913, 2004.

[19] M. Konig, S. Wiedmann, C. Brune, A. Roth, H. Buhmann, L. W. Molenkamp, X.-L. Qi, and S.-C. Zhang, “Quantum spin hall insulator state in hgte quantum wells,” *Science*, vol. 318, no. 5851, pp. 766–770, 2007.

[20] J. E. Moore and L. Balents, “Topological invariants of time-reversal-invariant band structures,” *Physical Review B*, vol. 75, no. 12, p. 121306, 2007.

[21] R. Roy, “Topological phases and the quantum spin hall effect in three dimensions,” *Physical Review B*, vol. 79, no. 19, p. 195322, 2009.

[22] D. Hsieh, D. Qian, L. Wray, Y. Xia, Y. S. Hor, R. J. Cava, and M. Z. Hasan, “A topological dirac insulator in a quantum spin hall phase,” *Nature*, vol. 452, no. 7190, pp. 970–974, 2008.

[23] A. Taskin and Y. Ando, “Quantum oscillations in a topological insulator bi 1- x sb x,” *Physical Review B*, vol. 80, no. 8, p. 085303, 2009.

[24] M. V. Berry, “Quantal phase factors accompanying adiabatic changes,” *Proceedings of the Royal Society of London. A. Mathematical and Physical Sciences*, vol. 392, no. 1802, pp. 45–57, 1984.

[25] B. A. Bernevig, *Topological insulators and topological superconductors.* Princeton university press, 2013.

[26] D. Vanderbilt, *Berry phases in electronic structure theory.* cambridge university press, 2018.

[27] S.-Q. Shen, *Topological insulators-dirac equation in condensed matter.* Springer Nature Singapore, 2017.

[28] H. Luo, *Advanced topological insulator.* Scrivener publishing, 2019.

[29] H. Li, L. Sheng, D. Sheng, and D. Xing, "Chern number of thin films of the topological insulator bi 2 se 3," *Physical Review B*, vol. 82, no. 16, p. 165104, 2010.

[30] Y. Hatsugai, "Chern number and edge states in the integer quantum hall effect," *Physical review letters*, vol. 71, no. 22, p. 3697, 1993.

[31] C. Xu and J. E. Moore, "Stability of the quantum spin hall effect - effects of interactions, disorder, and z 2 topology," *Physical Review B*, vol. 73, no. 4, p. 045322, 2006.

[32] C. Wu, B. A. Bernevig, and S.-C. Zhang, "Helical liquid and the edge of quantum spin hall systems," *Physical review letters*, vol. 96, no. 10, p. 106401, 2006.

[33] C. L. Kane and E. J. Mele, "Quantum spin hall effect in graphene," *Physical review letters*, vol. 95, no. 22, p. 226801, 2005.

[34] L. Fu and C. L. Kane, "Topological insulators with inversion symmetry," *Physical Review B*, vol. 76, no. 4, p. 045302, 2007.

[35] L. Fu, C. L. Kane, and E. J. Mele, "Topological insulators in three dimensions," *Physical review letters*, vol. 98, no. 10, p. 106803, 2007.

[36] Y. Chen, J. G. Analytis, J.-H. Chu, Z. Liu, S.-K. Mo, X.-L. Qi, H. Zhang, D. Lu, X. Dai, Z. Fang *et al.*, "Experimental realization of a three-dimensional topological insulator, bi2te3," *science*, vol. 325, no. 5937, pp. 178–181, 2009.

[37] D. Hsieh, Y. Xia, D. Qian, L. Wray, F. Meier, J. Dil, J. Osterwalder, L. Patthey, A. Fedorov, H. Lin *et al.*, "Observation of time-reversal-protected single-dirac-cone topological-insulator states in bi 2 te 3 and sb 2 te 3," *Physical review letters*, vol. 103, no. 14, p. 146401, 2009.

[38] Y. Zhang, K. He, C.-Z. Chang, C.-L. Song, L.-L. Wang, X. Chen, J.-F. Jia, Z. Fang, X. Dai, W.-Y. Shan *et al.*, "Crossover of the three-dimensional topological insulator bi2se3 to the two-dimensional limit," *Nature Physics*, vol. 6, no. 8, pp. 584–588, 2010.

[39] B. A. Bernevig, T. L. Hughes, and S.-C. Zhang, "Quantum spin hall effect and topological phase transition in hgte quantum wells," *science*, vol. 314, no. 5806, pp. 1757–1761, 2006.

[40] K. C. Nowack, E. M. Spanton, M. Baenninger, M. König, J. R. Kirtley, B. Kalisky, C. Ames, P. Leubner, C. Brüne, H. Buhmann *et al.*, "Imaging currents in hgte quantum wells in the quantum spin hall regime," *Nature materials*, vol. 12, no. 9, pp. 787–791, 2013.

[41] O. Pankratov, S. Pakhomov, and B. Volkov, "Supersymmetry in heterojunctions: Band-inverting contact on the basis of pb1-xsnxte and hg1-xcdxte," *Solid state communications*, vol. 61, no. 2, pp. 93–96, 1987.

[42] X. Dai, T. L. Hughes, X.-L. Qi, Z. Fang, and S.-C. Zhang, "Helical edge and surface states in hgte quantum wells and bulk insulators," *Physical Review B*, vol. 77, no. 12, p. 125319, 2008.

[43] E. Novik, A. Pfeuffer-Jeschke, T. Jungwirth, V. Latussek, C. Becker, G. Landwehr, H. Buhmann, and L. Molenkamp, "Band structure of semimagnetic hg 1- y mn y te quantum wells," *Physical Review B*, vol. 72, no. 3, p. 035321, 2005.

[44] X.-L. Qi, Y.-S. Wu, and S.-C. Zhang, "General theorem relating the bulk topological number to edge states in two-dimensional insulators," *Physical Review B*, vol. 74, no. 4, p. 045125, 2006.

[45] H. Zhang, C.-X. Liu, X.-L. Qi, X. Dai, Z. Fang, and S.-C. Zhang, "Topological insulators in bi2se3, bi2te3 and sb2te3 with a single dirac cone on the surface," *Nature physics*, vol. 5, no. 6, pp. 438–442, 2009.

[46] Y. Xia, L. Wray, D. Qian, D. Hsieh, A. Pal, H. Lin, A. Bansil, D. Grauer, Y. Hor, R. Cava *et al.*, "Electrons on the surface of bi2se3 form a topologically-ordered two dimensional gas with a non-trivial berry's phase," *arXiv preprint arXiv:0812.2078*, 2008.

[47] J. E. Moore, Y. Ran, and X.-G. Wen, "Topological surface states in three-dimensional magnetic insulators," *Physical review letters*, vol. 101, no. 18, p. 186805, 2008.

[48] X.-L. Qi, T. L. Hughes, and S.-C. Zhang, "Fractional charge and quantized current in the quantum spin hall state," *Nature Physics*, vol. 4, no. 4, pp. 273–276, 2008.

[49] Y. Ran, A. Vishwanath, and D.-H. Lee, "Spin-charge separated solitons in a topological band insulator," *Physical review letters*, vol. 101, no. 8, p. 086801, 2008.

[50] W. Zhang, R. Yu, H.-J. Zhang, X. Dai, and Z. Fang, "First-principles studies of the three-dimensional strong topological insulators bi2te3, bi2se3 and sb2te3," *New Journal of Physics*, vol. 12, no. 6, p. 065013, 2010.

[51] S. Urazhdin, D. Bilc, S. Mahanti, S. Tessmer, T. Kyratsi, and M. Kanatzidis, "Surface effects in layered semiconductors bi 2 se 3 and bi 2 te 3," *Physical Review B*, vol. 69, no. 8, p. 085313, 2004.

[52] D. Hsieh, Y. Xia, D. Qian, L. Wray, F. Meier, J. Osterwalder, L. Patthey, J. G. Checkelsky, N. Ong, A. V. Fedorov *et al.*, "A tunable topological insulator in the spin helical dirac transport regime," *Nature*, vol. 460, no. 7259, pp. 1101–1105, 2009.

[53] Y. Zhang, Y. Ran, and A. Vishwanath, "Topological insulators in three dimensions from spontaneous symmetry breaking," *Physical Review B*, vol. 79, no. 24, p. 245331, 2009.

[54] M. Bianchi, D. Guan, S. Bao, J. Mi, B. B. Iversen, P. D. King, and P. Hofmann, "Coexistence of the topological state and a two-dimensional electron gas on the surface of bi2se3," *Nature communications*, vol. 1, no. 1, pp. 1–5, 2010.

[55] M. Guo, Z. Wang, Y. Xu, H. Huang, Y. Zang, C. Liu, W. Duan, Z. Gan, S.-C. Zhang, K. He *et al.*, "Tuning thermoelectricity in a bi2se3 topological insulator via varied film thickness," *New Journal of Physics*, vol. 18, no. 1, p. 015008, 2016.

[56] B. Irfan, S. Sahoo, A. P. Gaur, M. Ahmadi, M. J.-F. Guinel, R. S. Katiyar, and R. Chatterjee, “Temperature dependent raman scattering studies of three dimensional topological insulators bi2se3,” *Journal of Applied Physics*, vol. 115, no. 17, p. 173506, 2014.

[57] W. Richter and C. Becker, “A raman and far-infrared investigation of phonons in the rhombohedral v2–vi3 compounds bi2te3, bi2se3, sb2te3 and bi2 (te1- xsex) 3 (0< x< 1),(bi1- ysby) 2te3 (0< y< 1),” *physica status solidi (b)*, vol. 84, no. 2, pp. 619–628, 1977.

[58] K. Shahil, M. Hossain, V. Goyal, and A. Balandin, “Micro-raman spectroscopy of mechanically exfoliated few-quintuple layers of bi2te3, bi2se3, and sb2te3 materials,” *Journal of Applied Physics*, vol. 111, no. 5, p. 054305, 2012.

[59] O. V. Yazyev, J. E. Moore, and S. G. Louie, “Spin polarization and transport of surface states in the topological insulators bi 2 se 3 and bi 2 te 3 from first principles,” *Physical review letters*, vol. 105, no. 26, p. 266806, 2010.

[60] C. Li, O. Van‘t Erve, J. Robinson, Y. Liu, L. Li, and B. Jonker, “Electrical detection of charge-current-induced spin polarization due to spin-momentum locking in bi2se3,” *Nature nanotechnology*, vol. 9, no. 3, pp. 218–224, 2014.

[61] X.-L. Zhang and W.-M. Liu, “Electron-phonon coupling and its implication for the superconducting topological insulators,” *Scientific Reports*, vol. 5, no. 1, pp. 1–6, 2015.

[62] R. C. Hatch, M. Bianchi, D. Guan, S. Bao, J. Mi, B. B. Iversen, L. Nilsson, L. Hornekær, and P. Hofmann, “Stability of the bi 2 se 3 (111) topological state: Electron-phonon and electron-defect scattering,” *Physical Review B*, vol. 83, no. 24, p. 241303, 2011.

[63] J. A. Sobota, S.-L. Yang, D. Leuenberger, A. F. Kemper, J. G. Analytis, I. R. Fisher, P. S. Kirchmann, T. P. Devereaux, and Z.-X. Shen, “Distinguishing bulk and surface electron-phonon coupling in the topological insulator bi 2 se 3 using time-resolved photoemission spectroscopy,” *Physical review letters*, vol. 113, no. 15, p. 157401, 2014.

[64] J. E. Moore, “The birth of topological insulators,” *Nature*, vol. 464, no. 7286, pp. 194–198, 2010.

[65] X.-L. Qi and S.-C. Zhang, “Topological insulators and superconductors,” *Reviews of Modern Physics*, vol. 83, no. 4, p. 1057, 2011.

[66] M. Z. Hasan and C. L. Kane, “Colloquium: topological insulators,” *Reviews of modern physics*, vol. 82, no. 4, p. 3045, 2010.

[67] P. A. M. Dirac, “The quantum theory of the electron. part ii,” *Proceedings of the Royal Society of London. Series A, Containing Papers of a Mathematical and Physical Character*, vol. 118, no. 779, pp. 351–361, 1928.

[68] ——, “The quantum theory of the electron,” *Proceedings of the Royal Society of London. Series A, Containing Papers of a Mathematical and Physical Character*, vol. 117, no. 778, pp. 610–624, 1928.

[69] Y. Xia, D. Qian, D. Hsieh, L. Wray, A. Pal, H. Lin, A. Bansil, D. Grauer, Y. S. Hor, R. J. Cava *et al.*, "Observation of a large-gap topological-insulator class with a single dirac cone on the surface," *Nature physics*, vol. 5, no. 6, pp. 398–402, 2009.

[70] H. Osterhage, J. Gooth, B. Hamdou, P. Gwozdz, R. Zierold, and K. Nielsch, "Thermoelectric properties of topological insulator bi2te3, sb2te3, and bi2se3 thin film quantum wells," *Applied Physics Letters*, vol. 105, no. 12, p. 123117, 2014.

[71] H.-Z. Lu and S.-Q. Shen, "Weak localization of bulk channels in topological insulator thin films," *Physical Review B*, vol. 84, no. 12, p. 125138, 2011.

[72] P. Iorio, C. Perroni, and V. Cataudella, "Plasmons in topological insulator cylindrical nanowires," *Physical Review B*, vol. 95, no. 23, p. 235420, 2017.

[73] S. S. Hong, Y. Zhang, J. J. Cha, X.-L. Qi, and Y. Cui, "One-dimensional helical transport in topological insulator nanowire interferometers," *Nano letters*, vol. 14, no. 5, pp. 2815–2821, 2014.

[74] F. Münning, O. Breunig, H. F. Legg, S. Roitsch, D. Fan, M. Rößler, A. Rosch, and Y. Ando, "Quantum confinement of the dirac surface states in topological-insulator nanowires," *Nature communications*, vol. 12, no. 1, pp. 1–6, 2021.

[75] A. Cook and M. Franz, "Majorana fermions in a topological-insulator nanowire proximity-coupled to an s-wave superconductor," *Physical Review B*, vol. 84, no. 20, p. 201105, 2011.

[76] G. Rosenberg, H.-M. Guo, and M. Franz, "Wormhole effect in a strong topological insulator," *Physical Review B*, vol. 82, no. 4, p. 041104, 2010.

[77] P. Iorio, C. A. Perroni, and V. Cataudella, "Quantum interference effects in bi2se3 topological insulator nanowires with variable cross-section lengths," *The European Physical Journal B*, vol. 89, no. 4, pp. 1–11, 2016.

[78] J. Ziegler, R. Kozlovsky, C. Gorini, M.-H. Liu, S. Weishäupl, H. Maier, R. Fischer, D. A. Kozlov, Z. D. Kvon, N. Mikhailov *et al.*, "Probing spin helical surface states in topological hgte nanowires," *Physical Review B*, vol. 97, no. 3, p. 035157, 2018.

[79] L. A. Jauregui, M. T. Pettes, L. P. Rokhinson, L. Shi, and Y. P. Chen, "Magnetic field-induced helical mode and topological transitions in a topological insulator nanoribbon," *Nature nanotechnology*, vol. 11, no. 4, pp. 345–351, 2016.

[80] R. Gutzler, M. Garg, C. R. Ast, K. Kuhnke, and K. Kern, "Light–matter interaction at atomic scales," *Nature Reviews Physics*, vol. 3, no. 6, pp. 441–453, 2021.

[81] C. V. Raman, "A new radiation," *Indian Journal of physics*, vol. 2, pp. 387–398, 1928.

[82] S. Jha, "Theory of light scattering from electronic excitations in solids," *Il Nuovo Cimento B (1965-1970)*, vol. 63, no. 1, pp. 331–354, 1969.

[83] A. Pinczuk and E. Burstein, *light scattering in solids I: chapter 2 Fundamentals of inelastic scattering in semiconductors and insulators.* Springer-verlag berlin heildelber, 1983.

[84] M. Cardona, *light scattering in solids I.* Springer-verlag berlin heildelber, 1983.

[85] R. Martin and L. Falicov, *light scattering in solids I: chapter 3 Resonance Raman scattering.* Springer-verlag berlin heildelber, 1983.

[86] W. Hayes, R. Loudon, and J. F. Scott, "Scattering of light by crystals," *American Journal of Physics*, vol. 47, no. 6, pp. 571–571, 1979.

[87] S. Naler, *Optical studies of ordering phenomena in manganese oxides.* University of Hamburg, 2005.

[88] M. Rübhausen, "Electronic correlations in cuprate superconductors- an inelastic light scattering study," *PhD Thesis, University of Hamburg*, pp. 107–140, 1998.

[89] H. A. Kramers and W. Heisenberg, "Über die streuung von strahlung durch atome," *Zeitschrift für Physik*, vol. 31, no. 1, pp. 681–708, 1925.

[90] P. A. M. Dirac, "The quantum theory of dispersion," *Proceedings of the Royal Society of London. Series A, Containing Papers of a Mathematical and Physical Character*, vol. 114, no. 769, pp. 710–728, 1927.

[91] A. Kawabata, "Green function theory of raman scattering," *Journal of the Physical Society of Japan*, vol. 30, no. 1, pp. 68–85, 1971.

[92] T. E. Glier, "Applications of functional one-dimensional nanostructures studied by light scattering," *PhD Thesis, University of Hamburg*, 2021.

[93] A. Bock, S. Ostertun, R. D. Sharma, M. Rübhausen, K.-O. Subke, and C. Rieck, "Anomalous self-energy effects of the b 1 g phonon in y 1- x (pr, ca) x ba 2 cu 3 o 7 films," *Physical Review B*, vol. 60, no. 5, p. 3532, 1999.

[94] T. E. Glier, S. Scheitz, C. Nweze, and M. Rübhausen, "Inelastic light scattering to study electron-phonon interaction in topological insulators," *Unpublished.*

[95] C. D. Spataru and F. Léonard, "Fermi-level pinning, charge transfer, and relaxation of spin-momentum locking at metal contacts to topological insulators," *Physical Review B*, vol. 90, no. 8, p. 085115, 2014.

[96] S. A. Maier *et al.*, *Plasmonics: fundamentals and applications.* Springer, 2007, vol. 1.

[97] V. Amendola, R. Pilot, M. Frasconi, O. M. Maragò, and M. A. Iatì, "Surface plasmon resonance in gold nanoparticles: a review," *Journal of Physics: Condensed Matter*, vol. 29, no. 20, p. 203002, 2017.

[98] U. Kreibig and M. Vollmer, "Theoretical considerations," in *Optical properties of metal clusters.* Springer, 1995, pp. 13–201.

[99] C. Bohren and D. Huffman, "Absorption and scattering of light by small particles (wiley-interscience, new york," 1983.

[100] S. Sarina, E. Jaatinen, Q. Xiao, Y. M. Huang, P. Christopher, J. C. Zhao, and H. Y. Zhu, "Photon energy threshold in direct photocatalysis with metal nanoparticles: key evidence from the action spectrum of the reaction," *The Journal of Physical Chemistry Letters*, vol. 8, no. 11, pp. 2526–2534, 2017.

[101] E. Minutella, F. Schulz, and H. Lange, "Excitation-dependence of plasmon-induced hot electrons in gold nanoparticles," *The journal of physical chemistry letters*, vol. 8, no. 19, pp. 4925–4929, 2017.

[102] D. Peckus, H. Rong, L. Stankevicius, M. Juodenas, S. Tamulevicius, T. Tamulevicius, and J. Henzie, "Hot electron emission can lead to damping of optomechanical modes in core–shell ag@ tio2 nanocubes," *The Journal of Physical Chemistry C*, vol. 121, no. 43, pp. 24 159–24 167, 2017.

[103] C. Voisin, N. Del Fatti, D. Christofilos, and F. Vallée, "Ultrafast electron dynamics and optical nonlinearities in metal nanoparticles," pp. 2264–2280, 2001.

[104] S. Link and M. A. El-Sayed, "Optical properties and ultrafast dynamics of metallic nanocrystals," *Annual review of physical chemistry*, vol. 54, no. 1, pp. 331–366, 2003.

[105] ——, "Size and temperature dependence of the plasmon absorption of colloidal gold nanoparticles," *The Journal of Physical Chemistry B*, vol. 103, no. 21, pp. 4212–4217, 1999.

[106] K. O. Aruda, M. Tagliazucchi, C. M. Sweeney, D. C. Hannah, G. C. Schatz, and E. A. Weiss, "Identification of parameters through which surface chemistry determines the lifetimes of hot electrons in small au nanoparticles," *Proceedings of the National Academy of Sciences*, vol. 110, no. 11, pp. 4212–4217, 2013.

[107] H. P. Paudel, V. Apalkov, X. Sun, and M. I. Stockman, "Plasmon-induced hot carrier transfer to the surface of three-dimensional topological insulators," *Physical Review B*, vol. 98, no. 7, p. 075428, 2018.

[108] Y. Yan, Z.-M. Liao, Y.-B. Zhou, H.-C. Wu, Y.-Q. Bie, J.-J. Chen, J. Meng, X.-S. Wu, and D.-P. Yu, "Synthesis and quantum transport properties of bi2se3 topological insulator nanostructures," *Scientific reports*, vol. 3, no. 1, pp. 1–5, 2013.

[109] S. Buchenau, L. O. Akinsinde, M. Zocher, D. Rukser, U. Schürmann, L. Kienle, B. Grimm-Lebsanft, and M. Rübhausen, "Scalable polyol synthesis for few quintuple layer thin and ultra high aspect ratio bi2se3 structures," *Solid State Communications*, vol. 281, pp. 49–52, 2018.

[110] S. Scheitz, T. E. Glier, C. Nweze, M. van Heek, I. Moch, R. Zierold, R. Blick, N. Huse, and M. Rübhausen, "Carrier injection observed by interface-enhanced raman scattering from topological insulators on gold substrates," *ACS Applied Materials & Interfaces*, vol. 14, no. 28, pp. 32 625–32 633, 2022.

[111] S. Coskun, B. Aksoy, and H. E. Unalan, "Polyol synthesis of silver nanowires: an extensive parametric study," *Crystal Growth & Design*, vol. 11, no. 11, pp. 4963–4969, 2011.

[112] X. Jiang, J. Bai, and T. Wang, "Basics for the preparation of quantum dots and their interactions with living cells," in *Quantum Dots: Applications in Biology.* Springer, 2014, pp. 165–175.

[113] B. Schulz, J. Bäckström, D. Budelmann, R. Maeser, M. Rübhausen, M. Klein, E. Schoeffel, A. Mihill, and S. Yoon, "Fully reflective deep ultraviolet to near infrared

spectrometer and entrance optics for resonance raman spectroscopy," *Review of scientific instruments*, vol. 76, no. 7, p. 097203, 2005.

[114] L. Westphal, "Mikro raman charakterisierung von nanostrukturierten proben," *Bachelor Thesis, University of Hamburg*, 2020.

[115] C. Nweze, T. E. Glier, S. Scheitz, L. Westphal, F. Biebl, S. Buchenau, L. Akinsinde, N. Kohlmann, L. Kienle, I. Gonzalez Diaz-Placio, R. Fromter, R. Zierold, R. Blick, N. Huse, and M. Rübhausen, "Quantum confinement of the spin berry phase on 1d topological surfaces of single bi2se3 nanowires," *ACS Nano Letters*.

[116] T. C. Damen, S. Porto, and B. Tell, "Raman effect in zinc oxide," *Physical Review*, vol. 142, no. 2, p. 570, 1966.

[117] C. Arguello, D. L. Rousseau, and S. d. S. Porto, "First-order raman effect in wurtzite-type crystals," *Physical Review*, vol. 181, no. 3, p. 1351, 1969.

[118] C. Nweze, T. E. Glier, M. Rerrer, S. Scheitz, Y. Huang, R. Zierold, R. H. Blick, W. J. Parak, N. Huse, and M. Rübhausen, "Plasmonic hot carrier injection from single gold nanoparticles into topological insulator bi2se3 nanoribbons." *Nanoscale*, 2022.

[119] C. Schormann, "Magneto-transport measurements of single superconducting nanotubes," *Bachelor Thesis, University of Hamburg*, 2021.

[120] S. Buchenau, S. Scheitz, A. Sethi, J. E. Slimak, T. E. Glier, P. K. Das, T. Dankwort, L. Akinsinde, L. Kienle, A. Rusydi *et al.*, "Temperature and magnetic field dependent raman study of electron-phonon interactions in thin films of bi 2 se 3 and bi 2 te 3 nanoflakes," *Physical Review B*, vol. 101, no. 24, p. 245431, 2020.

[121] S. Scheitz, *Temperature and magnetic field dependent Raman spectroscopy of topological insulator Bi2Se3 and Bi2Te3 2D nanostructures.* MSc thesis, University of Hamburg, 2019.

[122] G. Zhang, H. Qin, J. Teng, J. Guo, Q. Guo, X. Dai, Z. Fang, and K. Wu, "Quintuple-layer epitaxy of thin films of topological insulator bi 2 se 3," *Applied Physics Letters*, vol. 95, no. 5, p. 053114, 2009.

[123] Q. Yao, Y. Zhu, L. Chen, Z. Sun, and X. Chen, "Microwave-assisted synthesis and characterization of bi2te3 nanosheets and nanotubes," *Journal of Alloys and Compounds*, vol. 481, no. 1-2, pp. 91–95, 2009.

[124] P. Sharma, R. Sharma, V. Awana, T. Narayanan, B. K. Gupta, N. Vashistha, L. Tyagi, and M. Kumar, "Low-temperature ultrafast optical probing of topological bismuth selenide," *Journal of Alloys and Compounds*, vol. 886, p. 161235, 2021.

[125] H. Li, H. Peng, W. Dang, L. Yu, and Z. Liu, "Topological insulator nanostructures: Materials synthesis, raman spectroscopy, and transport properties," *Frontiers of Physics*, vol. 7, no. 2, pp. 208–217, 2012.

[126] Y. Zhao, X. Luo, J. Zhang, J. Wu, X. Bai, M. Wang, J. Jia, H. Peng, Z. Liu, S. Y. Quek *et al.*, "Interlayer vibrational modes in few-quintuple-layer bi 2 te 3 and bi 2 se 3 two-dimensional crystals: Raman spectroscopy and first-principles studies," *Physical Review B*, vol. 90, no. 24, p. 245428, 2014.

[127] M. Eddrief, P. Atkinson, V. Etgens, and B. Jusserand, “Low-temperature raman fingerprints for few-quintuple layer topological insulator bi2se3 films epitaxied on gaas,” *Nanotechnology*, vol. 25, no. 24, p. 245701, 2014.

[128] S. Cooper and M. Klein, “Light scattering studies of the low frequency excitation spectra of high temperature superconductors,” *Comments Cond. Mat. Phys*, vol. 15, no. 2, pp. 99–124, 1990.

[129] J. Zhang, Z. Peng, A. Soni, Y. Zhao, Y. Xiong, B. Peng, J. Wang, M. S. Dresselhaus, and Q. Xiong, “Raman spectroscopy of few-quintuple layer topological insulator bi2se3 nanoplatelets,” *Nano letters*, vol. 11, no. 6, pp. 2407–2414, 2011.

[130] U. Fano and J. Cooper, “Line profiles in the far-uv absorption spectra of the rare gases,” *Physical Review*, vol. 137, no. 5A, p. A1364, 1965.

[131] J. Li, J. J. Tu, and J. L. Birman, “Symmetry predicted transitions in 3d topological insulators,” *Solid state communications*, vol. 163, pp. 11–14, 2013.

[132] H. Kung, M. Salehi, I. Boulares, A. Kemper, N. Koirala, M. Brahlek, P. Lošták, C. Uher, R. Merlin, X. Wang *et al.*, “Surface vibrational modes of the topological insulator bi2se3 observed by raman.”

[133] V. Gnezdilov, Y. G. Pashkevich, H. Berger, E. Pomjakushina, K. Conder, and P. Lemmens, “Helical fluctuations in the raman response of the topological insulator bi 2 se 3,” *Physical Review B*, vol. 84, no. 19, p. 195118, 2011.

[134] M. Eddrief, F. Vidal, and B. Gallas, “Optical properties of bi2se3: from bulk to ultrathin films,” *Journal of Physics D: Applied Physics*, vol. 49, no. 50, p. 505304, 2016.

[135] Y. Sharma, P. Srivastava, A. Dashora, L. Vadkhiya, M. Bhayani, R. Jain, A. Jani, and B. Ahuja, “Electronic structure, optical properties and compton profiles of bi2s3 and bi2se3,” *Solid State Sciences*, vol. 14, no. 2, pp. 241–249, 2012.

[136] H. Tang, X. Wang, Y. Xiong, Y. Zhao, Y. Zhang, Y. Zhang, J. Yang, and D. Xu, “Thermoelectric characterization of individual bismuth selenide topological insulator nanoribbons,” *Nanoscale*, vol. 7, no. 15, pp. 6683–6690, 2015.

[137] A. Sharma, B. Bhattacharyya, A. Srivastava, T. Senguttuvan, and S. Husale, “High performance broadband photodetector using fabricated nanowires of bismuth selenide,” *Scientific reports*, vol. 6, no. 1, pp. 1–8, 2016.

[138] J. Gooth, J. G. Gluschke, R. Zierold, M. Leijnse, H. Linke, and K. Nielsch, “Thermoelectric performance of classical topological insulator nanowires,” *Semiconductor Science and Technology*, vol. 30, no. 1, p. 015015, 2014.

[139] N. F. Hinsche, S. Zastrow, J. Gooth, L. Pudewill, R. Zierold, F. Rittweger, T. Rauch, J. Henk, K. Nielsch, and I. Mertig, “Impact of the topological surface state on the thermoelectric transport in sb2te3 thin films,” *Acs Nano*, vol. 9, no. 4, pp. 4406–4411, 2015.

[140] B. Hamdou, J. Gooth, A. Dorn, E. Pippel, and K. Nielsch, "Aharonov-bohm oscillations and weak antilocalization in topological insulator sb2te3 nanowires," *Applied Physics Letters*, vol. 102, no. 22, p. 223110, 2013.

[141] S. Hikami, A. I. Larkin, and Y. Nagaoka, "Spin-orbit interaction and magnetoresistance in the two dimensional random system," *Progress of Theoretical Physics*, vol. 63, no. 2, pp. 707–710, 1980.

[142] S. Bäßler, B. Hamdou, P. Sergelius, A.-K. Michel, R. Zierold, H. Reith, J. Gooth, and K. Nielsch, "One-dimensional edge transport on the surface of cylindrical bixte3-ysey nanowires in transverse magnetic fields," *Applied Physics Letters*, vol. 107, no. 18, p. 181602, 2015.

[143] D.-X. Qu, Y. S. Hor, J. Xiong, R. J. Cava, and N. P. Ong, "Quantum oscillations and hall anomaly of surface states in the topological insulator bi2te3," *Science*, vol. 329, no. 5993, pp. 821–824, 2010.

[144] S. J. Lee, Z. Guan, H. Xu, and M. Moskovits, "Surface-enhanced raman spectroscopy and nanogeometry: The plasmonic origin of sers," *The Journal of Physical Chemistry C*, vol. 111, no. 49, pp. 17 985–17 988, 2007.

[145] G. Santoro, S. Yu, M. Schwartzkopf, P. Zhang, S. Koyiloth Vayalil, J. F. Risch, M. A. Rübhausen, M. Hernández, C. Domingo, and S. V. Roth, "Silver substrates for surface enhanced raman scattering: Correlation between nanostructure and raman scattering enhancement," *Applied Physics Letters*, vol. 104, no. 24, p. 243107, 2014.

[146] B. Friedl, C. Thomsen, and M. Cardona, "Determination of the superconducting gap in r ba 2 cu 3 o 7- $\delta$," *Physical review letters*, vol. 65, no. 7, p. 915, 1990.

[147] R. D. Mattuck, *A Guide to Feynman Diagram in Many Body Problem.* MacGraw-Hill Book Company, 1967.

[148] J. Huhn, C. Carrillo-Carrion, M. G. Soliman, C. Pfeiffer, D. Valdeperez, A. Masood, I. Chakraborty, L. Zhu, M. Gallego, Z. Yue *et al.*, "Selected standard protocols for the synthesis, phase transfer, and characterization of inorganic colloidal nanoparticles," *Chemistry of Materials*, vol. 29, no. 1, pp. 399–461, 2017.

[149] Y. Francescato, V. Giannini, and S. A. Maier, "Plasmonic systems unveiled by fano resonances," *ACS nano*, vol. 6, no. 2, pp. 1830–1838, 2012.

[150] H. S. Kim and D. Y. Lee, "Near-infrared-responsive cancer photothermal and photodynamic therapy using gold nanoparticles," *Polymers*, vol. 10, no. 9, p. 961, 2018.

[151] S. Link and M. A. El-Sayed, "Shape and size dependence of radiative, non-radiative and photothermal properties of gold nanocrystals," *International reviews in physical chemistry*, vol. 19, no. 3, pp. 409–453, 2000.

[152] P. Di Pietro, M. Ortolani, O. Limaj, A. Di Gaspare, V. Giliberti, F. Giorgianni, M. Brahlek, N. Bansal, N. Koirala, S. Oh *et al.*, "Observation of dirac plasmons in a topological insulator," *Nature nanotechnology*, vol. 8, no. 8, pp. 556–560, 2013.

[153] Y. Deshko, L. Krusin-Elbaum, V. Menon, A. Khanikaev, and J. Trevino, “Surface plasmon polaritons in topological insulator nano-films and superlattices,” *Optics Express*, vol. 24, no. 7, pp. 7398–7410, 2016.

[154] K. A. Willets and R. P. Van Duyne, “Localized surface plasmon resonance spectroscopy and sensing,” *Annual review of physical chemistry*, vol. 58, no. 1, pp. 267–297, 2007.

[155] M. W. Knight, Y. Wang, A. S. Urban, A. Sobhani, B. Y. Zheng, P. Nordlander, and N. J. Halas, “Embedding plasmonic nanostructure diodes enhances hot electron emission,” *Nano letters*, vol. 13, no. 4, pp. 1687–1692, 2013.

[156] P. Singhal and H. N. Ghosh, “Hot charge carrier extraction from semiconductor quantum dots,” *The Journal of Physical Chemistry C*, vol. 122, no. 31, pp. 17 586–17 600, 2018.

[157] Z. Fang, Y. Wang, Z. Liu, A. Schlather, P. M. Ajayan, F. H. Koppens, P. Nordlander, and N. J. Halas, “Plasmon-induced doping of graphene,” *ACS nano*, vol. 6, no. 11, pp. 10 222–10 228, 2012.

# Appendix A

# Creative Output/Publications

1. Scheitz, S.; Glier, T. E.; **Nweze, C.**; van Heek, M.; Moch, I.; Zierold, R.; Blick, R.; Huse, N.; Rübhausen, M. Carrier injection observed by interface-enhanced Raman scattering from topological insulators on gold substrates. Applied Materials & Interfaces 2022, 14, 32625

2. Akinsinde, L. O.; Glier, T. E.; Schwartzkopf, M.; Betker, M.; Nissen, M.; Witte, M.; Scheitz, S.; **Nweze, C.**; Grimm-Lebsanft, B.; Gensch, M.; Chumakov, A.; Baev, I.; Schürmann, U.; Dankwort, T.; Fischer, F.; Martins, M.; Roth, S. V.; Kienle, L.; Rübhausen, M. Surface characterization and resistance changes of silver-nanowire networks upon atmospheric plasma treatment. Applied Surface Science 2021, 550, 1493262.

3. **Nweze, C.**; Glier, T. E.; Rerrer, M.; Scheitz, S.; Huang, Y.; Zierold, R.; Blick, R.; Parak, W. J.; Huse, N.; Rübhausen, M. Plasmonic hot carrier injection from single gold nanoparticles into topological insulator $Bi_2Se_3$ nanoribbons. ACS Nano, under review.

4. **Nweze, C.**; Glier, T. E.; Scheitz, S.; Westphal, L.; Biebl, F.; Buchenau, S.; Akinsinde, L. O.; Kohlmann, N.; Kienle, L.; González Díaz-Placio, I.; Frömter, R.; Zierold, R.; Blick, R.; Huse, N.; Rübhausen, M. Quantum Confinement of the Spin-Berry phase on 1D topological surfaces of single $Bi_2Se_3$ nanowires. Nano Letters, under consideration.

# Appendix B

# Supplementary Information: Carrier injection observed by interface-enhanced Raman scattering from topological insulators on gold substrates

Supporting Information

# *Carrier injection observed by interface-enhanced Raman scattering from topological insulators on gold substrates*

**Sarah Scheitz*, Tomke Eva Glier, Christian Nweze, Malte van Heek, Isa Moch, Robert Zierold +, Robert Blick+, Nils Huse, Michael Rübhausen***

Institut für Nanostruktur- und Festkörperphysik, Center for Free Electron Laser Science (CFEL),
Universität Hamburg, Luruper Chaussee 149, 22761 Hamburg, Germany
\+ Institut für Nanostruktur- und Festkörperphysik, Center for Hybrid Nanostructures (CHyN), Universität Hamburg, Luruper Chaussee 149, Hamburg, 22761 Germany

*Corresponding to: sscheitz@physnet.uni-hamburg.de, mruebhau@physnet.uni-hamburg.de

## Content

# 1. Sample preparation

Two-dimensional nanoflakes (NFs) of $Bi_2Se_3$ and $Bi_2Te_3$ are grown via the wet-chemical polyol method following our earlier work.[1] Details on the procedure are given in [1] for $Bi_2Se_3$ and [2] for $Bi_2Te_3$ NFs. An overview of the used chemicals and quantities is given in Table S1. For both materials the synthesis exploits the selective binding of the polymer ligand polyvinylpyrollidone (PVP) to the (001) facet of growing nanocrystals, which hinders the growth in *c*-direction leading to a two-dimensional growth in the $\langle 11\overline{2}0 \rangle$ direction.[2] This yields highly anisotropic NFs with a high surface to bulk ratio that are only several nm thick. For $Bi_2Se_3$ and $Bi_2Te_3$ NFs, we find average heights of 7.7 ± 2.7 nm and 14.8 ± 5.2 nm, respectively.[2] Both chalcogenides have a rhombohedral crystal structure, schematically shown in the inset of Figure 1a in the main text, and are built up of layers of alternating Bi and Se/Te atoms. The strongly restricted growth in *c*-direction hence results in NFs consisting of a finite number of layers.

**Table S1.** Chemicals used in the sysnthesis of the topological insulator nanoflakes.

| | Bi-Precursor | Se/Te-Precursor | Solvent | Ligand | Additive | T (°C) | t |
|---|---|---|---|---|---|---|---|
| $Bi_2Se_3$ [1] | Bismuth nitrate pentahydrate ($Bi(NO_3)_3 \cdot 5(H_20)$, Sigma Aldrich, 98 %)<br>n = 0.0096 mol·$L^{-1}$ | Sodium selenite ($Na_2SeO_3$, Sigma Aldrich, 99 %)<br>n = 0.0144 moL·$L^{-1}$ | Ethylene glycol ($(C_2H_4(OH)_2$, VWR, 99.7 %)<br>V = 30 mL | PVP (55K M, Sigma Aldrich)<br>m = 0.33 g | - | 180 | 6 h |
| $Bi_2Te_3$ [2] | Bismuth nitrate pentahydrate ($Bi(NO_3)_3 \cdot 5(H_20)$, Sigma Aldrich, 98 %)<br>n = 0.02 mol·$L^{-1}$ | Potassium tellurite monohydrate ($K_2TeO_3 \cdot H_2O$, Alfa Aesar, 97 %)<br>n = 0.03 mol·$L^{-1}$ | Ethylene glycol ($(C_2H_4(OH)_2$, Carl Roth, 99 %)<br>V = 50 mL | PVP (30K M, Carl Roth)<br>m = 0.5 g | Sodium hydroxide (NaOH, Merck, 98 %) n = 0.2 mol·$L^{-1}$ | 180 | 22 h |

To remove solvent and precursor residues the as synthesized products were washed subsequently in isopropanol and aceton and stored in isopropanol as explained in Ref. [2]. Individual NFs on silicon or gold substrates were prepared by dropcasting the NF solution on the substrates and isopropanol was allowed to evaporate at room temperature. For the silicon substrate a Bor-doped Si(100) substrate was purchased (EM-Tec FG1 silicon finder grid substrate) which had a chrome grid of 1 mm pitch (25 mesh) deposited on its surface. The silicon substrate had no coating except a native oxide layer of about 2 nm. The grid allowed to identify individual NFs and measure the same NFs with several techniques like sub-micro-Raman spectroscopy and subsequent AFM and SEM analysis.

Gold substrates were prepared by sputtering a gold layer of about 100 nm thickness on a chromium adhesion layer (10 nm) on Si (100) substrates. Both metals have been deposited in a Cressington 308R coating system equipped with two DC sputter sources (Au, Cr) without vacuum break at 40 mA current for 10 min and 2 min, respectively. The base pressure was 1E-6 mbar and was adjusted to 0.01 mbar during deposition. Patterning of the Au substrate was achieved by scratching a grid of 500 µm pitch into the gold layer using a scalpel.

# 2. Raman measurements

## 2.1 Raman setup, used laser sources and laser spot characterization

Raman spectroscopy on individual $Bi_2Se_3$ and $Bi_2Te_3$ NFs was conducted using a custom made sub-micro-Raman setup in combination with the UT-3 Raman spectrometer.[3] The details of the sub-micro-Raman setup are given in [4]. The optical elements in the setup are optimized for laser light in the visible spectrum and allow for a resonance Raman study with excitations wavelengths from 705 nm to 400 nm. An overview of the laser sources used for the resonance study is in given in Table S2.

**Table S2.** Laser sources specifications.

| **Wavelength** | 704.96 nm | 632.82 nm | 593.72 nm | 560.35 nm | 532.04 nm |
|---|---|---|---|---|---|
| **Laser type** | Mode locked Ti:sapphire laser pumped by a Millenia eV | Gas | Diode | Diode | Diode |
| **Model** | Tsunami 3950-X1BB | 05-LHP-123-496 HeNe | OBIS 594LS 1233468 | OBIS 561LS 1223779 | Millenia Pro 10sJS |
| **manufacturer** | Spectra-Physics Lasers, Inc. | Melles Griot | Coherent, Inc. | Coherent, Inc. | Spectra-Physics Lasers, Inc. |
| **Focused Beam FWHM on sample** | 283 ± 3 nm | 211 ± 2 nm | 269 ± 2 nm | 389 ± 2 nm | 255 ± 4 nm |

Furthermore, the sub-micro-Raman setup allows to measure individual nanostructures with a high sample to substrate ratio by focusing the laser spot down to a full width at half maximum (FWHM) ~ 250 nm depending on wavelength. The sub-micron spot diameters are achieved by first widening the incoming laser beam with a spatial filter to homogenously illuminate an infinity corrected 50X objective (Plan Apo HR, Mitutoyo, Japan) with a numerical aperture of NA=0.75. Simultaneously, the sample and laser spot are monitored by a color industrial camera (DFK 37AUX264, The Imaging Source, Germany) in combination with a framegrabber software (IC Measure 2.0.0.161, The Imaging Source Europe GmbH). The focus and sample position are adjusted using a multi-axis piezo scanner (P-517) in combination with a controller (E-710.3CD, PI, Germany) enabling a correct positioning of the laser on the NFs. This also gives the possibility to scan the laser spot over a defined NF area during a measurement to reduce laser heating and exclude possible ionization damage.

The beam spot diameters were determined by evaluating laser spot images on a blank Si(111) wafer. In the recorded images, shown as insets in Figure S1, a resolution of 1 px = 69 nm is given. Horizontal and vertical line cuts through the grey value images of all laser spots are shown in Figure S1. Each intensity profile was fitted by a Gaussian profile resulting in an average FWHM. The nearly identical FWHM for vertical and horizontal line cuts, differing by less than 3 %, validate the symmetrical beam profiles generated by the setup.

The smallest beam diameter with FWHM = 212 ± 2 nm was achieved using the HeNe gas laser with an emission line of 632.82 nm. The semiconductor lasers with emission of 560.35 nm and 593.72 nm achieved similar beam widths of around 260 nm.

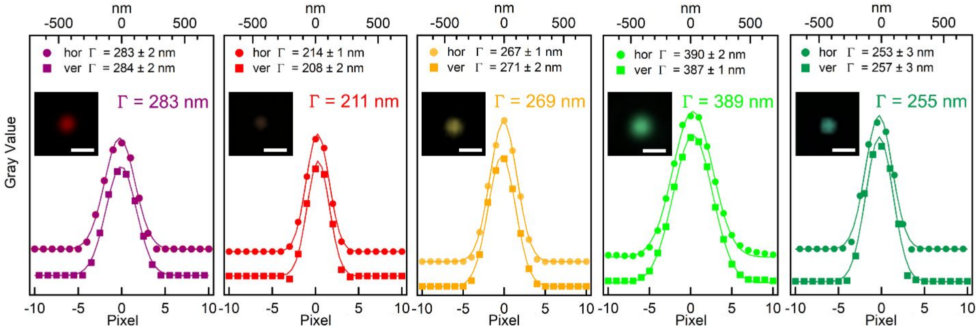

**Figure S1.** Laser spot characterization. Intensity line profiles of the shown laser spot microscope images without white light illumination. The panels from left to right show the recorded laser spot images of the used excitation sources with wavelength of 705 nm, 633 nm, 594 nm, 560 nm, and 532nm, respectively. The scale bars in the laser spot images (20 x 20 pixel) correspond to 500 nm. Horizontal (circles) and vertical (squares) intensity cuts were fitted by a Gaussian profile shown as solid lines. The FWHM of vertical and horizontal cuts were averaged to the value given in color. The grey value images are displayed in false color.

## 2.2 Employed Laser Powers

In Table S3 surface laser power densities employed for single NF measurements on silicon and gold substrates are presented. These powers and additional scanning over the NFs in areas of 2 to 4 µm$^2$ were chosen to allow for spectra recording with sufficient signal to noise ratio and at least three accumulations per measured NF. In general, for all wavelengths and samples extensive care was taken to exclude beam damage and obtain reproducible results from a large number of NFs. Please note, that for NFs on silicon longer integration times were chosen due to the much lower Raman signal compared to NFs on gold.

**Table S3.** Surface laser power densities *PD* in kW/cm$^2$ and integration times $t_{\mathrm{int}}$ in min for single NF measurements.

| wavelength | 705 nm | | 633 nm | | 594 nm | | 560 nm | | 532 nm | |
|---|---|---|---|---|---|---|---|---|---|---|
| | *PD* | $t_{\mathrm{int}}$ | *PD* | $t_{\mathrm{int}}$ | *PD* | $t_{\mathrm{int}}$ | *PD* | $t_{\mathrm{int}}$ | *PD* | $t_{\mathrm{int}}$ |
| $Bi_2Se_3$ on Au | 167 | 10 | 114 | 20 | 223 | 5 | 18 | 10 | 106 | 10 |
| $Bi_2Se_3$ on Si | 167 | 30 | 175 | 30 | 223 | 20 | 50 | 30 | 106 | 30 |
| $Bi_2Te_3$ on Au | - | | 255 | 30 | - | | - | | - | |

# 3. Data analysis

## 3.1 General data treatment of Raman spectra

Acquired Raman spectra were normalized to the used integration time and laser power. The laser power at the sample positioned was measured with a Si photodiode powermeter (PM160, Thorlabs). Furthermore, all normalized spectra were background corrected by subtraction of a substrate (Si or Au, respectively) measurement. The substrate measurements were also normalized to integration time and power and usually measured under the same conditions as the associated NF measurements.

## 3.2 Correction factors for resonance Raman study

To compare Raman intensities obtained from single NFs with varying thicknesses and measured with different excitation energies we determined a correction factor for each measured NF[3]. The Raman correction factor includes the varying spectral response of $Bi_2Se_3$ for the different excitation energies. The laser energy dependent refractive index *n* and absorption coefficient *k* of $Bi_2Se_3$ were determined from calculations by Zhang *et al.*[5] and selected values for our used excitation energies are given in Table S4. Furthermore, since several NFs were measured for the resonance study, the obtained spectra were corrected for the varying scattering volume of each corresponding NF.

First we determined the effective transmission $T_\mathrm{i}^\mathrm{eff}$ of laser signal into the NF since only a fraction $T_\mathrm{i}^\mathrm{eff} = |1 - R(\nu_\mathrm{i})|^2$ will transmit into the NF and contribute to the Raman process, with $R(\nu_\mathrm{i})$ being the reflectivity. The reflectivity $R(\nu_\mathrm{i})$ of $Bi_2Se_3$ as a function of excitation energy $\nu_i$ is given as

$$R(\nu_\mathrm{i}) = \left|\frac{n_1 - n_2}{n_1 + n_2}\right|^2, \tag{S1}$$

with $n_{1,2}(\nu_\mathrm{i})$ being the real refractive index of air ($n_1$=1) and $Bi_2Se_3$, respectively. The effective transmission $T_\mathrm{i}^\mathrm{eff}$ as a function of laser energy is shown in Figure S2(b). Secondly, we determine an effective scattering volume $V_\mathrm{i}^\mathrm{eff}$ of each measured NF. Due to the absorption of laser signal with increasing penetration depth in the NF each atomic layer will experience a different laser intensity and hence contribute less to the overall Raman signal. The change in laser intensity is given by Lambert-Beer's law $I(z) = e^{-\alpha_i z}$ , where $z$ is the NF thickness and $\alpha_i$ is the absorption coefficient determined by $\alpha_i = \frac{2k_i\nu_i}{c}$ with the extinction coefficient $k_i$ and speed of light in vacuum $c$. Additionally, the generated Raman signal can be reabsorbed before exiting the NF depending on the depth, which is also described by Lambert-Beer's law. Please note, that the penetration depth $\alpha_i$ of all used lasers is around 9 nm as shown in Figure S2(c) with only the 705 nm excitation line having a slightly larger penetration depth of 12 nm.

We account for the change in laser intensity by integrating $I(z)$ over the entire NF thickness. Furthermore, the overall contributing scattering volume will be different for each laser energy and NF thickness. Therfore, we have estimated the contributing NF volume by a cone that includes the varying dispersion of the used laser in the NF and the varying laser spot radii. A schematic illustration of the NF volume contributing to the Raman scattering is shown in Figure S2(a).

We, therefore, calculate an effective scattering volume $V_\mathrm{i}^\mathrm{eff}$, which includes the laser intensity integrated over the NF thickness and absorption of generated Raman signal as

$$V_\mathrm{i}^\mathrm{eff} = \int_0^z e^{\frac{-2k_\mathrm{i}\nu_\mathrm{i}}{c}z} \cdot \pi r_\mathrm{i}(z)^2 \cdot e^{\frac{-2k_\mathrm{i}\nu_\mathrm{i}}{c}z} dz\,. \tag{S2}$$

The contributing NF volume estimated by a cone will have a penetration depth dependent radius $r_\mathrm{i}(z)$ due to the dispersion of the laser, which we calculate by $r_\mathrm{i}(z) = r_0 + z \cdot \tan(\theta_\mathrm{i}')$. Here, $r_0$ is the laser spot radius and $\theta_i'$ is the laser energy dependent diffraction angle as indicated in Figure S2(a). The diffraction angle was determined according to Snellius' law $\sin(\theta_\mathrm{i}') = \frac{1}{n_\mathrm{i}} \cdot \sin(\theta)$, where $\sin(\theta) = 0.75$ is determined by the used focusing objective. Lastly, to account for the varying thicknesses of each measured NF the integration range was adapted according to the NF thickness $z$. Thicknesses of the measured NFs on silicon and gold substrates for the resonance study are given in Table S4. For the reference bulk sample an integration range for the effective scattering volume of 20 nm was selected for all energies, as the effective laser intensity for all energies has decreased below 20 %. The resulting correction factor *CF* shown in Figure S2(d) was calculated by

$$CF_\mathrm{i} = T_\mathrm{i}^\mathrm{eff} \cdot V_\mathrm{i}^\mathrm{eff}\,. \tag{S3}$$

To determine the Raman susceptibilities of the $Bi_2Se_3$ phonon modes at all excitation energies the modes were fit by a Lorentzian function

$$I(\omega) = \frac{I\omega\Gamma}{(\omega^2 - \omega_0^2)^2 + \omega^2\Gamma^2}, \tag{S4}$$

with the Raman shift $\omega$, the phonon mode eigenfrequencies $\omega_0$, and the spectral width $\Gamma$. From the fit parameters the maximum mode intensities were determined as $I^\mathrm{max} = I/\omega_0\Gamma$. Finally, the phonon mode intensities $I^\mathrm{max}$ obtained from Lorentzian fits of the resonance Raman spectra were divided by their associated correction factor to yield their Raman susceptibility

$$X^\mathrm{max}(\omega_\mathrm{i}) = \frac{I^\mathrm{max}(\omega_\mathrm{i})}{CF_\mathrm{i}}\,. \tag{S5}$$

**Table S4.** Critical parameters for the determination of resonance Raman correction factors.

| Laser Wavelength $\lambda_i$ (nm) | Laser Energy $\nu_i$ (eV) | $Bi_2Se_3$ $n_2$ | $Bi_2Se_3$ $k_i$ | Diffraction angle $\theta_\mathrm{i}'$ (°) | Laser spot $r_0$ (nm) | NF thickness $z$ on Si (nm) | NF thickness $z$ on Au (nm) |
|---|---|---|---|---|---|---|---|
| 704.96 | 1.76 | 5.78 | 4.59 | 7.46 | 141.5 | 11.8 | 15.1 |
| 632.82 | 1.96 | 4.26 | 5.47 | 10.14 | 106.0 | 11.8 | 15.1 |
| 593.72 | 2.09 | 3.51 | 5.30 | 12.34 | 134.5 | 17.1 | 15.1 |
| 560.35 | 2.21 | 2.87 | 4.92 | 15.15 | 194.0 | 11.3 | 15.1 |
| 532.04 | 2.33 | 2.42 | 4.70 | 18.05 | 127.5 | 15.8 | 14.5 |

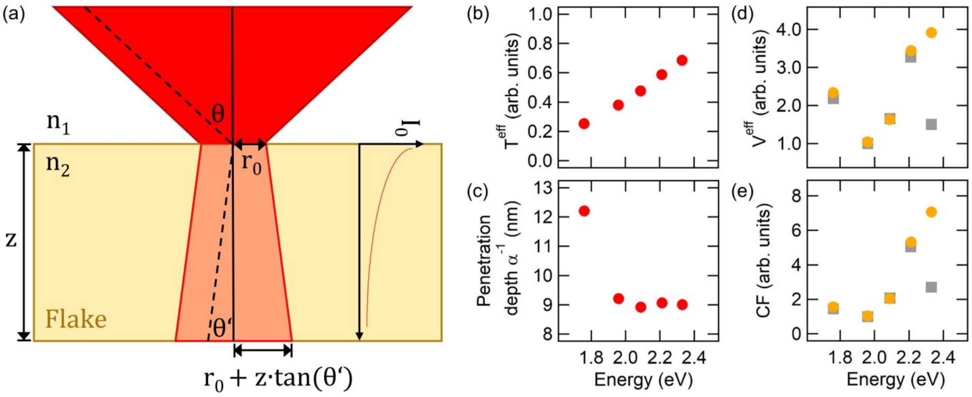

**Figure S2.** Effective scattering volume of NFs measured for the resonance Raman study. (a) Schematic cross section of a Bi$_2$Se$_3$ NF illuminated by the focused laser beam. The laser illustrated as red cone is focused onto the NF resulting in a beam spot radius of r$_0$ and will disperse into the NF according to the refractive index $n_2$ according to the used laser energy. The scattering volume of the NF contributing to the Raman signal is indicated by the bright red area and estimated by a truncated cone. The decreasing laser intensity $I$(z) with penetration depth according to Lambert-Beer's law is shown as an inset on the right side of the NF. (b-d) Excitation energy dependent values for the effective transmission $T_\mathrm{i}^\mathrm{eff}$ , penetration depth $\alpha_i$, effective scattering volume $V_\mathrm{i}^\mathrm{eff}$ and, correction factor *CF*, respectively. In (d,e) values depicted by grey squares correspond to the measured NFs on silicon and yellow circles correspond to NFs on Gold, respectively. The values in (d,e) are normalized to the smallest value of all investigated NFs.

# 4. Thickness dependent Raman study for $Bi_2Se_3$/$Bi_2Te_3$ NFs on gold

## 4.1 Quantification of NFs optical contrast on gold

The thickness *d* of the $Bi_2Se_3$ and $Bi_2Te_3$ NFs on gold can be directly correlated to their optical contrast *OC* to the underlying gold substrate. For quantification of the optical contrast microscopy images of all NFs were obtained with identical acquisition software settings. The optical contrast was calculated by determining the ratio of the average greyscale value of the NFs $GV^{\mathrm{Flake}}$ to the surrounding gold substrate $GV^{\mathrm{Au}}$:

$$OC = \frac{GV^{\mathrm{Au}} - GV^{\mathrm{Flake}}}{GV^{\mathrm{Au}}} \tag{S6}$$

To ensure comparability, the area to determine the average grey value of each NF was 20x20 pixel for $Bi_2Se_3$ (10x10 pixel for $Bi_2Te_3$) and the area on the gold substrate was 100x100 pixel as illustrated in Fig. S3(b) .

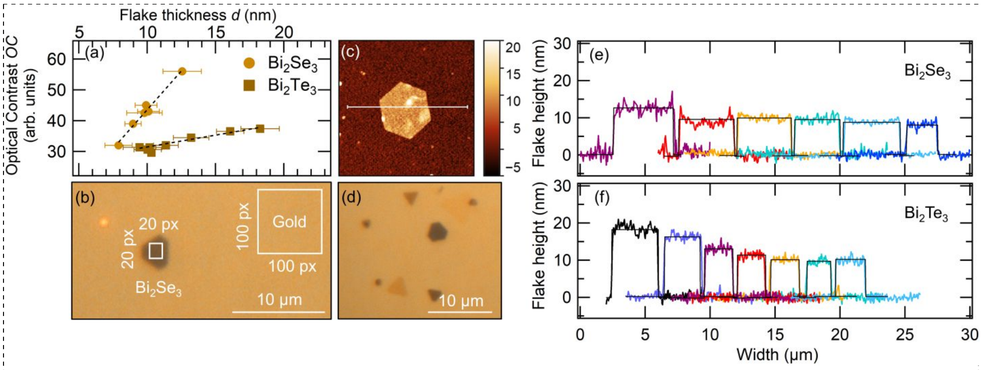

**Figure S3.** Correlation between NF thickness and optical contrast to gold. (a) $Bi_2Se_3$ and $Bi_2Te_3$ optical contrasts as a function of NF thickness determined from AFM measurements with a linear correlation fit (dashed lines). (b) Microscope image of $Bi_2Se_3$ NFs on gold substrate with indicated area sizes for grey value measurements. (c) AFM topography image of a $Bi_2Te_3$ NF on gold with indicated horizontal cut (white line) corresponding to the red height profile shown in (f). The height scale bar shown to the right is in units of nm. (d) Microscope image of a representative area on the $Bi_2Se_3$-Au sample. (e,f) Height (thickness) profiles of the selected NFs measured by Raman spectroscopy. All profiles are calculated by an average of 5 rows from the evaluated AFM micrograph. The colors of the profiles are in agreement with the corresponding Raman spectra of the measured NFs given in the main text in Figure 2 and Figure 3.

The strong difference in optical contrast for NFs differing in only a few numbers of quintuple layers (8 nm to 13 nm) makes the OC a reliable tool to estimate the NF thicknesses. Different color regimes can be assigned according to the NF heights with very bright, yellowish NFs (< 9 nm), brown-orange NFs (9-12 nm) and dark brown to almost black appearing NFs (> 12 nm). A representative area of the gold sample with

$Bi_2Se_3$ NFs of varying OC is shown in Figure S3(d) to give an impression of the strongly varying contrast for NFs on gold differening by only a few nm in thickness.

The OC was assigned to certain NF thicknesses by evaluating Atomic Force Microscopy (AFM) measurements of the NFs. AFM measurements were taken on a commercial AFM setup (Q-Scope TM250 Nomad, Ambios Technology Corporation, California) with a 40 x 40 µm scan head in tapping mode. For each $Bi_2Se_3$ ($Bi_2Te_3$) NF an area of 12 µm$^2$ (10 µm$^2$) was scanned with a scanning resolution of 300 rows, leading to a lateral resolution of of 0.04 µm (0.033 µm). A topography measurement of a representative $Bi_2Te_3$ NF is shown in Figure S3(c). Horizontal line profiles (parallel to the AFM scanning direction) of the NFs were fit by a step height function to determine the thickness of the NFs. Profiles of all NFs investigated by Raman spectroscopy are shown in Figure S3(e,f). The colors of the profiles correspond to the Raman spectrum of each NF shown in the main text in Figure 2 and Figure 3.

The correlation between the OC and NF thickness is readily fit by a linear function in the investigated thickness regime between 8 nm and 20 nm, as shown in Figure S3(a). We find a six times stronger dependency of the OC on the NF thickness for $Bi_2Se_3$ than for $Bi_2Te_3$:

$$OC^{\mathrm{Bi2Se3}} \propto -6.822 + (5.04\ \pm 0.357)\ \cdot d^{\mathrm{Bi2Se3}}$$

(S7)

$$OC^{\mathrm{Bi2Te3}} \propto 23.842 + (0.76\ \pm 0.068)\ \cdot d^{\mathrm{Bi2Te3}}$$

(S8)

Since the uncertainty in *d* determined from AFM measurements is about ± 1 nm the *OC* gives a precise value for the NF thickness and a direct control in the micro-Raman measurements. This is important as the NFs show a strong change in Raman response for thicknesses between only 8 nm and 13 nm. Hence, the linear dependence of *OC* with *d* allows to correlate the OC with a certain NF height. The correlated NF thicknesses $d^{\mathrm{corr}}$ according to the relations given in Eq.(S7) and Eq.(S8) (see Table S5) were used to plot the Raman spectra fit parameters as a function of NF thickness in Figure 2(b-d), Figure 3 (b-d) and Figure 4(a,e) in the main text. From Table S5 it is apparent that the correlated thicknesses $d^{\mathrm{corr}}$ vary by < 5 % from the actually measured thicknesses $d^{\mathrm{AFM}}$.

**Table S5.** Measured optical contrasts and NF thicknesses for the thickness dependent Raman study.

| **$Bi_2Se_3$** | | | **$Bi_2Te_3$** | | |
|---|---|---|---|---|---|
| ***OC*** | **$d^{\mathrm{AFM}}$ from height profiles (nm)** | **$d^{\mathrm{corr}}$ correlated to *OC* (nm)** | ***OC*** | **$d^{\mathrm{AFM}}$ from height profiles (nm)** | **$d^{\mathrm{corr}}$ correlated to *OC* (nm)** |
| 56.18 | 12.56 ± 1.4 | 12.47 ± 0.9 | 37.40 | 18.26 ± 1.4 | 17.74 ± 1.5 |
| 44.83 | 9.92 ± 0.8 | 10.23 ± 0.7 | 36.56 | 16.07 ± 1.0 | 16.69 ± 1.5 |
| 42.85 | 10.10 ± 0.8 | 9.89 ± 0.7 | 34.45 | 13.22 ± 1.3 | 13.88 ± 1.2 |
| 42.38 | 9.80 ± 1.3 | 9.79 ± 0.7 | 31.99 | 11.37 ± 0.9 | 10.66 ± 0.9 |
| 39.48 | 8.97 ± 0.6 | 9.10 ± 0.6 | 31.30 | 10.18 ± 0.9 | 9.76 ± 0.9 |
| 31.51 | 7.90 ± 1.0 | 7.71 ± 0.5 | 31.38 | 9.44 ± 1.2 | 9.86 ± 0.9 |
| | | | 30.62 | 10.04 ± 1.0 | 8.87 ± 0.8 |

## 4.2 Influence of NF lateral dimensions

For every NF at least three spectra were accumulated, which showed no change in phonon frequency or intensity warranting the robust laser spot positioning ensured by closed-loop piezos. The small laser spot size of *d* = 211 nm, larger lateral dimensions of the NFs (at least 1.5 µm), and optical control of laser spot position ensured that the NFs were illuminated at their center and not at the edge. Measurements at the edge would have resulted in lower spectra intensities due to the higher amount of contributing substrate. This ensures that all observed renormalizations are connected to the NFs thickness and not to their lateral dimensions or forms.

## 4.3 Symmetry properties of phonons – Polarization study

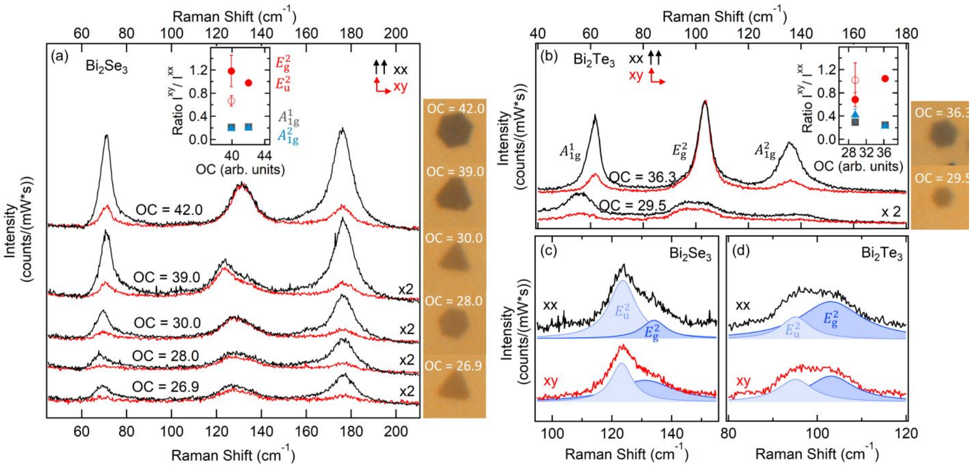

**Figure S4.** Polarization dependence of phonons in Bi$_2$Se$_3$ and Bi$_2$Te$_3$ NFs of varying thicknesses. (a,b) Raman spectra obtained in parallel (black) and cross (red) polarization configuration of five Bi$_2$Se$_3$ and two Bi$_2$Te$_3$ NFs with varying OC, respectively. Spectra of each NF are displayed with offsets and spectra of thinner NFs are multiplied by factor 2. The insets show the intensity ratio of the four phonon modes extracted from fits in both polarization configurations. For Bi$_2$Se$_3$ the results of the two thicker NFs with OCs of 39 and 42 are shown. (c,d) Deconvolution of the phonon mode contributions to the modes around 125 cm$^{-1}$ and 100 cm$^{-1}$ for Bi$_2$Se$_3$ and Bi$_2$Te$_3$ ,respectively. Deconvolutions are given for spectra obtained in both polarization configurations.

To confirm the symmetry properties of the measured bulk phonons and phonons emerging for thin Bi$_2$Se$_3$ and Bi$_2$Te$_3$ NFs placed on a gold substrate a polarization study was conducted. Both Bismuth chalcogenides crystallize with a rhombohedral crystal structure and belong to the point group D$_{3d}$[5]. With five atoms in the primitive unit cell there exist 15 lattice vibration modes whose irreducible representations at the Brillouin zone center (q=0) are given as $\Gamma = 2A_{1g} + 3A_{1u} + 2E_g + 3E_u$ .[6] Of these lattice vibration 12 correspond to optical phonons with symmetries $2A_{1g} + 2A_{1u} + 2E_g + 2E_u$ where the in-plane vibrational modes with E-symmetry are two-fold degenerate due to the hexagonal lattice structure. These modes are either Raman or infrared (IR) active due to the inversion symmetry of the crystal. There are four even-parity Raman active phonons, $E_g^1$+$A_{1g}^1$ + $E_g^2$+$A_{1g}^2$ and four odd-parity IR active phonons, $E_u^1$+$A_{1u}^1$+$E_u^2$+$A_{1u}^2$. It is known, that the IR active phonons can become Raman active upon the breaking of inversion symmetry at the crystal surface leading to the reduction of the point group to $C_{3v}$.[7] In Table S7 we give an overview about reported detection of IR modes in $Bi_2Se_3$ and $Bi_2Te_3$ by Raman spectroscopy. We can identify the symmetry of the bulk Raman modes and Raman-active IR modes emerging at the surface by exploiting the Raman selection rules for both point groups. In the $C_{3v}$ point group the irreducible representations $A_{1g}$ and $A_{2u}$ merge into $A_1$, $A_{2g}$ and $A_{1u}$ merge into $A_2$, and $E_g$ and $E_u$ merge into E.[7] The Raman selection rules for the bulk and surface point group for parallel (xx) and cross polarization (xy) scattering geometry are given in Table S6.

**Table S6.** Raman selection rules for the different point groups representing the bulk and the surface for different scattering geometries.[8]

| Scattering geometry | Bulk ($D_{3d}$) | Surface ($C_{3v}$) |
|---|---|---|
| XX (parallel) | $A_{1g}$ + $E_g$ | $A_1$ + E |
| YX (cross) | $A_{2g}$ + $E_g$ | $A_2$ + E |

**Table S7.** Overview of observed bulk IR modes becoming Raman active in Raman measurements of $Bi_2Se_3$ and $Bi_2Te_3$ samples in comparison with the values reported in this work. All frequencies from modes with A and E symmetry are given in $cm^{-1}$.

| Ref. | sample | Temperature | Bulk Raman modes | | | Raman active bulk IR modes | | | |
|---|---|---|---|---|---|---|---|---|---|
| | | | $A_{1g}^1$ | $E_g^2$ | $A_{1g}^2$ | $E_u^1$ | $A_{1u}^1$ | $E_u^2$ | $A_{1u}^2$ |
| | $Bi_2Se_3$ | | | | | | | | |
| [9] | Crystal | 3 K | 73.3 | 132.9 | 175.4 | 68 | 129 | 125 | 160 |
| [10] | Thin film (6 nm) | 80 K | 74.0 | 135.0 | 177.0 | - | - | 134 | 159 |
| [11] | Thin film | 13 K | 75 | 137 | 180 | 67 | 136 | 126 | 158 |
| [2] | NFs (~9 nm) | 160 K | 71.5 | 131.0 | 174.6 | - | - | - | 158 |
| This work | NF on Au (10 nm) | 300 K | 68 | 128 | 173 | - | - | 124 | - |
| | $Bi_2Te_3$ | | | | | | | | |
| [12] | Thin film (7 nm) | 300 K | 61 | 102 | 134 | - | 95 | - | 108 |
| [13] | Thin plates (11 nm) | 300 K | | | | | 93 | - | 113 |
| [2] | NFs (~13 nm) | 100 K | 63.2 | 105.2 | 137.8 | - | 98 | - | 113 |
| This work | NF on Au (~10nm) | 300 K | 61 | 102 | 133 | - | - | 93 | - |

Figure S4(a) and (b) shows Raman spectra of NFs on gold substrate with varying thicknesses in cross and parallel polarization configuration for $Bi_2Se_3$ and $Bi_2Te_3$, respectively. For both materials, the bulk $A_{1g}$

modes significantly decrease in cross polarization mode, whereas the intensity of the bulk $E_g$ mode stays constant in agreement with the $D_{3d}^5$ selection rules. The emerging modes splitting from the $E_g^2$ phonons at lower energies are detected in both parallel and cross polarization. This is shown in more detail in Figure S4(c) and (d) for a thin $Bi_2Se_3$ and $Bi_2Te_3$ NF, respectively. Since this mode is detected in both scattering configurations they can only belong to modes with E symmetry of the $C_{3v}$ point group. These modes include the bulk IR modes of $E_u$ symmetry. For $Bi_2Se_3$ the observed frequency of the emerging mode agrees well with frequencies for the IR $E_u^2$ mode around 125 $cm^{-1}$ from IR reflectance measurements[6,14] and ab-initio calculations.[15] Furthermore, the appearance of this mode in Raman spectra has been observed at for single crystal and thin film samples as shown in Table S7. Similarily, the emerging split mode in $Bi_2Te_3$ is also assigned to the IR $E_u^2$ mode whose frequency again fits well to frequencies of the bulk IR $E_u^2$ mode at 95 $cm^{-1}$ from experiments[6] and ab initio calculations.[15] According to literature a mode with very similar frequency around 93-95 $cm^{-1}$ has been observed in thin film samples (see Table S7) and was also assigned to a Raman active IR-mode, however, with $A_{1u}$ symmetry. The $A_{1u}^1$ and $E_u^2$ phonons in $Bi_2Te_3$ have very similar frequencies[6,15], hence making their differenciation difficult. Our polarization study excludes the possibility of this mode belonging to the $A_{1u}$ symmetry due to the Raman selection rules of the $C_{3v}$ point group, which mark the $A_2$ mode (includes the bulk $A_{1u}$) forbidden for the parallel scattering configuration. Since we detect the emerging IR mode with identical intensity in parallel and cross scattering configuration as shown in Figure S4(b) and (d) we unambiguously assign it to the Raman active IR $E_u^2$ phonon mode.

## 4.4 Estimated injected carrier density for $Bi_2Se_3$ NFs on gold

The injected carrier density $\sigma$ is estimated assuming a plate condensator geometry, where carriers from the gold are injected into the first quintuple layer of $Bi_2Se_3$. With an estimated band bending potential in the first $d$=1 nm of $\varphi$ =0.7 eV (see Figure 4) this corresponds to an injected carrier density of:

$$\sigma = \frac{U \varepsilon\, \varepsilon_0}{d\, e} \approx \frac{0.7\ \mathrm{V}\ \cdot 8.854 \cdot 10^{-12}\mathrm{C}\ (\mathrm{Vm})^{-1} \cdot \varepsilon}{10^{-9}\ \mathrm{m}\ \cdot\ 1.602\ 10^{-19}\ \mathrm{C}} \approx\ 3{,}8 \cdot 10^{12}\ \mathrm{cm}^{-2}$$

## 4.5 Interface-enhanced Raman scattering in $Bi_2Te_3$ NFs on gold

Additional Raman spectra of two thicker $Bi_2Te_3$ NFs are displayed in Figure S5(a) in comparison with Figure 3(a) in the main text. For $Bi_2Te_3$ NFs on gold substrates a similary strong non-linear increase in Raman response by about 65 % is observed for thick NFs ($d$ > 10 nm), as shown in Fig. S5(b). The scattering volume corrected intensities are constant for thick NFs and abruptly decrease at a critical thickness of 10.6 ± 0.8 nm, determined from sigmoidal fits of the $A_{1g}^2$ and $E_g^2$ mode intensities extracted from Lorentzian fits. Intensities extracted from the $A_{1g}^1$ mode show a slightly higher critical thickness of 13.6 ± 0.3 nm.

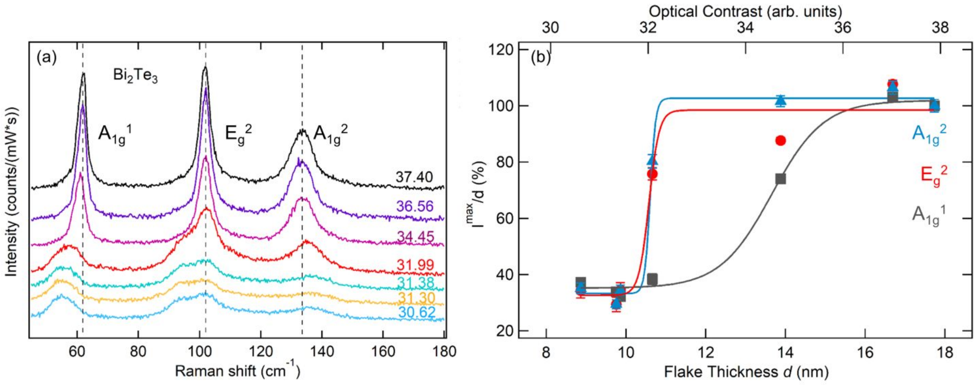

**Figure S5.** Carrier injection induced Raman enhancement in $Bi_2Te_3$ NFs on gold substrate. (a) Raman spectra of seven $Bi_2Te_3$ NFs with decreasing optical contrast given next to the spectra. (b) Scattering volume corrected intensities of the three measured phonon modes as a function of NF thickness with sigmoidal fits. Intensities are normalized to the value of the thickest NF.

## 5. Optical response of Au Substrate

Measurements of the complex dielectric function of the employed gold substrate were conducted on a SENpro spectroscopic ellipsometer (SENpro, SENTECH INstruments) in the spectral range between 1.4 eV to 3 eV with an incident angle of 70 °. The dielectric function shown in Figure S6(a,b) agrees well with measurements obtained from planar gold films in literature.[16,17] The Drude response at low energies corresponds to a plasma frequency of $\hbar\omega_p = 8.67$ eV and lies in the typical range for gold substrates.[16] Modelling the dielectric function by two additional Lorentz oszillators at 2.72 eV and 3.22 eV we extracted the refractive index *n* and extinction coefficient *k* shown in Figure S6(c,d). The Lorentz oscillators at higher energies are attributed to interband transitions that are characteristic for gold substrates. Our measurements do not indicate any significant features at our employed Raman excitation energy of 1.96 eV and, therefore, plasmonic SERS effects coupling to surface plasmon polaritons, which are present in nanoporous gold thin films,[17] can be excluded.

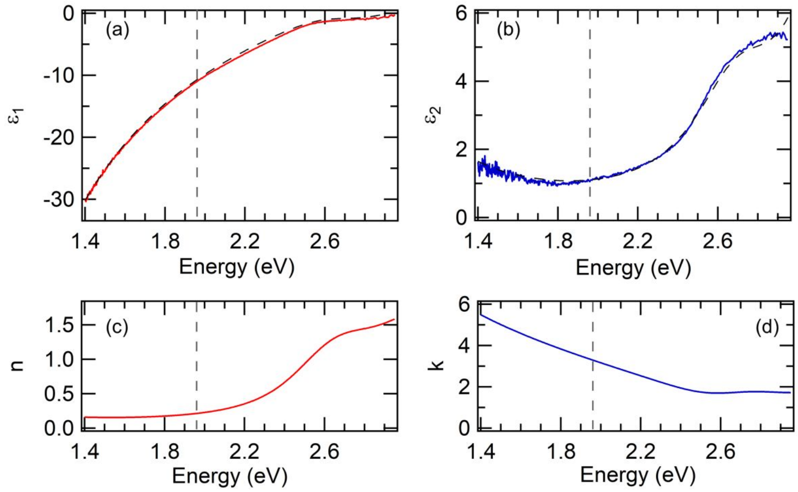

**Figure S6.** Pseudo dielectric function with the real part $\varepsilon_1$ in (a) and imaginary part $\varepsilon_2$ in (b) obtained from ellipsometrie measurements on the gold substrate employed for all Raman measurements. Dashed graph correspond to the Drude-Lorentz fit function. (c) Refractive index *n* and (d) extinction coefficient *k* of the gold substrate. The grey dashed line corresponds to the excitation laser energy of 1.96 eV used for the thickness dependent Raman studies.

## References

(1) Buchenau, S.; Akinsinde, L. O.; Zocher, M.; Rukser, D.; Schürmann, U.; Kienle, L.; Grimm-Lebsanft, B.; Rübhausen, M. Scalable Polyol Synthesis for Few Quintuple Layer Thin and Ultra High Aspect Ratio Bi2Se3 Structures. *Solid State Commun.* **2018**, *281* (March), 49–52. https://doi.org/10.1016/j.ssc.2018.07.003.

(2) Buchenau, S.; Scheitz, S.; Sethi, A.; Slimak, J. E.; Glier, T. E.; Das, P. K.; Dankwort, T.; Akinsinde, L.; Kienle, L.; Rusydi, A.; Ulrich, C.; Cooper, S. L.; Rübhausen, M. Temperature and Magnetic Field Dependent Raman Study of Electron-Phonon Interactions in Thin Films of Bi2se3 and Bi2te3 Nanoflakes. *Phys. Rev. B* **2020**, *101* (24), 1–8. https://doi.org/10.1103/PhysRevB.101.245431.

(3) Schulz, B.; Bäckström, J.; Budelmann, D.; Maeser, R.; Rübhausen, M.; Klein, M. V.; Schoeffel, E.; Mihill, A.; Yoon, S. Fully Reflective Deep Ultraviolet to near Infrared Spectrometer and Entrance Optics for Resonance Raman Spectroscopy. *Rev. Sci. Instrum.* **2005**, *76* (7).

https://doi.org/10.1063/1.1946985.

(4) Glier, T. E. Applications of Functional One-Dimensional Nanostructures Studied by Light Scattering Dissertation, Universität Hamburg, 2021.

(5) Zhang, J.; Peng, Z.; Soni, A.; Zhao, Y.; Xiong, Y.; Peng, B.; Wang, J.; Dresselhaus, M. S.; Xiong, Q. Raman Spectroscopy of Few-Quintuple Layer Topological Insulator Bi 2Se3 Nanoplatelets. *Nano Lett.* **2011**, *11* (6), 2407–2414. https://doi.org/10.1021/nl200773n.

(6) Richter, W.; Kohler, H.; Becker, C. R. A Raman and Far-Infrared Investigation of Phonons in the Rhombohedral V2-VI3 Compounds. *Phys. Stat. Sol.* **1977**, *84*, 619.

(7) Kung, H. H.; Salehi, M.; Boulares, I.; Kemper, A. F.; Koirala, N.; Brahlek, M.; Lošťák, P.; Uher, C.; Merlin, R.; Wang, X.; Cheong, S. W.; Oh, S.; Blumberg, G. Surface Vibrational Modes of the Topological Insulator Bi2Se3 Observed by Raman Spectroscopy. *Phys. Rev. B* **2017**, *95* (24), 1–9. https://doi.org/10.1103/PhysRevB.95.245406.

(8) Cardona, M. *Light Scattering in Solids II*; Cardona, M., Güntherodt, G., Eds.; Springer Berlin Heidelberg, 1982.

(9) Gnezdilov, V.; Pashkevich, Y. G.; Berger, H.; Pomjakushina, E.; Conder, K.; Lemmens, P. Helical Fluctuations in the Raman Response of the Topological Insulator Bi2Se3. *Phys. Rev. B - Condens. Matter Mater. Phys.* **2011**, *84* (19), 1–5. https://doi.org/10.1103/PhysRevB.84.195118.

(10) Eddrief, M.; Atkinson, P.; Etgens, V.; Jusserand, B. Low-Temperature Raman Fingerprints for Few-Quintuple Layer Topological Insulator Bi2Se3 Films Epitaxied on GaAs. *Nanotechnology* **2014**, *25* (24). https://doi.org/10.1088/0957-4484/25/24/245701.

(11) Kung, H. H.; Salehi, M.; Boulares, I.; Kemper, A. F.; Koirala, N.; Brahlek, M.; Lošťák, P.; Uher, C.; Merlin, R.; Wang, X.; Cheong, S. W.; Oh, S.; Blumberg, G. Surface Vibrational Modes of the Topological Insulator Bi2Se3 Observed by Raman Spectroscopy. *Phys. Rev. B* **2017**, *95* (24), 1–9. https://doi.org/10.1103/PhysRevB.95.245406.

(12) Wang, C.; Zhu, X.; Nilsson, L.; Wen, J.; Wang, G.; Shan, X.; Zhang, Q.; Zhang, S.; Jia, J.; Xue, Q. In Situ Raman Spectroscopy of Topological Insulator Bi2Te3 Films with Varying Thickness. *Nano Res.* **2013**, *6* (9), 688–692. https://doi.org/10.1007/s12274-013-0344-4.

(13) He, R.; Wang, Z.; Qiu, R. L. J.; Delaney, C.; Beck, B.; Kidd, T. E.; Chancey, C. C.; Gao, X. P. A. Observation of Infrared-Active Modes in Raman Scattering from Topological Insulator Nanoplates. *Nanotechnology* **2012**, *23* (45). https://doi.org/10.1088/0957-4484/23/45/455703.

(14) Laforge, A. D.; Frenzel, A.; Pursley, B. C.; Lin, T.; Liu, X.; Shi, J.; Basov, D. N. Optical Characterization of Bi2Se3 in a Magnetic Field: Infrared Evidence for Magnetoelectric Coupling in a Topological Insulator Material. *Phys. Rev. B - Condens. Matter Mater. Phys.* **2010**, *81* (12), 1–8. https://doi.org/10.1103/PhysRevB.81.125120.

(15) Cheng, W.; Ren, S. F. Phonons of Single Quintuple Bi2Te3 and Bi 2Se3 Films and Bulk Materials. *Phys. Rev. B - Condens. Matter Mater. Phys.* **2011**, *83* (9). https://doi.org/10.1103/PhysRevB.83.094301.

(16) Olmon, R. L.; Slovick, B.; Johnson, T. W.; Shelton, D.; Oh, S. H.; Boreman, G. D.; Raschke, M. B. Optical Dielectric Function of Gold. *Phys. Rev. B - Condens. Matter Mater. Phys.* **2012**, *86* (23), 1–9. https://doi.org/10.1103/PhysRevB.86.235147.

(17) Dixon, M. C.; Daniel, T. A.; Hieda, M.; Smilgies, D. M.; Chan, M. H. W.; Allara, D. L. Preparation, Structure, and Optical Properties of Nanoporous Gold Thin Films. *Langmuir* **2007**, *23* (5), 2414–2422. https://doi.org/10.1021/la062313z.

# Appendix C

# Supplementary Information: Quantum Confinement of the Spin Berry Phase on 1D topological surfaces of single $Bi_2Se_3$ nanowires

## Supplementary Information

# Quantum Confinement of the Spin Berry Phase on 1D topological surfaces of single $Bi_2Se_3$ nanowires

Christian Nweze*[1], Tomke E. Glier*[1], Sarah Scheitz[1], Lea Westphal[1], Florian Biebl[1], Sören Buchenau[1], Lewis O. Akinsinde[1,2], Niklas Kohlmann[2], Lorenz Kienle[2], Isabel González Díaz-Palacio[3], Robert Frömter[3], Robert Zierold[3], Robert Blick[3], Nils Huse[3], and Michael Rübhausen*[1]

[1]Institut für Nanostruktur- und Festkörperphysik, Center for Free Electron Laser Science (CFEL), Universität Hamburg, Luruper Chaussee 149, 22761, Hamburg, Germany

[2]Institute for Materials Science, Faculty of Engineering, Kiel University, Kaiserstrasse 2, 24143 Kiel, Germany

[3]Institut für Nanostruktur- und Festkörperphysik, Center for Hybrid Nanostructures (CHyN), Universität Hamburg, Luruper Chaussee 149, 22761, Hamburg, Germany

*corresponding authors: cnweze@physnet.uni-hamburg.de, tglier@physnet.uni-hamburg.de, ruebhausen@physnet.uni-hamburg.de – these authors contributed equally

## *SI 1 $Bi_2Se_3$ Nanowire Synthesis*

Single crystalline $Bi_2Se_3$ nanowires were fabricated inside a two-zone tube furnace equipped with a 2.5 cm diameter quartz tube in order to increase the vapour pressure. We followed the general approach outlined in ref. [1–5] and did a detailed optimization study. $Bi_2Se_3$ nanowires were grown on silicon ⟨100⟩ substrates *via* the vapour liquid solid (VLS) method using gold (Au) nanoparticles as catalyst. The silicon ⟨100⟩ substrates were cleaned in Piranha solution to remove organic residues, functionalized with a binding agent (0.1% w/v aqueous poly-L-lysine solution), and dipped in Au colloid solution (5–20 nm diameter) for 5 s.[3–8] Commercial grade $Bi_2Se_3$ granular (Sigma-Aldrich, purity 99.999 %) was used as source material. 0.2 g $Bi_2Se_3$ granular was placed in an alumina boat and loaded in the up-stream zone of the furnace. The Au coated silicon substrate was placed down-stream, pumped to a base pressure of 40 mTorr, and flushed multiple times with ultrapure argon gas to reduce oxygen residues. In a typical synthesis process, the up-stream and down-stream zone of the furnace were heated to 540 °C and 460 °C in 1 hour, respectively. The pressure was set to 780 mTorr and the carrier gas flow rate was 30 standard cubic centimetres per minute (sccm). The reaction duration was 1–3 hours (see Fig. S1(a) for schematic diagram). After reaction, the argon flow was switched off and the system was allowed to cool down in 2.5 h. This method provides selenium environment for passivating the wires forming a selenium oxide shell as confirmed by EFTEM (see Fig. S4). After the synthesis, we obtain nanowires on the silicon substrate as shown in Fig. S1(b). A custom-made X, Y, Z-positioner micro-manipulator with 51 mm long tungsten picoprobe tips (T-4-10) with a wire shaft diameter of 10 µm, a point radius < 0.1 µm, and a tip length of 3.3 mm was used to transfer the wires. The micro-manipulator was coupled to an optical microscope. By electrostatic charge, the wires were picked up by the tungsten picoprobe tip (Fig. S1(c)) and transferred onto silicon finder-grid substrates (Micro to Nano EM-Tec FG-1 Silicon Finder Grid Substrate with 144 fields of 1x1 mm).

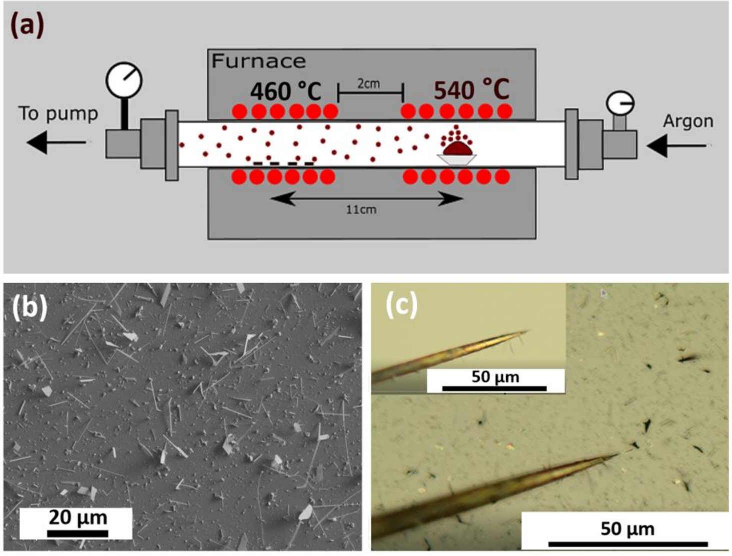

**Fig. S1:** (a) Schematic diagram of VLS**.** During synthesis, the up-stream zone and down-stream zone of the oven are accurately set to 540 °C and 460 °C, respectively. (b) SEM image of a silicon substrate containing mostly nanowires. (c) Tungsten picoprobe tip picking up nanowires (the inset shows the tungsten tip with some nanowires lifted above the silicon substrate).

## *SI 2 Sample Characterization*

### *SI 2.1 Scanning Electron Microscopy (SEM)*

Pre-characterization of all nanowires that were measured by Raman spectroscopy was carried out by SEM. The nanowires' shape and diameter were studied with a commercial field emission electron microscope (ZEISS ΣIGMA). For a good resolution and signal to noise ratio, the in-lens detector for secondary electrons was used with an acceleration voltage set between 1 kV and 8 kV and a working distance of approximately 3 mm with a magnification of up to 120,000 in order to determine the diameter of the nanowires. Fig. S2 shows nanowires of various diameters transferred on the silicon finder-grid for the Raman study. The diameters, lengths, and respective reaction times of all wires investigated *via* Raman spectroscopy are listed in Table S1.

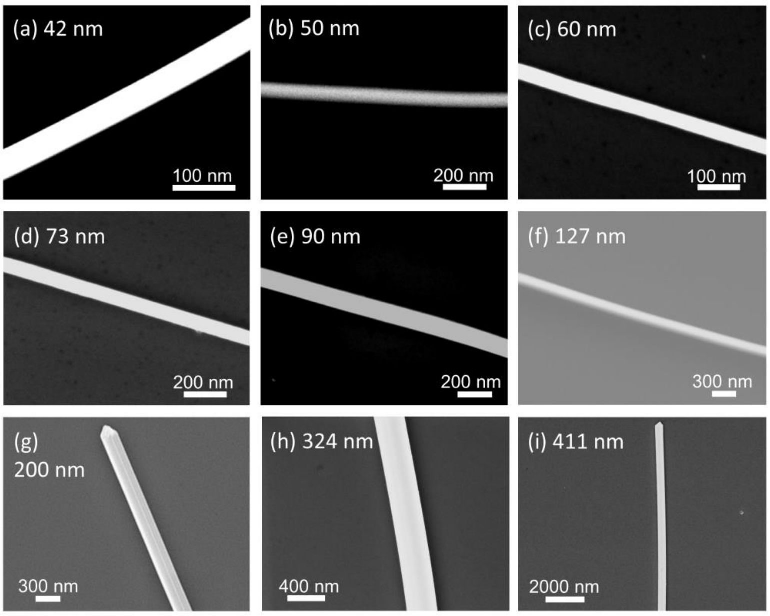

**Fig. S2:** SEM images of nanowires of various diameters transferred on silicon grids. The nanowires are arranged according to the diameter given in each panel.

**Table S1:** Diameter, length, and synthesis time for all $Bi_2Se_3$ nanowires that were measured by Raman spectroscopy.

| ***Diameter (nm)*** | ***Length (µm)*** | ***Reaction time (min)*** |
|---|---|---|
| 42 | 5.8 | 60 |
| 50 | 8.4 | 60 |
| 60 | 7.5 | 60 |
| 65 | 6.0 | 60 |
| 73 | 16.2 | 180 |
| 90 | 29.0 | 180 |
| 127 | 15.0 | 60 |
| 200 | 15.6 | 180 |
| 324 | 31.6 | 180 |
| 411 | 13.6 | 180 |

### *SI 2.2 Transmission Electron Microscopy (TEM) and Energy Dispersive X-ray Spectroscopy (EDX)*

TEM was carried out in order to determine the crystallinity as well as the growth direction of the nanowires as outlined in the main text. The nanowires were studied with a JEOL JEM-2100 TEM with 200 kV acceleration voltage and a LaB$_6$ cathode. The microscope is equipped with an Oxford Instruments EDX (Energy dispersive X-Ray) detector allowing the characterization of the stoichiometry of the wires. Energy filtered TEM and electron energy loss spectroscopy was carried out using a FEI Tecnai F30 G$^2$ STwin. The samples were transferred onto carbon coated Cu TEM grids by dry scraping from the Si wafer.

To ensure that the morphology of the wires matches those measured by SEM and micro-Raman, the examined samples were pre-characterized by SEM. Fig. S3(a) and (d) show comparisons between SEM images and TEM bright-field images of identical wires. Multiple wires with diameters ranging from 40 nm to 300 nm were measured by TEM, high resolution (HR)TEM, selected area electron diffraction (SAED), and EDX. Wires of all parameters were found to be single crystalline in Bi$_2$Se$_3$ $R\bar{3}m$ structure by SAED and HRTEM (see exemplary analysis in Fig. S3(b) and (e)). Very few crystal defects were found producing additional reflections in the SAED-patterns and FFTs. In combination with the TEM EDX giving on average a composition of 39 atm% Bi to 61 atm% Se with a standard deviation of 2 atm% , our synthesis route is proven to result in high-quality, single crystalline nanowires. The deviation from 2:3 ratio is within the margin of error. An exemplary spectrum can be seen in Fig. S3(c) where the bismuth and selenium peaks are clearly distinguishable. For the wire measured in Fig. S3(c) the composition was 38 atm% Bi to 62 atm% Se. The Cu peak is an artifact due to the use of a Cu TEM grid.

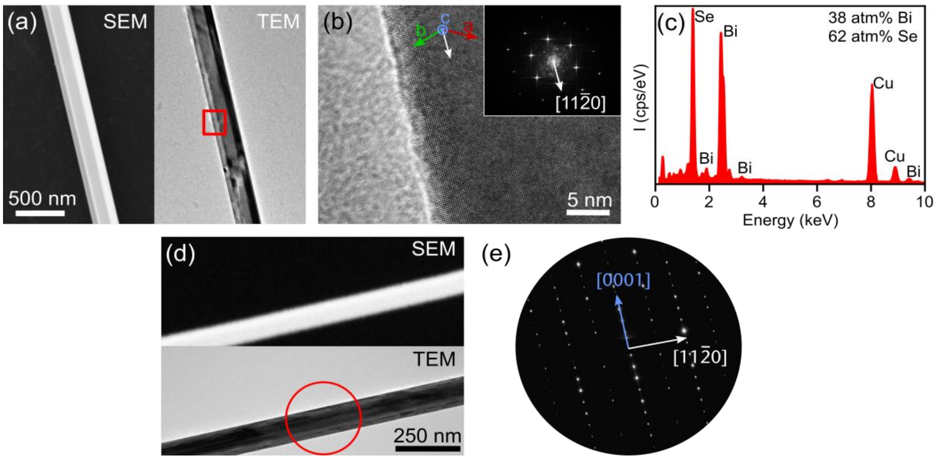

**Fig. S3:** SEM/TEM investigations of two nanowires with diameters of 280 nm, (a)-(c), and 105 nm, (d)-(e), respectively. (a) Comparison between SEM and TEM images of the same nanowire with a diameter of 280 nm. (b) HRTEM micrograph of the marked area from (a) with inset FFT showing the hexagonal symmetry due to the orientation along [0001]. (c) Energy dispersive X-ray (EDX) spectrum of the same wire with bismuth and selenium peaks as well as Cu from the TEM grid. A composition of 38 atm% Bi to 62 atm% Se was found for this wire. Averaging all measured wires gave a composition of 39 atm% Bi to 61 atm% Se with a variance of 2 atm%. (d) Comparison between TEM and SEM images of the identical wire with a diameter of 105 nm. (e) Selected area electron diffraction (SAED) pattern of the area marked in (d) confirming the growth of the wire orthogonal to the c axis. The wire was oriented along [2-1-10].

Specifically, with SAED and HRTEM, a growth direction of [11-20] was determined. The wires were oriented so that either the hexagonal symmetry of the structure becomes apparent in FFT/SAED, Fig. S3(b), or the stacking of the quintuple layers can be seen, Fig. 1(c). In the latter case, reflections (000l) are strongly excited in FFT/SAED (Fig. S3(e)), and the c direction is orthogonal to the elongated direction of the wire. These findings agree with other reports on $Bi_2Se_3$ nanowires grown by VLS.[1,3,5]

No difference in stoichiometry, crystallinity, and growth direction was found for wires of different diameters. This strongly indicates that the preparation method is robust and that the nanowires show no structural differences for different wire diameters.

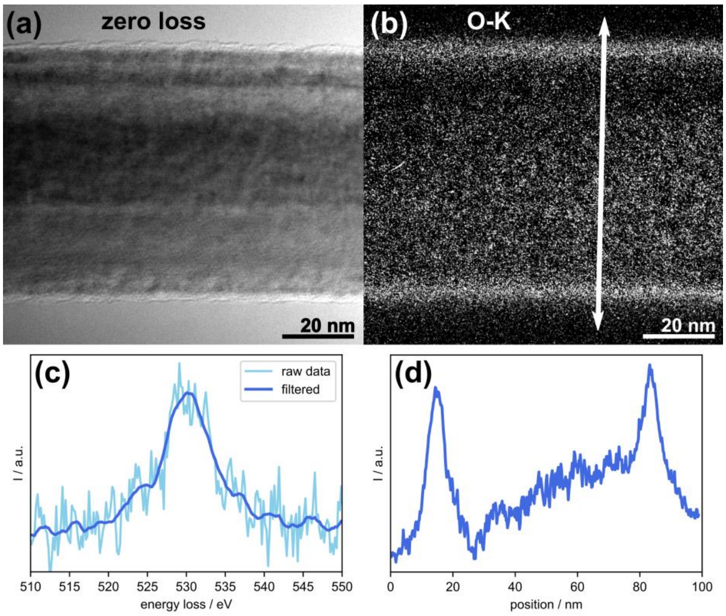

**Fig. S4:** (a) Zero loss filtered EFTEM micrograph of a single $Bi_2Se_3$ nanowire where an amorphous shell can clearly be seen. (b) EFTEM elemental map of the O-K edge at 530 eV of the identical nanowire and region from (a) showing oxygen to be mainly present towards the outer region of the nanowire. (c) Background subtracted O-K edge in the EEL spectrum. (d) Intensity scan across the O-K map from (b) with the intensity profile hinting at a core-shell like structure.

In Fig. S4(a) an amorphous oxide shell around the crystalline nanowire can clearly be observed (see also Fig. 1(c) in the main text). To investigate this shell, energy filtered TEM (EFTEM) as well as electron energy loss spectroscopy (EELS) are utilized. By comparing the zero loss filtered TEM micrograph in Fig. S4(a) with the O-K filtered micrograph in Fig. S4(b) it becomes evident that the amorphous layer coincides with the highest amount of oxygen. The clearly visible O-K edge in the EEL spectrum confirms the presence of oxygen (see Fig. S4(c)). Thus, the $Bi_2Se_3$ nanowires are found to have an amorphous oxide shell with a width of 1-2 nm as indicated by HRTEM and EFTEM. Detailed XPS studies show that $Bi_2Se_3$ both forms $SeO_2$ and $Bi_2O_3$ after prolonged exposure to ambient air [21]. It was found that the thickness of the oxide layer did not exceed 2 nm even after exposure to air for more than a week, which is in very good agreement with the findings from HRTEM. Additionally, first principle calculations showed that topological surface states in $Bi_2Se_3$ are robust against surface oxidation [22]. Thus, the nanowires in this work are both effectively protected against bulk oxidation by the formation of an oxide layer as well as having robustness in their topological surface states. From the Se rich atmosphere introduced towards the end of the synthesis process as well as the slight excess of Selenium observed in EDX it seems plausible that the oxide shell exhibits an excess of $SeO_2$ compared to $Bi_2O_3$.

### *SI 2.3 Atomic Force Microscopy (AFM)*

In order to obtain information on the nanowire shape, AFM measurements were conducted on several nanowires as shown in Fig. S5. A commercially available AFM Q-Scope 250 model with (40 x 40) µm scan head, a lateral resolution of 0.6 nm, and a vertical resolution of 0.05 nm was used to determine the shape of the nanowires. During the measurements, the cantilever was in intermittent contact and scanned along the x-axis (horizontal scan mode). The cylindrical cross-section of the nanowires (see Fig. 1(f) main text) confirms the shape obtained from SEM.

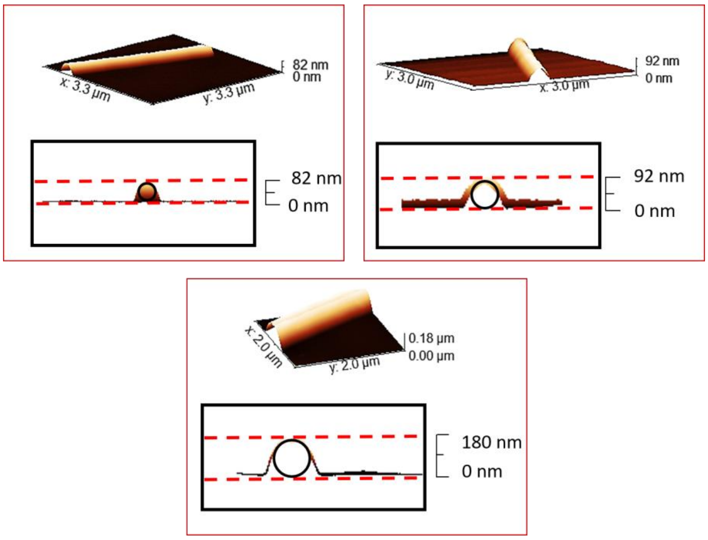

**Fig. S5:** 2D and cross-sectional AFM images of exemplary wires showing an effective circular cross section.

## *SI 3 Raman Measurements*

Raman measurements on $Bi_2Se_3$ nanowires were obtained by the UT-3 Raman spectrometer [9] and by using a custom-made Raman microscope with a spot FWHM of the focused beam on the sample of (544 ± 13) nm. A CAD drawing of this setup is shown in Fig. S6. As laser source, a 532 nm Millennia Pro Xs 10sJS diode laser (Spectra Physics Lasers Inc., California) was used. The incoming laser beam was widened with a spatial filter to a diameter of around 12 mm and focused on the sample through the infinity corrected 50X objective Plan Apo NA = 0.55 (Mitutoyo, Japan). At the sample, a laser power of 140 µW was measured. By using a multi-axis piezo scanner P-517 in combination with the controller E-710.3CD (PI, Germany), the sample was moved along the wire axis with a speed of 250 nm/s in order to avoid sample damage during the measurement by excessive heating. The reflected light and Raman signal were focused on the entrance objective using an objective IC50 (Olympus, Japan).

The Mitutoyo objective was used in combination with the MT-40 accessory tube lens (Mitutoyo, Japan), a color industrial camera DFK 37AUX264 (The Imaging Source, Germany), and a LED lamp QTH10/M (Thorlabs, USA) to obtain an optical microscope image of the nanostructure with a magnification of 50X. In this way, the laser spot could be placed precisely on the nanowire before and during the measurement. A motorized mirror was reproducibly driven in and out to switch between the optical microscope mode and the Raman mode (Nanotec, Germany). Fig. S7 shows an image of the green laser spot on a bare silicon substrate as well as intensity cuts through the 2D image in three different directions, which could be fitted with a gaussian profile resulting in a FWHM of around 540 nm.

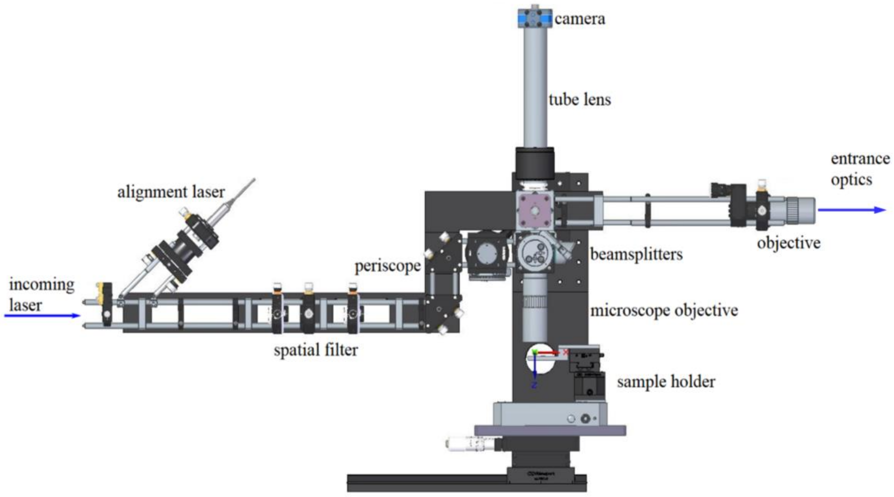

**Fig. S6:** CAD drawing (Solid Edge 2020, Siemens PLM Software) of the used Raman microscope setup. The incoming laser beam (532 nm, Millenia laser) passes a spatial filter and is focused on the sample with a microscope objective (Mitutoyo). In Raman mode, the reflected light is redirected and focused on the entrance objective. The motorized mirror that redirects the beam towards of the entrance objective can be moved out in order to create an optical microscope image. The optical microscope mode contains the LED lamp (Thorlabs), a tube lens (Mitutoyo) as well as the color industrial camera (The Imaging Source).

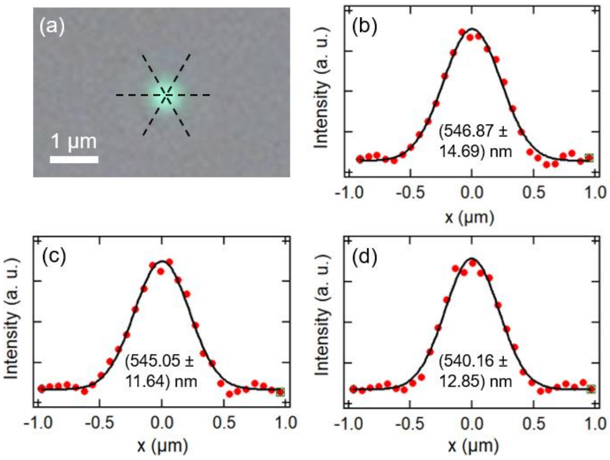

**Fig. S7:** (b) – (d) Intensity cuts through the 2D image of the green (532 nm) laser spot shown in (a) in three directions (dashed lines). The image was recorded with the color industrial camera DFK 37AUX264 (The Imaging Source, Germany) as described above (see Fig. S6). The laser spot was focused on a bare silicon substrate. The cuts were fitted by a Gaussian profile with a FWHM of around (544 ± 13) nm.

## *SI 4 Magnetic Field Dependent Raman Measurements*

Two bar magnets (each 500 mT) were used to create a magnetic field along the wire direction. An aluminum construction as shown in Fig. S8(a) was applied to hold the magnets. The distance between the magnets was set to 7 mm by using two screws. A magnetic field of 80 mT was measured at the sample position by using a Hall effect sensor GM05 (Hirst Magnetic Instruments Ltd., UK). The single $Bi_2Se_3$ nanowires on their silicon substrate were placed in the middle of the sample holder and aligned parallel to the polarization of the laser light and the magnetic field. Firstly, the sample was measured in the construction without the magnets, secondly the magnets were added to the setup and the Raman measurement was repeated. Thirdly, the measurement was reproduced without the magnets. This procedure was done for two wires – a 62 nm diameter wire as shown in the main text in Fig. 3(d) and a 90 nm wire as shown in Fig. S8(b).

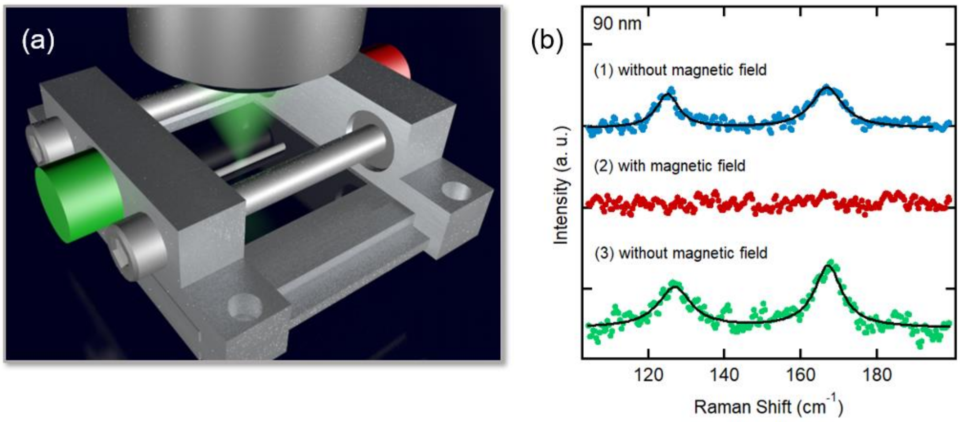

**Fig. S8:** (a) Sample holder with two movable clamps, which hold two bar magnets with a magnetic field of 500 mT. By using a distance of 7 mm between the magnets, a magnetic field of 80 mT was achieved at the sample position and the numerical aperture of the Mitutoyo 50X Plan Apo objective was not obscured. (b) Raman data of a 90 nm wire (1, blue) without magnetic field, (2, red) with magnetic field (80 mT) and (3, green) without magnetic field.

## *SI 5 Data Analysis*

The Raman spectra were corrected by subtraction of a substrate measurement, which was recorded under same conditions as the respective nanowire measurement. Furthermore, the data were divided by the laser power on the sample (140 µW) and used integration time (usually 1800 s). For Fig. 2(c) and (d) in the main text, the intensity was divided by the wire diameter squared in order to correct the Raman intensity for the scattering volume.

## *SI 6 Line Shape Analysis*

As expected, the line shapes to the phonons develop due to the interaction with plasmonic excitations into a Fano, i.e., an asymmetric line shape. For the analysis shown in Fig. S9 we have used the following simplified Fano equation [13]

$$I(\omega)_{Fano} = C_{Fano}\frac{(q+\varepsilon)^2}{(1+\varepsilon^2)} \qquad \text{(S1)}$$

with

$$\varepsilon = \frac{\omega - \omega_0}{\Gamma}\,. \qquad \text{(S2)}$$

Fig. S9 clearly reveals a strong enhancement of the Fano Parameter of the $E_g^2$-mode in the 1D case. The wire with a width of 411 nm, which we consider to be in the 2D-limit, shows sharp and symmetric line shapes with Fano parameters of $q$ = -67 and $q$ = +109. This strongly suggests Lorentzian type line shapes as expected from eq. (S1) in the limit of large Fano parameters. Clearly asymmetric are parameters with a magnitude below 30, which is evident for the $E_g^2$-mode with $q$ = -10.3 for the 50 nm wire. This change is accompanied by changes in mode frequencies and phonon widths, which we would expect from a phonon interacting with an electronic continuum due to the resulting phonon self-energy effects. Even though it is quite compelling now to fit the entire data set with Fano profiles instead of Lorentzian profiles we have to issue a number of warnings. Firstly, eq. (S1) and (S2) are just a simplified approximation for phonons interacting with an constant continuum of electronic states. Secondly, the assumption that there is only one type of electron-phonon interaction that needs to be considered might not hold. A more detailed analysis of the spectra requires an even better understanding of the observed electronic background (see e.g. [14]) and especially to make sure that there are no contributions coming from the Silicon substrate and from stray light. Thirdly, in order to make the fit meaningful with respect to the observed intensity of the phonon, we have to take into account that the asymmetry parameter also acts to amplify the mode intensity. Thus, $q$ and $C_{\text{Fano}}$ are coupled and it requires an excellent and constant signal to noise for all wire diameters to derive meaningful parameters of both $q$ and $C_{\text{Fano}}$. Since our signal and in the same regard the signal to noise ratio strongly varies with wire diameter, we refrain from doing a full Fano analysis according to eq. (S1) and (S2), especially as we would also expect that the required assumptions for theses simplified equations are not fulfilled. With all these warnings in mind, we show the fit results of a Fano-Fit to the data in Table S2. For exemplary samples in the 1D-limit (50 and 60 nm), we find reproducibly Fano paramters in the $E_g^2$ mode reaching -11.6 and below. Phonon frequencies increase in the 1D samples (hardening) and the widths are increased (broadening) compared to the 2D limit. These results indeed indicate the interaction of the phonons with a novel electronic state.

**Table S2:** Wire diameter and essential fit parameters of the samples with the strongest signal.

| ***Wire Diameter [nm]*** | ***$E_g^2$-Mode [Fit Parameters]*** | ***$A_{1g}^2$-Mode [Fit Parameters]*** |
|---|---|---|
| 411 (2D) | q = - 67,0 ± 0.009 | q = 109,3 ± 0.005 |
| | ω = 125,3 ± 0.005 | ω = 166,99 ± 0.004 |
| | Γ = 5.07 ± 0.005 | Γ = 6.2 ± 0.004 |
| 60 (1D) | q = -11,6 ± 2.52 | q = 140 ± 286 |
| | ω = 127,04 ± 0.24 | ω = 168,6 ± 0.29 |
| | Γ = 5.5 ± 0.247 | Γ = 7.3 ± 0.28 |
| 50 (1D) | q = -10,30 ± 1.9 | q = 156 ± 338 |
| | ω = 126,27 ± 0.23 | ω = 167,51 ± 0.22 |
| | Γ = 5.5 ± 0.236 | Γ = 6.98 ± 0.23 |

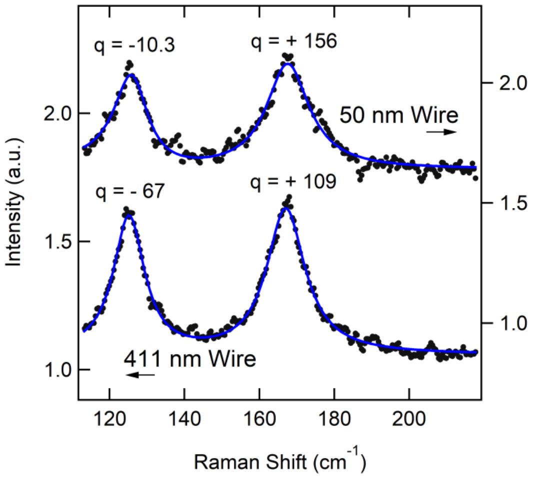

**Fig. S9:** Line shape analysis of a wire in the 1D-limit (50 nm diameter) and 2D-limit (411 nm diameter). The Fano parameters for the $E_g^2$- and $A_{1g}^2$-modes are given in the figure. Please note the substantial change in Fano-parameter of the $E_g^2$-mode from -67 (411 nm), which can be regarded as symmetric to -10.3 (50 nm), which is clearly asymmetric. Please note that the widths of the phonons for the 50 nm wire is clearly enhanced indicating substantial self-energy effects of the phonons in the 1D-limit.

## *SI 7 Calculation*

We follow in our calculation a non-resonant Raman matrix element that couples *via* a local field enhancement, conventionally by means of a plasmonic excitation, to a phonon mode. The Feynman diagram in Fig. S10(a) represents a four-photon Greens function encoding Stokes and Anti-Stokes processes.[11] The photon field is represented by the vector potential of the electromagnetic field. Coupling of photons to free charged particles occurs *via* the kinetic energy term of the electrons

$$H_{kin} = \frac{\vec{p}^2}{2m} \qquad \text{(S3)}$$

with $\vec{p} \rightarrow \vec{p} - \frac{e}{c}\vec{A}$ leading to

$$H = \frac{\vec{p}^2}{2m} + \frac{e^2}{c^2}\vec{A}^2 + \frac{e}{c}\vec{p}\vec{A} = H_{kin} + H_{A^2} + H_{pA} = H_{kin} + H_{\text{int}} \quad . \qquad \text{(S4)}$$

The quadratic term in the verctor potential $\vec{A}$ of the interaction Hamiltonian $H_{\text{int}}$ allows a non-resonant coupling in first order perturbation theory, whereas the linear term requires second order perturbation theory and becomes resonantly enhanced. In our case, however, without impurity activation, IR excitation, or in off-resonance conditions, we can disregard this term. A Raman process always requires two photon fields. One is the incident photon field and the second one is created together with an elementary excitation of matter. The coupling constant of the non-resonant term is determined by the ratio of $e^2/c^2$ with e being the elementary charge of an electron and c is the velocity of light. Since the photon energy is of the order of a few eV, the resonant term requires typically interband transitions leading to resonant Raman scattering. If the energy of the photon field and the excited electrons are drastically different, the non resonant term will dominate $H_{\text{int}}$. If the involved electronic excitations couple to phonons *via* the electron-phonon coupling constant $g(q)$, the four photon Greens function (ref [11]) can be expressed by a Feynman diagram shown in Fig. S10(a). However, the calculation of this Feynman diagram in our case is possible only with a number of strong simplifications, that we would like to outline in the following. Firstly, we assume that the non-resonant coupling constant gets amplified by a local field due to the build up of charges on the surface of a topological nanowire.[10] This enhances the coupling constant leading to an effective locally enhanced field. Secondly, since optical photons are in the long wavelength limit at small momentum and the topological properties of the nanowire are also dominated by the physics of small momenta, we consider the coupling constant, especially $g(q)$, only at $q = 0$ and all other parameters only at small $k$. Then the Feynman diagram in Fig. S10(a) can be approximated by an effective coupling constant $M_0$ multiplied by the square of the plasmonic susceptibility $\chi_{\text{Plas}}$ times the phonon susceptibility $\chi_{\text{Phon}}$ leading to

$$I\left(\omega, R_0\right) = -\operatorname{Im}\left[M_0^2 \chi_{Plas}^2(R_0)\, \chi_{Phon}\right] \qquad \text{(S5)}$$

with

$$M_0^2 = \left|A_{local}^2 / A^2\right|^2 g^2 \ . \qquad \text{(S6)}$$

$A_{local}^2$ is representing the local field enhancement, which we estimate to be of the order of 10 $A^2$. The plasmonic susceptibility can be approximated by (ref [12])

$$\chi_{Plas}(R_0) = \frac{1}{\omega^2 - \left(2\varepsilon_{k,m,r}(R_0)\right)^2 + 2i\dfrac{\varepsilon_{k,m,r}(R_0)}{\tau_k}} = \chi_{Plas}^{\text{Re}} + \chi_{Plas}^{\text{Im}} \qquad \text{(S7)}$$

so that

$$\chi_{Plas}^2(R_0) = \left(\chi_{Plas}^{\text{Re}}\right)^2 + \left(\chi_{Plas}^{\text{Im}}\right)^2 \qquad \text{(S8)}$$

is always real. The imaginary part required for equation (S5) to give a finite intensity results from the phonon susceptibility

$$\chi_{Phonon}\left(\omega_0, \Gamma\right) = \frac{1}{\omega^2 - \omega_0^2 + 2i\Gamma} \ . \qquad \text{(S9)}$$

In this sense the dominant effect of the plasmonic excitation of the topological nanowire is to enhance the Raman matrix element. The plasmon is characterized by its dispersion

$$\varepsilon_{k,m,r}(R_0) = \pm C_2 \sqrt{k^2 + (1 + 2m - 2r)^2 \tilde{\Delta}^2\left(R_0\right)} \ , \qquad \text{(S10)}$$

with a gap $\tilde{\Delta}(R_0)$ in the electronic excitation spectrum according to

$$\tilde{\Delta}(R_0) = \frac{C_1}{C_2}\frac{1}{2R_0} = \frac{\alpha}{d} \quad . \tag{S11}$$

The parameters $C_1$ and $C_2$ represent the inter-spin to inter-orbital coupling constants. For exact particle-hole symmetry they are identical with values of 3.33 eV Å taken from literature.[10] The plasmonic dispersion is key for the calculation of equation (S8). For fixed momentum, i.e. fixed photon energy it depends critically on the diameter of the nanowire due to equation (S11). It thus makes sense to plot the plasmonic energy as a function of diameter for a fixed momentum that is compatible with the wavelength of the photons. Exemplary curves are given in Fig. S10(b). With this dispersion and with a plasmonic life time of 500 ps we can now calculate the square of the plasmonic susceptibility according to equation (S8) in Fig. S10(c). We also denote as black dashed lines the respective energies of the two phonons that each would be described by equation (S9). However, it is already clear from Fig. S10(c) that the multiplication of the plasmonic susceptibility with the phonon susceptibility will lead to a strongly diameter dependent Raman matrix element with the strongest intensity when the wire diameter dependent plasmon energy matches the phonon energy. From this we would also clearly expect that the low-energy $E^2_g$-phonon mode gets enhanced at a larger diameter prior to the $A^2_{1g}$-mode at higher energies, which will experience its largest resonance enhancement at smaller diameters. The bare phonon parameters required for our model can be taken from fits to e.g. the data from a flake. These fits and parameters are given in Fig. S10(d). With these parameters, we can now calculate the Raman spectra as function of wire diameter as shown in Fig. S10(e). As shown in the main text this simple model accurately describes the intensity variation of both phonon modes due to the wire diameter dependent interference of a plasmon that is described by the dispersion given in equation (S10). Besides the wire diameter the dispersion of the plasmons in a cylindrical nanowire is critically dependent on the magnetic flux along the wire axis. The calculation of equation (S8) for different fractions of a flux quantum coupled along the axis of the wire is shown Fig. S10(f). The plasmonic susceptibility is shifting according to equation (S10) and, thus, reduces the interference between phonon and plasmon susceptibilities leading to a suppression of the phonon intensities as described in the main text and seen in section SI 4 for a 90 nm wire. With these arguments, we have shown that the phonon intensities in of 1D topological surface states in nanowires are determined by a plasmonic excitation following the quasi-particle dispersion (equation (S10)). It is worthwhile to remark, that these results are further supported by the observed phonon self-energy effects. The enhanced Fano-parameter indicates the presence of a low energy electronic state coupling to the phonons. The real part of equation (S8) would push the energy of the phonon towards higher Raman shifts resulting in the observed hardening (see Table S2) and the imaginary part would result in an enhanced broadening. These effects are reminiscent to effects observed in high temperature superconductors, where a low energy gap in the electronic continuum leads to a hardening and broadening in case the phonon mode energy is higher than the energy of the superconducting gap.[13-17] Nevertheless, a detailed theory accounting for an ab-initio self-consistent calculation is not intended and missing as our approach has a semi-phenomenological character due to the use of eq (S1) and eq (S2), which are approximated for a constant electronic continuum. The electronic spectrum of a SBP, however, cannot be approximated by such an assumption.

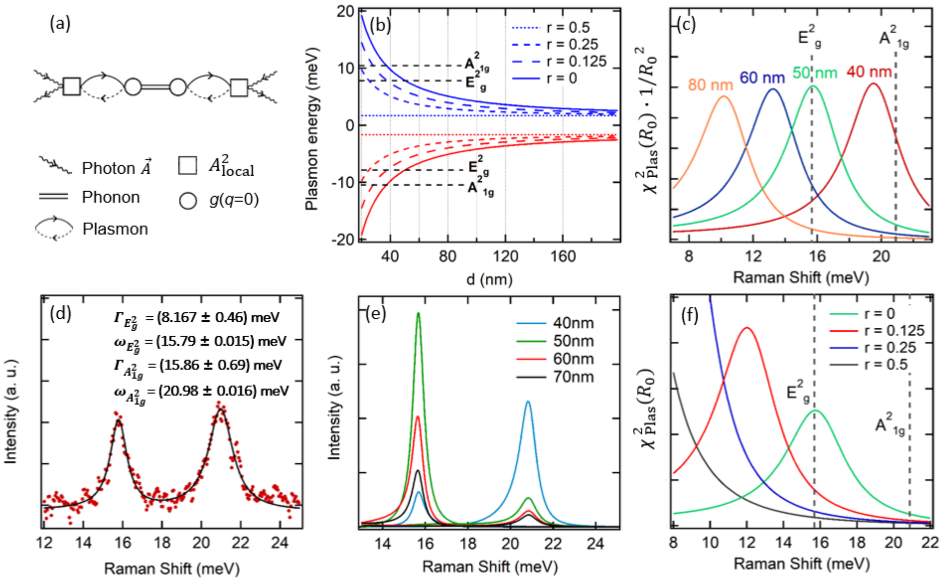

**Fig. S10:** (a) Raman scattering as Feynman diagram showing a four photon Greens function. Wavy lines represent the photon field represented by its vector potential. The squares reprensent the $A^2$ term in first order perturbation theory to a free particle. The polarization bubbles represent the plasmonic excitations and the double solid line the phonon. Circles represent the electron-phonon coupling. See text for more details. (b) Plasmon dispersion with finite and fixed *k* as a function of wire diameter. (c) Plasmonic susceptibilities as a function of wire diameter. (d) Raman measurements of $Bi_2Se_3$ flakes and fit to the phonon susceptibilities. (e) Dependence of the Raman intensity as a function of wire diameter for the $E^2_g$- and $A^2_{1g}$-modes when using the susceptibilties of (c) and (d). (f) Magnetic field dependence of the plasmonic susceptibility at a 50 nm diameter wire for different ratios r of a flux quantum coupled along the wire axis.

## *SI 8 Nanowires and Magneto-Transport Measurements*

Electrical transport measurements were performed on the device shown in Fig. S11. A Si wafer with 300 nm $SiO_2$ was cleaned with acetone, isopropanol, de-ionized water, dried with nitrogen, and was pre-baked at 115 °C for 60 s. The substrate was spin-coated with positive photoresist S1813 (Rohm and Haas electronic materials LLC) at 4000 rpm for 30 s and pre-baked at 115 °C for 60 s before exposing it to Heidelberg µPG 101 Laser Writer to imprint the mask of the contacts for precise identification of nanowires. The pattern was developed with microposit MF-319 developer (Dow Europe GmbH, c/o DSP Germany), gold coated in a sputtering chamber and removed with remover mr-Rem 400 (micro resist technology GmbH) to expose the device markers shown in Fig. S11 (a). A $Bi_2Se_3$ nanowire of about 260 nm diameter (see Fig. S11 (b)) was transferred on the design using a custom-made micromanipulator. The device was then subject to a second spin-coating step to manufacture the Cr-contacts on the nanowire. With precise alignment the electrode design was written on the nanowire, developed, and then etched with argon in the reactive ion etching system in order to remove the native oxide layer/photoresist on the surface of the nanowire before making the Cr coating for proper electrical contact (see Fig. S4 (c)). The etched nanowire was quickly transferred into the Physical Vapor Deposition (PVD) system to make Cr contacts on the nanowire and to minimize oxidation of the nanowire surface. Finally, the remaining photoresist was removed. Electrical magneto-transport measurements of the nanowire were performed in a PPMS Dynacool (Quantum Design) system equipped with the Electrical Transport Option (ETO) in magnetic field between ±9T from 300 K down to 2 K. Prior to the measurement, the samples had been glued to the standard measurement puck and thin Al wires had been bonded (TPT wire bonder) from the macroscopic bonding pads to the channel pads of the puck. Subsequently, 2-probe and 4-probe room temperature resistance measurements had been performed by utilizing the sample puck clamped on the PPMS user bridge (Quantum Design) in combination with a source-measurement-unit (Rohde&Schwarz, 6241A) to check the contacts.

The temperature dependent transport measurements are shown in Fig. S11 (c). The linearly decreasing resistance indicates the contact to metallic-like surface channels at the surface of the wire. In Fig. S11 (d) we reveal the ohmic behavior of the contacts at low temperatures that were used for the magneto-transport measurements shown in Fig. S12.

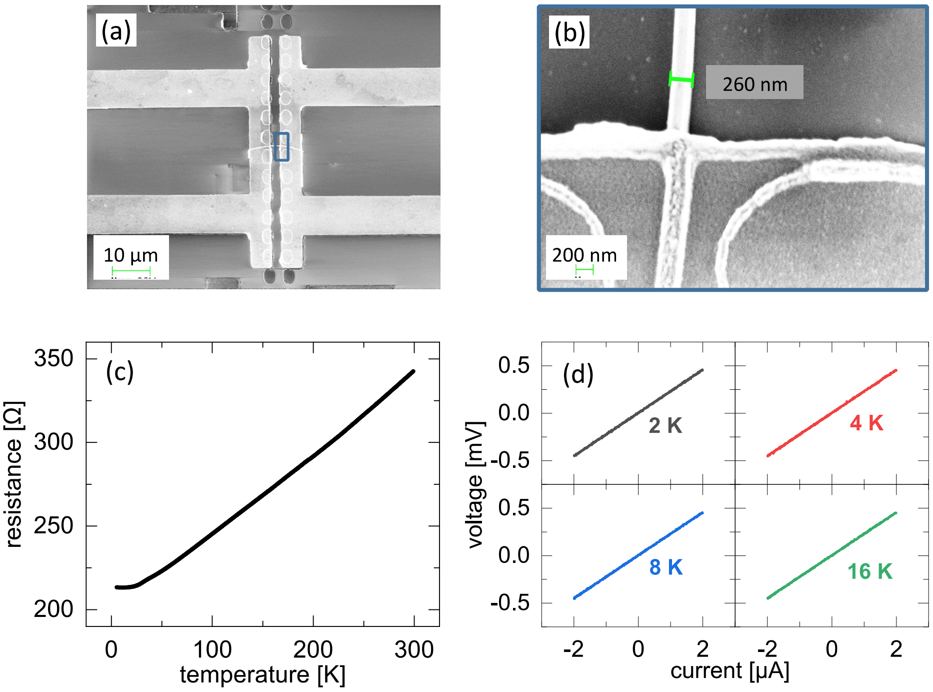

**Fig. S11:** Device for transport measurements. The SEM image shows the nanowire (horizontal line in the center) connected to the Cr contacts. (b) Shows the blue rectangle indicated in (a) to reveal a diameter of ~ 260 nm for the nanowire. (c) Resistance vs temperature plot. The resistance decreases with decreasing temperature indicating metallic transport channels. (d) Each panel shows the I-V curve of the setup for 2, 4, 8, and 16 K, respectively. The linearity of the curves confirms ohmic contacts.

Fig. S12 (a) shows the basic experimental configuration for the Shubnikov-de Haas oscillations measuring the resistance along $R_{xx}$ while the magnetic field is perpendicular to the plane of the Si-wafer used to fabricate the device. The temperature dependent magneto-transport measurements in the low-field limit are shown in Fig. S12(b). The Weak-Anti-Localization (WAL) effect can be observed for 2 K and is decreasing for increasing temperatures. The occurrence of the WAL effect proves the strong spin-orbit-coupling, which can be considered as a requirement for the presence of Dirac states in topological insulators.[18] From the magneto-transport data a polynomial fit was subtracted in order to unveil the resistance oscillations.[4] The resulting resistance in the high-field limit for the 4 K magnetoresistance measurement are shown in Fig. S12 (c). Vertical grey bars indicate the position of the minima. According to Bäßler *et al.* [19] the minima can be indexed and related to the Landau level *n*. In lower fields the dependence of the occupied Landau level with the magnetic field can be described by 2D tpological surface states giving rise to a linear dependence between index and the inverse magnetic field.

$$n_{2D} = \frac{\hbar k_F^2}{2e} \frac{1}{|B|} - \gamma \quad . \qquad \text{(S12)}$$

*n* is the index level, e the charge of an electron, $k_F$ is the Fermi wave vector, *B* the magnetic field, and $\gamma$ as the y-axis intercept. The index plot showing *n* as a function of inverse field and a linear fit according to eq. (S12) are shown as solid red line in Fig. S12(d). We can derive $k_F = (1.24 \pm 0.42) * 10^{-2}$ Å$^{-1}$ . With this value an effective carrier concentration can be estimated to be n = $(k_F)^2/2\pi = 4.9\ 10^{11}$ cm$^{-2}$, which puts the samples in agreement with the HRTEM studies in the low doping range for effectively stoichiometric samples. For Dirac states one would expect an intercept $\gamma$ at 0.5 , i.e. not an integer value. The fit yields $\gamma = 0.58 \pm 0.52$. One could interpret this also as supporting for our observations that we are dealing indeed with Dirac states. However, the large error bars already indicate that this value is rather susceptible to the details of the fit and should be considered with caution. For higher fields the index needs to be fitted with an expression in agreement with an effective 1D behavior.

$$n_{1D} = \frac{\hbar k_F^2}{2e} \frac{1}{|B|} \frac{1}{\sqrt{1 - \left( \frac{\hbar k_F}{er|B|} \right)^2}} - \gamma \quad . \qquad \text{(S13)}$$

With *r* being the radius of the wire. In the 2D limit, when r becomes large, eq. S13 can be approximated by eq. S12. The radius *r* of the nanowire is 130 nm (see Fig. S12 (b)). For large fields and a finite radius eq. S13 leads to a deviation from the linear behavior as can be clearly seen in Fig. S13 (d). Fitting eq. S13 to the high field data leads to $k_F = (1.24 \pm 0.42) * 10^{-2}$ Å$^{-1}$ ,i.e. a value for the Fermi vector close to the value obtained from the fit in the low field 2D limit. The intercept yields 0.56 ± 1.55 and is less reliable than the value obtained from the 2D fit. Nevertheless, our results show a very good agreement with Bäßler *et al.* indicating that we have fabricated nanowires in the low doping range. This view is also supported by our Raman data that we could model with effectively only one occupied sub-band and by the detailed HRTEM study showing samples in core-shell geometry with effectively exact stoichiometry. Note, other origins of resistance oscillations, such as universal conduction fluctuations, have been discussed in literature before and could complicate the data analysis.[20] Future studies to unveil electrical-transport phenomena on these ondimensional nanowires are on-going and would be in anyway beyond the scope of this Raman-based analysis.

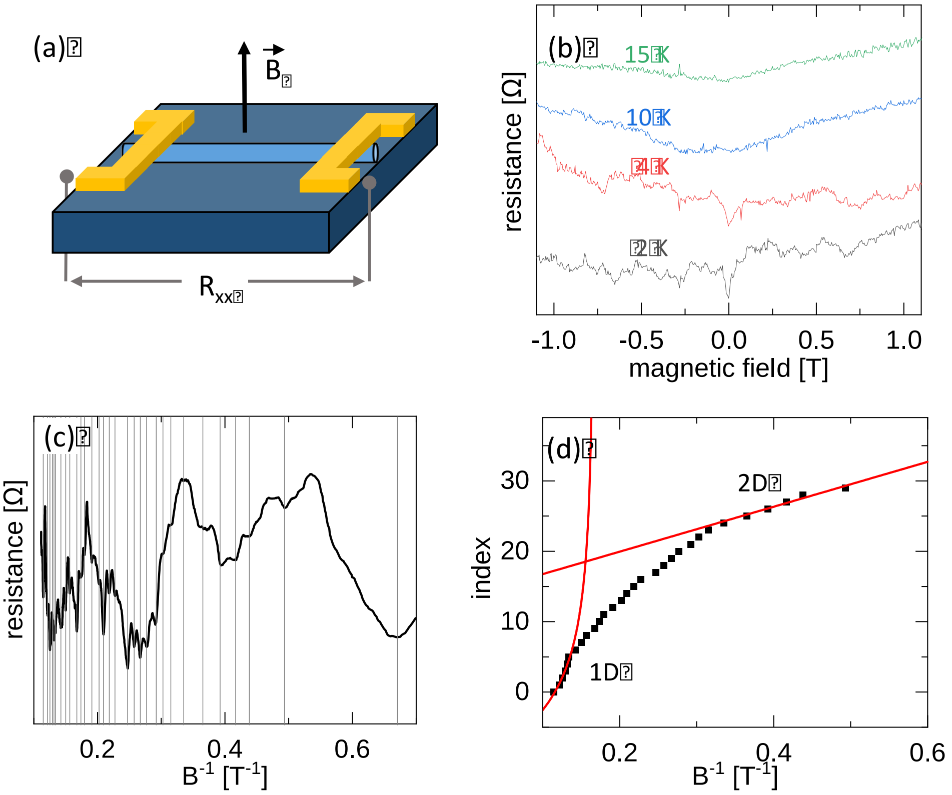

**Fig. S12:** Magnetoresistance measurements at low temperatures. (a) Experimental configuration to measure the Shubnikov-de Haas oscillations in $R_{xx}$. The magnetic field is aligned perpendicular to the wire and the resistance is measured parallel to the long axis of the wire. (b) Magnetoresistance curves in the low-field limit. The Weak-Anti-Localization (WAL) effect can be observed for 2 K and is decreasing for increasing temperatures. (c) Data set for the 4 K magnetoresistance measurement in the high-field range. Vertical grey bars indicate the position of the minima. (d) Index plot of the respective minima $n$ of the 4 K measurement vs the inverse magnetic field $B^{-1}$. The fits (red solid lines) are conducted with equations (S12) an (S13) for the magneto-transport in the 2D and 1D limit respectively.

## *SI 9 Literature*

[1] Yan, Y. *et al.* Synthesis and Quantum Transport Properties of Bi2Se3 Topological Insulator Nanostructures. Sci. Rep. **3**, 1264 (2013).

[2] Peng, H. *et al.* Aharonov–Bohm interference in topological insulator nanoribbons. *Nat. Mater.* **9**, 225–229 (2010)

[3] Shin, H. et al. The Surface-to-volume ratio: a key parameter in the thermoelectric transport of topological insulator of Bi2Se3 nanowires. Nanoscale Comm. **8**, 13552 (2016)

[4] Buchenau, S. et al. Symmetry breaking of the surface mediated quantum Hall Effect in Bi2Se3 nanoplates using Fe3O4 substrates. 2D Mater. 4, 015044 (2017).

[5] Kong, D. et al. Topological Insulator Nanowires and Nanoribbons. Nano Lett. **10**, 329 – 333 (2010).

[6] Han, M. et al. Two-step vapor transport deposition of large-size bridge-like Bi2Se3 nanostructures. CrystEngComm. **17**, 8449 – 8456 (2015).

[7] Liu, C. et al. Topological insulator Bi2Se3 nanowire/Si heterostructure photodetectors with ultrahigh responsivity and broadband response. J. Mater. Chem. C. **4**, 5648 – 5655 (2016).

[8] Hamdou, B. et al. The influence of a Te-depeleted surface on the thermoelectric transport properties of $Bi_2Te_3$ nanowires. Nanotechnology **26**, 365401 (2014).

[9] Schulz, B. *et al.* Fully reflective deep ultraviolet to near infrared spectrometer and entrance optics for resonance Raman spectroscopy. *Rev. Sci. Instrum.* **76**, 073107 (2005).

[10] P. Iorio, C.A. Perroni, and V. Cautadella, Plasmons in topological cylinder nanowires, Phys. Rev. B **95**, 235420 (2017).

[11] A. Kawabata, Green Function Theory of Raman Scattering, Journal of the Physical Society of Japan **30**, 68 (1971).

[12] R.D. Mattuck, A Guide to Feynman Diagrams in the Many Body Problem, MacGraw-Hill Book Company (1967).

[13] S.L. Cooper, M.V. Klein, Light scattering studies of the low frequency excitation spectra of high temperature superconductors, Comments Cond. Mat. Phys **15**, 99-124 (1990).

[14] A. Bock *et al.* Anomalous self-energy effects of the $B_{1g}$ phonon in $Y_{1-x}(Pr,Ca)_xBa_2Cu_3O_7$ films, Phys. Rev. B **60**, 3532-3537 (1999).

[15] B. Friedl, C. Thomsen, M. Cardona, Determination of the superconducting gap in $RBa_2Cu_3O_{7-\delta}$, Phys. Rev. Lett **65**, 915 (1990).

[16] T.P. Deveraux, A. Virosztek, and A. Zawadowski, Charge-transfer fluctuation, d-wave superconductivity, and the $B_{1g}$ Raman phonon in cuprates, Phys. Rev. B **51**, 505 (1995).

[17] X.K. Chen *et al.,* Oxygen-concentration dependence of the Raman continua in $YBa_2Cu_3O_y$ single crystals, Phys. Rev. B **48**, 10530 (1993).

[18] B. Hamdou, J. Gooth, A. Dorn, E. Pippel, and K. Nielsch, Aharonov-Bohm oscillations and weak antilocalization in topological insulator $Sb_2Te_3$ nanowires, Appl. Phys. Lett. **102**, 223110 (2013).

[19] S. Bäßler, B. Hamdou, P. Sergelius, A.-K. Michel, R. Zierold, H. Reith, J. Gooth, and K. Nielsch, One-dimensional edge transport on the surface of cylindrical $Bi_xTe_{3-y}Se_y$ nanowires in transverse magnetic fields, Appl. Phys. Lett. **107**, 181602 (2015).

[20] J. Kölzner *et al.*, Phase-coherent loops in selectively-grown topological insulator nanoribbons, Nanotechnology **31**, 325001 (2020).

# Appendix D

# Supplementary Information: Plasmonic hot carrier injection from single gold nanoparticles into topological insulator $Bi_2Se_3$ nanoribbons

# Supplementary Information

## Plasmonic Hot Carrier Injection from Single Gold Nanoparticles into Topological Insulator $Bi_2Se_3$ Nanoribbons.

Christian Nweze,*[a] Tomke E. Glier,[a] Mika Rerrer,[a] Sarah Scheitz,[a] Yalan Huang,[b] Robert Zierold,[b] Robert Blick,[b] Wolfgang J. Parak,[b] Nils Huse,[b] and Michael Rübhausen*[a]

[a]Institut für Nanostruktur- und Festkörperphysik, Center for Free Electron Laser Science (CFEL), Universität Hamburg, Luruper Chaussee 149, 22761, Hamburg, Germany

[b]Institut für Nanostruktur- und Festkörperphysik, Center for Hybrid Nanostructures (CHyN), Universität Hamburg, Luruper Chaussee 149, Hamburg, 22761 Germany

### A. Experimental procedure

Single crystalline $Bi_2Se_3$ nanoribbons were grown in a two-heating zone furnace in a chemical vapor deposition (CVD) set up. The furnace was equipped with a quartz tube of diameter 2.5 cm. The $Bi_2Se_3$ nanoribbons were grown on silicon ⟨100⟩ substrates with native oxide ($SiO_2$) layer. We followed a general approach in CVD method [1]–[3] with full optimization for growth of $Bi_2Se_3$ nanoribbons. The growth process involves: (a) cleaning the 1x1 cm silicon ⟨100⟩ substrates in Piranha solution and rinsing in deionized water in order to remove dirt, (b) functionalizing the substrates with 0.1% w/v aqueous poly-L-lysine to enhance gold attachment to the substrates, (c) dipping the substrates in colloid solution of gold (50 nm diameter) for 5 s, and (d) growth of $Bi_2Se_3$ nanoribbons on the functionalized substrates. The source material is a commercial grade $Bi_2Se_3$ granular (Sigma-Aldrich, purity 99.999%). 0.2 g of granular $Bi_2Se_3$ was used for the synthesis. The granular $Bi_2Se_3$ was placed in an alumina boat and loaded at the upstream zone of the furnace and the gold coated 1x1 cm silicon substrates were loaded at the downstream zone of the furnace. The tube was pumped to a pressure of 40 mTorr, and flushed multiple times with ultrapure argon gas to minimize oxygen contamination in the quartz tube. For synthesis, the downstream and upstream zones were heated in 1 hour from room temperature to 440 $^oC$ and 540 $^oC$ respectively. The carrier gas flow rate and the pressure were set to 30 standard cubic centimeters per minute and 780 mTorr, respectively. The reaction time was 1 hour. In order to provide a selenium environment and to protect the surface of $Bi_2Se_3$ with selenium powder, after the reaction, the argon flow was switched off and the system was allowed to cool down to room temperature in 2.5 h. To validate the quality of the grown samples, various characterization techniques were employed. A custom-made x, y, z – positioner micro-manipulator was used to transfer the nanoribbons to a custom-made silicon finder grid with 225 fields of 100 µm x 100 µm. The positioner has 51 mm long tungsten picoprobe tips (T-4-10) with a wire shaft diameter of 10 µm, a point radius < 0.1 µm, and a tip length of 3.3 mm. The atomic force microscopy (AFM, Q-Scope 250 model with 40 µm x 40 µm scan head with a lateral and vertical resolutions of 0.6 nm and 0.05 nm, respectively) was used to determine the thickness (height) of the nanoribbons. Scanning electron microscope (SEM, ZEISS ΣIGMA) was used to determine the width of the nanoribbons. Energy dispersive x-ray spectroscopy (EDX, ZEISS) was used to determine the stoichiometry of the nanoribbons.

## B. Synthesis and characterization of gold nanoparticles

The synthesis of the spherical citrate-stabilized gold nanoparticles (AuNPs) of different sizes was prepared as previously reported [4]. According to the chosen growth speed of the AuNPs in our method, the mean core size $\mathrm{d_{c,TEM}}$ of the AuNPs was expected to be around 100 nm. The AuNPs used in this manuscript were double phase-transferred and finally coated with PMA-g-dodecyl, an amphiphilic polymer which is based on a backbone of poly(isobutylene-alt-maleic anhydride), functionalized with dodecylamine [4].

The UV/vis absorption spectra of the PMA-g-dodecyl coated AuNPs as dispersed in water was recorded with an Agilent 8453 spectrophotometer as previously reported [4]. NPs were dispersed in water, see Fig. S1(a). The wavelength of the surface plasmon peak was $\lambda_{\mathrm{SPR}} = 578$ nm (table S1)

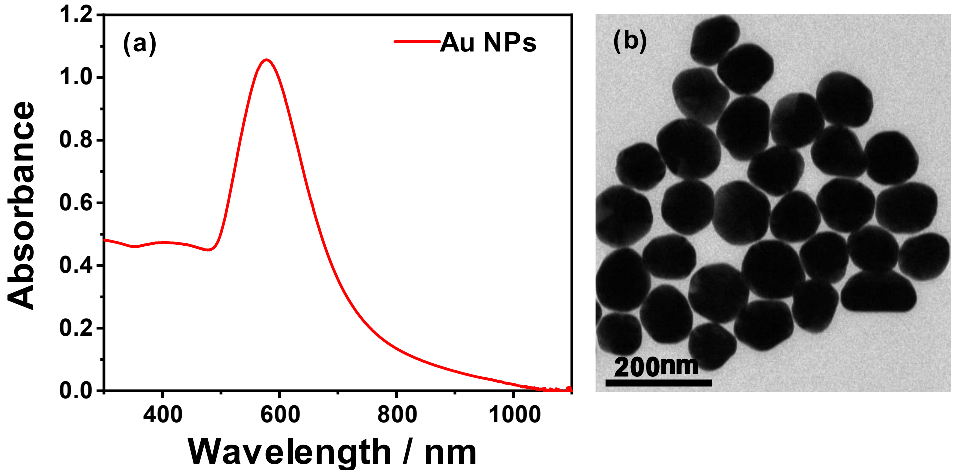

**Figure S1**. (a) UV/vis absorbance spectrum of the AuNPs. (b) Representative TEM image of the AuNPs.

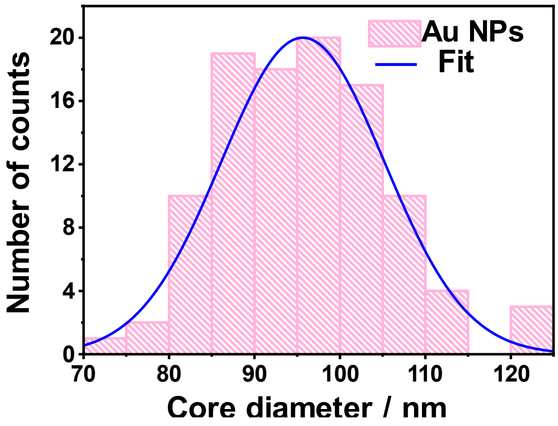

**Figure S2.** Histogram of the core diameter distribution N ($d_{c,TEM}$) as determined from the TEM images, and a corresponding Gaussian fit. The mean value of $d_{c,TEM}$ as displayed in Table S1 was calculated from 100 AuNPs.

Transmission electron microscopy (TEM) images were used to investigate the size distribution of the AuNP diameter. In order to determine the size distribution of the core diameter $d_{c,TEM}$ of the AuNPs, $d_{c,TEM}$ was determined as mean value from 100 NPs in the TEM images using the ImageJ software [4]. Illustrative TEM images of the AuNPs are displayed in Fig. S1(b) and the obtained size distribution histograms and further characterization can be seen in Fig. S2 and table S1.

**Table S1**. Characterization table of the AuNPs

| $\lambda_{SPR}$ /nm | $d_{c,TEM}$ / nm | $d_{h(N)}$ / nm | $d_{h(V)}$ / nm | $d_{h(I)}$ / nm | ζ /mV |
|---|---|---|---|---|---|
| 578 | 95.7±9.6 | 76.9 ± 3.7 | 127.5 ± 3.4 | 130.3 ± 2.7 | -39.0 ± 0.4 |

In order to determine the hydrodynamic diameters $d_h$ of the AuNPs as dispersed in water, dynamic light scattering (DLS) was used [4]. Also, the zeta potential ζ of the AuNP solution was measured with laser Doppler anemometry (LDA). DLS and LDA were carried out using a Malvern Zetasizer ZS instrument. Data are presented in Fig. S3 and table S1.

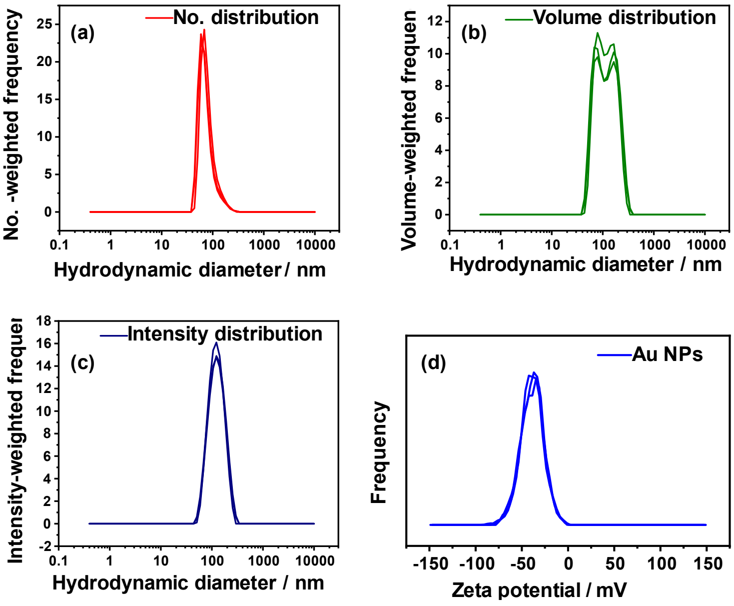

**Figure S3**. Distribution the hydrodynamic diameter $d_h$ of the AuNPs recorded by DLS based on (a) the number distribution $N(d_{h(N)})$, (b) the volume distribution $N(d_{h(V)})$, and (c) the intensity distribution $N(d_{h(I)})$. (d) Zeta potential of the AuNPs. The obtained mean values for the hydrodynamic diameters and zeta potential are shown in Table S1.

## C. Decorating the $Bi_2Se_3$ nanoribbons with gold nanoparticles

10 µL of the dispersed AuNPs in water was drop cast on the $Bi_2Se_3$ nanoribbons and dried before characterization.

## D. Characterization

$Bi_2Se_3$ nanoribbons were characterized before the Raman study. The width of the nanoribbons was measured via AFM and SEM. The exemplary SEM images for the $Bi_2Se_3$ nanoribbons of width 210 nm and 292 nm (thickness 100 nm and 90.1 nm) are shown in Figs. S4 (b and c), respectively. The quantitative analysis of the SEM-EDX data collected from the nanoribbons shows the correct stoichiometry (2:3 (Bi:Se)) as shown in Fig. S4 (a). The silicon peak in the spectra comes from the silicon substrate. The thickness of the $Bi_2Se_3$ nanoribbons was obtained with an AFM. Figs. S5 (a - d) show exemplary AFM images of the $Bi_2Se_3$ nanoribbons of thickness 47 nm and 90 nm.

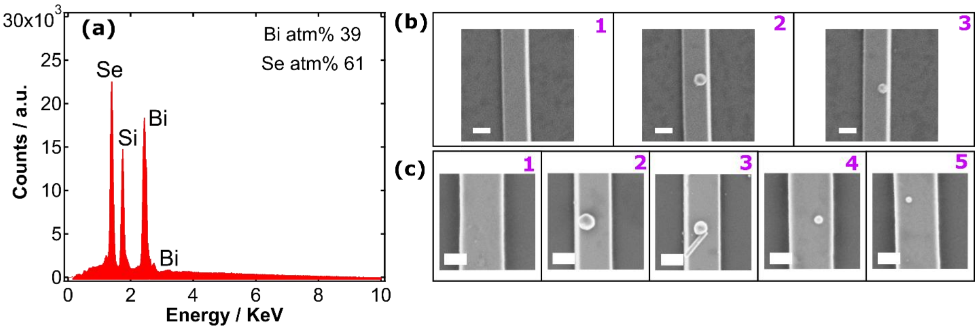

**Figure S4**. (a) EDX spectra acquired from $Bi_2Se_3$ nanoribbons. Quantitative analysis of the EDX data shows a composition of 39 atm% Bi and 61 atm% Se. The silicon peak comes from the silicon substrate. Exemplary SEM images of $Bi_2Se_3$ nanoribbons with (b) width of 210 nm and thickness of 100 nm, (c) width of 292 nm and thickness of 90.1 nm are shown. The $Bi_2Se_3$ nanoribbons have single AuNP of different sizes. The scale bar represents a length of 200 nm.

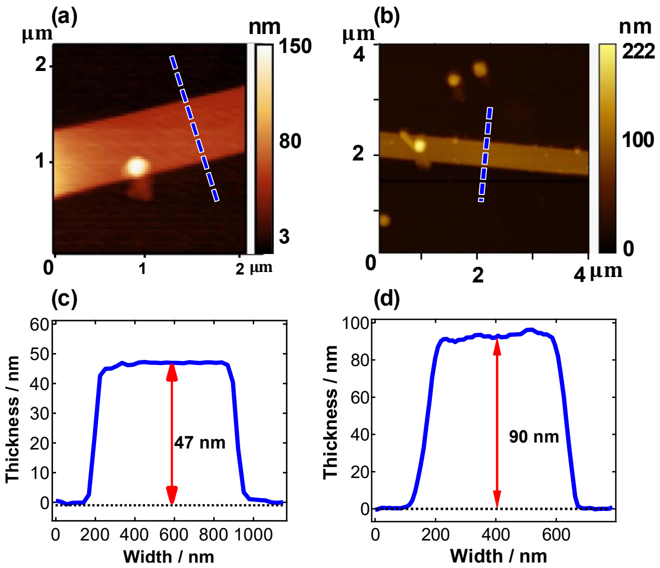

**Figure S5.** Exemplary AFM images and height profiles. The height of (c) 47 ± 1 nm, and (d) 90 ± 2 nm was obtained from the AFM images (a) and (b), respectively. Blue dotted lines indicate the location of the height profiles.

## E. Crystal structure, Raman tensors and atomic displacements of $Bi_2Se_3$

The crystal structure, Raman tensors and atomic displacements of the Raman active modes in $Bi_2Se_3$ are shown in Fig. S6. The Raman tensors show that the $E_g$ – mode has non-vanishing off-diagonal elements in comparison with the vanishing components in the off-diagonal elements of $A_{1g}$ – mode [5].

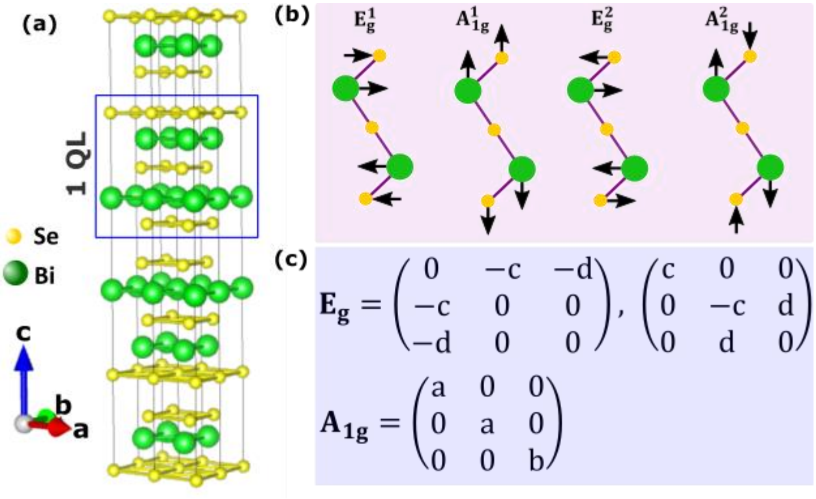

**Figure S6.** (a) Crystal structure showing quintuple layer, (b) atomic displacement of Raman active modes showing in and out of plane vibrations and (c) Raman tensors of $Bi_2Se_3$.

## F. Raman study

The $Bi_2Se_3$ nanoribbons were pre-characterized before Raman study. Raman spectroscopy of Au decorated single nanoribbons was carried out at room temperature with a custom-made micro-Raman set-up [6], [7]. With the aid of a 50x objective (Plan Apo HR, Mitutoyo, Japan), with numerical aperture (NA) of 0.75, the backscattered Raman signal was collected and focused into the entrance objective of the fully reflective UT-3 spectrometer [6]. The beam spot size of the micro-Raman is between 211 ± 3 – 389 ± 3 nm depending on the excitation wavelength. For a 633 nm wavelength, the full width at half maximum (FWHM) is 211 ± 3 nm. Fig. S7 shows an exemplary image of a 633 nm laser spot focused on silicon substrate and the intensity cuts in four different directions through the laser spot. The intensity is fitted with a Gaussian profile. The measurement was done in back-scattering configuration while employing Porto notation $\bar{Z}(XX)Z$ configuration [8] (Fig. S8(b)). The spectra were acquired in 20 mins. In order to exclude laser heating of the samples, the laser power on the sample surface is kept less than 50 µW. Several pre-test measurements were carried out on different $Bi_2Se_3$ nanoribbons before the actual measurement. The laser sources used for the resonance study were (a) red laser, 633 nm wavelength (Gas, 05-LHP-123-496 HeNe), (b) yellow laser, 594 nm wavelength (Diode, OBIS 594LS 1233468), (c) greenish-yellow laser, 560 nm wavelength (Diode, OBIS 561LS 1223779) and (d) green laser, 532 nm wavelength (Diode, Millenia Pro 10sJS). Note that the pre-test measurement was done on the $Bi_2Se_3$ nanoribbons from the same synthesis used in this study.

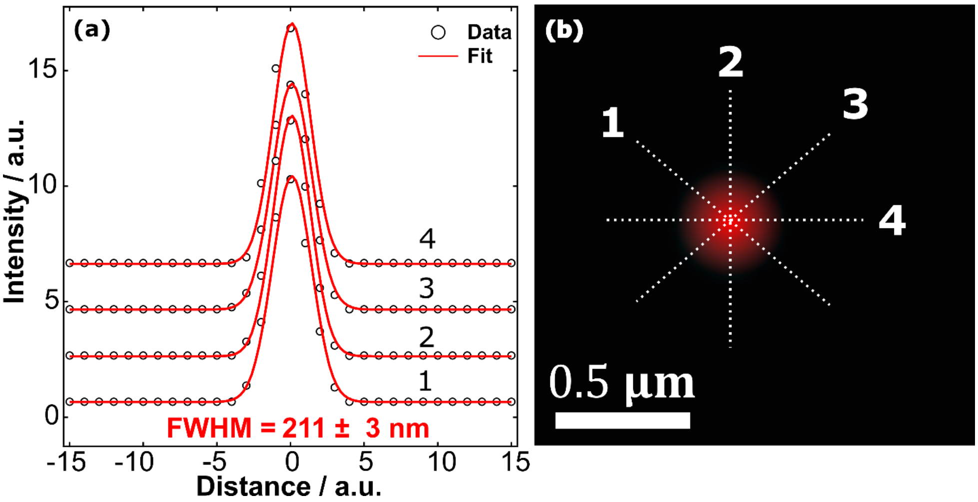

**Figure S7**. Exemplary red laser beam spot diameter. (a) The intensity profile for four different directions (1-4) fitted with a Gaussian profile. The resulting FWHM has an average value of 211 ± 3 nm. (b) 2D image of red laser spot showing intensity cuts in four different directions.

## G. Polarization dependence study

We conducted a polarization dependence study on our sample. The angle between the incident and scattered polarized light is tuned from 0° – 90°. For $\bar{Z}(XX)Z$, the angle is 0° and it corresponds to the x-x component of the Raman tensors (Fig. S8 (b)). For $\bar{Z}(YX)Z$, the angle is 90° and it corresponds to the y-x component of the Raman tensors (Fig. S8 (c)). Fig. S5(a) shows the Raman spectra of $Bi_2Se_3$ for On_AuNP (blue) and Off_AuNP (red) positions. The result shows that the intensities of $A^1_{1g}$ and $A^2_{1g}$ – modes have reduced considerably for the perpendicular polarized state in comparison to the parallel polarized state. Furthermore, the intensity of the $E^2_g$ remains unaltered in adherence to the Raman tensor of Fig. S6(c). This dependence of $A^1_{1g}$ and $A^2_{1g}$ – modes on polarization indicates that our $Bi_2Se_3$ sample is single crystalline [9]. Note that the sensitivity of the UT-3 spectrometer at 633 nm wavelength is 41% and 4% for horizontal (parallel) and vertical (perpendicular) polarized light, respectively [6].

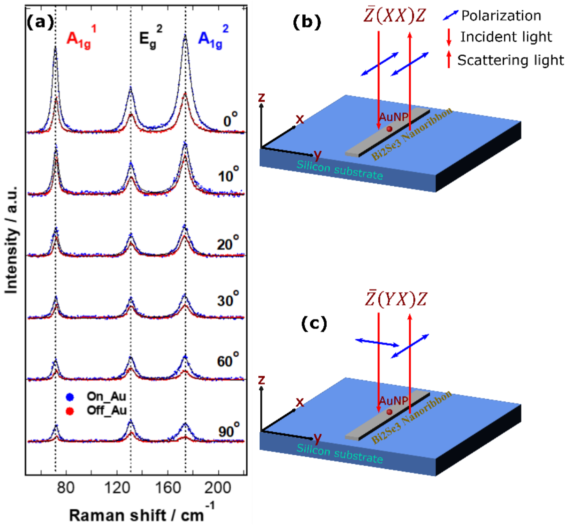

**Figure S8**. Polarization dependence Raman studies of $Bi_2Se_3$ nanoribbon with a thickness of 83 nm and width of 300 nm and decorated with a single AuNP of diameter 128 nm. (a) Raman spectra of $Bi_2Se_3$ nanoribbon at different polarized angles. The spectra acquired in On_AuNP and Off_AuNP positions are represented in blue and red colours, respectively. The parallel and perpendicular polarization of the incident and scattered lights are shown in (b) and (c), respectively.

## H. Ratio between the FWHM of $A_{1g}^{2}/A_{1g}^{1}$ and $E_{g}^{2}/A_{1g}^{1}$ modes

The ratio between the FWHM of $A_{1g}^{2}/A_{1g}^{1}$ (blue symbol) and $E_{g}^{2}/A_{1g}^{1}$ (black symbol) as a function of distance from the AuNP (Fig. S9). The solid blue and black lines are the Gaussian fit to the data. The broadening of the phonon modes at On_Au position shows strong electron-phonon interaction as a result of high density of hot injected electrons around the AuNP. The density of these hot electrons decreases with distance from AuNP along the nanoribbon and hence, the electron phonon interaction weakens on scanning away from the AuNP.

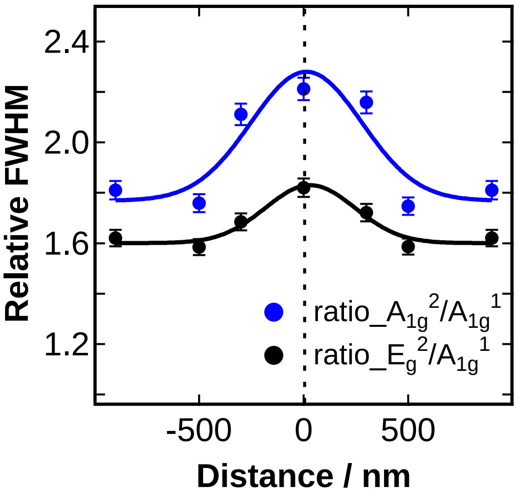

**Figure S9**. Plot of the relative FWHM as a function of distance from the AuNP. The blue and black symbols represent the ratio of $A_{1g}^{2}/A_{1g}^{1}$ and $E_{g}^{2}/A_{1g}^{1}$, respectively. The solid lines represent the Gaussian fit to the data.

# Appendix E

# Eidesstattliche Erklärung

Hiermit versichere ich an Eides statt, die vorliegende Dissertationsschrift selbst verfasst und keine anderen als die angegebenen Hilfsmittel und Quellen benutzt zu haben.

Die eingereichte schriftliche Fassung entspricht der auf dem elektronischen Speichermedium.

Die Dissertation wurde in der vorgelegten oder einer ähnlichen Form nicht schon einmal in einem früheren Promotionsverfahren angenommen oder als ungenügend beurteilt.

Hamburg, den 23.08.2022 Unterschrift: